Cavity Spintronics

Foundations and Applications of Spin-Photon Hybridization

by

Michael Harder

A Thesis submitted to the Faculty of Graduate Studies of
The University of Manitoba in partial fulfillment of the
requirements for the degree of

Doctor of Philosophy

Department of Physics and Astronomy
The University of Manitoba
Winnipeg, Canada
August 2018

Cavity Spintronics

Foundations and Applications of Spin-Photon Hybridization

by

Michael Harder

Examining Committee

Dr. Can-Ming Hu, Supervisor
(Department of Physics and Astronomy)

Dr. Gerald Gwinner, Departmental Member
(Department of Physics and Astronomy)

Dr. Jesko Sirker, Departmental Member
(Department of Physics and Astronomy)

Dr. Lotfollah Shafai, External Member
(Department of Electrical and Computer Engineering)

Dr. Robert Camley, Outside Member
(Department of Physics and Energy Science, University of Colorado Colorado Springs)

ABSTRACT

Light-matter interactions lie at the heart of condensed matter physics, providing physical insight into material behaviour while enabling the design of new devices. Perhaps this is most evident in the push to develop quantum information and spintronic technologies. On the side of quantum information, engineered light-matter interactions offer a means to drastically enhance coherence rates, while at the same time new insights into spin-photon manipulation would benefit the development of spintronic technologies. In this context the recent discovery of hybridization between ferromagnets and cavity photons has ushered in a new era of light-matter exploration at the crossroads of quantum information and spintronics. The key player in this rapidly developing field of cavity spintronics is a new type of quasiparticle, the cavity-magnon-polariton. In this dissertation we explore the fundamental behaviour of the cavity-magnon-polariton and exploit its unique properties to develop new spintronic applications. To understand the physical origins of spin-photon hybridization we develop a comprehensive theoretical framework, relating the basic characteristics of hybridization to a universal model of coupled oscillators, revealing the physical origin of the coupling through electrodynamic phase correlation, and describing detailed properties through a quantum approach. Based on this foundation we have performed in depth experimental investigations of the coupled spin-photon system. We discover that the coupling will influence spin current generated through the spin pumping mechanism, demonstrating a firm link between spin-photon coupling and spintronics. We also develop several in-situ coupling control mechanisms, which offer both physical insight and a means to develop cavity spintronic technologies. As one example, we have combined our local spin current detection technique and coupling control mechanism to realize non-local spin current manipulation over distances of several centimetres. Therefore by revealing the electrodynamic nature of strong spin-photon coupling, developing new control mechanisms, and demonstrating the influence on spin current, this dissertation sets the foundation of cavity spintronics, opening the door to the implementation of strong spin-photon coupling for new spintronic and quantum information technologies.

CONTENTS

LIST OF TABLES

LIST OF FIGURES

LIST OF PUBLICATIONS

This following publications, prepared during the course of the author's doctoral studies, serve as the basis for the content presented in this dissertation:

1. **Topological properties of a coupled spin-photon system induced by damping**
   M. Harder, L. H. Bai, P. Hyde and C.-M. Hu,
   Phys. Rev. B **95**, 214411 (2017)
   arXiv:1702.04797

2. **Cavity mediated manipulation of distant spin currents using a cavity-magnon-polariton**
   L. H. Bai, *M. Harder*, P. Hyde, Z. H. Zhang, C.-M. Hu, Y. P. Chen and J. Q. Xiao
   Phys. Rev. Lett. **118**, 217201 (2017)
   arXiv:1706.00347

3. **Tuneable magnon-photon coupling in a compensating ferrimagnet - from weak to strong coupling**
   H. Maier-Flaig, *M. Harder*, S. Klingler, Z. Qiu, E. Saitoh, M. Weiler, S. Geprägs, R. Gross, S. T. B. Goennenwein and H. Huebl
   Appl. Phys. Lett. **110**, 132401 (2017)
   arXiv:1701.08969

4. **Spin dynamical phase and anti-resonance in a strongly coupled magnon-photon system**
   M. Harder, P. Hyde, L. H. Bai, C. Match and C.-M. Hu
   Phys. Rev. B **94**, 054403 (2016)
   arXiv:1606.03056

5. **Study of the cavity-magnon-polariton transmission line shape**
   M. Harder, L. H. Bai, C. Match, J. Sirker and C.-M. Hu

Sci. China Phys. Mech. Astron. **59**, 117511 (2016)

arXiv:1601.06049

6. **Spin pumping in strongly coupled magnon-photon systems**
   H. Maier-Flaig, *M. Harder*, R. Gross, H. Huebl and S. T. B. Goennenwein
   Phys. Rev. B **94**, 054433 (2016)
   arXiv:1601.05681

7. **Control of the magnon-photon coupling**
   L. H. Bai, K. Blanchette, *M. Harder*, Y. P. Chen, X. Fan, J. Q. Xiao and C.-M. Hu
   IEEE Trans. Magn. **52**, 1000107 (2016)

8. **Spin pumping in electrodynamically coupled magnon-photon systems**
   L. H. Bai, *M. Harder*, Y. P. Chen, X. Fan, J. Q. Xiao and C.-M. Hu
   Phys. Rev. Lett. **114**, 227201 (2015)
   arXiv:1504.01335
   Selected as an "Editor's Suggestion"

The following publications, prepared during the course of the author's doctoral studies, were not presented in this dissertation:

9. **Influence of stripline coupling on the magnetostatic mode line width of an yttrium-iron-garnet sphere**
   Y. Yang, *M. Harder*, J. W. Rao, B. M. Yao, W. Lu, Y. S. Gui and C.-M. Hu
   AIP Advances **8**, 075315 (2018)

10. **Linking magnon-cavity strong coupling to magnon-polaritons through effective permeability**
    P. Hyde, L. H. Bai, *M. Harder*, C. Dyck and C.-M. Hu
    Phys. Rev. B **95**, 094416 (2017)
    arXiv:1703.00074

11. **Electrical detection of magnetization dynamics via spin rectification effects**
    M. Harder, Y. S. Gui and C.-M. Hu
    Phys. Rep. **661**, 1 (2016)
    arXiv:1605.00710

12. **Indirect coupling between two cavity photon systems via ferromagnetic resonance**
    P. Hyde, L. H. Bai, *M. Harder*, C. Match and C.-M. Hu
    Appl. Phys. Lett. **109**, 152405 (2016)
    arXiv:1606.03469

13. **On thermal fluctuations and the generating functional in relativistic hydrodynamics**
    M. Harder, P. Kovtun and A. Ritz
    JHEP **07**, 025 (2015)
    arXiv:1502.03076

ACKNOWLEDGEMENTS

My journey in physics and the completion of this dissertation would not have been possible without a wealth of support. First, I owe a great deal to my advisor Can-Ming Hu. Completing my PhD during the development of a new research field was an exciting and rare opportunity, made possible only by Can-Ming's remarkable foresight and intuition. Thank you for being such a great supporter of your students and for always championing my strengths while encouraging me to work on my weaknesses. Your willingness to discuss new ideas and allow free exploration all while taking great effort to train me in all aspects of science and scientific life was greatly appreciated.

I was also fortunate to work in a dynamic and supportive research group at the University of Manitoba. Thank you to all the members of the Dynamic Spintronics Group, with whom I had the pleasure of discussing new ideas and learning together. In particular I need to thank Lihui Bai. Your skill in the laboratory and boldness to always try something new were an inspiration. I greatly appreciated all of the discussions we had, whether about science or life, and the support you offered through both. I also must acknowledge Yongsheng Gui for his role in the final months of my PhD, supporting my time writing while guiding me through unexplored scientific territory.

During my PhD program I had the great opportunity to spend a summer at the Walther-Miessner-Institute. I thank Hans Huebl, Sebastian Goennenwein and Rudolf Gross for facilitating this research stay. Hans and Sebastien, thank you for welcoming me to the magnetism group and for the excellent scientific training you provided. In addition to the unique scientific environment, the large group of fellow students at the WMI created a truly memorable stay. Thank you to everyone at the WMI for including me in many fun adventures. In particular I want to thank Hannes Maier-Flaig for teaching me many new experimental techniques, introducing me to python and being a wonderful host and friend. I am also grateful to Daniel Jost for your friendship and hospitality, including a memorable weekend in Bad Reichenhall. Maybe one day we can get our beer exchange working.

Of course my journey in physics started well before my PhD and there were

many friends, colleagues and professors who contributed to my passion for science and physics. I would like to specially thank my former advisor Pavel Kovtun. Our many discussions greatly impacted my view and knowledge of physics. Without your guidance and support I would never have gained much of the physics insight which I value today. Thank you for always having an open door, an open mind and for supporting me through all of my endeavours.

There are also many people outside of the lab that I must thank. I have had the great fortune of participating in a variety of outreach activities, providing many of my favourite memories of grad school. I would like to thank everyone at Let's Talk Science, CanU, the Physics Department Outreach Committee, Science Rendezvous and the Dean's office for providing these opportunities. In particular I am grateful to Seema for facilitating and encouraging so much amazing STEAM outreach. Your passion and the amazing work that you do is truly remarkable.

Manitoba is a wonderful place to explore the natural beauty of Canada. Thank you to all the friends who joined me on various outdoor adventures. Your company made each journey more enjoyable. Thank you in particular to Guillaume for organizing so many great hikes, canoe trips, snowshoe excursions, runs etc. You are a great motivator and friend.

Since the first year of my undergraduate degree I have had the pleasure of knowing a remarkable physicist, educator and friend, Andriy Yamchuk. Throughout a decade of friendship you have always been there to discuss life, physics and philosophy and to share many adventures. My journey in physics would not have been the same without you. Thank you Andriy for the many shared lunches and coffee breaks, for offering support whenever needed and for making me feel like a true friend and family.

Finally, I am fortunate to have a wonderful and supportive family, which I thank for their love and encouragement. Jonathon, I truly appreciate everything you have done for me. You continue to be a most valuable friend and support. Thank you for always being there to listen and offer advice. And for my parents. You have provided endless support throughout life's highs and lows. A few lines in this acknowledgement cannot capture what that means to me. Thank you for always showing selfless love. For that I cannot adequately express my gratitude.

"But in every walk with Nature one receives far more than he seeks" - John Muir

1

INTRODUCTION

Emergence, the appearance of macroscopic properties which qualitatively differ from a system's microscopic behaviour, is one of the most intriguing concepts in physics. From hydrodynamics [1, 2], to spacetime [3–5], to superconductivity [6] to novel quantum materials [7], the concept of emergence underlies a wealth of physical phenomena,[1] even producing entirely new degrees of freedom through collective excitations. Most interestingly, emergent behaviour usually cannot be anticipated from the properties of the underlying constituents. For this reason, despite our knowledge of the fundamental laws governing many-body solid-state systems, condensed matter research still contains many unexplored paths to discovery [13, 14]. This dissertation follows one such path. We present here the theoretical and experimental foundations of a new field of condensed matter research, cavity spintronics, which emerges when low loss magnetic materials are combined with high quality microwave fields.

The foundation underlying cavity spintronics is a new type of quasiparticle, the cavity-magnon-polariton (CMP), which displays an intriguing dual spin-photon nature. This hybrid character highlights the CMP's position at the crossroads of cavity-quantum electrodynamics and magnetism [15]. Of course the venerable subject of magnetism stands on its own right as one of the pillars of condensed matter physics, inspiring millennia of scientific discovery and technological innovation [16]. Within this long history, one of the important modern discoveries was the observation that ferromagnetic materials could absorb microwave frequency radiation [17, 18]. This

---

[1]Actually the concept of emergence extends well beyond physics and even science, underlying the key characteristics of many complex systems. For example, cellular functions in molecular biology [8, 9], self organization in economics [10], scaling of large networks [11] and language development [12] are all emergent phenomena.

phenomena results from the emergence of collective spin dynamics,[2] which results in resonant motion of the magnetization [21, 22]. Ferromagnetic resonance has proven to be a powerful technique to investigate a material's magnetic properties and is now routinely used to probe, e.g., demagnetization effects, magnetic anisotropies and damping mechanisms [23]. As magnetic resonance techniques matured, including the development of electron paramagnetic resonance and nuclear magnetic resonance, it was realized that the loss of radiative energy due to inductive processes, known as radiation damping, could play a significant role for magnetization dynamics [24] (such effects have more recently become the topic of intense discussion [25–27]). Radiation damping can be viewed as one effect of the magnetization back action onto the driving microwave field. Heuristically, losing energy through the emission of radiation only requires coupling back to the environment, thereby influencing the damping at first order. However if the photons which drive magnetic resonance are trapped for a sufficiently long time, the radiated photon will in turn drive magnetization precession. It is in this context that cavity spintronics (termed spin cavitronics by some authors) has emerged; when the influence of the magnetization induction is appreciable, its effect on the local microwave field must be accounted for, resulting in a back and forth flow of energy between spin and photonic degrees of freedom which produces a hybridized quasiparticle, the cavity-magnon-polariton. Cavity spintronics is therefore the study and application of strongly coupled spin-photon physics in condensed matter systems.

From a theoretical perspective understanding the CMP requires the simultaneous solution of Maxwell's equations, which describe electrodynamics, and the Landau-Lifshitz-Gilbert (LLG) equation, which describes magnetization dynamics.[3] On the other hand, from an experimental perspective, realizing strong spin-photon coupling requires a high quality microwave cavity, to confine the photons for extended periods of time, and a large sample-to-cavity filling factor, to increase the number of spins in the microwave cavity. The latter can be realized using high spin density, low loss ferromagnetic materials, such as yttrium-iron-garnet (YIG) commonly found in spintronic devices.[4] The former has been realized for several decades in the field of

---

[2]From the onset of ferromagnetism at oxide interfaces [19] to the formation of magnetic polaritons [20], examples of emergence abound in magnetism.

[3]In contrast to the basic approach to magnetization dynamics, where one assumes that a fixed, applied field drives the magnetization, back action is ignored, and the LLG equation alone is solved.

[4]YIG is actually a ferrimagnetic material. However in this dissertation, and for the purpose of strong coupling physics, the distinction is not important and we will typically use ferromagnetic for generality.

cavity quantum electrodynamics, where the quantum nature of light is brought to the forefront [28].

The possibility of realizing hybridized spin-photon excitations in ferromagnetic systems was first discussed theoretically by Soykal and Flatté in 2010 [29, 30], but only realized experimentally in 2013 [31]. In this first experiment, Huebl et al. employed a YIG sphere coupled to a planar superconducting resonator at ultra low temperatures, using microwave transmission to measure the key coupling signature, an anticrossing in the eigenspectrum. Although the absorption of electromagnetic fields by ferromagnets in cavities had been studied for many decades before this observation, the increased filling factor, due to large, high quality samples and confined microwave fields, as well as the shift of focus from fixed to swept frequency experiments, enabled this new discovery. While initial experiments were performed at low temperatures, it was quickly realized that the experimental conditions for CMP formation could be relaxed, allowing observations at room temperature [32], in 3D microwave cavities [33, 34] and using split ring resonators [35–39]. Although YIG, due to its ultra low damping and high spin density, continues to be the prototypical magnetic material for CMP experiments, strong coupling has also been observed in gadollinium-iron-garnet (GdIG) [40], lithium ferrite [41] and the chiral magnetic insulator Cu_2OSeO_3 [42]. Furthermore, while initially motivated by the potential for hybrid quantum information systems [43–46] with the enhanced coupling of exchange-locked ferromagnets [47], the electrical detection of strong spin-photon coupling has further pushed the CMP into the realm of spintronics [48–50]. This variety of cavity spintronic measurement techniques which have been established since 2013 have led to a wealth of CMP exploration. For example, the ultrastrong coupling regime has been reached [51–53], spin wave strong coupling has been observed [49, 54–56], multimode cavity [57] and spin [50, 58–60] systems have been realized, exceptional points of the CMP eigenspectrum have been found [61, 62], coherent perfect absorption has been realized [62] and the effect of Kerr nonlinearities has been studied [63, 64]. Furthermore, a transition from microwave to optical frequencies has recently resulted in the exploration of cavity optomagnonics [65–70]. On the more applied side, voltage control of the CMP using on-chip devices [71], the observation of electromagnetically induced transparency [38, 72], novel quantum information architectures employing magnon dark modes [59], and the realization of microwave to optical frequency conversion [73] all point to a bright future for CMP based devices.

While all of the results mentioned above were based on classical spin-photon prop-

erties, recently the quantum frontier has also been encountered with the generation of a qubit-CMP interaction [33, 74], the observation of triplet and quintuplet states in active resonators [75] and low power experiments with single photon excitations [76]. All of these discoveries have occurred within the last five years, corresponding to the time period in which this dissertation research was undertaken. The fundamental question we have sought to answer is: How do we physically understand a strongly coupled spin-photon system? This entails not only the development of theoretical models, but also, for example, understanding the key features of, and methods needed to create, the CMP, as well as how to control and manipulate it. The main contributions we have provided to the continuing saga of cavity spintronics, and which are presented in this dissertation, are the elucidation of theoretical models and connections between differing models, the discovery that the CMP will influence spin current, and therefore holds potential for spintronic applications, the development of several methods to control the CMP and the discovery of antiresonance phenomena and the important role of damping on the CMP eigenspectrum. These foundational studies will be presented in the following seven chapters:

Chapter 2 introduces the basic concepts in spintronics and polaritonics which serve as a starting point for the research we will present. Particular emphasis is placed on the generation and detection of spin currents through spin pumping and the inverse spin Hall effect, respectively, as well as a broad conceptual description of polaritons.

Chapter 3 lays the theoretical foundation of the cavity-magnon-polariton. We first show how the key signatures of the CMP arise from a very general model of coupled oscillators. To gain insight into the physical mechanism of the spin-photon coupling, we next present a classical electrodynamic model which couples the electrodynamics of Maxwell's equations with the magnetization dynamics of the Landau-Lifshitz-Gilbert equation, revealing electrodynamic phase correlation as the source of spin-photon coupling. Finally we discuss a quantum treatment of the CMP, using both the Jaynes-Cummings Model and the input-output description of quantum optics, as well as a scattering formalism. All theoretical approaches are then compared, highlighting their similarities and complementary nature. The CMP dispersion following from the electrodynamic model was published in Phys. Rev. Lett. **114**, 227201 (2015) while a broader theoretical discussion including the harmonic description, an in-depth analysis of the

electrodynamic model and our scattering approach was published in Sci. China Phys. Mech. Astron. **59**, 117511 (2016). The author of this dissertation contributed to the results presented in this chapter by: Developing and interpreting all aspects of the harmonic model presented in Sec. 3.2; Testing and validating the matrix formulation of the electrodynamic phase correlation model presented in Sec. 3.3 and extending this approach, using microwave circuit theory, to calculate the transmission spectra; Providing the detailed implementation of the input-output formalism to describe the spin-photon system in Sec. 3.4; Developing the model simplifications and comparisons described in Secs. 3.2 and 3.5.

Chapter 4 focusses on the key experimental signatures of the CMP. We first introduce the relevant CMP components, namely the spin and photonic subsystems, and describe both microwave transmission and electrical detection measurement techniques. We then discuss the dispersion anticrossing and line width evolution, which form the basic fingerprints of the CMP, before addressing antiresonance behaviour, which may be used to characterize the spin subsystem. Finally, we discuss how the CMP antiresonance may also be used to analyze the phase properties of magnon-dark modes. Successful CMP measurements using electrical detection techniques, indicating the influence of the CMP on spin pumping, were first presented in Phys. Rev. Lett. **114**, 227201 (2015), while the antiresonance features and phase analysis were published in Phys. Rev. B **94**, 054403 (2016). The author of this dissertation contributed to the results presented in this chapter by: Designing and characterizing the microwave cavity described in Sec. 4.3 and performing the theoretical calculation of the cavity modes; Performing and analyzing all microwave transmission measurements using the UMS1 setup presented in Sec. 4.5.1; Performing the dispersion and line width analysis and modelling of the fundamental modes presented in Sec. 4.5.2; Performing all electrical detection and microwave reflection measurements using the WMI setup, including sample preparation, and analyzing/interpreting the $n = 7$ and $n = 9$ spin wave modes that are presented in Sec. 4.5.3; Performing the microwave transmission measurements, fitting, theoretical analysis and interpretation of the antiresonance behaviour presented in Sec. 4.5.4; Extending the matrix approach to describe the three mode case of Sec. 4.5.5.

Chapter 5 turns to the question of CMP control. By tuning the cavity damping

we control the CMP cooperativity in order to realize a strong to weak coupling transition, which is observed not only for ferromagnetic resonance, but also for several higher order spin wave modes. These results were published in Phys. Rev. B **94**, 054433 (2016). A strong to weak transition may also be observed by directly tuning the coupling strength itself. Using a compensating garnet, gadolinium iron garnet (GdIG), we demonstrate in situ temperature control of the CMP, confirming the $\sqrt{N_s}$ coupling strength dependence on the number of active spins, N_s. These results were presented in Appl. Phys. Lett. **110**, 132401 (2017). Unfortunately using low temperatures to control the coupling strength is a cumbersome proccess and a more robust procedure would benefit device applications of the CMP. A simpler approach is to manipulate the coupling strength by systematically controlling the rf-static magnetic field orientation. Such a procedure was published in IEEE Trans. Magn. **52**, 1000107 (2016) and is described here. Finally, by combining our techniques for angular coupling strength control and local electrical detection, we conclude this chapter by demonstrating non-local spin current manipulation using the CMP as a bridge between two well separated spintronic devices. This technique was published in Phys. Rev. Lett. **118**, 217201 (2017). The author of this dissertation contributed to the results presented in this chapter by: Characterizing the cavity quality control of the UMS1 and WMI setups, including all microwave transmission/reflection measurements, analysis and interpretation presented in Sec. 5.2; Preparing the GdIG samples and performing the microwave transmission measurements from liquid nitrogen to room temperature presented in Sec. 5.3; Collaborating with Lihui Bai on the angular dependence model used in Sec. 5.4 and measuring the systematic angular dependence of the cooperativity; Developing the detuning formalism for non local control in collaboration with Lihui Bai, as presented in Sec. 5.5.

Chapter 6 highlights an interesting feature of the non-Hermitian Hamiltonian which governs the CMP dynamics. In general the damping associated with spin and cavity dynamics defines an exceptional point in the CMP eigenspectrum. This exceptional point marks a degeneracy where CMP eigenvalues and eigenvectors coalesce and is intimately connected to the topological structure of the eigenspectrum. By exploiting this topological structure we demonstrate the presence of a dispersion crossing in the traditional strong coupling regime, as

well as a mode switching phenomena while encircling the exceptional point, which was published in Phys. Rev. B **95**, 214411 (2017). The author of this dissertation contributed to the results presented in this chapter by: Designing the experimental setup, performing and analyzing all experiments, performing all theoretical modelling and interpreting the results.

Chapter 7 concludes the dissertation with a summary of the research contributions presented in the preceding chapters.

2

BASIC CONCEPTS IN SPINTRONICS AND POLARITONICS

2.1 INTRODUCTION

The hybridization of eigenmodes due to strong light-matter interactions appears across a wide range of condensed matter systems, from phonons in dielectric crystals [77], to excitons in semiconductor microcavities [78], to plasmons in dielectric arrays [20]. Such excitations are both intriguing physically, for example they represent another striking example of emergence in condensed matter physics and can drastically modify the energetics of a material [79], and play an important role in technological development with, for example, exciton-polaritons being used for low power electrical switching [80] and plasmon-polaritons allowing optical microscopy well beyond the diffraction limit [81]. Within this context the addition of a new member to the polariton family offers great potential for new physical insights and technological development. Furthermore the discovery of such hybridization within a spin system coupled to a high quality microwave cavity draws connections between the physics of polaritons, spintronics, cavity quantum electrodynamics and quantum information technologies [15].

In the investigations presented in this dissertation the polariton arises due to the strong interaction between the magnetization dynamics of a ferrimagnetic system and the electrodynamics of a microwave cavity. Even without such a strong interaction, advances in understanding the magnetization dynamics of micro and nanostructure materials have led to major advancements in the field of spintronics over the past two decades [82]. New fields such as spin orbitronics [82–84], spin caloritronics [85], magnonics [86] and now cavity spintronics, have emerged through the maturation

of spintronics, advancing memory storage [87], magnetic sensing [88] and spin based logic [89, 90]. Central to the development of spintronics has been the reliable generation and manipulation of spin current [91]. Since magnetization precession is known to produce a non-equilibrium spin distribution, it seems plausible to generate spin currents by constructing device interfaces where such a spin accumulation is allowed to diffuse from one material into another, thereby injecting spin current. Indeed this heuristic picture describes the commonly used technique of spin pumping. In our work one of the central results is the demonstration that the spin current generated through such a spin pumping mechanism is influenced by the presence of spin-photon hybridization. For this reason, before embarking on a journey into the world of cavity spintronics, it is necessary to recall some of the key elements of both spintronics and polaritonics. In particular it is important to understand the basic behaviour of ferromagnetic resonance, which arises when an external field torque drives a material's magnetization, the mechanism of spin pumping, which generates spin current through a diffusive process, and the mechanism behind the electrical detection of spin currents. Reviewing this important background, and further elucidating the behaviour of polaritons, is the purpose of this chapter.

2.2 AN OVERVIEW OF SPINTRONICS

After millennia of mysticism, discovery and applications, the development of quantum mechanics in the early 20th century finally provided the theoretical basis to understand magnetism at its most fundamental level. This understanding is rooted in the behaviour of electronic spins, experimentally discovered by Goudsmit and Uhlenbeck in 1925 [92–94].[1] Mathematically the quantized spin of electrons is analogous to classical angular momentum, and will therefore undergo precession when acted on by a magnetic torque. This precessional motion can be easily ascertained by applying the Ehrenfest theorem to the spin operator $\mathbf{S}$,

$$i\hbar\frac{d\langle\mathbf{S}\rangle}{dt} = \langle[\mathbf{S}, H]\rangle \tag{2.1}$$

where $H = -|\gamma_e|\mathbf{S}\cdot\mathbf{B}$ is the Zeeman interaction between $\mathbf{S}$ and the magnetic field $\mathbf{B}$. Here $\gamma_e = g\mu_B/\hbar$ is the electron gyromagnetic ratio, with Landé g-factor g, Bohr

---

[1]Of course by 1925 Stern and Gerlach had already discovered the spin through their experiments on silver atoms [95–97].

magneton μ_B and reduced Planck constant $\hbar$. Using the canonical commutation relations for the spin operator, $[S_i, S_j] = i\hbar\epsilon_{ijk}S_k$, where ϵ_{ijk} is the Levi-Civita symbol, we can therefore write,

$$\frac{d\langle\mathbf{S}\rangle}{dt} = -|\gamma_e|\left(\langle\mathbf{S}\rangle \times \mathbf{B}\right). \tag{2.2}$$

Using the relationship between the expectation value of $\langle\mathbf{S}\rangle$, the sample volume V, and the magnetization $\mathbf{M}$, $\mathbf{M} = \gamma_e\langle\mathbf{S}\rangle/V$, the equation of motion for the magnetization becomes,

$$\frac{d\mathbf{M}}{dt} = -\gamma\mathbf{M} \times \mathbf{H} \tag{2.3}$$

where $\mathbf{B} = \mu_0\mathbf{H}$ and $\gamma = \mu_0\gamma_e$. Eq. (2.3) is the Landau-Lifshitz (LL) equation [98] without damping and describes the precessional motion of the magnetization (net spin alignment) driven by the magnetic field $\mathbf{H}$.[2] It is clear from Eq. (2.3) that the applied field acts as a torque on the magnetization, driving precession. This precession will undergo a ferromagnetic resonance (FMR) at a frequency ω_r, dependent on the field and material properties as addressed in Sec. 3.3.

In magnetically ordered materials spin-spin interactions between individual magnetic moments produce collective behaviour which can be described by the magnetization of Eq. (2.3). Excitations will occur when one of the moments undergoes an energetically unfavourable reorientation (a spin flip), which then propagates throughout the magnetic lattice. This process results in spin waves, as illustrated in Fig. 2.1, where the magnetic moments of neighbouring lattice sites precess out of phase. The
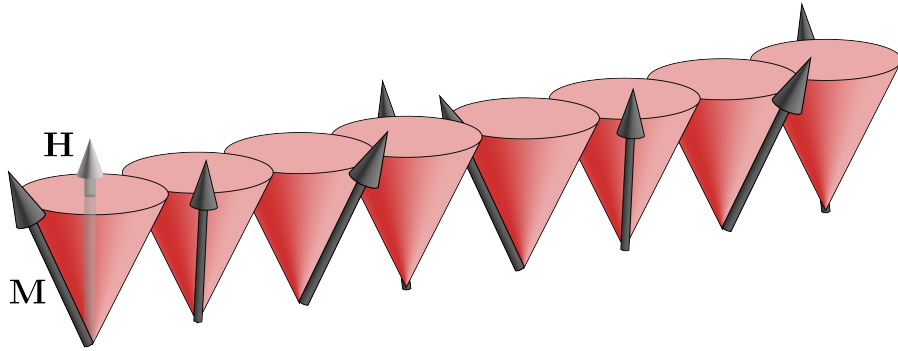
Figure 2.1: Illustration of a spin wave. Magnetic moments at neighbouring lattice sites precess out of phase, leading to the transport of angular momentum across the magnetic lattice.

---

[2]Damping plays an important role in magnetization dynamics and can be treated phenomenologically as discussed in Sec. 3.3 [21, 99, 100].

quantized version of spin waves can be treated as a bosonic quasiparticle, known as a magnon [101]. Magnons are therefore another example of collective and emergent behaviour in condensed matter systems and play a central role in spintronics, notably they transport angular momentum across the magnetic lattice; behaviour which underlies the concept of spin current – the flow of electronic spins with, or more interestingly, without, the flow of electronic charge.[3] It is the generation and manipulation of such spin currents that lies at the very heart of spintronics.[4]

Spin transport based electronics – spintronics – took off in the 1980's after the discovery of giant magnetoresistance [108, 109], which provided a striking example of magnetization controlled charge transport, and with a magnetoresistance ratio of $\sim 100\%$, revolutionized the magnetic recording industry. In the 30 years that have followed this discovery, spintronics has found an important role in data storage [103, 104], magnetic sensing [110], studies of magnetization dynamics [23] and provides the leading candidate for a universal memory [87, 111]. These advances are due in large part to improved fabrication techniques,[5] although the idea of spin dependent transport in materials can be traced back to Mott's 1936 development of a two-current model [112, 113] which was used to describe resistivity effects observed by Lord Kelvin as early as 1856 [114].

Although much has been learned about spin transport in recent decades, Mott's two-current model still provides an excellent physical picture of spin current behaviour. In Mott's description spin transport is assumed to result from the flow of two independent spin channels, $\mathbf{I}_\uparrow$ and $\mathbf{I}_\downarrow$, comprised of up and down spins respectively. The spin current, $\mathbf{I}_s$, may then be written as

$$\mathbf{I}_s = -\frac{\hbar}{2e}\left(\mathbf{I}_\uparrow - \mathbf{I}_\downarrow\right), \tag{2.4}$$

whereas the charge current would be $\mathbf{I}_q = \mathbf{I}_\uparrow + \mathbf{I}_\downarrow$. This model allows one to understand the different types of spin current shown in Fig. 2.2. When $\mathbf{I}_\uparrow = \mathbf{I}_\downarrow$, meaning the currents flows in the same direction and have equal magnitude, the spin currents from each channel will cancel and $\mathbf{I}_s = 0$. However $\mathbf{I}_q \neq 0$. This type of "spin current" is illustrated in Fig. 2.2 (a), and is nothing other than a conventional charge current.

---

[3]We note that in this dissertation we essentially use spin wave and magnon interchangeably, although a spin wave is a classical concept while the magnon has quantum connotations.

[4]For an in-depth study of spintronics, the reader is referred to the following reviews, Refs. [82, 102–105], and books, Refs. [91, 106, 107].

[5]Unlike charge current, spin current need not be conserved and decays on length scales of microns, making spintronics a nanoscale endeavour which generally requires advanced fabrication.
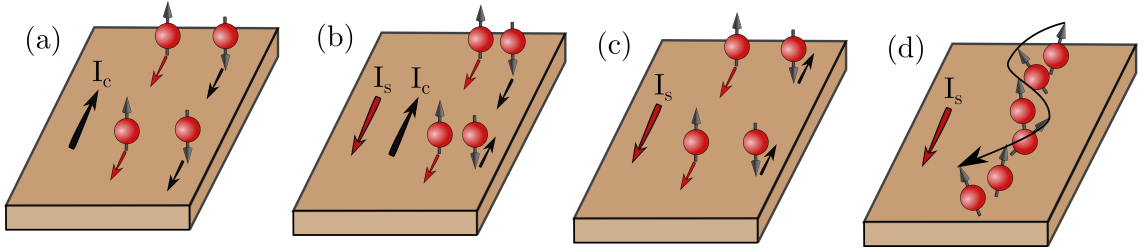
Figure 2.2: The four types of spin current. In all panels I_s and I_c are the spin and charge current respectively. (a) A pure charge current flows when electronic spins are completely incoherent. In this case no net spin angular momentum is transported ($I_s = 0$). (b) A spin-polarized charge current results when there is an imbalance between up and down spin currents, resulting in both charge and spin angular momentum flow. (c) A pure spin current carries pure spin angular momentum without any accompanying charge flow. In magnetic metals this may result from conduction-electron diffusion creating a balanced flow of up and down spin currents in opposite directions. (d) Without conduction-electrons a pure spin current, carried by spin waves, may still exist. This enables spin current propagation in magnetic insulators.

On the other hand, if $\mathbf{I}_\uparrow$ and $\mathbf{I}_\downarrow$ flow in opposite directions, $\mathbf{I}_s \neq 0$. There are then two possibilities. As illustrated in Fig. 2.2 (b), when $|\mathbf{I}_\uparrow| \neq |\mathbf{I}_\downarrow|$ a spin-polarized charge current will exist where both $\mathbf{I}_s \neq 0$ and $\mathbf{I}_q \neq 0$. However, when $|\mathbf{I}_\uparrow| = |\mathbf{I}_\downarrow|$ the opposite flow of charge currents will cancel, leaving a pure spin current as shown in Fig. 2.2 (c). The aforementioned spin currents all require a flow of conduction electrons, and therefore exist in metals or semiconductors. However, as shown in Fig. 2.2 (d), spin waves present an intriguing alternative possibility for pure spin currents – the flow of spin angular momentum without charge transport. An immediate consequence is the possibility of spin current flow in ferromagnetic insulators [115], which allows the separation of electric and magnetic degrees of freedom and eliminates extraneous electrical effects, such as spin rectification, which may be undesirable in spintronic applications [23]. Such spin wave based spin currents also offer other advantages, such as drastically enhanced spin wave propagation lengths due to the removal of conduction electron decay mechanisms. As a result ferromagnetic insulators have become a key piece of modern magnonics [86, 107].

2.2.1 *Insulating Magnetic Materials*

One of the most widely used insulating ferrimagnets in spintronics is yttrium-iron-garnet (YIG), $Y_3Fe_5O_{12}$ [86, 116–118]. YIG was first synthesized in the mid 1950's

[119, 120] and has become widely adopted due, in part, to: (i) its high Curie temperature, $T_c = 560$ K, making it ideal for room temperature experiments; (ii) its large band gap of 2.85 eV [121, 122], making it an excellent insulator; and (iii) its extremely low Gilbert damping, $\alpha \sim 10^{-4}$, resulting in the narrowest known ferromagnetic resonance line width and magnon lifetimes of a few hundred nanoseconds [86]. YIG belongs to the family of garnet ferrites which contain three cation sites, a dodecahedrally coordinated $c-$site, octahedrally coordinated $a-$site and a tetrahedrally coordinated $d-$site. This general garnet structure, $\{c_3\}[a_2](d_3)O_{12}$, is illustrated in Fig. 2.3. The magnetism of YIG results from the antiferromagnetically coupled a and d magnetic sublattices, which are occupied by Fe^{3+} cations.

The majority of experiments presented in this dissertation were performed on either single-crystal YIG spheres or thin film YIG/platinum (Pt) heterostructures grown on gadolinium-gallium-garnet (GGG) substrates [123, 124]. However one series of low-temperature experiments was performed using a GdIG thin film sample. The crystal structure of GdIG is similar to that of YIG, however Gd^{3+} cations occupy the c-sites. As a result, all three sublattices contribute to the GdIG magnetism. As in YIG, the Fe-sublattices are antiferromagnetically coupled to each other, while the Gd-sublattice is antiferromagnetically coupled to the octahedral Fe-sublattice and ferromagnetically coupled to the tetrahedral Fe-sublattice [116]. Due to this additional
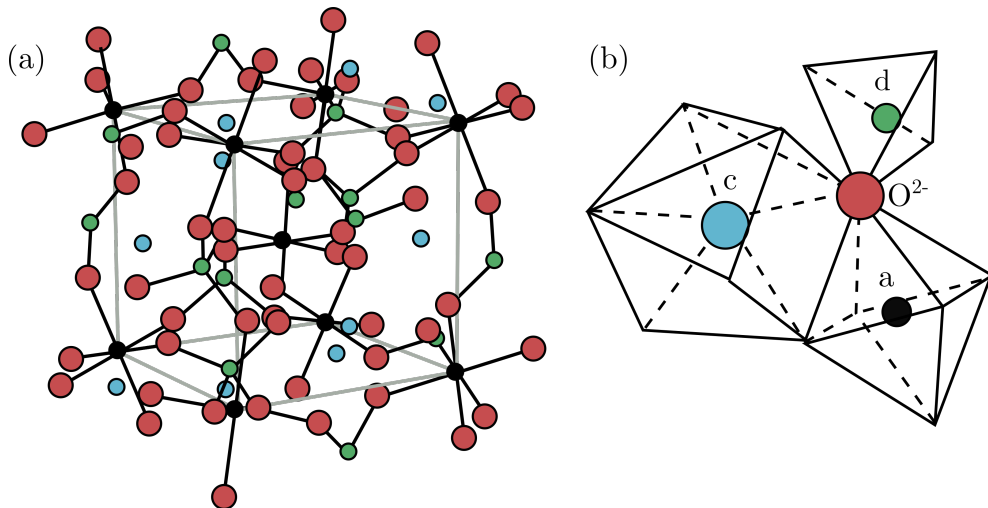
Figure 2.3: (a) The garnet structure, $\{c_3\}[a_2](d_3)O_{12}$, illustrated for one octant of the unit cell. (b) The three cation sites: dodecahedral c, octahedral a and tetrahedral d. For YIG and GdIG, the c-sites are occupied by Y^{3+} or Gd^{3+} respectively, while d and a cites are occupied by Fe^{3+}. Figure modified from Ref. [116].
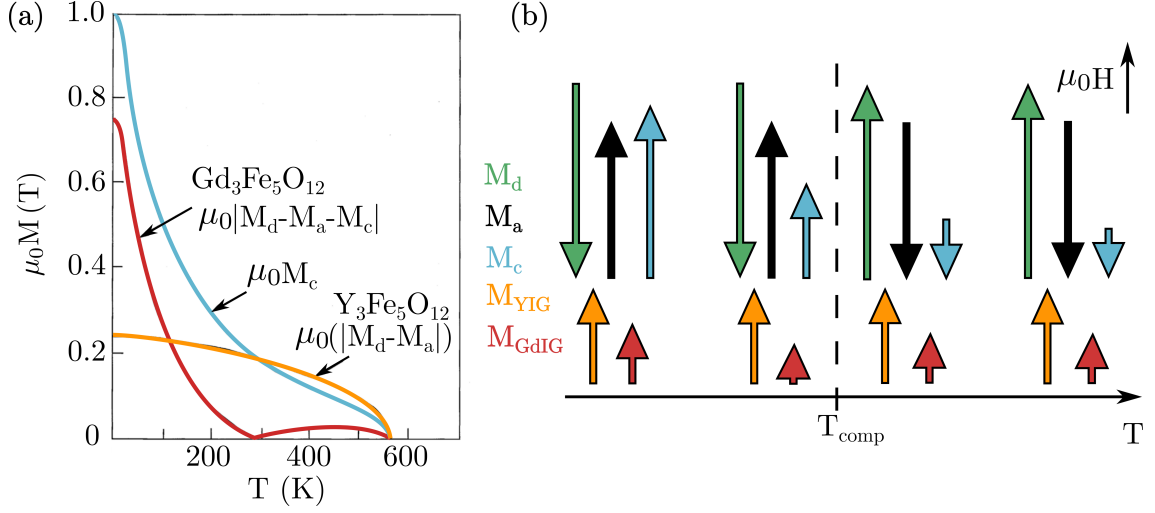
Figure 2.4: (a) Magnetization curves for GdIG and YIG, illustrating the strong temperature dependent magnetization, and compensation point, of GdIG. (b) A schematic illustration of the sublattice magnetizations above and below the compensation temperature, T_{comp}. Figure modified from Ref. [116].

magnetic sublattice, the GdIG magnetization displays interesting temperature dependent properties. While the Fe-sublattices display only weak temperature dependence below room temperature (which is why the YIG magnetization is nearly temperature independent, with $\mu_0 M_s \,(300 \text{ K}) = 175.8 \text{ mT}$ and $\mu_0 M_s \,(0 \text{ K}) = 246.2 \text{ mT}$ [125]) the Gd-sublattice is strongly temperature dependent due to a weaker sublattice exchange interaction. This behaviour is illustrated in Fig. 2.4 (b).[6] As a result the GdIG magnetization can be tuned from $\mu_0 M_s = 12.2 \text{ mT}$ at 300 K to $\mu_0 M_s = 769.1 \text{ mT}$ at 0 K [127]. In fact, at a certain compensation temperature, T_{comp}, the different sublattice contributions will cancel and $\mu_0 M_s \,(T_{\text{comp}}) = 0$. This behaviour is shown in Fig. 2.4 (a) where $T_{\text{comp}} \sim 270$ K. As discussed in Sec. 5.3, this temperature dependence can be used to control the spin-photon coupling strength in cavity spintronics.

2.3 CREATING SPIN CURRENTS: SPIN PUMPING

As already mentioned, the kernel of spintronics is the generation and manipulation of spin currents. One of the widely used methods for spin current generation is the transport of non-equilibrium magnetization pumped by FMR, known as spin pumping [128–136]. A key achievement of this dissertation was the experimental demonstration

---

[6]Although the magnitude of the Fe-sublattice magnetizations is approximately constant, the orientation changes above and below T_{comp} [126].
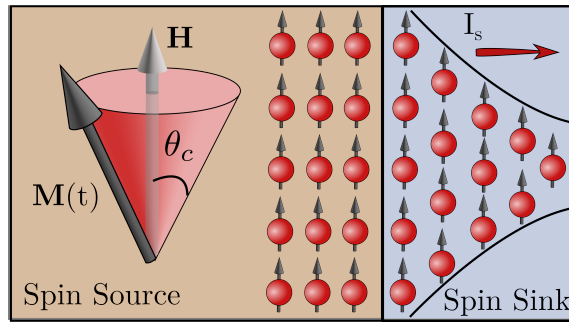
Figure 2.5: Spin pumping in a hybrid spintronic device. Due to magnetization precession a non-equilibrium spin distribution accumulates in a ferromagnetic spin source. The spins then diffuse into an adjacent spin sink.

that strong-spin photon coupling will affect the detected spin pumping signal [48–50]. This means that spin current is actually manipulated by strong-coupling, and, as we will show in Sec. 5.5, enables the non-local manipulation of spin current over macroscopic distances. Spin pumping occurs in hybrid spintronic devices where a material undergoing FMR acts as a spin source, generating a spin accumulation at the interface with another material acting as a spin sink, which allows for the diffusive absorption of this spin current. A variety of magnetic materials may serve as the spin source, such as ferromagnetic metals, ferromagnetic semiconductors or ferromagnetic insulators (FMI) [136], and even paramagnetic metals [137]. The only requirement of the spin sink is to allow spin diffusion, permitting a variety of materials to fill this role as well (although in practice it is typically a normal metal with large spin orbit coupling to enable detection of the spin current through the inverse spin Hall effect). In the work we will present here, all spin pumping experiments were performed on YIG/Pt bilayers where FMR in YIG pumps a spin current into Pt.

Fig. 2.5 provides a schematic illustration of spin pumping. The magnetization of the magnetic material, $\mathbf{M}(t) = \mathbf{M}_0 + \mathbf{m}(t)$, precesses at a cone angle θ_c from the equilibrium magnetization $\mathbf{M}_0$. This misalignment determines the non-equilibrium magnetization generated by the magnetization dynamics, $\mathbf{m}(t)$.[7] This non-equilibrium magnetization is partially dissipated due to damping inside of the FMI. However at the FMI/NM interface the remaining non-equilibrium magnetization diffuses into the NM as a flow of spin current, which contributes to additional dissipation of $\mathbf{m}(t)$.

The dc component of the spin current is typically detected via its conversion

---

[7]Although, as we discussed in Sec. 2.2.1, YIG is a two sublattice ferrimagnet, FMR in YIG can be treated by considering a single $M_{\text{total}} = |M_d - M_a|$. A similar approach can be taken for GdIG using $M_{\text{total}} = |M_d - M_a - M_c|$.

back into a charge current and subsequent generation of a dc voltage. This is the approach we will take in this work. It is therefore necessary to understand a few details about the theory of spin pumping [130, 131], in order to determine the form of the spin current. According to the basic theory of spin pumping, the spin current at the FM/NM interface depends on the reflectivity and transmission of NM electrons, which can be characterized by a spin mixing conductance, $G^{\uparrow\downarrow}$.[8] The spin current that is injected into the normal metal then relaxes over a characteristic length scale λ_{SD}, the spin diffusion length, and the spin current density decays away from the interface as [130, 131]

$$\mathbf{I}_s(y) = \left(\frac{\hbar G_r}{4\pi M_0^2} \mathbf{M} \times \frac{d\mathbf{M}}{dt} \right) f(y), \qquad f(y) = \left(\frac{\sinh\left[(t_s - y)/\lambda_{\mathrm{SD}} \right]}{\sinh\left[t_s/\lambda_{\mathrm{SD}} \right]} \right). \qquad (2.5)$$

Here $f(y)$ describes the spin current amplitude a distance y away from the interface (see Fig. 2.5), G_r is the real part of, $G^{\uparrow\downarrow}$ and t_s is the thickness of the spin sink. The dc spin current is determined by the time average of Eq. (2.5) over one period. If we define coordinates such that $\overline{\mathbf{M}}(t) = \mathbf{M_0} + \overline{\mathbf{m}}(t) = (m_x e^{-i\omega t}, m_y e^{-i\omega t}, M_0)$ then, we find

$$\left\langle \mathbf{M} \times \frac{d\mathbf{M}}{dt} \right\rangle = \left\langle \mathrm{Re}\left(\overline{\mathbf{M}} \right) \times \frac{d\mathrm{Re}\left(\overline{\mathbf{M}} \right)}{dt} \right\rangle = \omega \mathrm{Im}\left(m_x^* m_y \right) \widehat{z} \qquad (2.6)$$

where $\langle \ldots \rangle$ denotes time averaging over one period. The direction $\widehat{z}$, along the static magnetization, defines the spin polarization of the spin current and not the direction of diffusion which is always normal to the interface (since the current diffuses away from the interface). Alternatively, if we assume small cone angles, so that $\sin\left(\theta_c \right) \sim m/M_0$ and circular precession, so that $|m_x| = |m_y| = m$,[9] then we can write $\mathbf{M} = (m\cos\left(\omega t \right), m\sin\left(\omega t \right), M_0)$ and therefore

$$\mathbf{M} \times \frac{d\mathbf{M}}{dt} = \omega \sin^2\left(\theta_c \right) \widehat{z}. \qquad (2.7)$$

Thus the dc spin current due to spin pumping can be written as,

$$\mathbf{I}_s\left(y \right) = \frac{\hbar}{4\pi M_0^2} \omega G_r f\left(y \right) \mathrm{Im}\left(m_x^* m_y \right) \widehat{z} = \frac{\hbar}{4\pi M_0^2} \omega G_r f\left(y \right) \sin^2\left(\theta_c \right) \widehat{z}. \qquad (2.8)$$

---

[8]Though this theory was only developed in 2002 [130, 138], with experimental observations to follow in 2006 [132–134], the fact that magnetization precession and non-equilibrium diffusion could create a spin current was first revealed in transmission-electron-spin resonance experiments performed in the late 1970's [128, 129].

[9]This assumption is appropriate for a sphere.

Experimentally the magnetization $\mathbf{m}(t)$ is controlled by an rf magnetic field $\mathbf{h}(t)$ and will depend on a static external bias field $\mathbf{H}$. As we will discuss in detail in Sec. 3.3, $\mathbf{m}(\mathbf{h}, \mathbf{H})$ is determined by solving the Landau-Lifshitz equation presented in Sec. 2.2 (or more commonly the Landau-Lifshitz-Gilbert equation, which includes the effect of damping), leading to $\mathrm{Im}\,(m_x^* m_y) \propto (\Delta H)^2 / \left[(H - H_r)^2 + (\Delta H)^2 \right]$, where H_r and ΔH are the resonance field and line width respectively. Therefore the spin pumping current follows a Lorentz line shape. As we will discuss in Sec. 4.5.2, since both the magnetization dynamics and the magnetization dispersion (H_r) are modified by spin-photon coupling, the spin current is also affected by the coupling. We have exploited this discovery to develop new spin current control methods.

2.4 DETECTING SPIN CURRENTS: THE INVERSE SPIN HALL EFFECT

Once spin currents have been generated through spin pumping they must be measured. Though detection of spin currents is challenging, several approaches have been developed, such as characterization of enhanced damping [139–144] and x-ray pump probe methods [145]. However the most widely used technique is spin to charge conversion via spin Hall effects [146]. This method requires strong spin orbit scattering in the spin sink and therefore can prove both disadvantageous, as only select materials can be used, and advantageous, by enabling the identification of ideal spin to charge converters for device applications. As is often the case, the physics underlying the spin Hall effects was studied decades before modern nanotechnologies have made them practically useful [147, 148].

Fig. 2.6 schematically illustrates the spin Hall effect and inverse spin Hall effect,
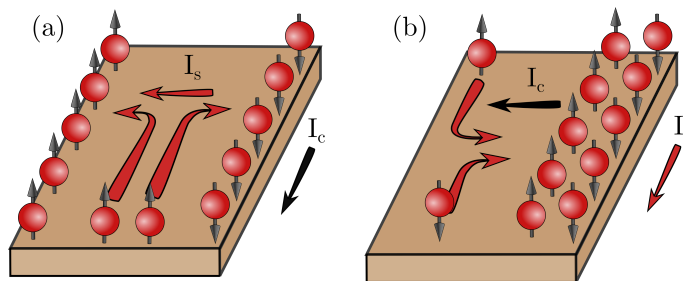
Figure 2.6: Schematic illustrations of (a) the spin Hall effect and (b) inverse spin Hall effect. I_c and I_s denote the charge current and the spatial direction of the spin current respectively. The spin polarization direction of the spin current is in the up-spin direction.

which results from spin dependent scattering due to spin orbit interactions, including skew-scattering, side jump scattering and intrinsic interactions [146]. These mechanisms create an effective spin dependent magnetic field, producing a spin dependent Lorentz force which acts on charge carriers, resulting in opposite deflection of spin up and spin down particles [149, 150]. As shown in Fig. 2.6 (a), in the spin Hall effect a charge current is converted to a spin current, and the resulting spin accumulation at the sample boundaries can be detected e.g. via Kerr rotation microscopy [151] or polarized electroluminescence [152]. The inverse spin Hall effect of Fig. 2.6 (b) is the inverse process, where a spin current is converted into a charge current according to

$$\mathbf{I}_c = \frac{2e\theta_{\mathrm{SH}}}{\hbar}\mathbf{I}_s \times \widehat{s}. \tag{2.9}$$

Here θ_{SH} is the spin Hall angle which characterizes the efficiency of spin to charge current conversion and is dependent on the strength of a material's spin-orbit interaction, while $\widehat{s}$ is the spin current polarization.

In spin pumping experiments the inverse spin Hall effect can be exploited to convert the spin current generated through spin pumping into a charge current which can be electrically measured [134]. Fig. 2.7 shows the combined spin pumping-inverse spin Hall effect mechanism. A microwave field $\mathbf{h}$, typically provided by a coplanar waveguide [153], drives magnetization precession producing a spin current via the spin pumping mechanism which is then converted into a charge current in the spin sink via the inverse spin Hall effect and is detected as a voltage across the bilayer, typically in the longitudinal direction ($\widehat{z}$ in Fig. 2.7). The spin pumping/inverse spin
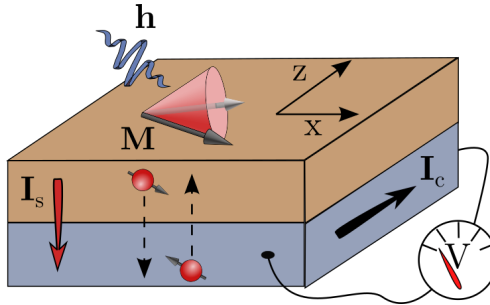
Figure 2.7: Spin current generation and detection in a bilayer device. A microwave field $\mathbf{h}$ drives magnetization precession, $\mathbf{M}(t)$ about the static field direction, $\mathbf{H}$. This precession pumps a spin current $\mathbf{I}_s$ into the sink layer, where it is converted into a charge current via the inverse spin Hall effect and detected as a voltage. This voltage is proportional to h^2 and therefore has a Lorentz lineshape.

Hall effect voltage can be determined by integrating the time averaged charge current density,

$$V_{\mathrm{SP}} = R \int \langle \mathbf{I}_c \left(y \right) \cdot \widehat{q} \rangle \, dA = R \frac{e\theta_{\mathrm{SH}}}{\hbar} \left[\int \langle I_s \left(y \right) \rangle \, dA \right] \left(\widehat{y} \times \widehat{s} \right) \cdot \widehat{q}, \qquad (2.10)$$

where $\widehat{q}$ is the measurement direction (either along the length or width of the sample; $\widehat{q} = \widehat{x}$ or $\widehat{z}$ in the coordinates of Fig. 2.7), $dA = dydz$ and R is the resistance of the spin sink. Using the result for the spin current in Eq. (2.8) to determine the charge current we have,

$$V_{\mathrm{SP}} = \frac{\theta_{\mathrm{SH}}\lambda_{\mathrm{SD}}}{\sigma} \left(\frac{e\omega}{4\pi} \right) \frac{G_r}{t_{\mathrm{s}}w} \tanh \left(\frac{t_{\mathrm{s}}}{2\lambda_{\mathrm{SD}}} \right) \mathrm{Im} \left(\frac{m_x^* m_y}{M_0^2} \right) \left(\widehat{y} \times \widehat{s} \right) \cdot \widehat{q}, \qquad (2.11)$$

where σ is the conductivity of the spin sink. Since the voltage depends on $m_x^* m_y$ we expect the line shape to be completely Lorentzian [23].[10] Also as a consequence of the magnetization dependence, once strong spin-photon coupling has been taken into account, which modifies the magnetization dispersion relation, we would expect that the V_{SP} would be modified. In this context it is useful to define the magnetization spectral function

$$\mathbb{S}_m = \frac{m_x^* m_y}{M_0^2}, \qquad (2.12)$$

in which case we can write

$$V_{\mathrm{SP}} = V_0 \omega \mathrm{Im} \left(\mathbb{S}_m \right) \left(\widehat{y} \times \widehat{s} \right) \cdot \widehat{q} \qquad (2.13)$$

where $V_0 = \frac{\theta_{\mathrm{SH}}\lambda_{\mathrm{SD}}}{\sigma} \left(\frac{e}{4\pi} \right) \frac{G_r}{t_{\mathrm{s}}w} \tanh \left(\frac{t_{\mathrm{s}}}{2\lambda_{\mathrm{SD}}} \right)$ is simply the geometry and sample dependent voltage amplitude. In accordance with our previous discussion of the spin pumping current, $\mathrm{Im} \left(\mathbb{S}_m \right) \propto \left(\Delta H \right)^2 / \left[\left(H - H_r \right)^2 + \left(\Delta H \right)^2 \right]$. Eq. (2.13) therefore suggests that modifications of the spectral function due to strong spin-photon coupling will affect the voltage spectra. In Sec. 4.5.2 we will see that this is in fact the case.

2.5 LIGHT-MATTER HYBRIDIZATION: POLARITONS

Thus far we have considered the effect of an rf magnetic field on the magnetization of a ferromagnetic material and discussed selected aspects of spintronics and mag-

---

[10]The form of Eq. (2.11) is true for both in-plane or out-of-plane $\mathbf{H}$. However once the dynamic magnetization has been determined, geometric details, such as magnetization orientation may contribute to the spin pumping voltage [23].

netism which are relevant to this dissertation. Throughout this discussion we have neglected the fact that the magnetization dynamics may also influence the rf magnetic field. In reality such a back and forth interaction between material dynamics and electrodynamics is common across a wide range of physical systems, underlying the general concept of the polariton; a solid-state excitation resulting from the strong coupling between electrodynamics and material dynamics. The general idea of the polariton is illustrated in Fig. 2.8 and can be understood as follows: In all materials the electrodynamic response is governed by Maxwell's equations [154], which determines the $\omega = ck/\sqrt{\epsilon\mu}$ dispersion of light, where ω, c and k are the frequency, speed and wavevector of light respectively. Macroscopically materials are distinguished from one another based on their response functions, ϵ, μ, and σ, the permittivity, permeability and conductivity respectively, which characterize a material's lattice, spin and charge dynamics. When the material dynamics result in a dipole carrying excitation, e.g. phonons, magnons, excitons or plasmons, the response functions are modified, directly influencing the electrodynamic properties of a material. In
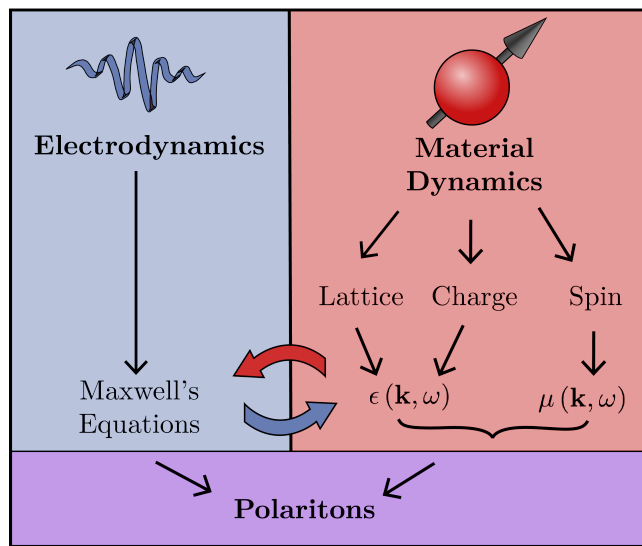
Figure 2.8: A polariton results from the coupling between electrodynamics and material dynamics in a condensed matter system. The electrodynamics of a material is described by Maxwell's equations and will depend on the material properties, such as the permittivity and permeability. Due to material dynamics – either lattice, charge or spin dynamics – the permittivity and permeability may become frequency and wave vector dependent. When this occurs and the material is subject to an electromagnetic field near the material's resonance, a polariton quasiparticle is produced, taking on both photon-like and material-like properties.

this case the response functions become frequency dependent, modifying the intrinsic light dispersion, $\omega = ck/\sqrt{\epsilon(\omega, k)\,\mu(\omega, k)}$. If $\epsilon(\omega, k)$ or $\mu(\omega, k)$ have resonances the deviation from a traditional dispersion may be significant. The result of this coupling between the material dynamics and electrodynamics creates a polariton, a quasiparticle which is a mixture of both light and material dynamics. Although the theoretical details of the polariton may be complex, their general treatment is a simple two step process: (1) determine the material response function in the presence of the excitations; and (2) solve Maxwell's equations using this response function. As there are many dipole carrying material excitations there are also many types of polaritons, e.g. phonon-polaritons [20, 79], exciton-polaritons [20, 155], magnon-polaritons [20, 79], plasmon-polaritons [20, 156, 157] and cavity-exciton-polaritons [158–160].

In many physical systems the wave vector can be controlled, and therefore the $\omega - k$ dispersion can be measured directly. For example, the well known case of the phonon-polariton [161–163] is shown in Fig. 2.9. In this case Raman scattering was used to observe the polariton dispersion in gallium phosphide [164]. In the absence of a strong light-matter interaction one would observe a flat frequency dispersion for the LO and TO phonon dispersions, ω_L and ω_T respectively, indicated by the black horizontal dashed lines, and a linear light dispersion, indicated by the diagonal dashed line. In the case of phonon-polaritons the LO phonon does not hybridize with light, and therefore the flat LO dispersion is still observed. However the TO phonon is significantly modified due to coupling with light and a band gap appears between ω_L and ω_T. This modification of the dispersion and introduction of an anticrossing is the traditional signature of a polariton, which we expect to observe if we indeed discover a new form of strong light-matter interaction.

Although here we have focused on the phonon polariton to provide a basis for physical intuition regarding polaritons, a wealth of literature also exists on the physics of magnetic polaritons [20, 165–167], which are actually more closely related to the cavity-magnon-polariton studied in this dissertation. Magnetic polaritons arise due to the resonant excitation of magnetic materials, governed by the properties of the magnetic permeability. The formation of such hybridized modes may be due to both surface [168, 169] or bulk [170, 171] magnetic excitations and exist in a range of magnetic materials from ferromagnets to antiferromagnets [20, 167]. Like the phonon-polariton, work on magnetic polaritons has focused on the hybridized $\omega - k$ dispersion, and results analogous to Fig. 2.9 (b) can be found in the context of magnon-polaritons as well [171]. However in our experiments light is confined in a cavity and therefore
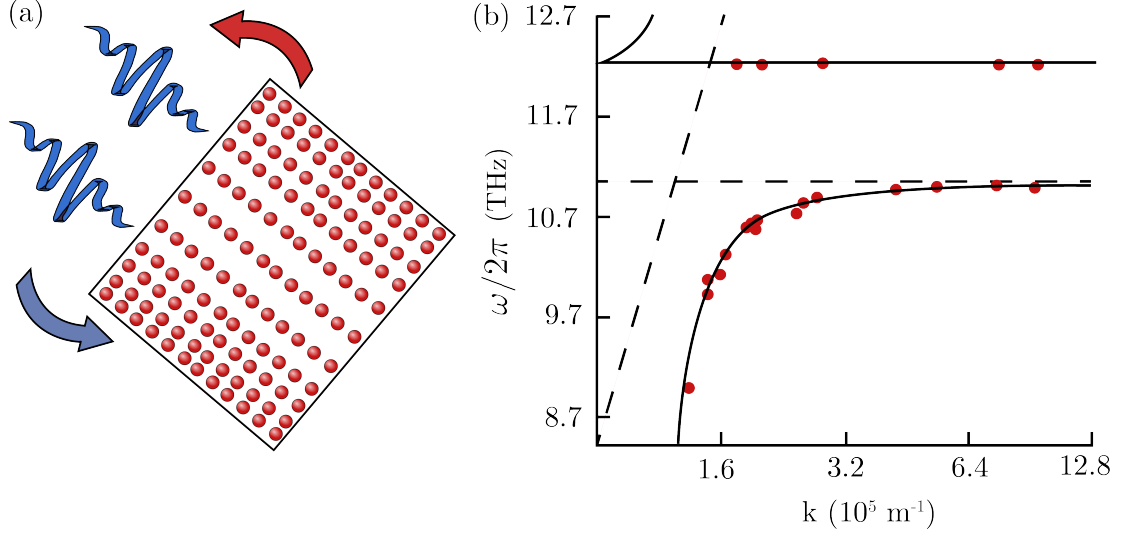
Figure 2.9: The canonical example of the phonon-polariton, which serves as an introduction to the cavity-magnon-polariton. (a) Schematic illustration of the phonon-polariton resulting from coupling between light and resonant lattice vibrations. (b) The phonon-polariton dispersion measured in gallium phosphide. Data from Ref. [164] is shown as symbols with the expected dispersions as solid black curves. The dispersion shows an anticrossing between the uncoupled light and TO phonon dispersions, shown as diagonal and horizontal dashed lines, respectively.

boundary conditions fix the wavevector.[11] This means that k can no longer be used to tune the resonance condition.[12] However in order to observe the polariton behaviour it is not necessary to tune the light dispersion, but rather to approach the case of uncoupled resonance crossing. In our case, where we study a spin-photon system, this can therefore be accomplished by tuning the resonance of the spin system, which is easily controllable through an external bias magnetic field. Therefore, as we will see in the rest of this dissertation, our focus will be on measuring the $\omega - H$ dispersion of the cavity-magnon-polariton under different experimental conditions.

---

[11]The use of confined fields to create the CMP increases its relevance to device design and application compared to traditional magnetic polaritons, which is a strong motivator for cavity spintronics.

[12]Although recently it was demonstrated that a height tuneable cavity could be used to measure the $\omega - k$ dispersion of the cavity-magnon-polariton [57].

3

MODELLING SPIN-PHOTON HYBRIDIZATION

3.1 INTRODUCTION

Condensed matter physics is a science that requires an active interplay between theory and experiment. This is a necessity born out of a difficult challenge — in a system comprised of $\sim 10^{23}$ interacting particles, how can one hope to understand the complex and nuanced behaviour key to physical insight and technological development? The answer is to not consider the minutia of a given system in its entirety, but rather to reveal the key physical elements which drive the relevant emergent behaviour.[1] From the tunnelling of supercurrents which underly the Josephson effect [175] to the phase transition of the Ising model [176], examples of the insights gained in this manner abound in condensed matter systems.

In order to develop physical intuition no model is more universally applied than that of the harmonic oscillator. RLC circuits, phonons [77] and even quantum fields [177] are all characterized by sets of oscillators. As the nature of the cavity-magnon-polariton is the coupling of two resonant systems (spin and photon) one would therefore expect that a model of coupled harmonic oscillators would describe the most fundamental properties of the hybridization. Indeed we show in Sec. 3.2 that such an approach works, calculating the transmission spectra for the spin-photon system using an input-output type of formalism. Importantly this approach reproduces the key signatures of coupling, including mode anticrossing and line width evolution, and provides physical intuition for the coupled spin-photon behaviour. However in order

---

[1]As is often the case, this approach is not unique to condensed matter, but is also fundamental to all fields of physics. Even in the reductionist realm of high energy physics, effective field theories play an important role [172], and also provide perhaps the most successful description of quantum gravity [173, 174].

to understand the physical nature of spin-photon hybridization we delve deeper in Sec. 3.3. Since polaritons result from the coupling of electrodynamics and material dynamics, in the case of a spin-photon system this means coupling together the magnetization dynamics of the Landau-Lifshitz-Gilbert equation and the electrodynamics of Maxwell's equations. By developing a model based on these two bedrocks of physics the true origin of spin-photon coupling is revealed — electrodynamic phase correlation due to the interplay of Ampère's and Faraday's laws. This insight is extremely beneficial from the perspective of spintronic development. Since the spin-photon coupling can be understood through the magnetization dynamics, spintronic techniques which rely on the magnetization, such as spin pumping, will be impacted. This sets the stage for the development of cavity spintronics, where spin-photon hybridization is incorporated into the design of new spintronic technologies.

In this chapter we develop these models in detail, and go even further, using a quantum approach to reveal new coupling control techniques in Sec. 3.4. These models allow us to view the cavity-magnon-polariton from different perspectives, revealing the key properties of mode hybridization, and provide a basis for interpreting our experimental results.

3.2 GENERAL BEHAVIOUR: HARMONIC OSCILLATORS

Harmonic oscillators serve as an instructive toy model of many physical systems, and will serve as our starting pointing in understanding the basic characteristics of the CMP [34]. Consider a system of two equal mass (m) oscillators, O_1 and O_2, coupled together via a spring κ as shown in Fig. 3.1 (a). O_1, shown in blue, represents the cavity and is connected to an input plunger, O_{in}, via a spring with resonance frequency ω_c. The plunger is driven in constant motion at frequency $\omega/2\pi$ so that $x_{\mathrm{in}}(t) = x_{\mathrm{in}}e^{-i\omega t}$. Physically this plunger represents the constant microwave input to the cavity, providing a driving force, $f(t) = \omega_c^2 x_{\mathrm{in}}(t)$, to O_1. O_2, shown in red, represents the FMR and is attached to a fixed wall with a spring of resonant frequency ω_r. Damping is introduced via a viscous force with coefficient β for O_1, which models the intrinsic conductive losses of the cavity, and α for O_2, modelling losses due to magnetization damping. We do not consider a damping associated with the input.

To extract the complex CMP dispersion it is sufficient to set $x_{\mathrm{in}} = 0$ and solve the corresponding eigenvalue problem. This means that the dispersion and line width are determined solely by the properties of the O_1, O_2 system, the coupling κ and

the uncoupled resonances and damping, $\omega_c, \omega_r, \beta$ and α, and is independent of how the system is driven [34]. The energy absorption of the coupled oscillators can also be calculated in a standard way using a dissipative function for the system [178]. However, calculating the full transmission spectra will depend on the coupling of energy into and out of the system and therefore we must also consider an "output port". To do so we connect an energy absorber, O_{out}, to O_1 using a spring k_{out} as shown in Fig. 3.1 (a). The transmission through the system is then $|S_{21}|^2 = E_{\text{out}}/E_{\text{in}}$ where E_{out} and E_{in} are the kinetic energies of the output and input oscillators respectively.
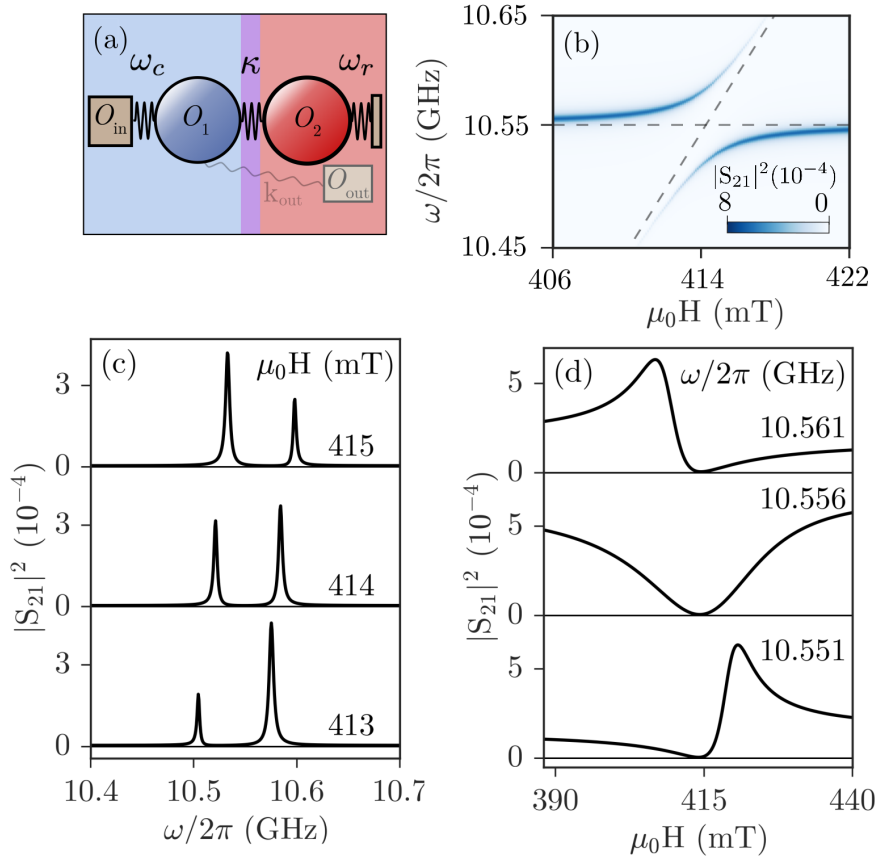
Figure 3.1: CMP transmission spectra in the harmonic coupling model. (a) Schematic illustration of two coupled oscillators. O_1, representing the cavity, experiences a sinusoidal driving force, and has its motion "detected" by coupling to O_{out} through a stiff spring. The FMR is represented by the red O_2, while the purple region indicates the coupling between the cavity and spin systems. (b) The full $\omega - H$ dispersion calculated according to Eq. (3.6) using experimental parameters from Sec. 4.5. (c) Fixed field and (d) frequency cuts made above, at and below the crossing point $\omega_r = \omega_c$ calculated according to Eq. (3.6). A modified version of this figure was originally published in Ref. [34].

27

For high quality cavities, the output coupling $k_{\text{out}} \ll 1$, and in particular $k_{\text{out}} \ll \kappa$. There is also no damping associated with the output. Therefore the equations of motion for O_1, O_2 and O_{out} are, respectively,

$$\ddot{x}_1 + \omega_c^2 x_1 + 2\beta\omega_c \dot{x}_1 - \kappa^2 \omega_c^2 x_2 = f e^{-i\omega t}, \tag{3.1}$$

$$\ddot{x}_2 + \omega_r^2 x_2 + 2\alpha\omega_c \dot{x}_2 - \kappa^2 \omega_c^2 x_1 = 0, \tag{3.2}$$

$$\ddot{x}_{\text{out}} - k_{\text{out}}^2 \omega_c^2 x_1 = 0. \tag{3.3}$$

Here we have defined the damping coefficients α and β as well as the couplings κ and k_{out} to be dimensionless by normalizing to ω_c. Additionally since $k_{\text{out}} \ll 1$ the action of O_{out} on O_1 does not need to be included in Eq. (3.1) and there is no resonance in Eq. (3.3). Taking $(x_1, x_2, x_{\text{out}}) = (A_1, A_2, A_{\text{out}}) e^{-i\omega t}$, Eqs. (3.1) and (3.2) can be written in the matrix form $\boldsymbol{\Omega}\mathbf{A} = \mathbf{f}$ where $\mathbf{A} = (A_1, A_2)$, $\mathbf{f} = (-f, 0)$ and

$$\boldsymbol{\Omega} = \begin{pmatrix} \omega^2 - \omega_c^2 + 2i\beta\omega_c\omega & \kappa^2 \omega_c^2 \\ \kappa^2 \omega_c^2 & \omega^2 - \omega_r^2 + 2i\alpha\omega_c\omega \end{pmatrix} \tag{3.4}$$

while Eq. (3.3) becomes

$$A_{\text{out}} = -\frac{k_{\text{out}}^2 \omega_c^2}{\omega^2} A_1. \tag{3.5}$$

Solving for A_1, $\mathbf{A} = \boldsymbol{\Omega}^{-1}\mathbf{f}$, the transmission is determined to be

$$|\text{S}_{21}(\omega, H)|^2 = \frac{E_{\text{out}}}{E_{\text{in}}} = \frac{m_{\text{out}} A_{\text{out}}^2}{m_{\text{in}} x_{\text{in}}^2} = \eta \frac{\omega_c^8}{\omega^4} \frac{|\omega^2 - \omega_r^2 + 2i\alpha\omega\omega_c|^2}{|\det(\boldsymbol{\Omega})|^2}. \tag{3.6}$$

Here we have used $x_{\text{in}} = \omega_c^2 f$. $\eta = (m_{\text{out}}/m_{\text{in}})k_{\text{out}}^4$ acts as an impedance matching parameter, depending not only on the output coupling k_{out} but also the matching of the input/output ports determined by $m_{\text{out}}/m_{\text{in}}$. The determinant is given by

$$\det(\boldsymbol{\Omega}) = \left(\omega^2 - \omega_c^2 + 2i\beta\omega_c\omega\right)\left(\omega^2 - \omega_r^2 + 2i\alpha\omega_c\omega\right) - \kappa^4 \omega_c^4 \tag{3.7}$$

and defines the spectral function of the coupled system.

The role of the output absorber is apparent from Eqs. (3.6) and (3.7), it is needed to model the output port and calculate the transmission, since the amplitude of S_{21} in Eq. (3.6) is proportional to k_{out}. However the output plays no role in the dispersion which is determined by the roots of the determinant in Eq. (3.7). These facts also illustrate the simplicity of generalizing the model to multiple cavity/multiple spin

wave modes since the dispersion and line width will be determined solely from the coupling between any cavity and spin wave modes while the form of the output energy needed to determine the microwave transmission will remain the same as Eq. (3.5) [34].

Due to the general nature of the harmonic model, there are several detailed features which are not accounted for in this description. For example, we have not considered the wave vector dependence of either the spin or photon subsystem. This is justified since the microwave photon wavelength is much larger than the relevant magnon wavelength and the sample size, and therefore the driving field will be approximately uniform over the sample. Furthermore, since the hybridization occurs with a cavity photon, the wave vector is fixed and therefore the most relevant feature to consider is the field dependence of the FMR, which we can account for by allowing ω_r to vary. Actually, even in situations where the photon wave vector is controlled through tuning the cavity height, the relevant physical influence is to tune ω_c and therefore the length scales between the photon and magnon wavelengths do not influence the observed behaviour [57]. We have also not accounted for any polarization effects of the photons. In our experimental configuration this is most relevant in determining the orientation between the local microwave magnetic field and the saturation magnetization, determined by the external bias field. As we will discuss in Sec. 5.4 this orientation does play an important role in the coupling, and can be included by introducing an orientation dependence to the coupling strength [50, 179]. However even with such detailed behaviour missing, at this point we do have a working model of the CMP which, via Eq. (3.6), allows us to calculate the microwave transmission, and using Eq. (3.7), allows us to determine the complex CMP dispersion, including both the dispersion and damping behaviour of the hybridized modes. In comparing the model behaviour to experiment we will see that this general model captures all key features of the CMP. $|S_{21}(\omega, H)|^2$ is calculated and plotted in Fig. 3.1 (b) using the experimentally realistic parameters (see Sec. 4.5) $\alpha = 0.8 \times 10^{-4}$, $\beta = 3 \times 10^{-4}$ and $\omega_c/2\pi = 10.556$ GHz. We also use a coupling strength of $|\kappa| = 0.077$ and calculate ω_r according to the Kittel formula for a magnetized sphere [21, 180, 181], $\omega_r = \gamma (H + H_A)$ with gyromagnetic ratio $\gamma = 2\pi \times 28 \, \mu_0$GHz/T and shape anisotropy $\mu_0 H_A = -37.7$ mT.[2] The value of the impedance matching, $\eta = 2.3 \times 10^{-10}$, was fit

---

[2]The value of the coupling strength can be treated as a fitting parameter or determined experimentally from the Rabi gap as we will discuss in detail further on [34]. We only include the explicit value here for completeness as the important point is the plot in Fig. 3.1 (a).

to experimental results. The diagonal dashed line shows the uncoupled FMR dispersion following the Kittel formula and the horizontal dashed line is the uncoupled cavity mode. The most striking feature of the transmission spectra is an anticrossing in the dispersion, which reflects the coupled nature of the system. At the crossing point, $\omega_c = \omega_r$, the hybridized modes have the greatest deviation from their uncoupled counterparts. Also at the crossing point the hybridized modes have their minimum frequency separation, ω_{gap}, which is an increasing function of the coupling strength. Another intriguing feature of the hybridization is the line width broadening/narrowing that can be observed as H is tuned. These characteristics of the CMP will be investigated experimentally in Sec. 4.5.

Eq. (3.6) can also be used to calculate the line cuts at fixed field and frequency, shown in Figs. 3.1 (c) and (d) respectively. As may be anticipated for a resonance process, we see that the fixed H cuts are symmetric in ω, appearing as Lorentz-like peaks. On the other hand, while for fixed $\omega = \omega_c$, $|S_{21}(H)|^2$ has a symmetric dip, above and below ω_c the fixed field line shape has an asymmetry and the polarity of the line shape changes as we pass through ω_c. Interestingly all of these features can already be captured by the general harmonic oscillator model and can be made even more transparent by implementing experimentally justified approximations.

3.2.1 *Simplification of Transmission Spectra*

To compare the harmonic model to other CMP descriptions and to experimental data it is important to simplify Eq. (3.6). Since the effect of hybridization is greatest near $\omega_r = \omega_c$ we can make a classical rotating wave approximation to find [34],[3]

$$|S_{21}|^2 = \eta \frac{\omega_c^2}{4} \frac{|\omega - \tilde{\omega}_r|^2}{|\,(\omega - \tilde{\omega}_c)(\omega - \tilde{\omega}_r) - \frac{1}{4}\kappa^4 \omega_c^2|^2}. \tag{3.8}$$

Here we have dropped higher order terms in $\alpha\omega$ and $\beta\omega$ and defined $\tilde{\omega}_c = \omega_c - i\beta\omega_c$ and $\tilde{\omega}_r = \omega_r - i\alpha\omega_c$. Using this notation the eigenvalues at fixed H, determined by the poles of S_{21}, take the simple form

$$\tilde{\omega}_\pm = \frac{1}{2}\left[\tilde{\omega}_r + \tilde{\omega}_c \pm \sqrt{(\tilde{\omega}_r - \tilde{\omega}_c)^2 + \kappa^4 \omega_c^2}\right]. \tag{3.9}$$

---

[3]In this approximation we write $\omega^2 - \omega_{c,r}^2 \sim (\omega - \omega_{c,r})\,2\omega_c$. We will discuss the rotating wave approximation in detail in Sec. 3.4.1.

The real and imaginary contributions of the eigenvalues are plotted in Fig. 3.2 (a) and (b) respectively.[4] Panel (a) shows a clear anticrossing, which we already observed in the full dispersion mapping, with horizontal and vertical dashed lines indicating the uncoupled cavity and FMR dispersions respectively. The strength of the spin-photon interaction determines the size of the eigenmode separation observed in Fig. 3.2 (a),
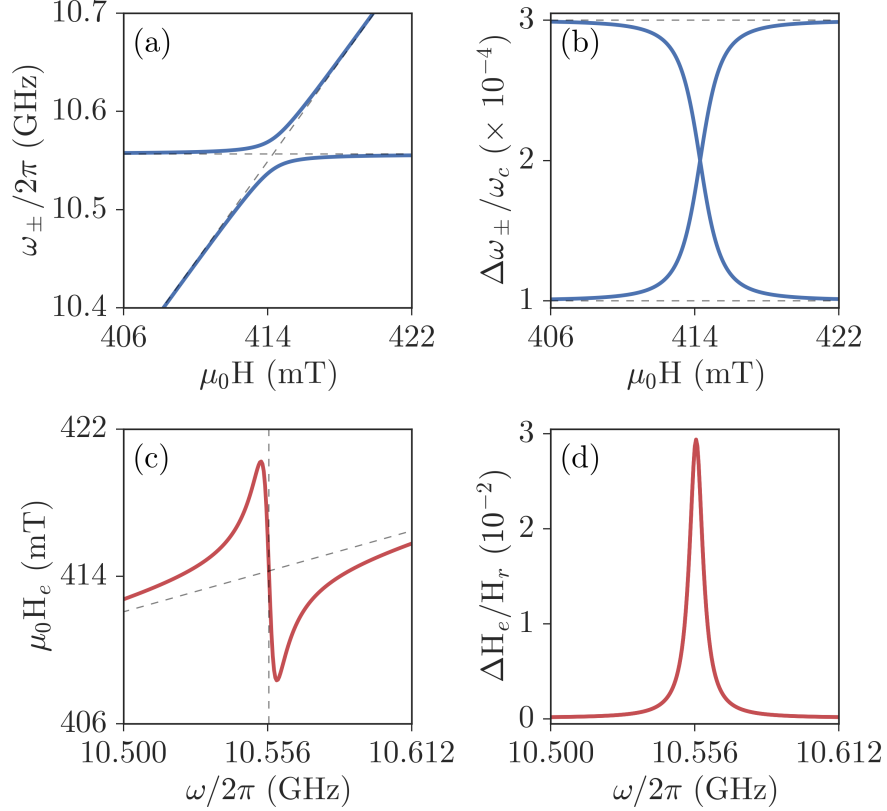
Figure 3.2: (a) $\omega_{\pm}$ and (b) $\Delta\omega_{\pm}$ calculated according to Eq. (3.9) showing the anticrossing and line width evolution signatures of the spin-photon coupling respectively. The horizontal and diagonal dashed lines in (a) show the uncoupled cavity and FMR dispersions respectively, while the horizontal dashed lines in (b) indicate the damping limits due to α and β. (c) H_e and (d) ΔH_e calculated according to Eq. (3.12). The vertical and diagonal dashed lines in (c) indicate the uncoupled cavity and FMR dispersions respectively. Spin-photon coupling induces an antisymmetric deviation in the frequency swept dispersion at the crossing point and a Lorentz type enhancement of the frequency swept line width.

---

[4]Analytic expressions for the real and imaginary components can be determined from Eq. (3.9) using de Moivre's theorem as described in Appendix A Sec. A.1.

and therefore it is useful to define the Rabi gap,[5]

$$\omega_{\text{gap}} = (\omega_+ - \omega_-)\,|_{\omega_c=\omega_r}, \tag{3.10}$$

which can be calculated using Eq. (3.9) as

$$\omega_{\text{gap}} = \sqrt{\kappa^4\omega_c^2 - \omega_c^2\,(\beta - \alpha)^2}. \tag{3.11}$$

Typically $\beta - \alpha \ll \kappa^2$ and therefore $\omega_{\text{gap}} = \kappa^2\omega_c$. Thus we see that in the strongly coupled regime the size of the Rabi gap depends directly on the coupling strength, which can be used to quickly determine the coupling strength experimentally. However, Eq. (3.11) also indicates that we may have $\omega_{\text{gap}} = 0$ even when $\kappa \neq 0$. This special condition actually indicates the presence of an exceptional point in the eigenmode spectrum due to the non-Hermiticity of our spin-photon system [61], which we will explore further in Ch. 6.

Fig. 3.2 (b) shows $\Delta\omega_\pm$, illustrating another feature of coupling, line width evolution. From Eq. (3.9) we immediately see that $\Delta\omega_+ + \Delta\omega_- = \omega_c\,(\alpha + \beta)$, indicating that although coupling enables energy exchange between the spin and photon subsystems it does not introduce additional dissipation channels, and therefore if $\kappa^4 > 0$ then $\Delta\omega_\pm$ is bounded above and below by α and β.

For fixed ω we can similarly find a pole in the transmission spectra from Eq. (3.8),

$$\tilde{\omega}_e = \omega - \frac{\kappa^4\omega_c^2\,(\omega - \omega_c)}{4\left[(\omega - \omega_c)^2 + \beta^2\omega_c^2\right]} + i\left[\alpha\omega_c + \frac{\beta\omega_c^3\kappa^4}{4\left[(\omega - \omega_c)^2 + \beta^2\omega_c^2\right]}\right]. \tag{3.12}$$

This is the field swept analogue of Eq. (3.9) however in this case there is only one solution. The real and imaginary components of $\tilde{\omega}_e$ are plotted in Fig. 3.2 (c) and (d) respectively, where we have introduced the notation $\omega_e = \text{Re}\,(\tilde{\omega}_e)$, $\Delta\omega_e = \text{Im}\,(\tilde{\omega}_e)$, $\omega_e = \gamma H_e$, $\Delta\omega_e = \gamma\Delta H_e$ and $\omega_r = \gamma H_r$. The effects of coupling are evident in the field dispersion plotted in Fig. 3.2 (c) from the asymmetric deviation from the dashed line, which indicates the uncoupled FMR behaviour. Again the deviation due to hybridization is greatest near the crossing point of the uncoupled modes and has a dispersive line shape, with a polarity determined by the sign of the coupling strength κ^4. On the other hand the line width, shown in Fig. 3.2 (d), has a Lorentz peak at

---

[5]The *generalized* Rabi gap is defined as $\omega_+ - \omega_-$ without the constraint $\omega_r = \omega_c$. Therefore we see that the Rabi gap is the minimum value of the generalized Rabi gap.

$\omega = \omega_c$. This resonant enhancement of the FMR line width is in addition to the usual linear ω dependence and the influence of inhomogeneous broadening and therefore plays an important role in the characterization of FMR, as we will discuss in Sec. 5.2.

Finally, the transmission spectra itself can be simplified which proves beneficial for experimental analysis. For fixed field measurements we expand S_{21} near $\omega = \omega_\pm$ to find [34] (see Appendix A Sec. A.2),

$$|S_{21}|_\pm^2 \propto L + (\omega_\pm - \omega_r)^{-1} D \tag{3.13}$$

where

$$L = \frac{(\Delta\omega_\pm)^2}{(\omega - \omega_\pm)^2 + (\Delta\omega_\pm)^2}, \qquad D = \frac{\Delta\omega_\pm (\omega - \omega_\pm)}{(\omega - \omega_\pm)^2 + (\Delta\omega_\pm)^2} \tag{3.14}$$

are the usual Lorentz and dispersive line shapes. Therefore the fixed field transmission spectra of the coupled system generally consists of both Lorentz and dispersive contributions, which differs from the Lorentz nature of a single mode. However generally the term in front of D will suppress the dispersive character unless one of the modes approaches the FMR frequency, where it will be more greatly distorted by the FMR antiresonance, as we will explore in Sec. 4.5.4. Therefore in most cases when analyzing experimental data it is appropriate to fit each peak in the frequency swept CMP transmission spectra independently as a Lorentzian in order to determine the frequency and line width.

On the other hand for the field swept case we can expand the transmission spectra near $\tilde{\omega}_e$ to find [34] (see Appendix A Sec. A.2)

$$|S_{21}|^2 \propto \frac{(q\Delta\omega_e + \omega_r - \omega_e)^2}{(\omega_r - \omega_e)^2 + \Delta\omega_e^2} \tag{3.15}$$

where $q(\omega) = (\omega_e - \omega)/\Delta\omega_e$. The asymmetric transmission of Eq. (3.15) is actually a Fano line shape, which typically arises in scattering problems due to the interference between background and resonance processes [182, 183], with the Fano factor q controlling the degree of asymmetry. In our case $q(\omega > \omega_c) < 0, q(\omega = \omega_c) > 0$ and $q(\omega < \omega_c) > 0$, which explains the change in asymmetry of the field swept line shape observed in Fig. 3.1. The Fano line shape is very similar to the sum of dispersive and Lorentz line shapes. Therefore, from a practical perspective, the resonance frequencies and line widths of the hybridized modes can also be accurately determined by fitting the transmission spectra to a function that has the form $|S_{21}(H)|^2 \propto L + D$,

where L and D are Lorentz and dispersive line shapes with resonance frequency ω_e and line width $\Delta\omega_e$. This provides a simple way to analyze experimental results.

3.2.2 *CMP Eigenvectors and Energy Distribution*

From the dispersion we have found that the CMP is a hybridization of magnon and photon states. This fundamental property is also reflected in an important way through the CMP eigenvectors. Denoting the CMP states as $X_\pm$ we find (see Appendix A Sec. A.3)

$$\begin{pmatrix} X_+ \\ X_- \end{pmatrix} = \begin{pmatrix} \eta_- & \eta_+ \\ -\eta_- & \eta_+ \end{pmatrix} \begin{pmatrix} x_1 \\ x_2 \end{pmatrix}, \tag{3.16}$$

where $\eta_\pm = \sqrt{\Omega \pm \Delta}/\sqrt{2\Omega}$ with frequency detuning $\Delta = \tilde{\omega}_r - \tilde{\omega}_c$ and generalized Rabi frequency $\Omega = \sqrt{(\tilde{\omega}_r - \tilde{\omega}_c)^2 + \kappa^4 \omega_c^2}$. Eq. (3.16) describes a Hopfield like transformation [160] between the polariton modes ($X_\pm$) and the photon and spin states ($x_{1,2}$), which determines the spin and photon fractions of each CMP branch, as shown in Fig. 3.3. At low fields the upper CMP branch is dominated by the cavity photons, which is why the dispersion approaches that of the uncoupled cavity, whereas at high fields the spin fraction dominates and the dispersion becomes FMR-like. This situation is reversed for the lower CMP branch. Since the microwave transmission is sensitive to the photon-like nature of the hybridized modes, the mode composi-
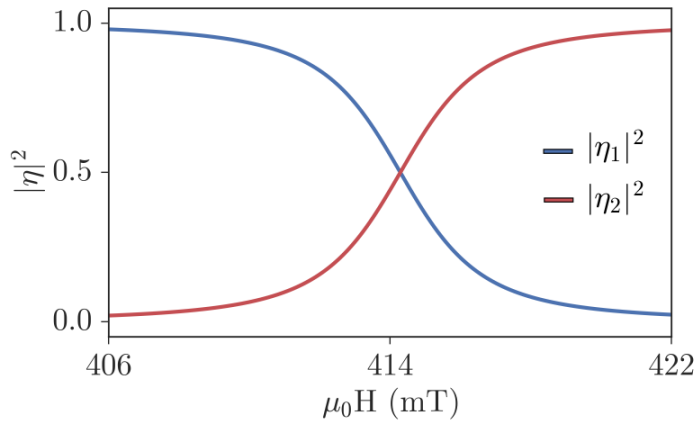
Figure 3.3: The Hopfield-like coefficients $\eta_{1,2}$ determine the composition of the polariton branches. The evolution of $\eta_{1,2}$ with $\mu_0 H$ corresponds to the upper CMP branch transitioning from photon-like to spin-like as the field is increased, with the opposite behaviour for the lower branch.

tion explains why we observe the strongest signal for the upper (lower) branch when $H \ll H_r$ ($H \gg H_r$). Meanwhile at the crossing point both upper and lower branches have equal spin and photon contributions, and therefore both branches have equal transmission amplitudes at this point.

At the crossing point, where the fractional composition is equal, and in the absence of damping, we find that

$$X_{\pm} = \begin{pmatrix} \pm \text{sign}\,(\kappa^2) \\ 1 \end{pmatrix}. \qquad (3.17)$$

Therefore the coherent nature of the hybridized modes is determined by the sign of the coupling strength. We can physically interpret this behaviour by considering the Hamiltonian of our coupled oscillator system [184]

$$2H/m = \dot{x}_1^2 + \dot{x}_2^2 + \omega_c^2 x_1^2 + \omega_r^2 x_2^2 + \kappa^2 \omega_c^2 x_1 x_2. \qquad (3.18)$$

Here the first two terms are the kinetic energies of O_1 and O_2 respectively, the third and fourth terms are the potential energies of each oscillator and the final term is the interaction energy. Therefore the coupling strength determines the sign of the interaction potential and as a result determines the coherent properties of the hybridization. In the case of the CMP, $\kappa^2 > 0$ and therefore the higher energy mode $X_+ = (1,1)$ has in-phase motion while the lower energy mode $X_- = (-1,1)$ has out-of-phase motion.

The generality of the oscillator model allows us to compare the situation of the CMP to the well known case of molecular bonding, where two atoms combine to form bonding and anti-bonding orbitals [184]. In that case the bonding potential is attractive, meaning that the analogous κ^2 would be negative. Therefore the bonding orbitals have lower energy than either of the two separate atoms and correspond to in-phase oscillations, while the anti-bonding orbitals have out-of-phase motion and a higher energy. Of course for the CMP the spring which we use to model the spin-photon interaction creates a repulsive potential, leading to the opposite behaviour. We note that since we experimentally determine the gap, which is proportional to κ^4, the sign of κ^2 is experimentally ambiguous. However the fact that $\kappa^2 > 0$ can be further justified by comparison to the quantum model as described in Sec. 3.4 and in detail in Ref. [184].

The in-phase and out-of-phase oscillations are a special example of the more general phase relationship between magnon and photon states which create the CMP.

By examining the full eigenmodes we can more generally write

$$X_{\pm} \propto \frac{\pm\sqrt{\Omega^2 - \Delta^2}}{(\Omega \pm \Delta)} x_1 + x_2 = e^{i\phi_{\pm}} x_1 + x_2 \tag{3.19}$$

where

$$e^{i\phi_{\pm}} = \frac{\pm\sqrt{\Omega^2 - \Delta^2}}{(\Omega \pm \Delta)} = \frac{1}{2}\frac{\kappa^2 \omega_c}{\tilde{\omega}_{\pm} - \tilde{\omega}_c} \tag{3.20}$$

defines the phase $\phi_{\pm}$. This relationship reveals an important physical insight into the CMP, which is actually a general property of polaritons: the CMP results from a strict phase correlation between magnon and photon states. Essentially this reflects the fact that at any given configuration of our system, defined by the magnetic bias field, the hybridized state will have a strictly defined composition of photon and spin states.

Although we have gained significant insight based solely on the general principles of harmonic coupling an important question remains. What is the physical origin of the phase correlation? To answer this question we have developed a more physical model which directly incorporates the coupling between magnetization dynamics and electrodynamics underlying spin-photon hybridization.

3.3 THE ORIGIN OF HYBRIDIZATION: ELECTRODYNAMIC PHASE CORRELATION

To understand the origin of the phase correlation we must carefully examine the material dynamics of our system. Thanks to the great insight of Landau and Lifshitz [98] we know that a magnetic field $\mathbf{H}_f$ acts on a spin system, characterized by the magnetization $\mathbf{M}$, as an external torque which drives precession and can be described as,

$$\frac{d\mathbf{M}}{dt} = \gamma\mathbf{M} \times \mathbf{H}_f - \frac{\alpha}{M}\left(\mathbf{M} \times \frac{d\mathbf{M}}{dt}\right). \tag{3.21}$$

Eq. (3.21) is the famous Landau-Lifshitz-Gilbert equation, which is just the Landau-Lifshitz equation we derived in Sec. 2.2 with a phenomenological damping term proportional to the so-called Gilbert damping parameter α. The later term accounts for losses which will align the magnetization with a bias field direction. To solve the LLG equation we split $\mathbf{M}$ into a static contribution $\mathbf{M}_0$ along the $\hat{\mathbf{z}}$ direction and dynamic components $\mathbf{m}(t)$ in the x-y plane, $\mathbf{M} = \mathbf{M}_0 + \mathbf{m}(t) = M_0\hat{\mathbf{z}} + \mathbf{m}(t)$. Similarly we write $\mathbf{H}_f = \mathbf{H} + \mathbf{h}(t) = H\hat{\mathbf{z}} + \mathbf{h}(t)$. Assuming a harmonic time dependence,

$\mathbf{m}(t) = \mathbf{m}e^{-i\omega t}$ and $\mathbf{h}(t) = \mathbf{h}e^{-i\omega t}$ and accounting for sample geometry through the demagnetization fields which send, $h_x \rightarrow h_x - N_x m_x, h_y \rightarrow h_y - N_y m_y$ and $H \rightarrow H - N_z M_z$, the linear response is governed by

$$\mathbf{m} = \chi \mathbf{h} \qquad (3.22)$$

where the response function χ is given by

$$\chi = A^{-1} \begin{pmatrix} \omega_m \left[\omega_m N_y + \omega_0 - i\alpha\omega \right] & i\omega\omega_m \\ -i\omega\omega_m & \omega_m \left[\omega_m N_x + \omega_0 - i\alpha\omega \right] \end{pmatrix} \qquad (3.23)$$

with $A = \omega_r^2 - \omega^2 - i\alpha\omega \left(\omega_m \left(N_x + N_y \right) + 2\omega_0 \right)$, $\omega_m = \gamma M_0, \omega_0 = \gamma \left(H_0 - N_z M_0 \right)$ and $\omega_r^2 = \gamma^2 \left[H_0 + \left(N_y - N_z \right) M_0 \right] \left[H_0 + \left(N_x - N_z \right) M_0 \right]$. Physically ω_r is the FMR resonance frequency and ω_0 is the resonance frequency in the limit of zero demagnetization fields. For small damping, so that terms of order α^2 may be neglected, the eigenvectors of the response function are the elliptically polarized modes $m^+ = Dm_x + im_y$ and $h^+ = m_x + iDm_y$ with ellipticity D,

$$D = \sqrt{\frac{\omega_m N_x + \omega_0 - i\alpha\omega}{\omega_m N_y + \omega_0 - i\alpha\omega}}. \qquad (3.24)$$

The magnetization dynamics in terms of the elliptically polarized modes is exceptionally simple,

$$m^+ = \frac{-\omega_m}{\omega - \omega_r + i\alpha\omega} h^+. \qquad (3.25)$$

Here we have also made the approximation $\omega_r \approx \omega_0 + \frac{1}{2}\omega_m \left(N_x + N_y \right)$, which holds well for small demagnetizing fields or in a narrow field range. The latter is always true for our examination of the CMP.

Eq. (3.25) is generally true for any magnetization dynamics described by the LLG equation. Typically the microwave fields are taken to be plane waves and the magnetization dynamics then studied. However to consider the CMP we must examine the case when the microwave fields are confined to a high quality microwave cavity, which requires a solution of Maxwell's equations. The important considerations are: (i) our field modes have a resonance and damping and (ii) since they are long lived states inside of the cavity, the back action of the magnetization dynamics they excite must be accounted for. To model this behaviour, we take inspiration from the seminal work of Bloembergen and Pound on the behaviour of radiation damping in

nuclear magnetic resonance [24] and consider an artificial RLC circuit with current $j^+(t) = Dj_x(t) + ij_y(t)$ [34, 48]. The dynamics of $j^+(t)$ is governed by the RLC equation,

$$Rj^+(t) + \frac{1}{C}\int j^+(t)dt + L\frac{dj^+(t)}{dt} = V^+(t) \tag{3.26}$$

where R, L and C are the resistance, inductance and capacitance of the model circuit, respectively. Most importantly this circuit contains a voltage $V^+(t) = iK_cL\frac{dm^+(t)}{dt}$ produced by the precessing magnetization according to Faraday's law. Here K_c is a coupling parameter which characterizes the back action of the magnetization dynamics onto the cavity field. The inclusion of V^+ is the key step in modelling the CMP [34, 48]. Assuming harmonic time dependence, $j^+(t) = j^+e^{-i\omega t}$ and $m^+ = m^+e^{-i\omega t}$ the circuit equation becomes

$$\left(\omega^2 - \omega_c^2 + 2i\beta_{\text{int}}\omega_c\right)j^+ = -i\omega^2 K_c m^+ \tag{3.27}$$

where we have defined $\omega_c = \sqrt{\frac{1}{LC}}$ and $\beta_{\text{int}} = \frac{R}{2}\sqrt{\frac{C}{L}}$. Since the field that drives the FMR is generated by the current due to Ampére's law, j_x and j_y will produce fields h_x and h_y according to the phase relation $h_x = K_m j_y$ and $h_y = -K_m j_x$. Therefore we have $h^+ = -K_m j^+$, where K_m is a coupling constant which characterizes the microwave current induced field, and the coupled equations of motion for the CMP system may be written as,

$$\begin{pmatrix} \omega^2 - \omega_c^2 + 2i\beta_{\text{int}}\omega_c\omega & i\omega^2 K_c \\ -i\omega_m K_m & \omega - \omega_r + i\alpha\omega \end{pmatrix}\begin{pmatrix} j^+ \\ m^+ \end{pmatrix} = 0. \tag{3.28}$$

The determinant of the matrix in Eq. (3.28) determines the CMP dispersion. We can see that in the classical rotating wave approximation, and to lowest order in coupling strength and damping near the crossing point, this dispersion is identical to the coupled oscillator system. Therefore all of the behaviour we have already discussed is automatically captured by this electrodynamic model. Importantly however, this more physical approach reveals to us the origin of the phase correlation in the CMP. Due to Ampère's law, which locks the phase of the rf current with that of the rf magnetic field, the phase difference between the rf current carried by the cavity mode and the rf magnetization excited in the YIG is fixed to form the hybridized modes of the CMP.

In order to determine the full transmission spectra, as opposed to the dispersion
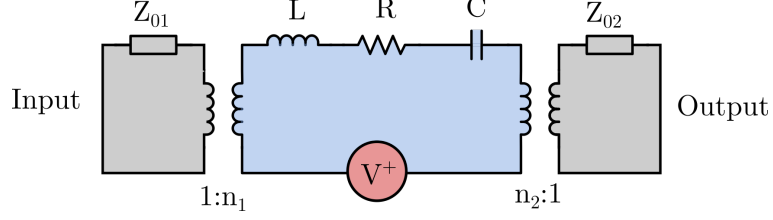
Figure 3.4: Circuit model of the cavity-magnon-polariton. The RLC circuit in blue models the microwave cavity, with a voltage source, shown in red, representing the effect of the magnetization precession. Input and output fields are inductively coupled into the microwave cavity.

alone, we can apply microwave circuit theory to our RLC circuit. Our artificial circuit used to model the cavity is shown in Fig. 3.4 and is inductively coupled to input and output ports of impedance and number of turns in the inductor Z_{01}, n_1 and Z_{02}, n_2 respectively. The total impedance of the circuit and voltage source is $Z = Z_c + Z_m$ where, from Eq. (3.25) and the definition of V^+,

$$V^+ = \frac{i\omega_m K_c K_m L\omega}{\omega - \omega_r + i\alpha\omega} j^+,$$ (3.29)

the inductance due to the voltage source is,

$$Z_m = \frac{i\omega_c K_c K_m L\omega}{\omega - \omega_r + i\alpha\omega}.$$ (3.30)

From Eq. (3.27) the inductance due the RLC circuit is

$$Z_c = -i\frac{L}{\omega} \left(\omega^2 - \omega_c^2 + 2i\beta_{\mathrm{int}}\omega_c\omega\right).$$ (3.31)

Having defined the impedance of our system, we can use a standard approach to define the transfer matrix which determines the relationship between the voltages in the input and output circuits [185],

$$T = \begin{pmatrix} A & B \\ C & D \end{pmatrix} = \begin{pmatrix} \frac{n_2}{n_1} & \frac{Z}{n_1 n_2} \\ 0 & \frac{n_1}{n_2} \end{pmatrix}.$$ (3.32)

Therefore the transmission can be calculated as [34]

$$S_{21} = \frac{2\left(Z_{01}Z_{02}\right)^{1/2}}{AZ_{02} + B + CZ_{01}Z_{02} + DZ_{01}}$$ (3.33)

39

and therefore

$$S_{21} = \frac{2i\omega_c\omega\beta_L\overline{S}_{21}\left(\omega - \omega_r + i\alpha\omega\right)}{\left(\omega^2 - \omega_c^2 + i\beta_L\omega\omega_c\right)\left(\omega - \omega_r + i\alpha\omega\right) - \omega^2\omega_m K^2}. \tag{3.34}$$

Here we have defined the input and output couplings, $2\omega_c\beta_i^{\text{ext}} = Z_{0i}n_i^2/L$, which characterize how microwaves are coupled into and out of our RLC circuit, the loaded damping $\beta_L = \beta_{\text{int}} + \beta_1^{\text{ext}} + \beta_2^{\text{ext}}$ and $K^2 = K_cK_m$. The transmission amplitude in the zero coupling limit, $\overline{S}_{21} = \sqrt{\beta_1^{\text{ext}}\beta_2^{\text{ext}}}/\beta_L = S_{21}\left(\omega = \omega_c, K^2 = 0\right)$, physically defines the power input into the microwave cavity. The microwave reflection, S_{11} can also be
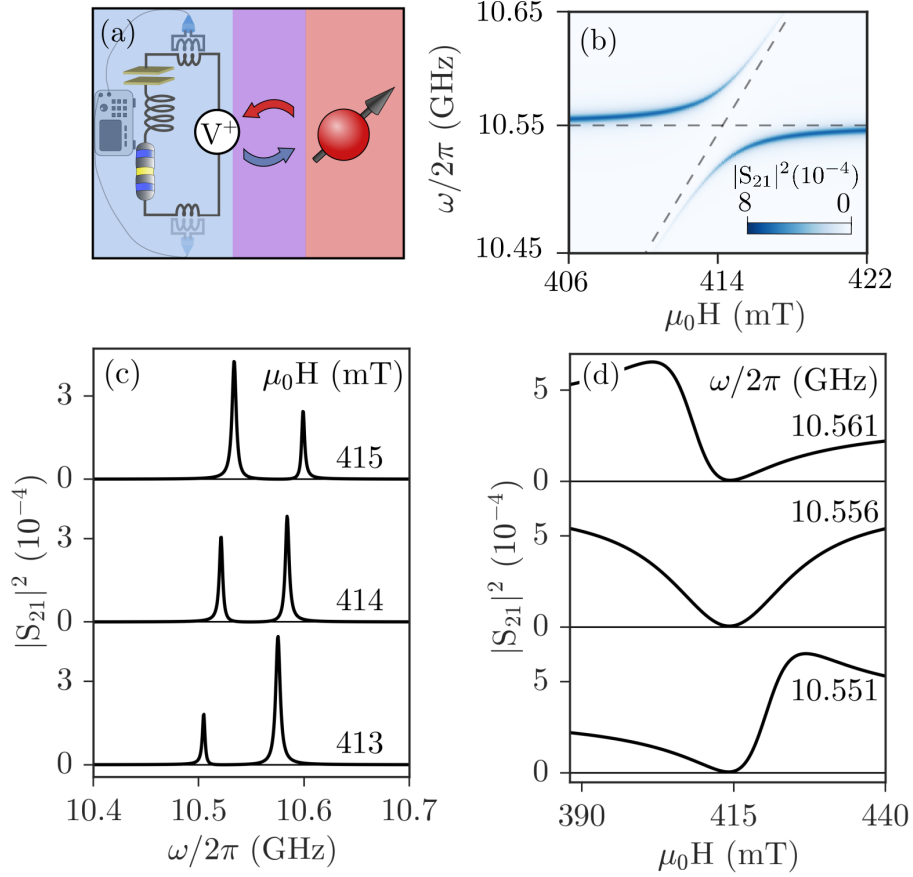
Figure 3.5: (a) Schematic illustration of the electrodynamic phase correlation which produces the CMP. The current in an RLC circuit produces a microwave field which drives magnetization precession. The precessing magnetization induces a voltage via Faraday's law, coupling back to the magnetic field. (b) The full transmission spectra calculated using Eq. (3.34) and experimentally relevant parameters. (c) Frequency and (d) field line cuts of the transmission spectra. A modified version of this figure was originally published in Ref. [34].

found directly from the transfer matrix. We note that in our system, since we can assume $n_1 = n_2$ and $Z_{01} = Z_{02}$, we find the simple relationship $S_{11} = -1 + S_{21}$.

The full transmission spectra calculated using Eq. (3.34) is plotted in Fig. 3.5 (b) using the experimentally relevant parameters $\omega_c/2\pi = 10.556$ GHz, $\alpha = 0.8 \times 10^{-4}, \beta_{\text{int}} = 2.9 \times 10^{-4}, \beta_1^{\text{ext}} = \beta_2^{\text{ext}} = 3.8 \times 10^{-6}$ and $|K| = 6.4 \times 10^{-3}$. The FMR dispersion is determined by the gyromagnetic ratio $\gamma = 2\pi \times 28 \; \mu_0$GHz/T, anisotropy $\mu_0 H_A = -37.7$ mT and saturation magnetization $\mu_0 M_0 = 178$ mT. We again observe the key signatures of an anticrossing and line width evolution, while both the frequency and field cuts, shown in panels (c) and (d) respectively, show the same characteristics we have discussed in the oscillator model. In fact if we make the rotating wave approximation and neglect higher order contributions so that $\alpha\omega \sim \alpha\omega_c$, S_{21} becomes

$$S_{21} = \frac{i\omega\beta_L \overline{S_{21}} \left(\omega - \omega_r + i\alpha\omega_c\right)}{\left(\omega - \omega_c + i\beta_{\text{int}}\omega_c\right)\left(\omega - \omega_r + i\alpha\omega_c\right) - \frac{\omega_c\omega_m K^2}{2}}, \tag{3.35}$$

which has the same form as the oscillator simplification of Eq. (3.8). Therefore all of the properties, such as line shape, Rabi gap and mode composition, that were discussed in Sec. 3.2.1 apply for the phase correlation model as well.

More rigorous electrodynamic approaches also confirm the key results of the circuit model we have described here. For example, Maksymov et al. [186] used numerical solutions of the LLG and Maxwell equations, obtained using a finite-difference time-domain method, to demonstrate the same strongly coupled transmission features in a dielectric-magnetic multilayer, where high dielectric constant layers act as an effective cavity. Though this approach did not reveal new information about the coupling itself, it did demonstrate a new platform in which to explore magnon-photon hybridization and confirmed the behaviour seen in our circuit model. Furthermore, Cao et al. [187] and Yao et al. [188] used a scattering approach in a simplified 1D configuration to examine the effects of coupling, with the influence of spin waves explicitly accounted for in Ref. [187]. Finally, the behaviour of the dispersion was rigorously examined by Krupka et al. [189] and Pacewicz et al. [190]. In the former work the authors revisited the role of perturbation theory for sample characterization in traditional cavity based FMR measurements by numerically computing the cavity quality factor in regimes where magnon-photon coupling may play a dominant role. Indeed they find that proper characterization of the FMR line width should carefully account for the influence of coupling, as we discuss and analyze in Sec. 5.2 based on our circuit model. Similarly, in Ref. [190] the authors accounted for the intrinsic

permeability of the ferromagnetic material and numerically solved the transcendental equation for the electromagnetic field, finding similar coupling behaviour as our model. Compared to these rigorous electrodynamic approaches, a key contribution of the circuit method is that by capturing the physical origin of phase correlation in an analytical way without introducing complicating geometric or sample dependent details, the coupling mechanism becomes more transparent. This also allows us to understand the physical origin of the two coupled oscillators in the harmonic oscillator model. One oscillator represents the precessing magnetization of the spin system and the other represents the microwave current of the cavity (or equivalently the microwave field in the cavity). Therefore we can now define the spectral functions of the coupled system in a physically meaningful way. In the limit that $K_c \to 0$, the microwave cavity mode will be described by a single Lorentz peak at the cavity frequency ω_c. This behaviour can be described by the spectral function

$$\mathbb{S}_c = \frac{1}{\omega^2 - \omega_c^2 + 2i\beta_{\text{int}}\omega_c\omega} \tag{3.36}$$

in which case the transmission spectra of Eq. (3.34) can be written as

$$\mathrm{S}_{21} = 2i\beta_L\omega_c\omega\overline{\mathrm{S}}_{21}\left[\mathrm{Re}\left(\mathbb{S}_c\right) + i\mathrm{Im}\left(\mathbb{S}_c\right)\right] \tag{3.37}$$

and therefore

$$|\mathrm{S}_{21}| = \overline{\mathrm{S}}_{21} = \sqrt{2\beta_L\omega\omega_c}|\mathrm{Im}\left(\mathbb{S}_c\right)|. \tag{3.38}$$

The full spectral function for the cavity, when coupled to the spin system, is defined analogously,

$$\mathbb{S}_c^{\text{coup}} = \frac{\omega - \omega_r + i\alpha\omega}{\left(\omega^2 - \omega_c^2 + 2i\beta_L\omega\omega_c\right)\left(\omega - \omega_r + i\alpha\omega\right) - \omega^2\omega_m K^2}. \tag{3.39}$$

The transmission of the coupled system can then be described by Eqs. (3.37) and (3.38) by replacing $\mathbb{S}_c \to \mathbb{S}_c^{\text{coup}}$. Similarly, we can define a spectral function of the magnetic system, which would determine the spin pumping voltage through Eq. (2.13), as

$$\mathbb{S}_m^{\text{coup}} = \frac{-i\omega_m K_m}{\left(\omega^2 - \omega_c^2 + 2i\beta_L\omega\omega_c\right)\left(\omega - \omega_r + i\alpha\omega\right) - \omega^2\omega_m K^2}. \tag{3.40}$$

The spin pumping voltage would then be $V_{\text{SP}} \propto |m|^2 = |\mathbb{S}_m|^2$ [191]. Taking the plane wave limit, $\omega_c \to 0$, and removing the magnetization back action by setting $K_c \to 0$,

we therefore recover the result of Eq. (2.13) that $V_{\mathrm{SP}} \propto (\Delta H)^2 / \left[(H - H_r)^2 + (\Delta H)^2\right]$. In the coupled case this expression will be modified due to the modification of the spectral function.

Although the classical electrodynamic and oscillator models produce the same spectra and dispersion, by taking a different approach to describe the CMP we have gained physical insight into the coupling mechanism. Therefore it is fruitful to explore one final model with the following question in mind: Given the nature of magnons and photons, how is our system described quantum mechanically?

3.4 MICROSCOPIC BEHAVIOUR: A QUANTUM TREATMENT

3.4.1 *The Jaynes-Cummings Model*

To explore the quantum nature of the CMP we should turn our attention to the well known behaviour of quantum optics and cavity quantum electrodynamics. The canonical Hamiltonian of quantum optics is the Jaynes-Cummings model, originally proposed to describe spontaneous emission [47, 192].[6] Consider an ensemble of N_s spins coupled to a single mode of a resonant cavity, ω_c. Assuming $N_s \gg 1$, the Holstein-Primakoff transformation [194, 195] applies and we can treat the excitations of the spin system (magnons) as bosonic. Furthermore, we will restrict ourselves to the lowest spin excitation at ω_r (the FMR mode). The simplest Hamiltonian which describes such a spin-photon interaction should contain a kinetic term for each degree of freedom, plus all possible quadratic interactions, and may therefore be written as,

$$H_{\mathrm{JC}} = \hbar\omega_c a^\dagger a + \hbar\omega_r b^\dagger b + \hbar g \left(a + a^\dagger\right)\left(b + b^\dagger\right). \tag{3.41}$$

Here $a^\dagger$ (a) and $b^\dagger$ (b) are the creation (annihilation) operators for the photon and magnon, respectively, and g is the coupling strength. In the interaction picture, the time evolution of a and b is governed by the non-interacting Hamiltonian, $H_0 = \hbar\omega_c a^\dagger a + \hbar\omega_r b^\dagger b$,

$$\dot{a} = -\frac{i}{\hbar}\left[a, H_0\right], \qquad \dot{b} = -\frac{i}{\hbar}\left[b, H_0\right], \tag{3.42}$$

and therefore

$$a\left(t\right) = e^{-i\omega_c t}a(0), \qquad b\left(t\right) = e^{-i\omega_r t}b(0). \tag{3.43}$$

---

[6]Technically here we describe the Tavis-Cummings model, which is the N_s-spin generalization of the single spin Jaynes-Cummings model [193]. However for our purposes the collection of spins act as a single macrospin and the distinction in terminology is unimportant.

As a result, the spin-photon interactions take the form $ab \sim e^{-i(\omega_c+\omega_r)t}$ and $ab^\dagger \sim e^{-i(\omega_c-\omega_r)}$ plus Hermitian conjugates. If $\omega_c \sim \omega_r$, $e^{-i(\omega_c+\omega_r)t}$ is rapidly oscillating and has a small time averaged effect. We therefore neglect these terms leaving,

$$H_{\mathrm{JC}} = \hbar\omega_c a^\dagger a + \hbar\omega_r b^\dagger b + \hbar g \left(ab^\dagger + a^\dagger b \right). \tag{3.44}$$

Neglecting the rapidly oscillating interactions is known as the rotating wave approximation, and results in an analytically solvable Hamiltonian. This approximation amounts to keeping the component of the interaction whose time evolution (closely) co-rotates with the interaction picture eigenstates, dropping the counterrotating term. To physically understand this approximation we can imagine a classical precessing dipole which represents transitions in a two-level system. A linearly oscillating driving field can be decomposed into two counterrotating fields. One of these fields will co-rotate with the dipole moment, applying a constant torque over many periods. However the torque due to the counterrotating field component will reverse (with respect to the dipole precession) every period, and therefore will have little average effect [196].

We can now use the Hamiltonian of Eq. (3.44) to determine the microwave transmission properties of the CMP. However before doing so it is instructive to reexamine the origin of this Hamiltonian. While the Jaynes-Cummings model is well motivated physically, it turns out we can also derive Eq. (3.44) by taking an approach closer to our electrodynamic model and consider the second quantization of a Heisenberg ferromagnet coupled to light via the Zeeman interaction [34].

3.4.2 *Heisenberg Ferromagnet Coupled to Cavity Photons*

At our energy scales, YIG can be treated in terms of an effective spin-s Heisenberg ferromagnet on a cubic lattice. The effective Hamiltonian contains both exchange and dipole-dipole interactions [197],

$$H_s = -\frac{1}{2} \sum_{i,j} \sum_{\alpha,\beta} \left[J_{ij}\delta^{\alpha\beta} + D_{ij}^{\alpha\beta} \right] S_i^\alpha S_j^\beta - g\mu_B B_z \sum_j S_j^z. \tag{3.45}$$

Here S_i and S_j are the spin operators at the ith and j^{th} lattice sites respectively, J_{ij} is the exchange coupling with $J_{ij} = J$ for nearest neighbours ($J_{ij} \sim 0$ otherwise) and $D_{ij}^{\alpha\beta}$ is the dipole tensor. We sum over all lattice sites i and j and over all components

of the spin, α and β. The last term describes coupling of the YIG to a static external field, B_z. To simplify Eq. (3.45) we can use linear spin-wave theory for the lowest magnon band and express the spin operators in terms of the bosonic operators b using the Holstein-Primakoff [194, 195] transformation for a large number of spins, N_s,

$$S_j^z = s - b_j^\dagger b_j, \qquad S_j^+ = \sqrt{2s} b_j^\dagger, \qquad \sqrt{2s} b_j, \qquad (3.46)$$

where $S_j^\pm = S_j^x \pm i S_j^y$ are the ladder operators. Fourier transforming the bosonic operators

$$b_j = \frac{1}{\sqrt{N_s}} \sum_k b_k e^{i\mathbf{k}\cdot\mathbf{r}_j} \qquad (3.47)$$

H_s becomes (see Appendix B.1)

$$H_s = \hbar \sum_k \omega_k^s b_k^\dagger b_k + E_0 \qquad (3.48)$$

where ω_k^s is the frequency of the kth magnon mode and E_0 is the ground state energy due to the exchange interaction and Zeeman energy of the spins and external magnetic field.

In addition to H_s, the full Hamiltonian of our system includes a photon contribution, H_{ph}, which is simply that of a harmonic oscillator,

$$H_{\text{ph}} = \hbar \sum_q \omega_q \left(a_q^\dagger a_q + \frac{1}{2} \right), \qquad (3.49)$$

where q is a mode index, and the coupling between the microwave field and the spins, H_{int}

$$H_{\text{int}} = g\mu_B \sum_j \mathbf{b}_j \cdot \mathbf{S}_j. \qquad (3.50)$$

Here $\mathbf{b} = (b_x, b_y)$ is the circularly polarized microwave field which has the quantized form [198]

$$\mathbf{b} = \frac{1}{c} \sum_q \sqrt{\frac{\hbar\omega_q}{4\epsilon_0 V}} \left[\left(a_q e^{i\mathbf{q}\cdot\mathbf{r}} + a_q^\dagger e^{-i\mathbf{q}\cdot\mathbf{r}} \right) \widehat{\mathbf{x}} + i \left(a_q e^{i\mathbf{q}\cdot\mathbf{r}} - a_q^\dagger e^{-i\mathbf{q}\cdot\mathbf{r}} \right) \widehat{\mathbf{y}} \right], \qquad (3.51)$$

where c is the speed of light, V is the cavity volume, ϵ_0 is the vacuum permittivity and we have assumed that we can locally expand the field in a plane wave basis. In

terms of the spin ladder operators,

$$H_{\text{int}} = \frac{g\mu_B}{c} \sum_{j,q} \sqrt{\frac{\hbar\omega_q}{4\epsilon_0 V}} \left(a_q S_j^+ e^{i\mathbf{q}\cdot\mathbf{r}_j} + a_q^\dagger S_j^- e^{-i\mathbf{q}\cdot\mathbf{r}_j} \right). \tag{3.52}$$

Therefore, making the Hostein-Primakoff transformation, Fourier transforming the magnon operators and using the identity $\sum_j e^{i(\mathbf{q}-\mathbf{k})\cdot\mathbf{r}_j} = N_s\delta(\mathbf{q}-\mathbf{k})$, we have

$$H_{\text{int}} = \hbar\sqrt{N_s}\alpha_c \sum_k \left(a_k b_k^\dagger + a_k^\dagger b_k \right) \tag{3.53}$$

where

$$\alpha_c = \frac{g\mu_B}{\hbar c} \sqrt{\frac{s\hbar\omega_q}{2\epsilon_0 V}} \tag{3.54}$$

is the coupling constant. Combining these Hamiltonians we find [34]

$$H_{\text{sys}} = \hbar \sum_k \omega_k^s b_k^\dagger b_k + E_0 + \hbar \sum_q \omega_q \left(a_q^\dagger a_q + \frac{1}{2} \right) + \hbar\sqrt{N_s}\alpha_c \sum_k \left(a_k b_k^\dagger + a_k^\dagger b_k \right). \tag{3.55}$$

Eq. (3.55) describes a system of coupled harmonic oscillator modes. Further simplification can be achieved by considering our experimental conditions of a single cavity mode, ω_c, coupling to the FMR mode, $\omega_{k\to 0}^s = \omega_r$, and neglecting the ground state energies of the magnon and photon which will not influence the experimentally relevant field dispersions. In this case Eq. (3.55) becomes [34]

$$H = \hbar\omega_r b^\dagger b + \hbar\omega_c a^\dagger a + \hbar\sqrt{N_s}\alpha_c \left(ab^\dagger + a^\dagger b \right). \tag{3.56}$$

which is the same as the Jaynes-Cummings model of Eq. (3.44). Therefore we can obtain a quantum model consistent with the Jaynes-Cummings approach by simply quantizing our electrodynamic approach.

Before examining the transmission spectra, we can easily obtain the eigenspectrum of the coupled system by diagonalizing the Hamiltonian through a Bogoliubov transformation

$$a = -\sin\phi c_1 + \cos\phi c_2, \qquad b = \cos\phi c_1 + \sin\phi c_2 \tag{3.57}$$

where $c_{1,2}$ are new bosonic operators describing the eigenmodes of the system (the

cavity-magnon-polaritons) and the angle ϕ is given by

$$\tan(2\phi) = \frac{2\sqrt{N_s}\alpha_c}{\omega_c - \omega_r}. \tag{3.58}$$

In terms of the polariton operators the Hamiltonian then becomes

$$H = \hbar\omega_- c_1^\dagger c_1 + \hbar\omega_+ c_2^\dagger c_2 \tag{3.59}$$

with the eigenspectrum given by

$$\omega_\pm = \frac{1}{2}\left[\omega_c + \omega_r \pm \sqrt{(\omega_r - \omega_c)^2 + 4N_s\alpha_c^2}\right]. \tag{3.60}$$

While Eq. (3.60) will of course display the same anticrossing behaviour we have observed in our other models, by taking this microscopic approach we can now see that the coupling strength depends directly on the number of spins [34]. Again by viewing the CMP from another "angle" we have gained additional insight into its behaviour.

3.4.3 *Input-Output Formalism*

In order to use the Jaynes-Cummings model of Eq. (3.44) to describe the microwave transmission through our system, we must couple the cavity photons to the external photon bath which exists in the microwave feedlines. To do so we will follow the input-output formalism of quantum optics outlined in Refs. [198, 199]. We consider a Hamiltonian of the form

$$H = H_{\text{sys}} + H_{\text{bath}} + H_{\text{int}}^{\text{bath}}, \tag{3.61}$$

where H_{sys} consists of the cavity photons and its contents (e.g. magnons in the Jaynes-Cummings model) and $H_{\text{int}}^{\text{bath}}$ is the interaction between the bath photons and the cavity photons. As shown in Fig. 3.6, for a two-sided cavity we have two sets of bath photons, labelled by c and d. Treating the bath photons as harmonic oscillators we have

$$H_{\text{bath}} = H_{\text{bath}}^c + H_{\text{bath}}^d = \sum_q \hbar\omega_q c_q^\dagger c_q + \sum_q \hbar\omega_q d_q^\dagger d_q. \tag{3.62}$$
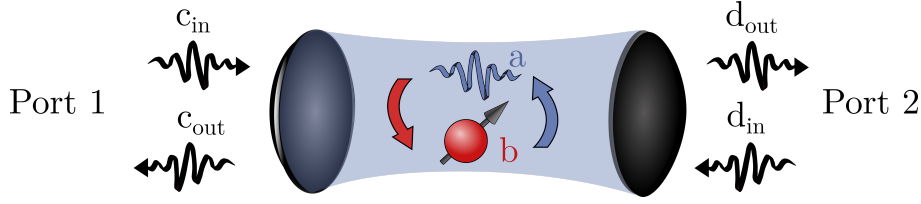
Figure 3.6: In the input-output formalism the bath photons at ports 1 and 2 are coupled to the cavity photons, enabling calculation of the cavity transmission properties.

In the rotating wave approximation the bath-cavity interaction is,

$$H_{\text{int}}^{\text{bath}} = -i\hbar\lambda_c \sum_q \left(a^\dagger c_q - c_q^\dagger a\right) - i\hbar\lambda_d \sum_q \left(a^\dagger d_q - d_q^\dagger a\right) \tag{3.63}$$

where $\lambda_{c,d}$ are the bath-cavity coupling rates for ports 1 and 2 respectively, which we assume are mode independent. Note the difference from the interaction in the Jaynes-Cummings Hamiltonian of Sec. 3.4.1. This may be surprising since in both cases we are coupling together harmonic oscillators. However as we will see below the baths act as an additional source of dissipation for the cavity photons, which means that the overall coupling strength should be imaginary. Anticipating this we choose $\lambda_{c,d}$ to be real, add an explicit imaginary factor and, to ensure that H_{int} is Hermitian, introduce an additional negative sign between terms. Using the entire Hamiltonian we can find the cavity equation of motion as

$$\dot{a} = -\frac{i}{\hbar}\left[a, H_{\text{sys}}\right] - \lambda_c \sum_q c_q - \lambda_d \sum_q d_q. \tag{3.64}$$

The last terms in Eq. (3.64) can be evaluated by solving the bath equations of motion in terms of suitably defined incoming and outgoing wave packets of the baths,

$$\lambda_c \sum_q c_q(t) = -\sqrt{2\kappa_c}c_{\text{in}}(t) + \kappa_c a(t), \tag{3.65}$$

$$\lambda_c \sum_q c_q(t) = \sqrt{2\kappa_c}c_{\text{out}}(t) - \kappa_c a(t), \tag{3.66}$$

where κ_c is the external coupling rate of c-bath photons into the cavity. Similar equations exist for d_q. Eqs. (3.65) and (3.66) have a simple physical purpose: they link the bath modes to the coupling of a wave packet into (c_{in}) or out of (c_{out}) the cavity system. This can most easily by understood by noticing that Eqs. (3.65) and

(3.66) imply

$$c_{\text{in}}(t) + c_{\text{out}}(t) = \sqrt{2\kappa_c}a(t),$$
$$d_{\text{in}}(t) + d_{\text{out}}(t) = \sqrt{2\kappa_d}a(t), \tag{3.67}$$

which simply states that a wave packet of the bath incident on a given port will either be reflected at that port (becoming an outgoing wave) or couple into the cavity. Eqs. (3.65) and (3.66) are rigorously derived in Appendix B.2. With the sums over bath photons determined the cavity equation of motion becomes

$$\dot{a} = -\frac{i}{\hbar}[a, H_{\text{sys}}] + \sqrt{2\kappa_c}c_{\text{in}} + \sqrt{2\kappa_d}d_{\text{in}} - (\kappa_c + \kappa_d)a(t). \tag{3.68}$$

We now take $H_{\text{sys}} = H_{\text{JC}}$ and include the intrinsic damping of the cavity photon and magnon systems by replacing $\omega_c \to \omega_c - i\kappa_a$ and $\omega_r \to \omega_r - i\kappa_b$. Therefore

$$[a, H_{\text{sys}}] = \hbar(\omega_c - i\kappa_a)a + g\hbar b \tag{3.69}$$

and the cavity equation of motion becomes

$$\dot{a} = -i\omega_c a - \kappa_L a - igb + \sqrt{2\kappa_c}c_{\text{in}} + \sqrt{2\kappa_d}d_{\text{in}} \tag{3.70}$$

where the loaded damping $\kappa_L = \kappa_c + \kappa_d + \kappa_a$ includes losses due to both bath couplings as well as the intrinsic losses of the cavity.[7]

Since magnons do not couple directly to the baths, no additional input and output magnons are necessary when considering the magnon equation of motion,

$$\dot{b} = -\frac{i}{\hbar}[b, H_{\text{sys}}] = -i(\omega_r - i\kappa_b)b - iga, \tag{3.71}$$

which can be solved in terms of a as

$$b = \frac{ga}{\omega - \omega_r + i\kappa_b}. \tag{3.72}$$

---

[7]This equation of motion does not include quantum jumps which would appear in a Master equation treatment of an open quantum system [200]. For the CMP this behaviour is suppressed by the large number of spins and photons in the semiclassical limit.
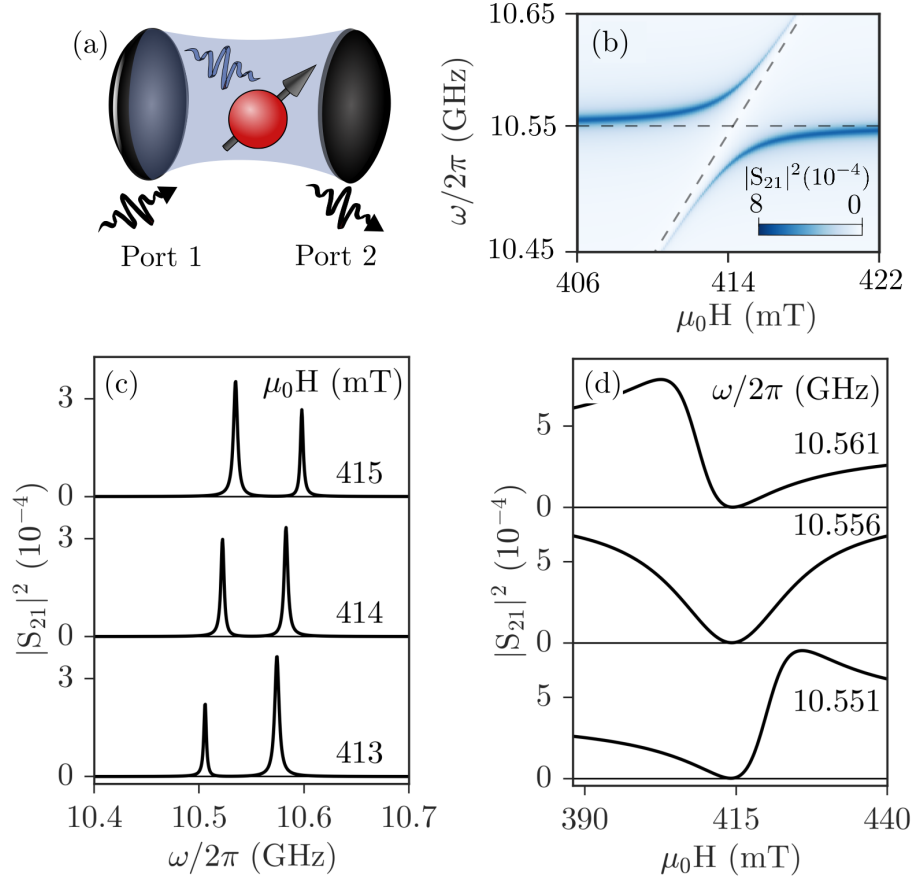
Figure 3.7: Transmission spectra in the input-output formalism. (a) A bath photon at port 1 (c_{in}) is scattered off of the spin-photon system into a final bath photon (d_{out}). The input-output fields relevant for transmission are shown. (b) The full $\omega - H$ dispersion calculated according to Eq. (3.76) using experimentally realistic parameters. (c) Fixed field and (d) frequency cuts made above, at and below the crossing point $\omega_r = \omega_c$ calculated according to Eq. (3.76).

Taking the Fourier transform of the cavity photon equation of motion we find

$$a = -iA^{-1}\left(\sqrt{2\kappa_c}\,c_{\text{in}} + \sqrt{2\kappa_d}\,d_{\text{in}}\right), \tag{3.73}$$

where,

$$A = \omega - \omega_c + i\kappa_L - \frac{g^2}{\omega - \omega_r + i\kappa_b}. \tag{3.74}$$

We now define the transmission parameters in a physically intuitive way where S_{21} is determined by measuring the output photons at port 2 when we have input photons at port 1 but no input to port 2 and S_{11} is determined by measuring the output photons at port 1 when we have input photons at port 1 but no input to port 2.

Mathematically this means that,

$$S_{21} = \left.\frac{d_{\text{out}}}{c_{\text{in}}}\right|_{d_{\text{in}}=0}, \qquad S_{11} = \left.\frac{c_{\text{out}}}{c_{\text{in}}}\right|_{d_{\text{in}}=0}$$

$$S_{12} = \left.\frac{c_{\text{out}}}{d_{\text{in}}}\right|_{c_{\text{in}}=0}, \qquad S_{22} = \left.\frac{d_{\text{out}}}{d_{\text{in}}}\right|_{c_{\text{in}}=0}. \tag{3.75}$$

Therefore using Eqs. (3.67) and (3.74) we find

$$S_{21} = S_{12} = -\frac{2\sqrt{\kappa_c \kappa_d}}{i\left(\omega - \omega_c\right) - \kappa_L + \frac{g^2}{i(\omega-\omega_r)-\kappa_b}}, \tag{3.76}$$

$$S_{11} = -\left[1 + \frac{2\kappa_c}{i\left(\omega - \omega_c\right) - \kappa_L + \frac{g^2}{i(\omega-\omega_r)-\kappa_b}}\right], \tag{3.77}$$

$$S_{22} = -\left[1 + \frac{2\kappa_d}{i\left(\omega - \omega_c\right) - \kappa_L + \frac{g^2}{i(\omega-\omega_r)-\kappa_b}}\right]. \tag{3.78}$$

The transmission spectra calculated according to Eq. (3.76) is plotted in Fig. 3.7 (b) using the same experimentally relevant parameters as the oscillator and phase correlation calculations with $\kappa_c = \kappa_d = 3.6 \times 10^{-5}$ GHz, $\kappa_a = 2.9 \times 10^{-3}$ GHz and $|g| = 3.1 \times 10^{-2}$ GHz. The anticrossing, line width evolution and both the (c) field and (d) frequency cuts agree well with the classical models. Of course this is expected based on the form of Eq. (3.76) since it has the same form as Eqs. (3.8) and (3.35). The fact that all three models agree again confirms that the key coupling features of the CMP arise due to linear harmonic coupling.

3.4.4 *Green's Function Formalism*

In keeping with the theme of viewing the CMP from a variety of perspectives, we can also take an alternative to the input-output derivation of S_{21} and instead treat the scattering problem using a Green's function formalism with the simplified Heisenberg spin-cavity Hamiltonian of Eq. (3.56) [34]. The quantum mechanical scattering matrix between an initial state $|i\rangle$ and final state $|f\rangle$ at times $t_i \to -\infty$ and $t_f \to \infty$ is the limit of the time evolution operator $U(t_f, t_i)$,

$$S = \lim_{\substack{t_f \to \infty \\ t_i \to -\infty}} U(t_f, t_i) = \lim_{\substack{t_f \to \infty \\ t_i \to -\infty}} T \exp\left(-\frac{i}{\hbar}\int_{t_i}^{t_f} H_{\text{int}}(\tau)\, d\tau\right), \tag{3.79}$$

where T is the time ordering operator and $H_{\text{int}}(\tau)$ is the interacting part of the Hamiltonian in the interaction picture. The matrix elements can then be expressed in terms of the transmission matrix (T-matrix), $\mathcal{T}$, as

$$\langle f|S|i\rangle = \delta_{fi} + 2\pi i\delta\left(E_f - E_i\right)\langle f|\mathcal{T}|i\rangle. \tag{3.80}$$

Although Eq. (3.80) defines the on-shell T-matrix following from the definition of Eq. (3.79), it can also be understood intuitively through conservation of energy.

Experimentally, the initial and final states of our system will be photons in the feedlines which couple into the cavity. Therefore we must again consider a photon bath which couples to the cavity photons. Integrating out these bath photons we find that

$$\mathcal{T}\left(\omega\right) \propto \lambda^2 G_R\left(\omega\right), \tag{3.81}$$

where G_R is the retarded Green's function of the cavity photons and λ is the coupling of the cavity photons to the external photon bath, which we assume is the same for both the input and output baths and is independent of the mode (i.e. we make a Markov approximation). The derivation of Eq. (3.81) is presented in Appendix B.4. Now, as was implicitly done when examining the input-ouput formalism, we assume that the density of states of the bath photons, $\rho\left(\omega\right)$, varies slowly around the cavity mode and therefore from Eq. (3.79) we can identify the transmission amplitude, $t\left(\omega\right)$, as

$$t\left(\omega\right) = 2\pi i\rho\left(\omega\right)\mathcal{T}\left(\omega\right). \tag{3.82}$$

Therefore, neglecting the asymmetric contribution from the real part of the Green's function, we find [34]

$$|\mathrm{S}_{21}\left(\omega\right)|^2 \propto -\lambda^2\mathrm{Im}\left[G_R\left(\omega\right)\right]. \tag{3.83}$$

For the non-interacting system the retarded photon Green's function is (see Appendix B.3),

$$G_R^0\left(\omega\right) = \frac{\hbar}{2\omega_c}\left[\frac{1}{\omega - \omega_c + i\Gamma_c} - \frac{1}{\omega + \omega_c - i\Gamma_c}\right]. \tag{3.84}$$

Here we have introduced the cavity damping parameter $\Gamma_c = \beta\omega_c$. The magnon Green's function is analogous to Eq. (3.84) but with all photon parameters replaced by magnon parameters. From this bare Green's function, the full photon Green's

function can be easily determined diagrammatically (Appendix B.5),

$$G_R\left(\omega\right) = \left(\omega - \omega_c + i\Gamma_c - \frac{N_s\alpha_c^2}{\omega - \omega_r + i\Gamma_r}\right)^{-1} - \left(\omega + \omega_c + i\Gamma_c - \frac{N_s\alpha_c^2}{\omega + \omega_r + i\Gamma_r}\right)^{-1}.$$

(3.85)

Using the Green's function of Eq. (3.85) with our previous result of Eq. (3.83) the transmission spectra is given by [34]

$$|S_{21}|^2 \propto \lambda^2 \left[\frac{\Gamma_c + \frac{N_s\alpha_c^2\Gamma_r}{(\omega - \omega_r)^2 + \Gamma_r^2}}{\left(\omega - \omega_c - \frac{N_s\alpha_c^2(\omega - \omega_r)}{(\omega - \omega_r)^2 + \Gamma_r^2}\right)^2 + \left(\Gamma_c + \frac{N_s\alpha_c^2\Gamma_r}{(\omega - \omega_r)^2 + \Gamma_r^2}\right)^2} \right.$$
$$\left. \frac{\Gamma_c + \frac{N_s\alpha_c^2\Gamma_r}{(\omega + \omega_r)^2 + \Gamma_r^2}}{\left(\omega + \omega_c - \frac{N_s\alpha_c^2(\omega + \omega_r)}{(\omega + \omega_r)^2 + \Gamma_r^2}\right)^2 + \left(\Gamma_c + \frac{N_s\alpha_c^2\Gamma_r}{(\omega + \omega_r)^2 + \Gamma_r^2}\right)^2} \right].$$

(3.86)

The full transmission spectra of Eq. (3.86) is shown in Fig. 3.8, calculated using the same parameters as mentioned previously with $N_s\alpha_c^2 = 900$ MHz and a proportionality constant of 2×10^{-6}. Again we see an anticrossing and line width evolution indicative of strong coupling as well as frequency and field cuts in agreement with those previously investigated. If we assume we investigate the CMP near the the crossing point (i.e. near the resonant features for positive frequencies) then we can neglect the second term in Eq. (3.86), which is not resonant near $\omega = \omega_c$ and only contributes an overall background signal. Furthermore since $\Gamma_r = \alpha\omega_c$ is typically ~ 1 MHz, much less than the frequency range examined experimentally, the second term in the numerator can be neglected, leaving

$$S_{21} = \frac{i\bar{S}_{21}\Gamma_c\left(\omega - \omega_r + i\Gamma_r\right)}{\left(\omega - \omega_c + i\Gamma_c\right)\left(\omega - \omega_r + i\Gamma_r\right) - N_s\alpha_c^2}$$

(3.87)

where $\bar{S}_{21}$ is again the transmission amplitude at $\omega = \omega_c$ in the absence of coupling. This simplified transmission again has the same form as all other models, which is not surprising since we expect all forms of transmission to agree in this harmonic limit. However, once again by taking a new approach we have gained additional insight into the CMP system. Notably, through the quantum approach we have learned that the coupling strength will grow as $\sqrt{N_s}$ and have also developed a formalism which can be easily extended to include higher order quantum effects of the CMP.
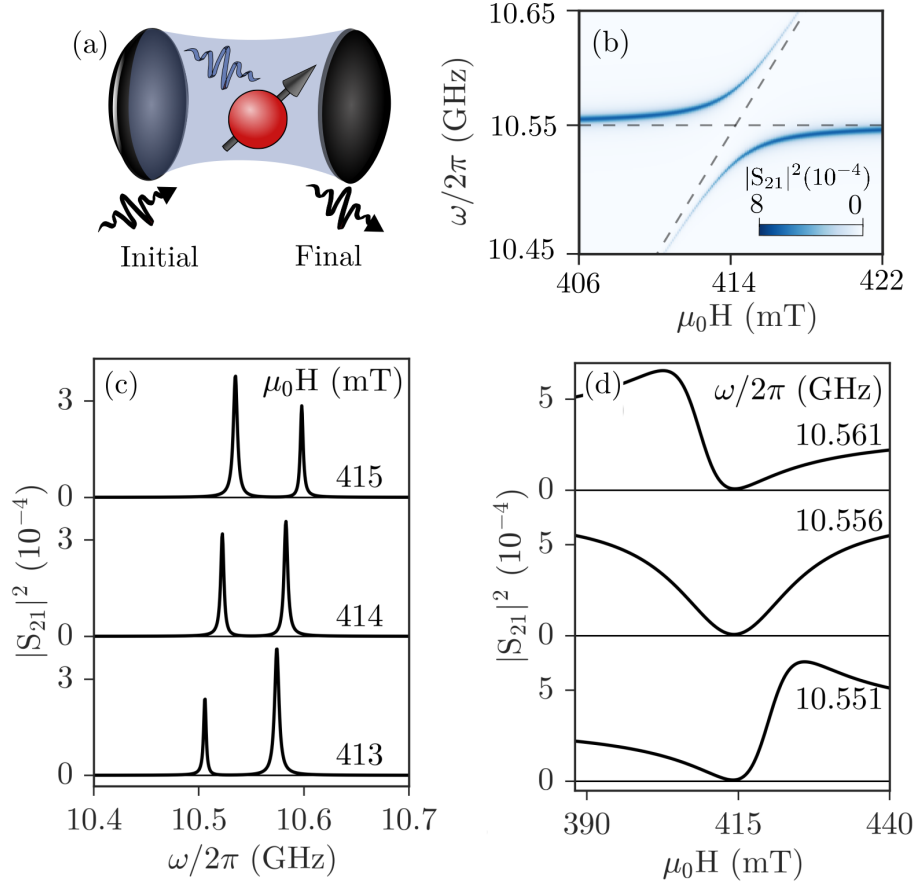
Figure 3.8: Transmission spectra in the Green's function formalism. (a) An initial bath photon is scattered off of the spin-photon system into a final bath photon state. (b) The full $\omega - H$ dispersion calculated according to Eq. (3.86) using experimentally realistic parameters. (c) Fixed field and (d) frequency cuts made above, at and below the crossing point $\omega_r = \omega_c$ calculated according to Eq. (3.86). A modified version of this figure was originally published in Ref. [34].

3.5 CONCLUSION AND COMPARISON OF MODELS

In this chapter we have presented several ways to model strongly coupled spin-photon systems. These approaches are generally split into two categories: we can either solve the problem classically, which means solving the coupled LLG and Maxwell's equations, or we can use a quantum approach, which means defining a Hamiltonian and determining the eigenfrequencies and transmission properties. Here we have developed two approaches to solve the problem classically and two approaches to solve the quantum problem. It is worth noting that other classical approaches have also been used, differing mainly in their application to specific geometries or experimental con-

figurations, such as a transfer matrix approach [188], classical scattering approaches [187, 201] as well as full analytical [202] or numerical [186] solutions of Maxwell's equations. Regardless of the approach our work has shown that CMP hybridization results from the key physics of phase correlation [48], and, using the rotating wave approximation near the crossing point $\omega_r = \omega_c$, all models reduce to a set of coupled equations which have the form,

$$
\begin{pmatrix} \omega - \tilde{\omega}_c & g \\ g & \omega - \tilde{\omega}_r \end{pmatrix} \begin{pmatrix} h \\ m \end{pmatrix} = \begin{pmatrix} \omega_c h_0 \\ 0 \end{pmatrix}. \tag{3.88}
$$

Here $\tilde{\omega}_c = \omega_c - i\beta\omega_c$ and $\tilde{\omega}_r = \omega_r - i\alpha\omega_c$ are the two complex resonance frequencies, h_0 is a driving microwave field at frequency ω and g is the coupling rate. The top and bottom equations in Eq. (3.88) describe the behaviour of the cavity (h) and magnetization (m) respectively. The dispersion of the hybridized modes is then determined by the pole of the matrix determinant from Eq. (3.88) by solving

$$
(\omega - \tilde{\omega}_c)(\omega - \tilde{\omega}_r) - g^2 = 0, \tag{3.89}
$$

and the microwave transmission is determined to be

$$
S_{21} \propto h = \frac{\omega_c h_0 (\omega - \tilde{\omega}_r)}{(\omega - \tilde{\omega}_c)(\omega - \tilde{\omega}_r) - g^2}. \tag{3.90}
$$

We note that, in accordance with Eq. (3.77), the simplified microwave reflection spectra is determined by

$$
S_{11} = -1 + S_{21}. \tag{3.91}
$$

Since all models reproduce the same general behaviour, such as mode anticrossing, line width evolution, a Lorentz line shape for frequency swept spectra and a Fano line shape for field swept spectra,[8] it is worth discussing what we gain from each approach. The real advantage to describing spin-photon hybridization using different methods is that each approach views the spin-photon system from a different angle, revealing new insights which, when put together, offer a more a complete picture of spin-photon coupling. The insights offered by these different models are both physical and technical in nature. Physically, the harmonic oscillator model provides a very general basis for understanding CMP physics. Since the basic features of spin-photon

---

[8]Of course this general behaviour must be reproduced by all models in the harmonic limit.

hybridization can be described by coupled oscillators, the main physics is universal and can be observed in many other systems, for example in cavity optomechanics and atomic systems. This also means that features observed in other systems, or more interestingly, features not observed due to experimental limitations, may be realized through spin-photon coupling.

While the generality of the harmonic oscillator model is a strength, it is also a weakness in that it does not reveal the origin of the phase correlation which produces the CMP. Attempting to answer this question has led us to develop the dynamic phase correlation model of spin-photon coupling, which clearly reveals the electrodynamic origin of CMP phase correlation. This approach also unveils the nature of the two oscillators, one represents the cavity mode while the other describes the magnetization dynamics. Furthermore by establishing this relationship a connection to spin pumping is also revealed, as we know that the voltage is proportional to the spectral function of the magnetization.

Turning to the quantum descriptions allows us to can gain further insight into the nature of the coupling, for example this approach allows us to easily determine the microscopic origin of the coupling strength, revealing new avenues for coupling control through the N_s dependence. The quantum formalism can also be extended to explore quantum effects of hybridization. For example, the Green's function calculation explicitly demonstrates that the transmission can be calculated by the spin-photon system alone, without considering the properties of the bath photons, which allows straight forward extensions to calculate higher order interactions by accounting for higher order terms in the Dyson expansion.

Additionally there are a variety of minor advantages to one approach or another. For example, if we wish to decouple our system we need the ability to independently control (theoretically) each coupling strength independently. This is because even without the magnetization back action ($K_c \to 0$) the cavity field still drives the magnetization. This functionality is provided most naturally by the electrodynamic phase correlation model. On the other hand, by using the RLC description of the circuit more complex planar resonators can easily be described [38, 203]. Alternatively, if we wish to describe the reflection spectra of our system, the input-output formalism naturally provides the relation $S_{11} = -1 + S_{21}$, which we can then adopt in other approaches. Input-output theory can also be easily generalization to other resonator systems, such as a waveguide. Finally the simplified model of Eq. (3.88) has a very simple structure, which may easily be extended to multimode systems where several

cavity or spin wave modes are present. Solutions of the hybridized dispersions are also simpler in this approach.

Therefore the combined understanding of all theoretical approaches we have developed provides a more complete picture of spin-photon coupling. Keeping this complete view of the CMP in mind, in the experimental studies that follow we will make use of the general formalism defined by Eqs. (3.88) and (3.90) whenever possible.

3.6 ACKNOWLEDGEMENTS

<div style="text-align: right; font-size: 3em;">4</div>

OBSERVING SPIN-PHOTON HYBRIDIZATION

4.1 INTRODUCTION

Without experimental input it would be virtually impossible to make progress in condensed matter research. Again, this fact is due to the complex nature of many-particle systems and the need to develop a give and take between theory and experiment. Based on our considerations of strong-spin photon coupling we now anticipate that the physical origin of hybridization lies in electromagnetic phase correlation which couples the electrodynamics of a microwave cavity to the magnetization dynamics of a ferromagnetic material. However we have yet to confirm these expectations. In conventional systems many insights into magnetization dynamics have been gained from microwave transmission and electrical detection methods [23] and therefore to study our hybridized system we will employ these techniques. These methods are described in Sec 4.4 after first reviewing the individual spin and photon subsystems in Sec. 4.2 and Sec. 4.3 respectively.

Microwave transmission probes the global absorption properties of a system and therefore reveals the resonance properties of a system under test. Using an in-house 3D microwave cavity coupled to a YIG sphere we can observe spin-photon hybridization at room temperature using microwave transmission, as presented in Sec. 4.5.1. Experimentally we observe mode anticrossing and line width evolution, in excellent agreement with the predictions of our model. These observations lead to new insights into the physics of spin-photon coupling, such as the fact that the hybridized line width is bounded by the uncoupled dissipation rates, physically reflecting the fact that hybridization does not open any new dissipation channels but simply allows energy exchange between the spin and photon subsystems. Interestingly we also con-

<div style="text-align: right;">59</div>

firm the large FMR line width enhancement due to coupling. This implies that the conventional mechanisms of Gilbert damping and inhomogeneous broadening cannot account for the damping behaviour of the strongly coupled system.

To take our experimental investigations further we employ electrical detection. These techniques became commonplace within the spintronics community in the mid 2000's, motivated by the theoretical proposal of spin pumping and input from the semiconductor spintronics community [23].[1] Applying this experimental technique we again observe the tell-tale signatures of hybridization, as we present in Sec. 4.5.1. This finding means that the spin current is influenced by strong coupling, which sets the foundation for the development of cavity spintronics, opening the door to the electrical generation, manipulation and detection of strong coupling in spintronic devices. Electrical detection also provides an ideal way to search for strong coupling with spin waves, which we discuss in Sec. 4.5.3. This search is successful and we make the first detection of an anticrossing between standing spin waves and the microwave cavity. This observation allows us to verify the expected coupling strength and mode index dependence. By enabling systematically variable coupling strengths, spin waves may prove advantageous in the development of cavity spintronic technologies.

Interestingly the signatures of strong coupling are not restricted to anticrossing and line width properties, but also include the presence of an antiresonance in the spectra. We explore this phenomena in Sec. 4.5.4. Similar features appear across a wide range of physical systems, from light scattering in metamaterials [207] to coupled atom-photon systems [208], and have been used to characterize strongly coupled quantum circuits [208]. In our case we show that the antiresonance can be used to interpret the phase behaviour of the hybridized modes, with phase jumps at both resonances and the antiresonance. Such phase information has played an important role in early applications of cavity spintronics, such as in bridging CMP and qubit systems [33] or multiple magnetic moments [58], or in the development of novel memory architectures [59]. In the latter example, magnon dark modes have been used to demonstrate enhanced storage times and as an application of our phase analysis technique we quantify the phase behaviour in the magnon dark mode for the first time in Sec. 4.5.5. The range of experimental results presented in this chapter reveals the intriguing nature and exciting possibilities of the strongly coupled spin-photon system.

---

[1]The origins of these effects can be traced back much further to the pioneering work of Juretscke in the 1960's [204, 205] and Johnson and Silsbee in the 1980's [206].

4.2 THE SPIN SYSTEM (MAGNETIC MATERIAL)

In our experiments we used two types of magnetic devices. Generally, when we only required microwave transmission measurements, spherical, single crystal YIG samples purchased from Ferrisphere Inc. were used. These highly polished spheres had a surface roughness of 50 μm and saturation magnetization of $\mu_0 M_0 = 178$ mT with a gyromagnetic ratio of $\gamma = 28 \times 2\pi\ \mu_0$GHz/T, Gilbert damping of $0.8 \times 10^{-5} < \alpha < 1 \times 10^{-5}$ and a shape anisotropy of $|H_A| \sim 30$ mT. Typically 1-mm diameter spheres were used, in order to maximize the coupling strength. For the experiments presented here knowledge of the crystal orientation was unimportant, and therefore no special sample mounting was required.[2]

For electrical detection experiments thin film bilayer devices were used. Experiments performed at the University of Manitoba used YIG(2.6 μm)/Pt(10 nm) bilayers (bracketed values denote thickness), with typical lateral dimensions of ~ 10 mm $\times$ 7 mm. The YIG samples, provided by the group of John Q. Xiao at the University of Delaware, were grown by liquid phase epitaxy (LPE) on a (111) oriented gadolinium iron garnet (GGG) substrate. Via sputtering at the University of Manitoba, the Pt was patterned into strips covering the length of the YIG with typical strip widths of ~ 50 μm. The FMR properties were defined by typical parameters of $\gamma = 2\pi \times 27.5$ μ_0GHz/T, $\mu_0 M_0 \sim 170$ mT and $\alpha \sim 4 \times 10^{-4}$. The YIG (2.8 μm)/Pt(5 nm) bilayer samples used at the Walther-Meissner-Institute were again grown by liquid phase epitaxy on (111) oriented GGG substrates with Pt deposited using electron beam evaporation. The FMR parameters were similar to the Delaware samples. In addition to the YIG/Pt bilayers, a series of temperature dependent experiments, presented in Sec. 5.3, was performed using GdIG(2.6 μm) grown by liquid phase epitaxy on a GGG substrate in the group of Eiji Saitoh at Tohoku University.

4.3 THE PHOTON SYSTEM (MICROWAVE CAVITY)

Various cavity systems were used throughout our experiments. At the Walther-Meissner-Institute experiments were performed in a commercial Bruker Flexline MD5 dielectric ring cavity, while the majority of experiments at the University of Manitoba were performed using an in-house cylindrical 3D cavity made of oxygen free copper.

---

[2]Note however that nonlinear experiments which depend on the sign of the Kerr coefficient do require consideration of the crystal axis [63, 209].

A schematic diagram of the cylindrical cavity is shown in Fig. 4.1. The cavity had a radius of $R = 12.5$ mm and an adjustable height of 24 mm $< h <$ 44 mm. This height adjustable feature allowed us great flexibility in accessing different modes and mode frequency ranges within a single system. In particular we could tune individual cavity modes over a frequency range of ~ 1 GHz, allowing us to isolate individual modes for our experiments to ensure that a single cavity mode was responsible for strong coupling over a wide frequency range. Furthermore the height adjustment capability enabled tuning the wavevector which supported the investigation of polariton type gaps observed in the phonon-polariton [211]. The in-plane mode profiles of the four lowest order modes are shown in Fig. 4.1 (b), where dashed lines indicate the microwave magnetic fields. Two ports on the cavity allowed us to inject and measure microwaves, enabling both reflection and transmission measurements. Furthermore, by adjusting the pin lengths inserted into the ports we could control the cavity quality. We typically operated in the critically coupled regime, which afforded the best balance between cavity quality and microwave amplitude [185], with typical critically coupled quality factors of $1200 < Q < 1800$.[3]

To better understand the behaviour of spin-photon coupling it is crucial to characterize the behaviour of the individual spin and photon subsystems. In the case of the cavity this means characterizing the resonance modes, which is easily done using
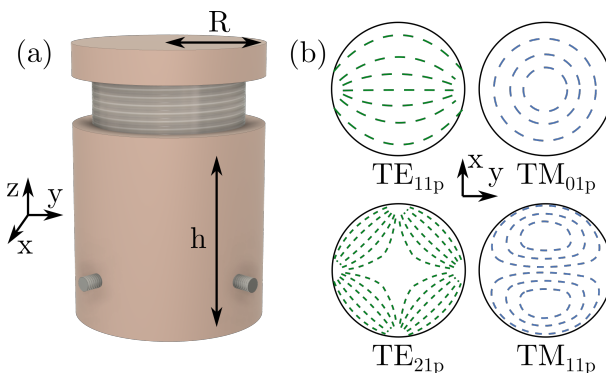
Figure 4.1: (a) Schematic diagram of a cylindrical cavity with radius R and adjustable height h, which enables resonance frequency tuning. Two ports allowed for microwave injection and detection. (b) Magnetic field mode profiles in the x-y plain for the four lowest modes. The amplitude, determined by the mode index p which defines the sinusoidal behaviour in the z direction, is not accounted for here, see e.g. Refs. [154, 210] for a discussion of cylindrical cavity modes.

---

[3]$Q = \omega_c/2\Delta\omega_c$, where $\Delta\omega_c$ is the half-width-half-maximum (HWHM) of the cavity mode and ω_c is the mode frequency.

classical electrodynamics [154]. In the cylindrical cavity the field profile of the transverse magnetic (TM) modes, which have a vanishing field along the z axis, are given by,

$$E_{\mathrm{T}}(x,y,z) = -\frac{p\pi}{h\gamma^2} \sin\left(\frac{p\pi z}{h}\right) \nabla_{\mathrm{T}} \psi(x,y), \tag{4.1}$$

$$E_z(x,y,z) = \psi(x,y) \cos\left(\frac{p\pi z}{h}\right), \tag{4.2}$$

$$H_{\mathrm{T}}(x,y,z) = \frac{i\epsilon\omega}{\gamma^2} \cos\left(\frac{p\pi z}{h}\right) \widehat{z} \times \nabla_{\mathrm{T}} \psi(x,y) \tag{4.3}$$

while the transverse electric (TE) mode profiles, which have a vanishing electric field along z, are,

$$E_{\mathrm{T}}(x,y,z) = \frac{i\omega\mu}{\gamma^2} \sin\left(\frac{p\pi z}{h}\right) \widehat{z} \times \nabla_{\mathrm{T}} \psi(x,y), \tag{4.4}$$

$$H_{\mathrm{T}}(x,y,z) = \frac{p\pi}{h\gamma^2} \cos\left(\frac{p\pi z}{h}\right) \nabla_{\mathrm{T}} \psi(x,y), \tag{4.5}$$

$$H_z(x,y,z) = \psi(x,y) \sin\left(\frac{p\pi z}{h}\right). \tag{4.6}$$

Here μ and ϵ are the permeability and permittivity of the cavity, respectively,[4] $\gamma^2 = \mu\epsilon\omega^2 - \left(\frac{p\pi}{h}\right)^2$ and, owing to the cylindrical symmetry in the x-y plane, ψ is most easily expressed in cylindrical coordinates (ρ, θ) using the Bessel functions J_m as $\psi(\rho, \phi) = J_m(\gamma_{mn}\rho) e^{im\phi}$ with $\gamma_{mn} = x_{mn}/R$ for TM modes and $\gamma_{mn} = x'_{mn}/R$ for TE modes, where x_{mn} is the nth root of J_m and x'_{mn} is the nth root of J'_m. $\nabla_{\mathrm{T}} = \widehat{x}\partial_x + \widehat{y}\partial_y$ and m, n and p are mode indices with $m = 0, 1, 2, \ldots$ and $n = 1, 2, 3, \ldots$ for both TE and TM modes while $p = 0, 1, 2, \ldots$ for TM modes and $p = 1, 2, 3, \ldots$ for TE modes. The mode behaviour along the z axis is sinusoidal and determined by the p index, which therefore sets the overall amplitude. However we will see that for spin-photon coupling the behaviour of the in-plane profiles are most relevant (provided the amplitude is not zero) and therefore we have used the transverse part of Eqs. (4.1), (4.3), (4.4) and (4.5) to plot the in-plane behaviour in Fig. 4.1 (b). There we have introduced the notation TM_{mnp} and TE_{mnp}, which we will use whenever referring to specific TE and TM modes. Modes with lower indices of course have less nodes and therefore simpler field profiles. In particular the TM_{01p} mode has a simple circular magnetic field profile, meaning that the orientation between the rf magnetic field and the bias magnetic field can be easily defined. For this reason we will use the TM_{011}

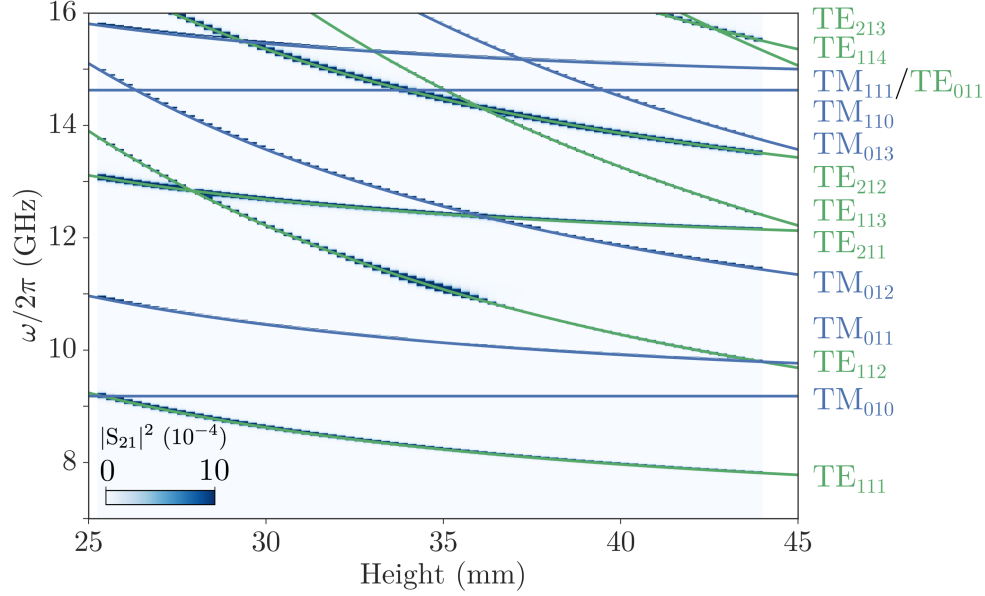[4]In our experiments $\epsilon = \epsilon_0$, and, aside from the magnetic sample volume, $\mu = \mu_0$.

Figure 4.2: Measured microwave transmission using a cylindrical microwave cavity made of oxygen free copper with $R = 12.5$ mm and 24 mm $< h <$ 44 mm. Solid curves are calculations of the mode dispersions according to Eq. (4.7) for TM modes (blue) and Eq. (4.8) for TE modes (green).

mode in the majority of our experiments.

Finally the resonance frequencies of the TE and TM modes are given by,

$$\text{TM: } \omega_{mnp} = \frac{1}{\sqrt{\mu\epsilon}}\sqrt{\left(\frac{x_{mn}}{R}\right)^2 + \left(\frac{p\pi}{h}\right)^2}, \tag{4.7}$$

$$\text{TE: } \omega_{mnp} = \frac{1}{\sqrt{\mu\epsilon}}\sqrt{\left(\frac{x'_{mn}}{R}\right)^2 + \left(\frac{p\pi}{h}\right)^2}. \tag{4.8}$$

The frequency height dispersions for all cavity modes in our cylindrical cavity from 7 GHz $< \omega/2\pi <$ 16 GHz are plotted in Fig. 4.2 as green and blue curves for the TE and TM modes respectively. These calculations can be compared to the experimental microwave transmission, S_{21}, of the empty cavity, which has been measured by a vector network analyzer (VNA) and is also plotted in the same figure. It is evident that our cavity is well characterized by the expected frequency dispersions of Eqs. (4.7) and (4.8). Although our cavity has many modes which we could use in our strong coupling experiments, we choose to use the TM_{011} mode. This mode is chosen due to the spherical symmetry of its magnetic field, its ideal frequency range which can be easily accessed by low magnetic fields (~ 400 mT) and the fact that for $h < 35$ mm it

is well separated, by more than 1 GHz, from other cavity modes, which ensures that it will be the only mode responsible for strong coupling in a wide frequency range.

4.4 MEASUREMENT TECHNIQUES

4.4.1 *Microwave Transmission and Reflection*

The microwave frequency response of the CMP was measured via microwave transmission/reflection using the experimental setup shown in Fig. 4.3. The YIG sample was placed inside our in-house microwave cavity, typically near the cavity edge, with a microwave field supplied by an Agilent N5230C vector network analyzer (VNA) and a static magnetic field, which controls the spin resonance, supplied by an external Lakeshore EM7 electromagnet. To maximize the coupling strength, by most efficiently driving magnetization precession, the YIG sphere was generally placed at a location where the local microwave field was perpendicular to the static magnetic field. Therefore the optimal sample placement was dependent on the field mode used in a given experiment. This is discussed at length in Sec. 5.4. The two SMA ports of our cavity enable both transmission (S_{21}) and reflection (S_{11}) VNA measurements and in this setup the entire transmission line can be calibrated. However even with such a calibration standing waves, which have the largest impact on S_{11}, may be present in the transmission line. For this reason we use S_{21} measurements when possible.
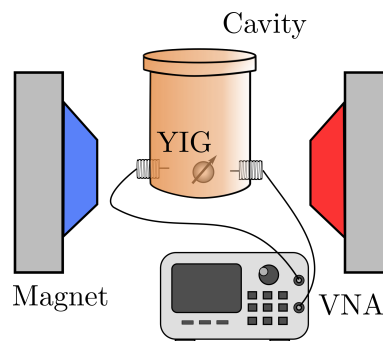

Figure 4.3: Schematic diagram of the UMS1 experimental system for microwave transmission measurements. A VNA injects (and measures) a microwave signal into the cavity which contains the magnetic sample. An external bias field provided by an electromagnet controls the spin resonance properties.

4.4.2 *Electrical Detection*

In our electrical detection experiments we measured the dc voltage generated due to spin pumping and the inverse spin Hall effect, as outlined in Secs. 2.3 and 2.4, in order to determine if the spin current was influenced by the presence of strong coupling. One potential complication with such measurements is the small magnitude of the dc signal, typically on the order of μV, requiring some form of amplification.[5] Fortunately standard techniques for electrical detection of spintronic systems now enable routine measurements of nV signals. The two approaches used in this work are shown in Figs. 4.4. Experiments performed at the University of Manitoba used the experimental setup shown in panel (a). An Anritsu MG3692C microwave generator was used to inject a microwave signal into the cavity through one of the two ports. This microwave signal was sinusoidally modulated at a reference frequency of 8.33 kHz by a Stanford SR 830 lock-in amplifier. This allowed us to use the lock-in technique, whereby the measured voltage signal was again multiplied by the reference signal
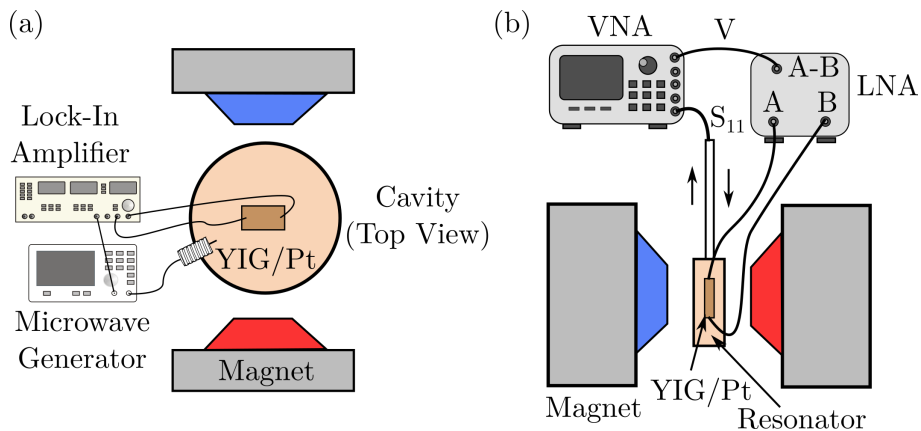
Figure 4.4: (a) Schematic diagram of the UMV1 electrical detection system used at the University of Manitoba. A microwave generator injects a signal into the cavity, which undergoes a low-frequency sinusoidal modulation applied by the lock-in amplifier. The lock-in amplifier measures the voltage generated through spin-pumping/inverse spin Hall effect. (b) Schematic diagram of the WMI electrical detection system used at the Walther-Meissner-Institute, which simultaneously measures the microwave reflection. A VNA injects a microwave signal into the cavity. The DC voltage generated in the YIG/Pt bilayer is amplified using a low noise differential voltage amplifier (LNA) and recorded through the auxiliary port of the VNA.

---

[5]In early studies of voltage generation by magnetic thin films, (through spin rectification, not spin pumping) small voltage signals were one of the reasons that exceptionally large microwave powers, of several kW, were necessary [23, 205, 212].

and time integrated, allowing extraction of the DC signal. Due to the configuration of our in-house cavities, we opted to avoid the use of a chip carrier, which would drastically reduce the quality of the loaded cavity, and instead mechanically fixed the electrical leads to the Pt layer of our YIG/Pt bilayer samples. Again a Lakeshore EM7 electromagnet was used to apply a static magnetic bias field to tune the spin resonance. As shown in Figs. 4.4 (a) the voltage was measured along the long axis of the YIG/Pt bilayer and the static magnetic field was applied in-plane, but perpendicular to the measurement direction.

Fig. 4.4 (b) shows the experimental setup used at the Walther-Meissner-Institute, which simultaneously performs electrical detection and microwave reflection measurements. The sample was wire bonded onto a printed circuit board sample carrier and placed inside a Bruker Flexline MD5 dielectric ring cavity in an Oxford Instruments CF935 gas flow cryostat. The tuneable unloaded quality factor of this cavity ranged from $0 < Q < 8000$, however due to loading, $Q \sim 1000$ at critical coupling. An Agilent N5242A VNA injected a microwave signal into the cavity and recorded the reflection signal. The DC signal was measured along the axis of the cavity, perpendicular to the static magnetic field provided by a Lakeshore electromagnet. This voltage signal was amplified using a Stanford 560 low noise differential voltage amplifier (LNA) and recorded through the auxiliary input of the VNA.

4.5 EXPERIMENTAL CHARACTERISTICS OF SPIN-PHOTON HYBRIDIZATION

4.5.1 *Transmission and Voltage Spectra*

Having characterized the individual spin and photon subsystems, and equipped with several experimental techniques to probe the properties of the coupled system, we performed detailed studies of the spin-photon hybridization. The key characteristics of the CMP observed through microwave transmission measurements in the UMS1 setup are shown in Fig. 4.5. In this experiment the height of the cylindrical copper cavity was set to $h = 29$ mm, which resulted in a TM_{011} mode with a loaded resonance frequency and quality of $\omega_c/2\pi = 10.556$ GHz and $Q = 1700$ ($\beta = \Delta\omega/\omega_c = 3 \times 10^{-4}$) respectively. This loaded resonance frequency was red shifted by 0.2% from the unloaded value. The YIG FMR follows the linear dispersion $\omega_r = \gamma\,(\text{H} + \text{H}_A)$, where, in our experiment, $\gamma = 28 \times 2\pi\ \mu_0$GHz/T and the shape anisotropy $\mu_0 H_A = -37.7$ mT, resulting in a cavity/FMR crossing field of 414.5 mT (the Gilbert damping is
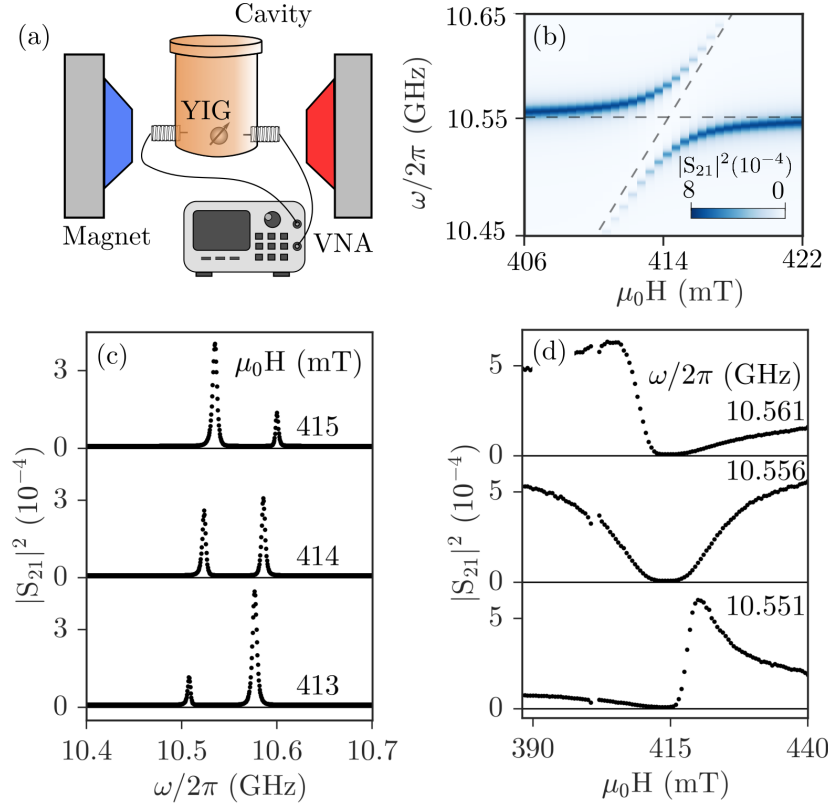
Figure 4.5: (a) UMS1 experimental setup. (b) The $\omega - H$ transmission mapping of the CMP. Diagonal and horizontal dashed lines indicate the uncoupled FMR and cavity dispersion respectively. (c) Fixed field and (d) frequency cuts made at, above and below the crossing point $\omega_c = \omega_r$. A modified version of this figure was originally published in Ref. [34].

$\alpha = 0.8 \times 10^{-5}$). The coupling of the TM_{011} mode to the 1-mm diameter YIG sphere can be seen in Fig. 4.5 (b). A clear gap emerges in the eigenspectrum at $\omega_r = \omega_c$, removing the degeneracy at the crossing point and signalling the presence of strong spin-photon coupling. To illustrate the significance of this deviation, the uncoupled dispersions of the cavity and FMR are shown as horizontal and diagonal dashed lines respectively. The observation of such an anticrossing is the "smoking gun" of strong spin-photon coupling and shows the dramatic influence of hybridization on the eigenspectrum. In our experiment the Rabi gap was found to be $\omega_{\text{gap}} = 63$ MHz, corresponding to a coupling strength of 31.5 MHz. Using the effective spin density of iron atoms in YIG, $\rho_s = 2.1 \times 10^{22} \frac{\mu_B}{\text{cm}^3}$ [213], we can use the sample volume to estimate $N_s = 5.2 \times 10^{18}$ spins in our YIG sample [34]. Therefore using Eqs. (3.54) and (3.55) we calculate from first principles a gap of $\omega_{\text{gap}}/2\pi = 74$ MHz which agrees

extremely well with the experimental observation given the complex nature of our system and the simplicity of our theoretical model.

The frequency line cuts $|S_{21}(\omega)|^2$ at fixed H are examined in Fig. 4.5 (c). These fixed field line cuts show both CMP branches. The separation between the two branches at the crossing point $\mu_0 H_c = 414.5$ mT defines ω_{gap}. This spectra nicely illustrates the influence of hybridization — without coupling the two modes observed at $\omega_r = \omega_c$ would overlap and their line width would be very different. However due to the spin-photon interaction we instead find two well separated modes of equal amplitude and equal line width. Above (below) the crossing point the amplitude of the upper (lower) branch decreases sharply as the cavity mode moves away from the FMR frequency and can no longer effectively drive precession [34]. Both branches have a clear Lorentz line shape, as we predicted in Sec. 3.2.1. This is also consistent with our expectations of a resonant process. Defining the frequency and field detunings, $\delta\omega = \omega - \omega_r$ and $\delta H = H - H_c$ the field swept spectra is seen to satisfy $|S_{21}(\omega_r + \delta\omega, H_c + \delta H)|^2 = |S_{21}(\omega_r - \delta\omega, H_c - \delta H)|^2$, which represents the reflection symmetry about the uncoupled dispersions which is evident in Fig. 4.5 (b).

In microwave transmission measurements one typically measures the frequency swept spectra as we have just discussed, while spin pumping measurements usually measure the field swept spectra. However in our experiment, since we have a full $\omega - H$ data set, we can examine the CMP from both perspectives using just the microwave transmission. The fixed frequency cuts, $|S_{21}(H)|^2$, are highlighted in Fig. 4.5 (d). As anticipated based on our theoretical considerations, this behaviour is distinctly different than the frequency swept spectra. At $\omega = \omega_c$ we have a broad symmetric dip, with the transmission line shape becoming asymmetric when $\omega \neq \omega_c$. A striking feature is that this symmetry change occurs immediately away from the cavity frequency and is opposite above and below ω_c. In this case we observe a similar reflection symmetry about the uncoupled dispersions, $|S_{21}(\omega_c + \delta\omega, H_c + \delta H)|^2 = |S_{21}(\omega_c - \delta\omega, H_c - \delta H)|^2$. However a key difference between this line shape symmetry and the analogue for fixed fields is that ω_c is field independent, whereas ω_r depends on the field. Interestingly $S_{21}(H)$ reveals a new feature that is not easily seen in either the full mapping, $S_{21}(\omega, H)$, or the frequency spectra, $S_{21}(\omega)$. Examining the spectra near $\mu_0 H = 404$ mT an additional resonance structure is observed. This feature is actually the observation of strong coupling with a spin wave, rather than the fundamental FMR mode, and will be discussed in more detail in Sec. 4.5.3.

All of the experimental features of the CMP which are observed in the mapping

and spectra of Fig. 4.5, including a gap in the dispersion, the ω symmetry of fixed H cuts, the rapid decrease of the transmission amplitude of the upper (lower) branches above (below) the crossing point, the symmetric dip in the fixed ω spectra at $\omega = \omega_c$, the general asymmetry when $\omega \neq \omega_c$, and the polarity change in the fixed ω cuts above and below ω_c, are in excellent agreement with the theories presented in Ch. 3, supporting the electrodynamic phase correlation origin of strong-spin photon coupling [34].

The fact that we observe strong spin-photon coupling through microwave transmission measurements is not too surprising, since these measurements probe the cavity properties which must be modified. Whether or not such effects can be observed through spin pumping is less clear. Of course within our theoretical formalism spin pumping should also be influenced since the magnetization determined by the LLG equation is modified. However from an experimental perspective it is not immediately obvious that such an effect could be detected and therefore the observation of hybridization through spin pumping provides powerful confirmation that the physical picture painted by our electrodynamic model is indeed correct. In Fig. 4.6 we present typical spin pumping measurements made using our UMV1 setup [48]. In this case a fixed geometry aluminum cavity was used with a resonance frequency of $\omega_c/2\pi = 10.506$ GHz and a loaded quality of $Q_L = 278$ ($\beta_L = 1.8 \times 10^{-3}$). The YIG(2.6 μm)/Pt(10 nm) bilayer had lateral YIG dimensions of 5 mm $\times$ 5 mm, with a Pt layer patterned into a strip of dimension 50 μm $\times$ 5 mm. Using the in-plane field configuration the FMR follows the Kittel equation $\omega_r = \gamma\sqrt{H(H + M_0)}$ with $\gamma = 27.5 \times 2\pi \, \mu_0$ GHz/T and $\mu_0 M_0 = 169$ mT in our sample. In the absence of coupling the line width follows the well-known relation $\Delta H = \Delta H_0 + \alpha\omega/\gamma$ [21, 214] and we find a Gilbert damping of $\alpha = 3.6 \times 10^{-4}$ with a line width broadening of $\mu_0 \Delta H_0$ = 0.31 mT. The typical voltage mapping presented in Fig. 4.6 (b) indeed shows the same anticrossing feature that we observed in the transmission spectra, with $\omega_{\text{gap}}/2\pi$ = 168 MHz. This indicates that the spin current is in fact manipulated by the presence of strong coupling! If we examine the fixed field behaviour of $V(\omega)$ in panel (c) of Fig. 4.6 and the fixed frequency behaviour of $V(H)$ in panel (d) we see the same characteristic features that we observed in the microwave transmission and that we expected based on our theoretical analysis. These experimental observations support the conclusion that the spin current is manipulated by the presence of strong spin-photon coupling, again providing support for our model [48]. Since the experimental signatures observed through microwave transmission and electrical detection mea-
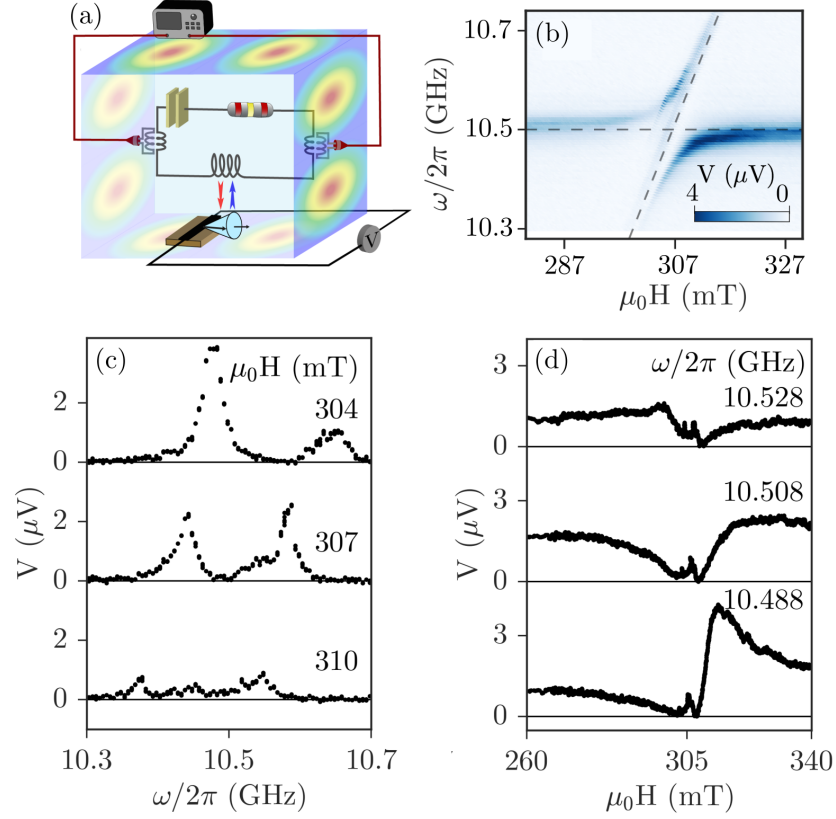
Figure 4.6: (a) Schematic illustration of the CMP coupling mechanism, which is measured here in the UMV1 experimental setup. (b) The ω-H voltage mapping of the CMP. Diagonal and horizontal dashed lines indicate the uncoupled FMR and cavity dispersion respectively. (c) Fixed field and (d) frequency cuts made at, above and below the crossing point $\omega_c = \omega_r$.

surements appear to be the same, all of our discussion and analysis of the microwave transmission spectra also applies to the electrical detection spectra. Yet despite the similarities there are some advantages and disadvantages to each experimental approach when investigating strong spin-photon coupling. As we can see from Figs. 4.5 and 4.6, the transmission measurements typically have a better signal to noise ratio and, as we will see in the next section, this reduces the uncertainty in the line width measurements extracted from microwave transmission. On the other hand, higher order spin wave modes can more easily be observed using electrical detection, which is less sensitive to the dominant cavity mode. However perhaps the most important distinction between the two techniques is that the electrical detection method locally probes the spin system, whereas the microwave transmission technique measures the global properties of the entire system [50]. Therefore spin pumping actually provides

a method to truly probe the coupling influence on a specific spin device. This capability is necessary for the development of cavity spintronics and was exploited to demonstrate non-local spin current control, as will be discussed in Sec. 5.5.

4.5.2 *Avoided Crossing and Line Width Evolution*

Thus far all of the insights we have presented from our experimental data were gained directly from the raw measurements without detailed data analysis. However by fitting the transmission spectra to our model we can determine the exact behaviour of the full complex CMP dispersion. For the fixed field spectra we fit each of the CMP modes to a Lorentz line shape, in accordance with the simplification derived in Sec. 3.2.1. The resulting resonance position and line width are plotted in Fig. 4.7 (a) and (c) respectively. Here the open and solid triangles are the upper and lower polariton branches respectively and the solid curves are calculated according to Eq.

Figure 4.7: (a) Frequency swept transmission dispersion and (c) line width. (b) Field swept transmission dispersion and (d) line width. Symbols are experimental results, with hollow and solid triangles corresponding to the upper and lower CMP branches respectively. Solid curves are calculations according to Eq. (3.9) and Eq. (3.12) for the field and frequency swept spectra respectively. A modified version of this figure was originally published in Ref. [34].

(3.9). The horizontal and vertical dashed lines in panel (a) indicate the uncoupled cavity and FMR dispersions respectively. The dispersion again highlights the mode hybridization, which is strongest near the crossing point $\omega_r = \omega_c$ in agreement with the mode composition described by Fig. 3.3. However our fitting reveals that the dispersion is not the only signature of coupling [34, 48]. By extracting the full complex eigenmodes we also observe line width evolution as a signature of hybridization. This feature is actually already evident in the transmission mapping of Fig. 4.5 (b) in a subtle way, but becomes a striking feature of Fig. 4.7 (c). Interestingly we find that the line widths are bounded by $\alpha < \Delta\omega_\pm/\omega_c < \beta$, and are equal at the crossing point.[6] Furthermore, as can be verified by our model, $(\Delta\omega_+ + \Delta\omega_-)/\omega_c = \alpha + \beta$. This relationship is independent of coupling strength, field or frequency and physically indicates that, although the spin-photon coupling enables energy exchange between the two subsystems, coupling does not introduce any additional dissipation channels. Fig. 4.7 (c) experimentally confirms this relationship.

The frequency swept dispersions and line width are plotted in Fig. 4.7 (b) and (d) respectively with symbols representing experimental data extracted by fitting to a Fano line shape and solid black lines calculated according to Eq. (3.12). The vertical and diagonal dashed lines in panel (b) indicate the uncoupled cavity and FMR dispersions respectively. As expected based on the theoretical predictions of Eq. (3.12), the frequency swept dispersion is purely dispersive, while the line width is purely Lorentzian, with a maximum at $\omega = \omega_c$. In this case our experimental results suggest that the FMR line width will be drastically influenced by the resonant coupling process. A similar analysis can be performed for the voltage measurements and is shown in Fig. 4.8. Having already demonstrated that all coupling features can also be observed through spin pumping we of course expect to see the same dispersion and line width characteristics. From Fig. 4.8 the effects of decreased signal to noise in this technique are evident, resulting in more scattered fitting results, especially for the line width measurements. However we still find good agreement with our model and observe the key coupling signatures of mode anticrossing and line width evolution.

Despite the fact that α is not changed by the coupling, ΔH increases drastically at the crossing point where resonant coupling is observed [48]. This increase occurs

---

[6]Recent unpublished investigations indicate that this bound may be broken, indicating important extensions of the coupling mechanism. However in standard hybridized systems these bounds are a strict result of the coupling.
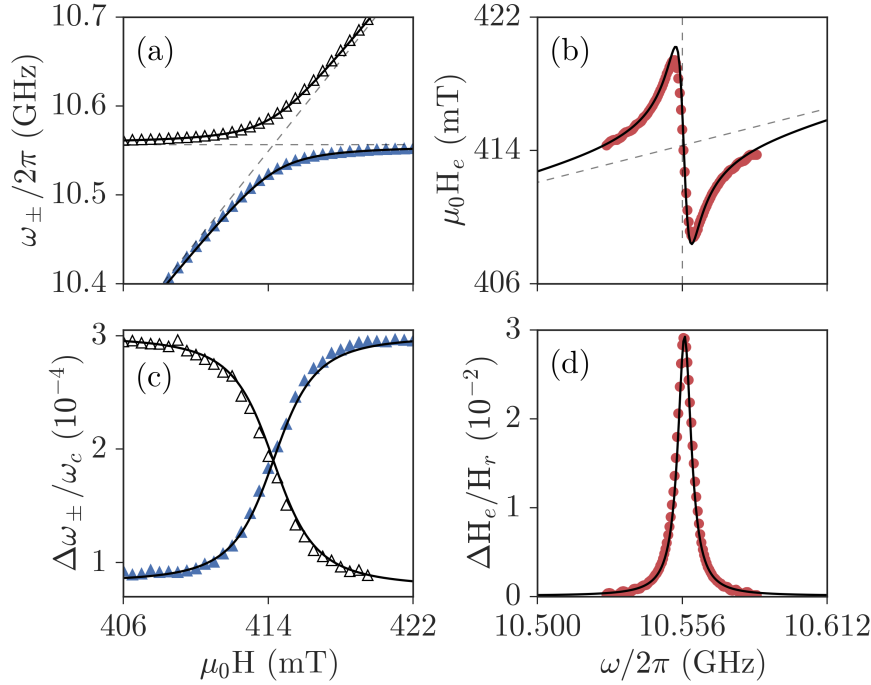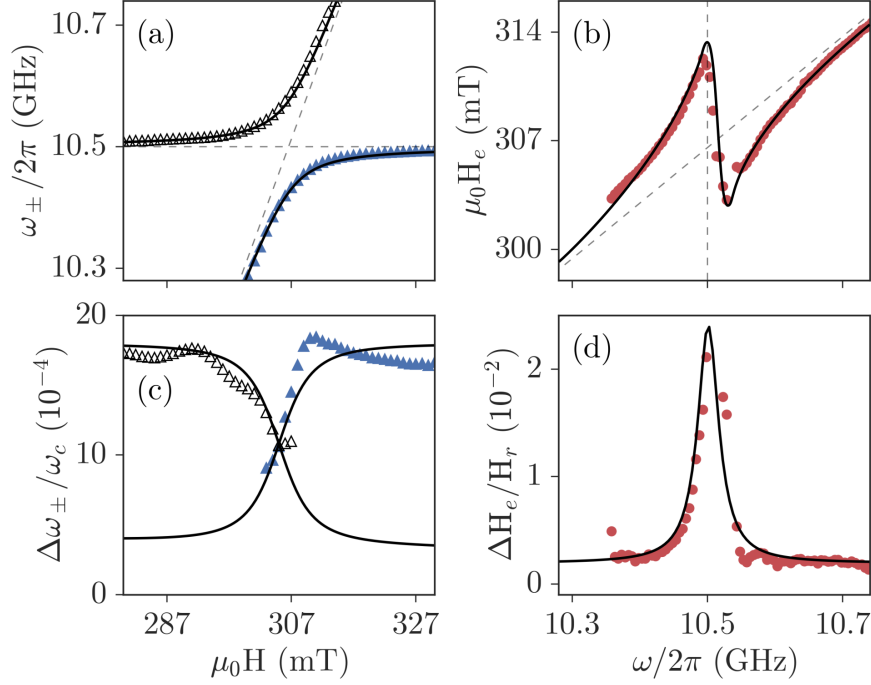
Figure 4.8: (a) Frequency swept voltage dispersion and (c) line width. (b) Field swept voltage dispersion and (d) line width. Symbols are experimental results, with hollow and solid triangles corresponding to the upper and lower CMP branches respectively. Solid curves are calculations according to Eqs. (3.9) and (3.12) for the field and frequency swept spectra respectively.

independently of the damping magnitudes, in contrast to the frequency swept spectra, where one mode increased and another decreased depending on the relative size of α and β. Normally the FMR line width is described by the relation $\Delta H = \Delta H_0 + \alpha\omega/\gamma$ [214], where ΔH_0 is the inhomogeneous broadening resulting from disorder, for example due to inhomogeneities in the crystal structure which produce fluctuations in the anisotropy and magnetization and can result in two magnon scattering which couples the FMR mode to higher order degenerate spin waves [214]. However our observation of line width enhancement due to coupling indicates that this relation is no longer valid in the coupled spin-photon system. We can most easily characterize this behaviour by rewriting the dispersion of Eq. (3.12) using our definition of the uncoupled photon spectra function, $\mathbb{S}_c = 1/\left(\omega^2 - \omega_c^2 + 2i\beta\omega_c\right)$,

$$\Delta H\left(\omega\right) = \Delta H_0 + \frac{\alpha\omega}{\gamma} + \frac{\omega^2\omega_m}{\gamma}K^2\mathrm{Im}\left(\mathbb{S}_c\right). \tag{4.9}$$

In writing Eq. (4.9) we have used the dispersion from the general electrodynamic

phase correlation model, rather than its simplification, so that this expression applies even away from resonance. This interesting and important result, which deviates from the traditional FMR line width, will be explored further in Sec. 5.2.

4.5.3 *Strong Coupling of Spin Waves*

Thus far we have discussed strong coupling with the FMR mode of our spin system. However, the data of Fig. 4.6 (d) indicated the presence of a standing spin wave mode (SSW) [21, 214], which may also strongly couple with the cavity. The spectra presented in Fig. 4.9 (a) takes a closer look at this spin wave mode, which is highlighted by a red arrow. The hybridized dispersion of the spin wave mode may be determined using a straightforward extension of our theoretical formalism by expanding the 2×2 matrix of Eq. (3.88) to a 3×3 matrix which includes both the FMR magnon, m_f with resonance frequency ω_{rf}, and the standing spin wave magnon, m_s with resonance
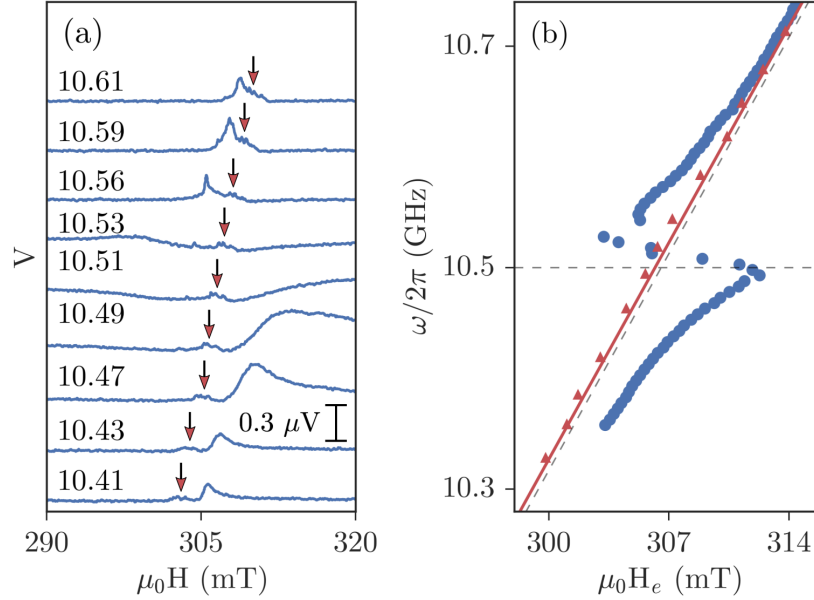
Figure 4.9: (a) Voltage spectra measured using the UMV1 setup (same data as Fig. 4.6) with a weak standing spin wave (SSW) mode highlighted by a red arrow. The frequency in GHz is indicated for each spectra. (b) Blue circles and red triangles are the experimental FMR and SSW dispersions respectively. The black curve and red line are the dispersion calculated using Eq. (4.10). A modified version of this figure was originally published in Ref. [48].

frequency ω_{rs} [48],

$$\begin{pmatrix} \omega - \omega_c + i\beta\omega_c & g_f & g_s \\ g_f & \omega - \omega_{rf} + i\alpha\omega_c & 0 \\ g_s & 0 & \omega - \omega_{rs} + i\alpha\omega_c \end{pmatrix} \begin{pmatrix} j \\ m_f \\ m_s \end{pmatrix} = 0. \qquad (4.10)$$

Here g_f is the coupling strength between the cavity mode and the FMR, g_s is the coupling strength between the spin wave and cavity modes, and the off diagonal zeros indicate that there is no direct coupling between the FMR and the SSW. In Fig. 4.9 (b) the experimental resonance positions of the FMR and the SSW are shown as blue circles and red triangles respectively. The calculated FMR dispersion, shown as a black curve, is determined from the determinant of Eq. (4.10) and is the same as that of Fig. 4.8 (b) for $g_s^2 \ll g_f^2$, which is true for the much weaker SSW observed in this experiment, where we find $g_s = 0.1g_f$. Meanwhile the SSW dispersion can also be calculated from the determinant of Eq. (4.10), taking $\omega_{rs} - \omega_{rf} = 21$ MHz to account for the exchange coupling which separates the SSW from the FMR. This curve is plotted in red in Fig. 4.9 and agrees well with our data. Interestingly, in the presence of spin-photon coupling we find that $\omega_{rf} > \omega_{rs}$ for $\omega < \omega_c$ and $\omega_{rf} < \omega_{rf}$ when $\omega > \omega_c$. This is in contrast to the uncoupled case where, due to the exchange interaction, the resonant frequency ω_{rs} of the SSW is always higher than ω_{rf} of the FMR. This new effect is due to the large deviations of the FMR dispersion induced by strong coupling, which are clearly observed in Fig. 4.9.

Due to the small amplitude coupling strength of the SSW we have just described, this data set does not display a clear spin wave anticrossing, which would be the "smoking gun" of spin wave strong coupling. To search for this signature, a series of experiments was performed using several YIG/Pt bilayers at the Walther-Meissner-Institute [49]. Typical reflection spectra using the WMI setup are shown in Fig. 4.10. In this measurement we used a YIG(2.8 μm)/Pt(5 nm) bilayer with lateral dimensions 5 mm × 2 mm where $\gamma = 29.3 \times 2\pi \ \mu_0$GHz/T, $\mu_0 M_0 = 140$ mT and $\alpha = 3.4 \times 10^{-4}$. The TE$_{011}$ mode of the Bruker cavity had a loaded resonance frequency of $\omega_c/2\pi = 9.651$ GHz and a loaded quality of $Q_L = 706$ ($\beta_L = 7 \times 10^{-4}$). The mapping of Fig. 4.10 (a) again shows a dominant SSW passing through the main FMR anticrossing and also illustrates the $S_{11}(\omega, H) = S_{11}(\omega, -H)$ symmetry of the microwave reflection spectra. In the WMI experimental setup the transmission lines can only be calibrated up to the cavity SMA connection, leaving the entire

Figure 4.10: (a) Microwave reflection mapping showing several strongly coupled spin wave modes in a YIG/Pt bilayer. (b) $|S_{11}(\omega)|^2$ at several values of negative and (c) positive $\mu_0 H$. (d) $|S_{11}(-|H|)|^2$ and (e) $|S_{11}(|H|)|^2$ for several values of ω. The multiple spin waves are most clearly seen in the $\omega = \omega_c$ cut shown in black in panels (d) and (e). The scale in panels (b) - (e) is the same as panel (a). Data used in this figure was originally published in Ref. [49].

length of the sample holder uncalibrated. This produces a significant standing wave background in the raw reflection data which we have corrected using the full complex S parameter and the inverse mapping technique [215], which is outlined in Appendix C. This method is known to enable excellent background correction even for entirely uncalibrated data [49]. Here we present the final, calibrated measurements. Fig. 4.10 (b) and (c) show $S_{11}(\omega)$ for several positive and negative H fields. These spectra
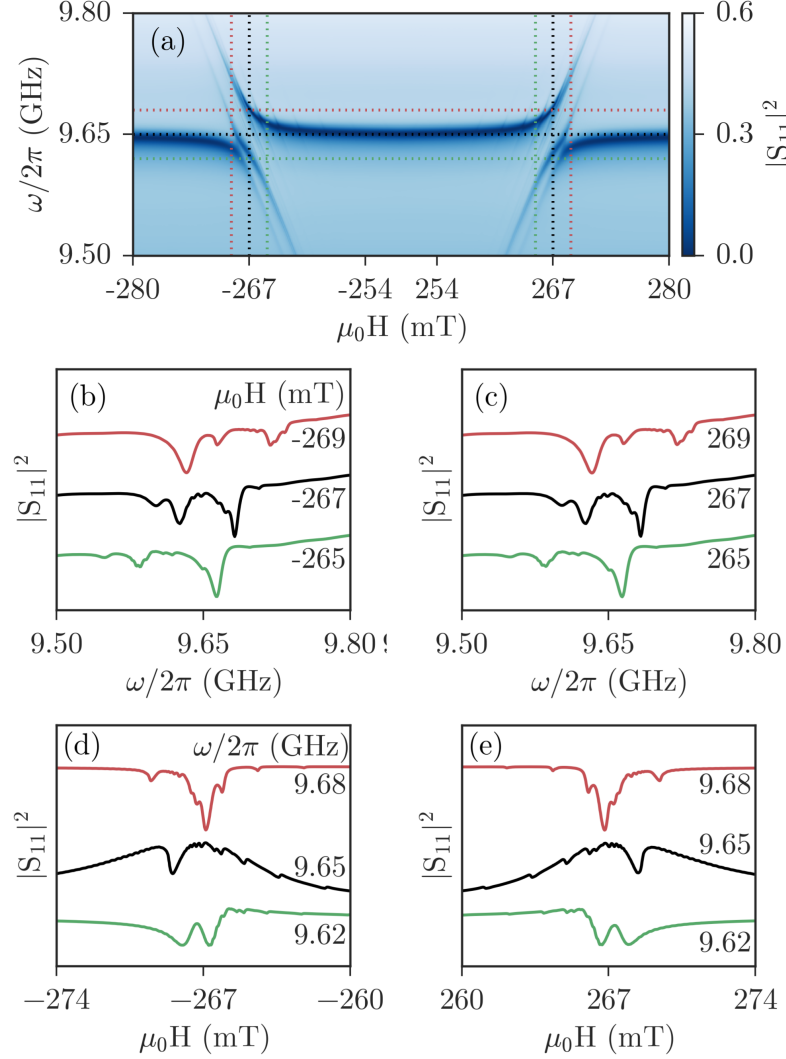
77
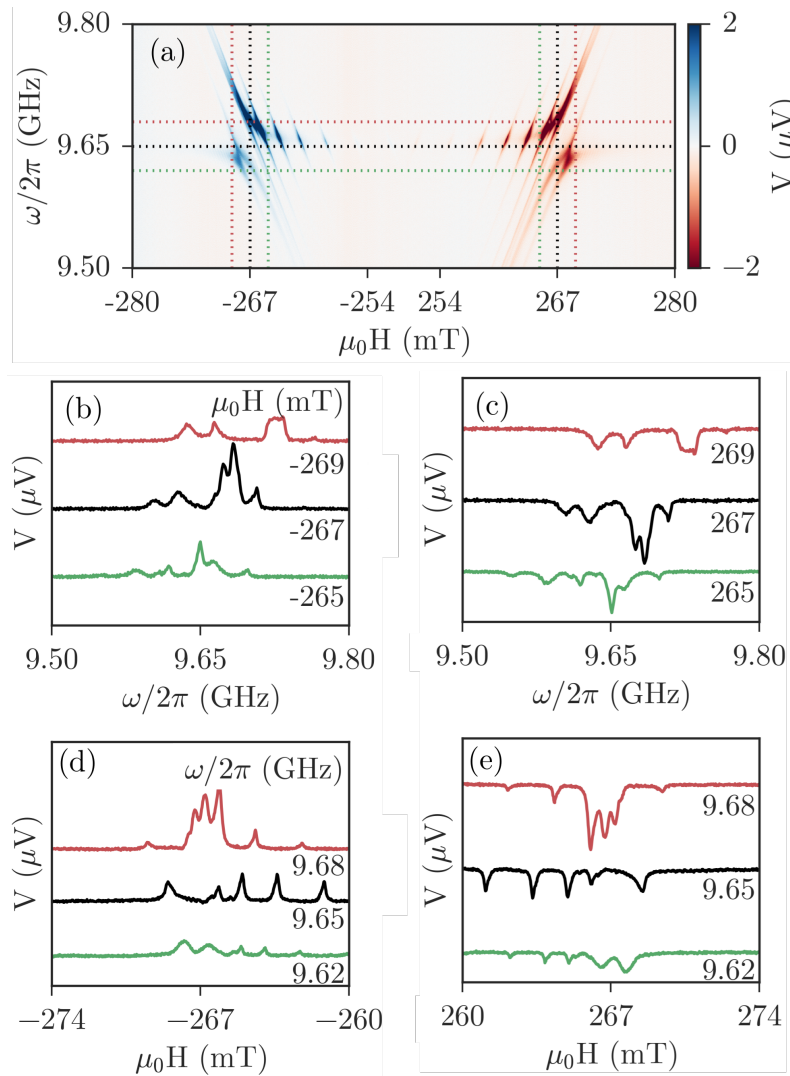
Figure 4.11: (a) Voltage mapping showing several strongly coupled spin wave modes in a YIG/Pt bilayer. (b) $|S_{11}(\omega)|^2$ at several values of negative and (c) positive $\mu_0 H$. (d) $|S_{11}(-|H|)|^2$ and (e) $|S_{11}(|H|)|^2$ for several values of ω. The multiple spin waves are most clearly seen in the $\omega = \omega_c$ cut shown in black in panels (d) and (e). The scale in panels (b) - (e) is the same as panel (a). Note the $V(H) = -V(-H)$ symmetry which is evident in all panels. Data used in this figure was originally published in Ref. [49].

further emphasize the symmetry of $S_{11}(\omega)$ under $H \rightarrow -H$. This symmetry is also evident in Fig. 4.10 (d) and (e) which display $S_{11}(H)$ for various ω. Although the influence of spin waves can be seen in all of the transmission spectra, they are most clearly identified in the $S_{11}(H)$ spectra at $\omega = \omega_c$, shown as the black curve in Fig. 4.10 (d) and (e).

The presence of spin waves is even more striking when viewed in the voltage spectra of Fig. 4.11, which does not have the strong cavity mode background observed in the analogous transmission measurements [49]. This experiment was again performed using the WMI setup with the same sample as Fig. 4.10. In all panels the expected spin pumping voltage symmetry $V(H) = -V(-H)$ is evident, and contrasts the field symmetry of S_{11}. The multiple spin wave modes can be observed in all panels, but are most clearly illustrated in the $V(H)$ spectra measured at $\omega = \omega_c$ in panels (d) and (e).

Interestingly, in this experiment we were able to make the first observation of a clear spin wave anticrossing. To highlight this feature Fig. 4.12 shows a "zoomed in" view of a typical spin wave, using the microwave reflection data for panel (a) and the voltage spectra for panel (b). The solid white line indicates the main anticrossing (in the absence of spin wave modes), which is calculated using Eq. (3.89) with a fitted
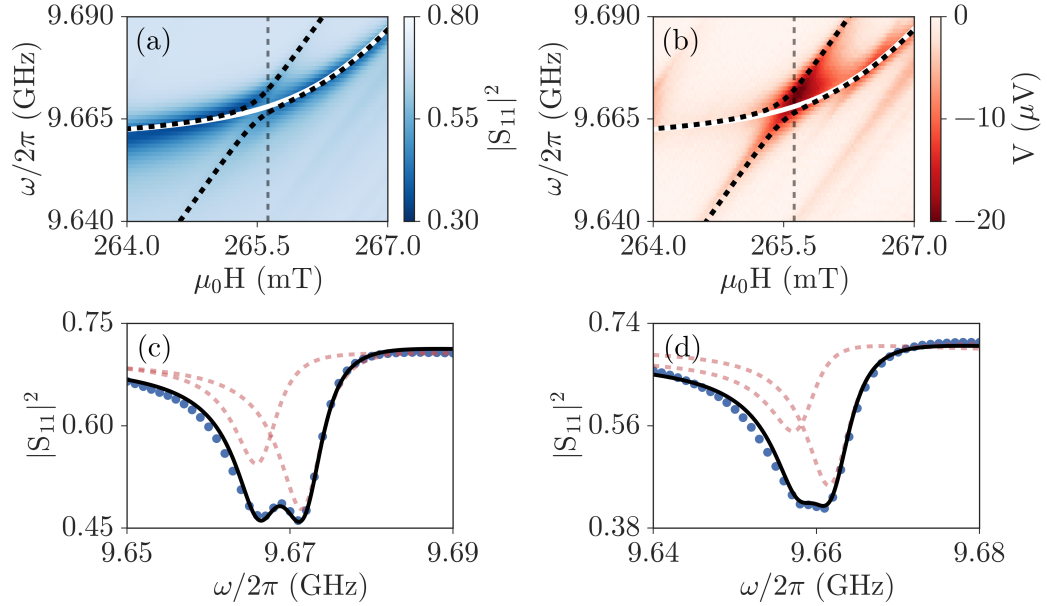
Figure 4.12: (a) The reflection and (b) voltage mappings of the $n = 7$ spin wave mode. This is the same data as Figs. 4.10 and 4.11 (a). The vertical dashed line indicates the crossing point for the $n = 7$ spin wave. (c) Reflection spectra at $\mu_0 H = 265.62$ mT (the $n = 7$ crossing point) for the $n = 7$ and (d) $\mu_0 H = 263.62$ mT (the $n = 9$ crossing point) for the $n = 9$ spin wave modes. The red dashed curves indicate the two mode peaks which are summed together to give the black fitting curve. Data used in this figure was originally published in Ref. [49].

coupling strength of $g/2\pi = 31.8$ MHz.[7] The spin wave dispersion can be calculated using the expanded three mode model of Eq. (4.10), which would produce a single solution for the entire spectrum and also include the main anticrossing. However this approach can become cumbersome when many spin wave modes are present, since, for example, in the case of n-modes we must find the roots of an nth order polynomial (the roots of the corresponding $n \times n$ matrix determinant). Since we assume no direct spin wave coupling, a simpler approach is to allow the hybridized FMR-cavity mode to act as a "new cavity mode" which couples to the spin wave, that is, to describe the spin wave mode coupling we can use the 2×2 matrix of Eq. (3.88) by replacing ω_c with ω_+ due to the FMR-cavity coupling (the white curve in Fig. 4.12 (a) and (b)). The result we obtain through this approach, using a spin wave coupling strength of 3 MHz, is shown as the black dashed curve in Fig. 4.12 (a) and (b). The excellent agreement with the experimentally observed dispersion demonstrates the accuracy of this alternative approach.

It is also possible to assign a mode label to the observed spin waves. To do so we first recall that, since we drive the magnetization with a uniform microwave field, only odd numbered modes will be excited[8]. In our experiment the $n = 3$ and $n = 5$ modes are too close to the main anticrossing to be analyzed quantitatively, and therefore the $n = 7$ mode is the first strongly coupled spin wave mode from which we can accurately determine the coupling strength. This mode assignment also leads to resonant frequencies in agreement with values of the exchange stiffness and gyromagnetic ratios reported in the literature [49, 217, 218]. For example, by reducing the cavity quality to destroy the hybridization (as shown in Fig. 5.2 (c) and (f)), we determine an effective magnetization of $M_{\text{eff}} = 147$ kA m^{-1} in agreement with values reported for YIG [217].

The dispersion of the $n = 7$ mode is presented in Fig. 4.12 (a). The reflection spectra at the crossing point of $\mu_0 H_c = 265.62$ mT for the $n = 7$ mode is shown in Fig. 4.12 (c). Mode splitting due to hybridization is evident, with a gap of 6 MHz (corresponding to $g_7/2\pi = 3$ MHz). Here the red dashed curve indicates the

---

[7]It is worth noting that, taking into account the number of spins in the sample, this corresponds to a single spin coupling rate of $g_0/2\pi = 0.1$ Hz [49], in agreement with experiments on paramagnetic systems [46].

[8]This assumes that the magnetization is pinned at both interfaces. Such conditions generally depend strongly on the device fabrication [216] and are difficult for us determine a priori for our device. However we find that this assumption leads to consistent spin wave assignment with regard to the expected index dependence of the coupling strength and determination of the exchange parameters and effective magnetization [49].

two resonance peaks which are summed to produce the black fitting curve, with the amplitude asymmetry resulting from the asymmetric standing wave background. Similarly the analysis of the $n = 9$ SSW is shown in Fig. 4.12, where the crossing point is at $\mu_0 H_c = 263.62$ mT and the coupling strength is found to be $g_9/2\pi = 2$ MHz. Having assigned mode labels we can now determine how the coupling strength changes for different modes. It has been predicted that the coupling strength of the nth SSW will follow a $g_n \propto 1/n$ behaviour, decreasing with increasing mode index [187]. From our $n = 7$ and $n = 9$ mode analysis we indeed see a decrease with the appropriate $1/n$ slope. However if we analyze the coupling strengths quantitatively using the value of $g_1/2\pi = 31.8$ MHz extracted from the main peak splitting, we would predict $g_7/2\pi \sim 4.5$ MHz and $g_9/2\pi \sim 3.5$ MHz. This discrepancy can be addressed by accounting for the poorly resolved $n = 3$ mode which contributes to the main anticrossing, mimicking an enhanced peak splitting of the hybridized FMR-cavity mode [49]. By extrapolating the behaviour of the $n = 7$ and $n = 9$ modes we find $g_3/2\pi = 7.6$ MHz, which can be subtracted from our previous value of 31.8 MHz, yielding $g_1/2\pi = 24.2$ MHz, in agreement with the extrapolated value. Our study therefore confirms the expected $1/n$ decrease of the spin wave coupling strength. For even higher order modes, which can be observed in, for example, Fig. 4.11, the coupling strength is to small to produce an anticrossing. However such weakly coupled modes have been examined through their line width broadening and also confirm the $g \propto 1/n$ behaviour [49].

Based on the observations presented in this section we can conclude that higher order spin waves will also hybridize with the microwave cavity. This hybridization is well described by our model of spin-photon coupling and also allows us to verify the $1/n$ coupling strength scaling with spin wave mode index n. From a technical standpoint the fact that higher order spin waves with systematically variable coupling strengths can also be observed, most notably in spin pumping experiments, may be useful for the development of cavity spintronic devices.

4.5.4 *Antiresonance Behaviour*

In addition to the dispersion anticrossing, line width evolution and spin wave strong coupling, another fundamental feature of spin-photon hybridization is the presence of an antiresonance in the microwave spectra. In contrast to a resonance, which is a maximum in the microwave transmission, an antiresonance is a position of minimum
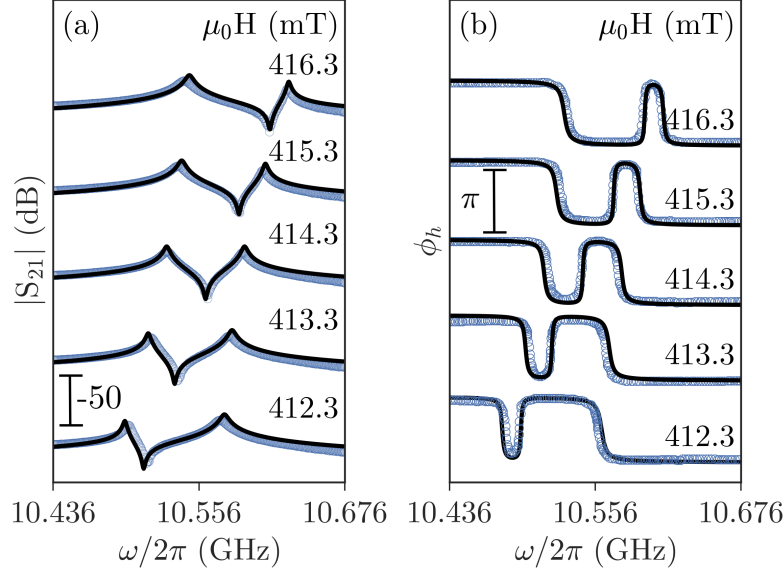
Figure 4.13: (a) Transmission spectra measured at different $\mu_0 H$ using the UMS1 experimental setup and displayed on a logarithmic scale, highlighting the presence of an antiresonance between the two CMP modes. Blue circles are experimental data and the solid black curves are calculated according to Eq. (3.90). (b) The corresponding transmission phase ϕ_h, which displays a π phase jump at each of the CMP resonances as well as at the antiresonance position. A modified version of this figure was originally published in Ref. [219].

transmission. In the case of spin-photon coupling an antiresonance will always occur at a frequency ω_{anti} in between the two hybridized modes, $\omega_- < \omega_{\text{anti}} < \omega_+$. This feature is highlighted in Fig. 4.14 (a) where experimental transmission spectra $S_{21}(\omega)$ are shown using blue circles for several H fields. This data was collected using the UMS1 setup and is actually the same data that was presented in Fig. 4.5 (a), however here the antiresonance feature is highlighted by using a logarithmic scale. The corresponding transmission phase behaviour, ϕ_h, is shown in panel (b). In each spectra we observe three π phase jumps. These occur at the CMP locations, $\omega = \omega_\pm$ and at the antiresonance, $\omega = \omega_{\text{anti}}$. In both panels the solid black curves are calculated according to Eq. (3.90).

The presence of an antiresonance can be anticipated from our CMP model. Examining Eq. (3.90) we find that

$$\frac{1}{S_{21}} \propto \frac{1}{\omega - \tilde{\omega}_r}, \tag{4.11}$$

and therefore S_{21}^{-1} will be maximized (S_{21} will be minimized) at $\omega = \omega_r$. The line width of the S_{21}^{-1} peak will be $\sim \alpha\omega_c$. Physically an antiresonance at the uncoupled FMR frequency also makes sense. At $\omega = \omega_r$ the magnetic material in the cavity will have the greatest absorption, minimizing the cavity transmission [219].

The fact that the antiresonance occurs at ω_r can be exploited in a useful way. Since we have a strongly coupling system, the mode hybridization means we cannot generally determine the uncoupled system properties directly from the transmission spectra, as would be done in traditional cavity based FMR experiments. However, if we look instead at the antiresonance, we can extract direct information of the spin subsystem, even though we are still in a strongly coupled regime. This type of analysis is illustrated in Fig. 4.14. The transmission spectra at the crossing point $\mu_0 H_c =$ 414.5 mT where $\omega_r = \omega_c$ is shown in Fig. 4.14 (a). Experimental data are shown as blue circles and the black curve is a calculation according to Eq. (3.90). The antiresonance location is marked by the vertical dashed line and we see that it lies directly in-between the two hybridized modes. This is because this spectra has been measured at the crossing point. By inverting the spectra of panel (a), as shown in Fig. 4.14 (b), we can immediately see the influence of the antiresonance. The experimental antiresonance positions are plotted as symbols in Fig. 4.14 (c) and the solid curve is a calculation of the FMR dispersion. As anticipated the antiresonance positions follow the uncoupled FMR dispersion. This means that in a strongly coupled system where, for example, the gyromagnetic ratio and Gilbert damping are not characterized, we can still directly access this information by examining the antiresonance.

The antiresonance can also be used to understand the phase behaviour of our system. It is well known that an oscillating system will display a phase jump upon passing through a resonance [178]. This can be observed in Fig. 4.14 (d) where we see two π phase jumps at the two CMP resonances. Here blue symbols are experimental data and the solid black curve is calculated using Eq. (3.90). However in addition to the resonance phase jumps we observe an additional π phase shift which occurs at a frequency in between ω_+ and ω_-. This shift exactly corresponds to the antiresonance location, as denoted by the vertical dashed line. Therefore we can account for all of the phase shifts which are observed through either resonance or antiresonance phenomena [219].

Experimentally we can only access the phase information of the microwave transmission, which in our model corresponds to the phase of h, ϕ_h. However our model
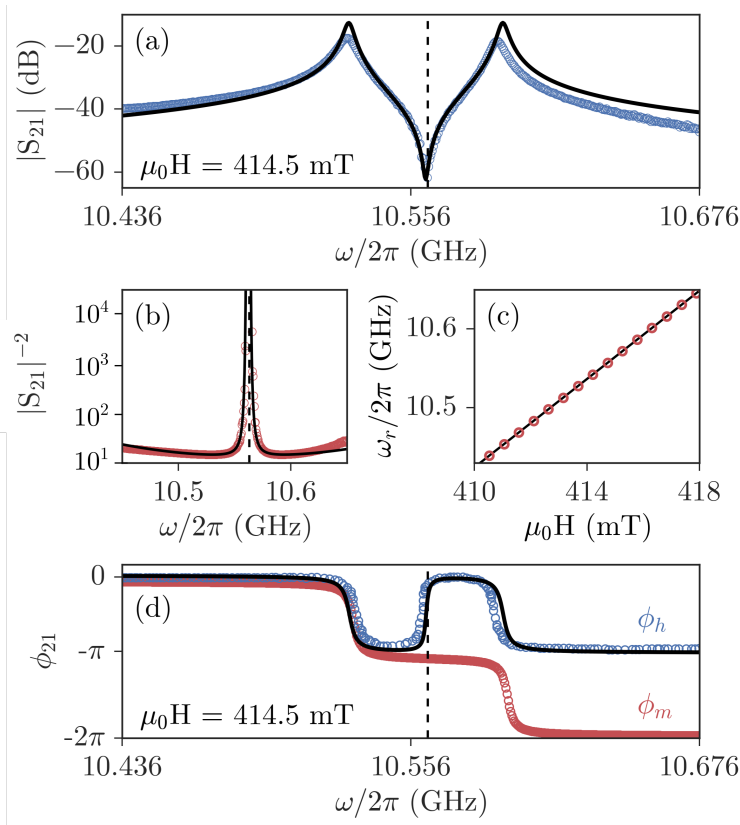
Figure 4.14: Phase and dispersion analysis based on the antiresonance. (a) Transmission spectra at the crossing point where $\omega_c = \omega_r$. Blue circles are experimental data and the black solid curve is calculated according to Eq. (3.90). The vertical dashed curve indicates the antiresonance position. (b) The inverted transmission spectra which further highlights the antiresonance. (c) A comparison between the antiresonance locations and the FMR dispersion. Red circles are the experimental antiresonance positions and the solid black line is the calculated FMR dispersion. (d) The transmission phase information. The blue circles are the experimentally measured transmission phase while the red circles are the calculated magnetization phase using Eq. (4.12). The solid black curve is calculated according to Eq. (3.90) and the vertical dashed line indicates the antiresonance position. A modified version of this figure was originally published in Ref. [219].

does allow us to calculate the magnetization phase ϕ_m. From Eq. (3.88) we see that

$$\phi_m = \phi_h + \operatorname{arccot}\left(\frac{\omega - \omega_r}{\alpha \omega_c}\right). \tag{4.12}$$

Therefore given the transmission phase ϕ_h it is also possible to determine the magnetization phase behaviour [219]. Such a ϕ_m calculation is shown in Fig. 4.14 (d)

84

as red circles, using the blue ϕ_h data. Although ϕ_h undergoes a phase shift at the antiresonance this phase shift does not influence ϕ_m — mathematically it is compensated by the second term in Eq. (4.12) — resulting in two, not three, phase shifts observed in the ϕ_m spectra. We have therefore developed a procedure which allows us to determine the magnetization phase behaviour, and relate this behaviour to the antiresonance phenomena. An interesting application of this procedure is to the characterization of magnon dark modes, which we discuss in the next section.

4.5.5 *Phase Analysis of Magnon-Dark Modes*

An intriguing application of strongly coupled spin-photon systems was proposed by Zhang et al. [59]. Using multiple YIG spheres in a microwave cavity they developed a gradient memory architecture based on magnon dark modes. By applying a field gradient between the YIG samples, they were able to generate "bright" magnon modes, which would couple to the cavity, and "dark" magnon modes, which did not interact with the cavity. As the dark modes do not couple to the cavity, they are longer lived and can be used to enhance storage times in memory applications. As was qualitatively revealed in Ref. [59], a key characteristic of the multiple YIG system is the phase behaviour. However this behaviour was not experimentally investigated previously. Now using our antiresonance and phase analysis method we are able to explore exactly such multi-resonant the behaviour [219].

Our two magnon system consisted of two nearly identical 1-mm diameter YIG spheres. These samples had the same gyromagnetic ratio of $\gamma = 28 \times 2\pi \ \mu_0 \text{GHz/T}$ and a Gilbert damping of $\alpha = 1 \times 10^{-4}$. However the two samples had slightly different shape anisotropies, $\mu_0 H_A = 92.5$ and 22.5 mT. As a result their dispersions are offset, as if there was a field gradient applied between them. These spheres were both placed at the outside edge of our cylindrical copper cavity, 2 mm apart (angular separation of $10°$), with the cavity height set to $h = 29$ mm which set the loaded TM_{011} resonance frequency to $\omega_c/2\pi = 10.556$ GHz with $Q = 1700$ ($\beta = \Delta\omega/\omega_c = 3 \times 10^{-4}$). The resulting transmission spectra is shown in Fig. 4.15 (a). In the case of two YIG spheres, m_1 and m_2, coupled to a single cavity mode, we can easily extend Eq. (3.88) so that our three mode system is described by the matrix [219],

$$\begin{pmatrix} \omega - \tilde{\omega}_c & g_1 & g_2 \\ g_1 & \omega - \tilde{\omega}_{r1} & 0 \\ g_2 & 0 & \omega - \tilde{\omega}_{r2} \end{pmatrix} \begin{pmatrix} h \\ m_1 \\ m_2 \end{pmatrix} = \begin{pmatrix} \omega_c h_0 \\ 0 \\ 0 \end{pmatrix} \tag{4.13}$$

85

so that the transmission spectra is given by,

$$S_{21} \propto \frac{(\omega - \tilde{\omega}_{r1})(\omega - \tilde{\omega}_{r2})\,\omega_c}{(\omega - \tilde{\omega}_c)(\omega - \tilde{\omega}_{r1})(\omega - \tilde{\omega}_{r2}) - g_1^2(\omega - \tilde{\omega}_{r2}) - g_2^2(\omega - \tilde{\omega}_{r1})}. \tag{4.14}$$

Here $\tilde{\omega}_{r1} = \omega_{r1} - i\alpha\omega_c$ and $\tilde{\omega}_{r2} = \omega_{r2} - i\alpha\omega_c$. The dispersion of the three mode system can be determined by calculating the roots of the S_{21} denominator. This yields the black curves in Fig. 4.15 (a), which agree well with the experimental data. We find a coupling gap of $\omega_{\text{gap}} = 65$ MHz for each sphere. At the magnetic field indicated by
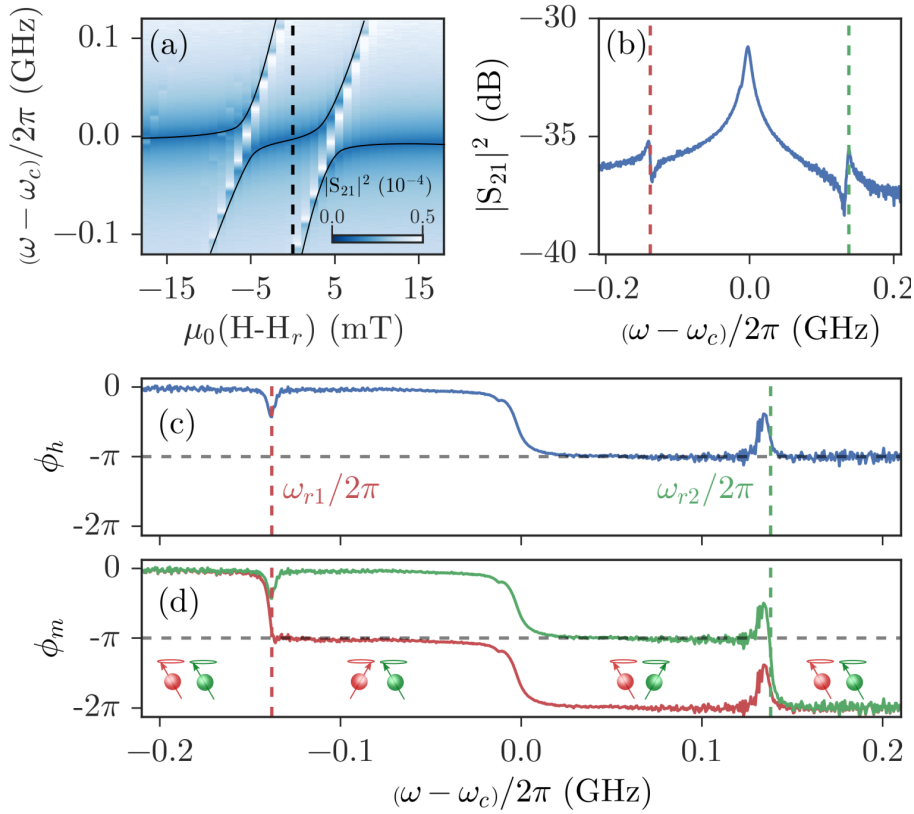
Figure 4.15: Phase analysis of a two YIG system. (a) A microwave transmission mapping, $|S_{21}|^2$, as a function of microwave frequency and magnetic field for a microwave cavity coupled to two YIG spheres. At the magnetic field indicated by the vertical dashed line, we plot the microwave transmission spectra as a function of frequency in (b), which shows two antiresonance frequencies. (c) The measured microwave transmission phase has two opposite phase jumps due to the two antiresonances. (d) The phases of the dynamical magnetization for each YIG FMR are calculated. The inset sketch shows that the two FMRs are out of phase between the two antiresonance frequencies (ω_{r1} and ω_{r2}). A modified version of this figure was originally published in Ref. [219].

the vertical dashed line in panel (a), we plot the transmission spectra as a function of frequency in Fig. 4.15 (b). As expected in this spectra we see three hybridized modes and two antiresonance locations, corresponding to the FMR positions of the two YIG spheres. The antiresonance positions are indicated by the red and green vertical dashed lines. The presence of two antiresonances is also confirmed by two positive phase jumps which are observed in the microwave transmission phase ϕ_h, as clearly shown in Fig. 4.15 (c). Here we also observe the expected three phase delays due to the three hybridized resonances. In analogy with our phase analysis of the previous section, the two magnetization phases, ϕ_{m1} and ϕ_{m2}, can be related to the microwave transmission phase as,

$$\phi_{m1} = \phi_h + \text{arccot}\left(\frac{\omega - \omega_{r1}}{\alpha\omega_c}\right), \tag{4.15}$$

$$\phi_{m2} = \phi_h + \text{arccot}\left(\frac{\omega - \omega_{r2}}{\alpha\omega_c}\right). \tag{4.16}$$

Using Eqs. (4.15) and (4.16) both magnetization phases were calculated and are plotted in Fig. 4.15 (d), where the relative phase of the two FMRs is shown by the insets. Before the first antiresonance frequency, ω_{r1}, the magnetizations of both FMRs are in phase with the microwave magnetic field. In between ω_{r1} and ω_{r2} the magnetizations of the two YIG spheres are out of phase by π with each other, forming a magnon dark mode (which is visible here since the anisotropy fields are chosen to be distinct). However, even within this range, while remaining out of phase with one another, the YIG magnetizations both experience a π-phase shift due to a hybridized mode near the cavity frequency ω_c. Finally, after the second antiresonance frequency ω_{r2}, the magnetizations from both FMRs are still in phase with each other but out of phase by π with the microwave magnetic field. Therefore a combination of antiresonance and phase analysis enables a phase characterization of the magnon dark mode system [219]. In particular we have directly revealed the in-phase/out-of-phase properties which enable the formation of dark modes. Notably the fact that both systems undergo a simultaneous phase shift while maintaining a phase difference of π in the dark mode region was previously unknown and could be useful in the implementation of such a memory architecture.

4.6 CONCLUSION

In this chapter we have examined the basic properties of the coupled spin-photon system. We found that the tell-tale signatures of coupling, mode anticrossing and line width evolution, can be observed using both microwave transmission and electrical detection techniques. The former method globally probes the hybridized states of the CMP, while the later technique demonstrates that spin current is influenced by the spin-photon coupling. This final finding is key to the development of cavity spintronic technologies. The fact that strong coupling, which can be controlled and manipulated, influences the spin current means than the vast array of existing spintronic systems should be reexamined within the new framework of strong spin-photon interactions. We also presented the observation of spin wave strong coupling, which allowed us to verify the coupling strength dependence on mode index and provided an interesting stress test of our theoretical model. Finally by revealing the features of the spin-photon antiresonance we were able to characterize the spin subsystem even during strong coupling. With the realization that strong coupling can easily be achieved even in conventional magnetic systems this is an important result, as it allows robust characterization of the spin system when traditional resonance analysis is no longer applicable. Furthermore, by utilizing the antiresonance we were able to understand the phase properties of the CMP and use this method to elucidate the behaviour of a two YIG system which forms dark magnon modes. With these basic properties of CMP physics established and the potential for spintronic development revealed, we now turn to the question of CMP control.

4.7 ACKNOWLEDGEMENTS

4.6 and Fig. 4.9 as well as the dark mode data presented in Fig. 4.15. He also contributed to the understanding and interpretation of the spin wave data presented in Fig. 4.9 as well as the antiresonance behaviour discussed in Sec. 4.5.4 and the phase analysis presented in Sec. 4.5.5; and Can-Ming Hu supervised and provided insight on all aspects of the presented work performed at the University of Manitoba. Outside of these contributions, all work and development presented in this chapter was performed by the author of this dissertation.

CONTROLLING SPIN-PHOTON HYBRIDIZATION

5.1 INTRODUCTION

Having already realized two reliable techniques which probe strong spin-photon coupling, and a powerful set of models which sets the foundation for our understanding, perhaps the most important question to ask is: How can we control the spin-photon hybridization and what could we achieve by doing so? This simple question actually opens the floodgates to a plethora of intriguing inquiries, such as: How does strong coupling arise? How can we move between the strong and weak regimes? How do we actually define strong coupling? Is there any residual impact of strong coupling on conventional FMR behaviour? Of course by exploring these questions the door to new applications and insights are sure to open. In order to address these issues the development of techniques that can be used to control and manipulate the spin-photon coupling in-situ is of particular interest. Such techniques would not only make the investigation of cavity spintronics more efficient and robust, but would also allow cavity spintronic techniques to be adapted for device applications.

The key parameter that characterizes the behaviour of spin-photon hybridization is the cooperativity, defined as the ratio of the coupling strength to the spin and photon loss rates. The larger the cooperativity, the greater the influence of hybridization. At low cooperativities the influence of coupling may not be observed in the dispersion. Intuitively the fact that the cooperativity controls the coupling behaviour makes sense, since the coupling strength defines the gap between hybridized modes, and large dissipation rates would wash out this gap. Therefore to answer the question of how we can control spin-photon hybridization we should explore cooperativity control. To

do so we have employed several experimental methods. As we demonstrate in Sec. 5.2, by controlling the cavity loss rate we are able to continuously tune between the strong and weak regimes. Through this approach we learn that even with a moderate cavity quality factor it is possible to observe the influence of hybridization. This implies that one must take caution when using conventional cavity FMR techniques in systems with large sample to cavity filling factors, since the impact of strong coupling may still have a large influence. As an example of this behaviour we analyze the FMR line width and discover that a large non-resonant influence of the coupling may exist, highlighting again the need to cautiously disentangle the influence of strong coupling from our understanding of conventional magnetism characterization techniques. Furthermore, we directly tune the coupling strength, and hence control the cooperativity, using both the magnetization temperature dependence in a compensating garnet, as outlined in Sec. 5.3 and careful control of the field torque which drives FMR, discussed in Sec. 5.4. Through our temperature control technique we verify the $g \propto \sqrt{N_s}$ scaling of the coupling strength and by tuning the field torque we develop an easy to use approach to systematically control the strong to weak transition. As an important and interesting application of this latter technique we use electrical detection of a multi spin system to demonstrate non-local spin current control over macroscopic distances. This result, presented in Sec. 5.5, highlights the interplay between fundamental physical insight, we reveal the key difference between microwave transmission and voltage measurement schemes, and experimental development, this technique enables a new spin current control mechanism which can be applied over distances much larger than exchange or dipole-dipole type interactions.

5.2 CONTROL OF CAVITY DAMPING

In our experimental investigations of strong spin-photon coupling we have already seen the influence of the coupling strength and damping on the behaviour of hybridization. For example, a large coupling strength will mean that ω_{gap} is large, while small dissipation rates are required to observe well separated modes. Therefore it is beneficial to define the cooperativity, $C = g_\eta^2/\alpha\beta$, where $g_\eta = g/\omega_c = \omega_{\text{gap}}/2\omega_c$ is a dimensionless coupling strength normalized to the cavity resonance frequency. C is the key parameter which determines the behaviour of our strongly coupled system. In a practical experimental setting the cooperativity determines whether or not we can resolve mode splitting at the crossing point due to hybridization. When the co-

operativity is large, $C \gg 1$, then ω_{gap} is much larger than the line width of either mode and we can clearly resolve both peaks. On the other hand, when $C \ll 1$ we will only see a single peak at the crossing point, even though we may have $g_\eta \neq 0$.[1] Therefore we can tune the cooperativity by controlling either of the damping rates α and β, or by tuning the coupling strength g directly. Tuning the damping of the spin system would be challenging, especially in a controllable way (for example we could change the magnetic sample, but within the regime where strong coupling can still be observed this would only change the damping by a factor of $\sim 2 - 5$). However it is possible to systematically control the cavity damping.

To understand how we can experimentally control the cavity damping, recall that the loss rate of the loaded cavity has two contributions, $\beta_L = \beta_{\text{int}} + \beta_{\text{ext}}$.[2] The intrinsic loss rate, β_{int}, is primarily determined by the cavity conductance and can therefore be increased by polishing or the use of superconducting materials, but is not easily tuneable. However the total extrinsic loss rate, β_{ext}, is determined by the coupling of external microwaves from the feedlines into the cavity and is therefore controllable. The loaded quality factor, $Q = 1/2\beta_L$,[3] actually depends on the loaded cavity loss rate, and can therefore be tuned by controlling β_{ext}. Fig. 5.1 (a) illustrates how we experimentally tune the loss rate in our 3D cavity. In this cavity we can control the pin length entering the cavity from the SMA connector, which enables quality factor control between $0 < Q < 1800$. Similarly the Bruker cavity, shown in Fig. 5.1 (b), contains a tuneable iris which couples microwaves from the waveguide into the cavity. By tuning the size of this iris we are able to control the extrinsic cavity loss rate. The Q factor control achieved in the Bruker cavity is shown in Fig. 5.1 (c) and (d). In panel (c) several reflection spectra are shown at different feedline couplings (iris sizes). The best quality factor of $Q \sim 1400$ is shown at the top (labelled by 1), while the lowest quality factor of $Q \sim 50$ is shown at the bottom (labelled by 6). Spectra 3 at $Q \sim 700$ is the critically coupled spectra, which offers the best balance between quality factor and signal amplitude.[4] The actual quality

---

[1] Actually it is possible that one can have $C > 1$ (although very close to 1) and still find $\omega_{\text{gap}} = 0$. An alternative interpretation of the condition $\omega_{\text{gap}} = 0$ will be discussed in Ch. 6.

[2] In describing our electrodynamic phase correlation model we considered the general case of two different loss rates at each port, β_1^{ext} and β_2^{ext}. Here we write $\beta_{\text{ext}} = \beta_1^{\text{ext}} + \beta_2^{\text{ext}}$ for simplicity. The important point is that we control the total extrinsic loss rate. Whether we do this at port 1 or 2 is irrelevant.

[3] For simplicity in discussing our experimental results we adopt the notation Q for the loaded cavity quality, $Q = Q_L$.

[4] The ideal scenario from a quality perspective would be to realize $\beta_{\text{ext}} = 0$, in which case β_L would be minimized. However if this happened we would no longer be coupling microwaves into
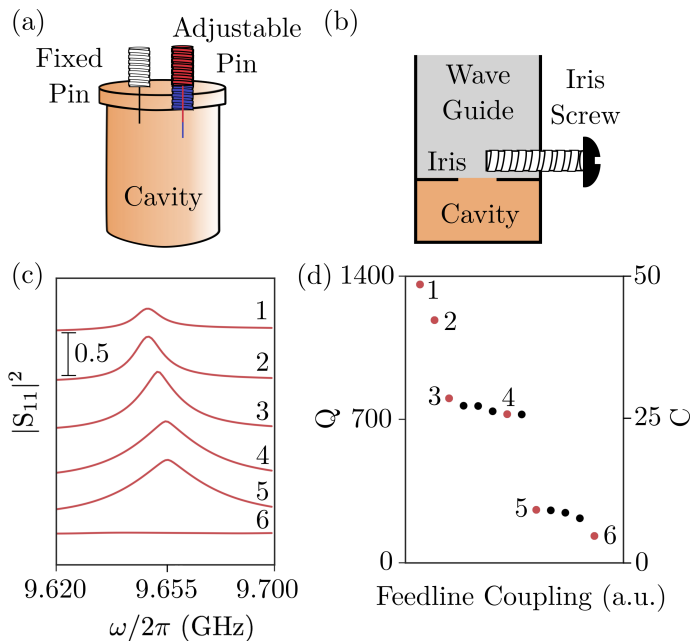
Figure 5.1: (a) The quality of our cylindrical cavity can be tuned by adjusting the pin length in the SMA connector. (b) In the Bruker cavity the size of the iris, which controls the feedline coupling between the waveguide and the cavity, can be adjusted to control the cavity damping. (c) Reflection spectra at several iris diameters, showing the broadening of the cavity mode as the quality is reduced. The quality factors of the numbered curves are shown by red circles in panel (d), demonstrating that in this cavity we can control $0 < Q < 1400$.

factors measured in the Bruker cavity as the feedline coupling is tuned are shown in Fig. 5.1, with red circles indicating the quality factors extracted from the spectra in panel (c). In this system we are therefore able to tune between $0 < Q < 1400$. The corresponding cooperativity using a YIG/Pt bilayer with $g = 63$ MHz, $\omega_c = 9.651$ GHz and $\alpha = 4 \times 10^{-4}$ is indicated on the right scale. Traditional cavity based FMR experiments would correspond to very low cooperativities (due to the low sample to cavity volume filling factors), whereas we see that our experiments operate in the $C \gg 1$ regime.

The influence of cavity damping control on the CMP spectra, as measured in the Bruker cavity of the WMI setup, is shown in Fig. 5.2. The top panels show the reflection spectra as we increase the coupling of the cavity to the feedline, thereby

the cavity and could not make any measurements! In other words if $\beta_{\text{ext}} = 0$ the amplitude of the microwave transmission would be zero. The ideal balance between signal amplitude and quality factor occurs when $\beta_{\text{int}} = \beta_{\text{ext}}$ [185]. This condition is known as critical coupling and is generally used in our experiments.
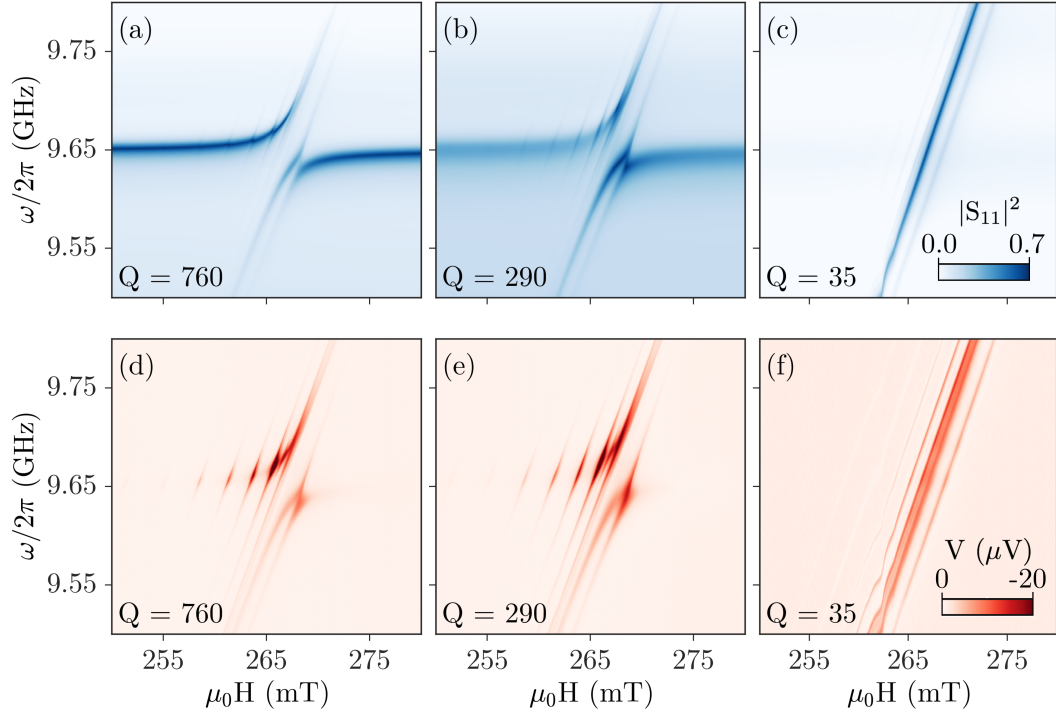
Figure 5.2: By tuning the loss rate in the Bruker cavity we can transition from strong to weak coupling, which is demonstrated by moving from left to right across the figure. Such a transition is marked by moving from a large anticrossing at the critically coupled value of $Q = 760$ to the near destruction of the cavity mode and the resulting mode crossing at $Q = 35$. Top panels are microwave reflection spectra and bottom panels are simultaneously measured voltage spectra using the WMI setup. A modified version of this figure was originally published in Ref. [49].

decreasing Q (increasing β_{ext}). Panel (a) is measured at critical coupling, where $Q = 760$, corresponding to spectra 4 in Fig. 5.1 (c). A clear anticrossing is observed indicating that we are in the strongly coupled regime. In panel (b) $Q = 260$, corresponding to spectra 5 in Fig. 5.1 (c). At this value of the cavity damping we can see the broadening of the cavity mode, indicated by a decrease in amplitude, and observe an apparent decrease in ω_{gap}. This decrease is mainly an "optical illusion" due to the broadening of the hybridized modes, as ω_{gap} is independent of damping while in the strongly coupled regime. Finally in Fig. 5.2 (c) we have reduced the cavity quality to $Q = 35$, corresponding to spectra 6 in Fig. 5.1 (c), and have completely destroyed the cavity mode, clearly entering the weakly coupled regime where no anticrossing is observed. In this case we essentially observe the FMR mode directly, and our experiment resembles a traditional cavity based FMR measurement. The multi-

ple diagonal lines which can be observed in Fig. 5.2 (c) correspond to higher order spin wave modes. The slope of these lines could be used to determine the effective gyromagnetic ratio and saturation magnetization of these modes [49].

The behaviour observed in Fig. 5.2 (a) - (c) highlights the role of the microwave cavity as a filter. When the cavity mode is narrow, as in panel (a), the bandwidth of microwaves which excite the magnetization is narrow. As a result we only see FMR absorption roughly in the range 9.55 GHz $< \omega/2\pi <$ 9.75 GHz. However, as the quality of the cavity is decreased, the bandwidth of the cavity increases and therefore the FMR resonance can be observed over a much wider frequency [49]. In the extreme case of $Q = 35$, as shown in Fig. 5.2 (c), the microwave reflection is essentially flat over the observed frequency range (as also indicated by spectra 6 in Fig. 5.1 (c)) except at the FMR and spin wave resonances.

Fig. 5.2 (f) - (h) show the corresponding behaviour in the spin pumping voltage. Again we observe the transition from strong to weak coupling as the cavity decay rate is increased, with the direct FMR and spin wave dispersions visible at low Q. An interesting feature which is more clearly seen in the voltage spectra is the influence of the microwave field amplitude. As the cavity quality decreases the amplitude of the microwave field at any given frequency also decreases. Therefore the amplitude of the spin pumping voltage, which depends on the fixed frequency microwave power, is decreased. This effect is greatest for the higher order spin wave modes. We note that the voltage amplitude corresponding to the fundamental mode does not decrease as drastically, which results from the fact that the absorbed power of the spin-photon system is still approximately constant (it is just spread out in frequency, see Fig. 5.1 (c)), and the coupling strength does not change when changing the cavity decay rate [49]. Thus we can nicely demonstrate the influence of dissipation on the characteristics of strong coupling in both the microwave transmission and voltage spectra. Such an understanding is important for device applications where the system properties must be carefully designed in order to achieve the desired functionality.

The tuneable cavity quality can be used to highlight the importance of characterizing strong coupling before performing cavity FMR experiments. Fig. 5.3 shows the reflection spectra, $|S_{11}|$, at $\omega = \omega_c$. In the case of weak coupling (red curve) the spin-photon hybridization does not distort the dispersion and we can extract the most accurate FMR and spin wave dispersions and line widths. However when strong coupling is present (blue curve) we observe no mode at the uncoupled FMR position. In this case the only signature of the original mode is the broad slope which leads to the
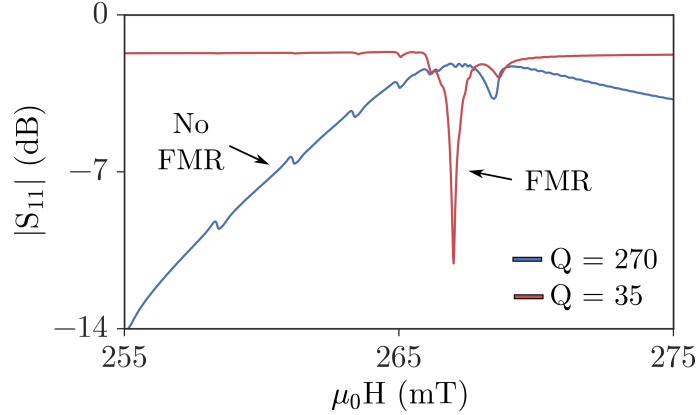
Figure 5.3: Reflection spectra for a strongly coupled system (blue) and a weakly coupled system (red). In the case of weak coupling the true FMR and spin wave properties can be characterized. However when the spin-photon system is strongly coupled, the FMR peak is shifted due to hybridization and we cannot directly access the spin subsystem using conventional resonance properties. A modified version of this figure was originally published in Ref. [49].

hybridized mode. The fact that we observe this behaviour for easily realized sample volumes indicates the importance of considering coupling effects when attempting to characterize magnetic systems [49]. This behaviour is consistent with our discovery of the drastic FMR line width enhancement due to resonant coupling [48]. Both of these observations indicate the importance of considering the influence of strong coupling when characterizing magnetic systems, even in supposedly traditional spintronic devices. It is worth noting that in these experiments (and all experiments made in this thesis), non linear effects were negligible. This is due to the low powers used (maximum of 30 mW delivered by the VNA, which is much greater than the power at the sample) and the large cavity volumes, resulting in low power densities. The results reported here were consistent over a range of input powers between 10 μW and 30 mW. Although the exact field strength at the sample is strongly dependent on the mode and configuration, we can roughly estimate the power (or field strength) in the cavity at ω_c using the relation $|S_{21}(\omega_c)| = |h(\omega_c)|/|h_0|$ where h_0 is the field strength supplied to the cavity by the VNA. Under critically coupled conditions, for a typical experiment we have $P = \mu_0 h^2/2 \sim 1$ mW, which is then further suppressed by the small filling factor, V_s/V_c, which depends on the sample, V_s, and cavity, V_c, volume ratio, and in our experiments was typically on the order of 1×10^{-4}.[5] For the

---

[5]CST simulations confirm that the actual power delivered to the cavity is typically much less
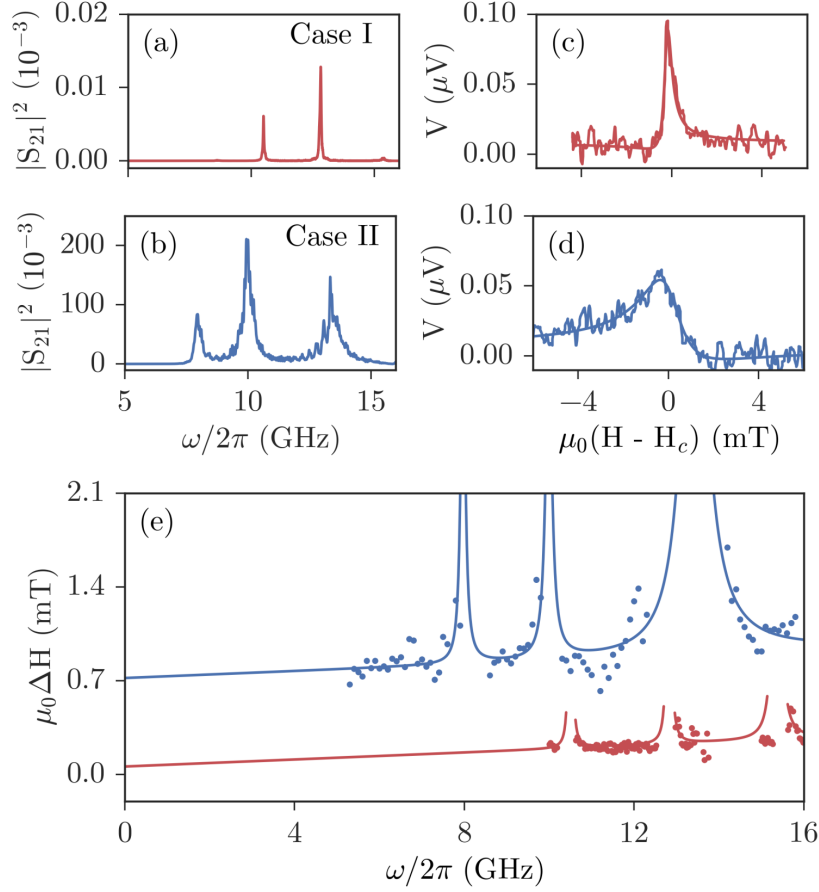
Figure 5.4: Transmission spectra S_{21} measured (a) before and (b) after tuning an adjustable pin inserted in Port 1 of the cavity. The voltage spectra measured at $\omega/2\pi = 10$ GHz (c) before and (d) after tuning the pin length. A significant change in the voltage line shape is observed. The smooth solid curves are fits according to an asymmetric Lorentz line shape as discussed in Sec. 3.2.1. These fits produce $\mu_0 \Delta H = 0.20$ mT and $\mu_0 \Delta H = 1.03$ mT for case I and II respectively. (e) Comparison of the frequency dependent FMR line width measured before and after tuning the pin length. The solid curves are fits according to Eq. (5.1), which yield $\mu_0 \Delta H_0^I = 0.06$ mT and $\mu_0 \Delta H_0^{II} = 0.72$ mT. A modified version of this figure was originally published in Ref. [48].

Bruker cavity, we should mention that even up to 1 W of input power, non-linear effects were not observed, although at these high powers the influence of higher harmonic modes generated by the signal generator were apparent. However by increasing the local power density at the sample non linear effects have been observed in other configurations [63, 209].

---

than 1% of the applied microwave power.

The final effect we have studied using our quality tuneable cavity is the influence of the damping on the voltage spectra line shape and the non-resonant line width enhancement. This experiment was performed in the UMV1 experimental setup, where the cavity quality can be tuned by adjusting the length of the pin which injects microwaves into the cavity. In this experiment we studied two different pin length configurations which resulted in a cavity configuration with the three cavity modes shown by the transmission spectra in Fig. 5.4 (a) and (b). In case I, shown in Fig. 5.4 (a), three cavity modes of $(\omega_c/2\pi \text{ (GHz)}, \beta, Q) = (10.502, 1.2 \times 10^{-3}, 420)$, $(12.822, 1.2 \times 10^{-3}, 420)$, and $(15.362, 3.5 \times 10^{-3}, 140)$ were excited. In case II, shown in Fig. 5.4 (b), three modes of $(\omega_c/2\pi \text{ (GHz)}, \beta, Q) = (7.969, 7.9 \times 10^{-3}, 63)$, $(9.990, 8.8 \times 10^{-3}, 57)$ and $(13.414, 2.38 \times 10^{-2}, 21)$ are observed. As shown in Fig. 5.4 (c) and (d), the line shape of the spin pumping spectrum $V(H)$ measured at $\omega/2\pi$ = 10 GHz is significantly tuned by the strongly coupled microwaves. As we have discussed, without the influence of strong coupling the voltage spectra would have a Lorentz line shape. However the presence of the cavity and the behaviour of the cavity modes influences this behaviour in a striking way [48]. The solid curves shown in Fig. 5.4 (c) and (d) are fits using an asymmetric line shape function as discussed in Sec. 3.2.1.[6] By systematically fitting the data over a wide frequency range we can determine the broad band behaviour of $\Delta H(\omega)$, which includes non-resonant regions between the cavity modes. The experimental data from such an analysis is plotted as symbols in Fig. 5.4 (e). Using the obvious generalization of Eq. (4.9) to the case of multiple cavity modes we can fit $\Delta H(\omega)$ to our theoretical expectation [48],

$$\Delta H(\omega) = \Delta H_0 + \frac{\alpha\omega}{\gamma} + \frac{\omega^2\omega_m}{\gamma}\sum_l K_l^2 \text{Im}(S_{c,l}). \tag{5.1}$$

The last term in Eq. (5.1) describes the coupling enhanced FMR line width near each cavity mode with l summing over all cavity modes. In our fitting we set $K_l = 0.016$ for all modes (corresponding to $g \sim 130$ MHz) except for the third mode at 13.414 GHz with $\beta = 2.38 \times 10^{-2}$ for case II, for which we use $K_3 = 0.032$ (corresponding to $g \sim 260$ MHz). The anomalously large value of K and β for this mode indicate that in this cavity configuration there are likely two closely spaced modes which both contribute to the coupling. From our fits we obtain $\alpha^I = 3.6 \times 10^{-4}$ and $\mu_0\Delta H_0^I = 0.06$ mT for case I and $\alpha^{II} = 3.6 \times 10^{-4}$ and $\mu_0\Delta H_0^{II} = 0.72$

---

[6]Such asymmetric voltage line shapes have previously been studied in detail in the context of spin rectification. See e.g. [220, 221].

mT for case II. As expected, the frequency slope which determines α is constant, independent of the cavity properties and the spin-photon coupling. A surprising result is that the inhomogeneous broadening differs in the two cases. Moreover, both of these results differ from the value of the inhomogeneous broadening that was characterized before loading the sample into the cavity, $\mu_0 \Delta H_0 = 0.31$ mT. This effect may be attributed to a difference in the microwave density of states in the cavity [48, 222]. From Fig. 5.4 (a) we see that the non-resonant microwave density of states is small in case I, whereas the broad modes and significantly enhanced transmission amplitude observed for case II, as shown in Fig. 5.4 (b), indicate an increase in the microwave density of states. As a result, the measured ΔH_0 is increased not only near each cavity mode, but also in the non-resonant regions between modes, as seen in Fig. 5.4 (e). We note that this extrinsic damping caused by the coherent spin-photon coupling is even larger than the intrinsic Gilbert damping of YIG, indicating the significant effect of FMR broadening due to non-resonant spin-photon coupling. Analogous effects have recently been studied in spin systems driven by microwave striplines, where radiation damping plays an important and confounding role in the line width characterization, see, for example, Refs. [25, 26]. This again highlights the importance of careful system characterization in order to disentangle the influence of strong coupling from traditional FMR behaviour. Therefore we hope that the understanding of the damping dependent behaviour which we have demonstrated here will not only benefit cavity spintronic development but also traditional FMR characterization in the new era of strongly coupled spin-photon systems.

5.3 TEMPERATURE CONTROL OF COUPLING STRENGTH

Having explored cooperativity control through a tuneable damping, we now turn to manipulation of the spin system in order to control the coupling strength directly. As we saw in Sec. 3.4.2, the coupling strength depends on the filling factor, V_s/V_c as $g \propto \sqrt{V_s/V_c}$, where $V_s \propto N_s$ is the sample volume (N_s is the number of spins) and V_c is the cavity volume. Therefore by increasing the number of spins or decreasing the cavity volume the coupling strength may be increased. This leads to a brute force method of coupling strength control which involves using different magnetic samples or cavities. Zhang et al. used this method to systematically verify the $g \propto \sqrt{V_s/V_c}$ scaling behaviour in Ref. 32 and research groups routinely use different sample sizes and cavity geometries to fit the needs of their experiment [31, 32, 34, 48, 51]. However
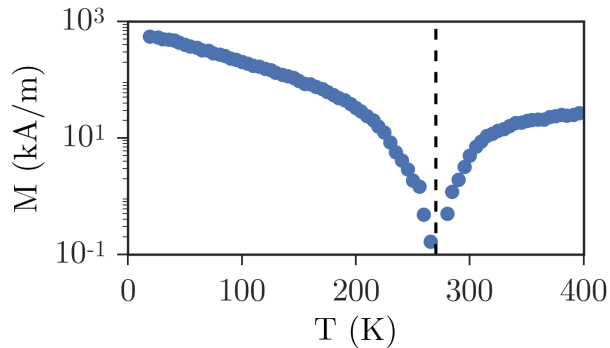
Figure 5.5: SQUID magnetization curve of GdIG measured at $\mu_0 H = 100$ mT, normalized to the effective magnetization at 15 K. The shape anisotropy dominates in our sample and therefore the net magnetization is equal to the effective magnetization. The dashed line indicates the compensation temperature at $T_{\mathrm{comp}} = 270$ K. A modified version of this figure was originally published in Ref. [40].

it would be more appealing to tune the coupling strength in-situ. One way to do so is to use a compensating garnet, as discussed in Sec. 2.2.1, where the effective number of spins, as determined by the magnetization, can be controlled through temperature.

To investigate this effect we used a 2.6 μm thick GdIG film grown by liquid phase epitaxy on a GGG substrate with lateral dimensions of 5 mm × 2 mm. At room temperature the magnetization of GdIG is dominated by the magnetization of the iron sublattices, showing only a weak temperature dependence. However below room temperature the strongly temperature dependent Gd sublattice begins to dominate the net magnetization, which vanishes at the compensation temperature T_{comp}. To characterize this behaviour the net magnetization of the sample was measured using standard SQUID magnetometry at a field of 100 mT, as shown in Fig. 5.5 [223]. As the shape anisotropy dominates the magnetic anisotropy of our sample, the net magnetization we measure is equal to the effective magnetization which appears in the Kittel dispersion [40]. From this magnetization curve we find a compensation temperature of $T_{\mathrm{comp}} = 270$ K, which, as anticipated [224], is slightly lower in our thin film sample than the bulk value of 285 K [116].

Microwave reflection measurements of the GdIG sample were performed using the WMI setup, where the sample is placed at the magnetic field anti-node of the Bruker cavity. The cavity was placed inside of a gas flow cryostat which enabled temperature control of the magnetic sample. As in all of our experiments, the microwave power to the cavity is low (0 dBm in this case), to avoid non-linear processes. As we have
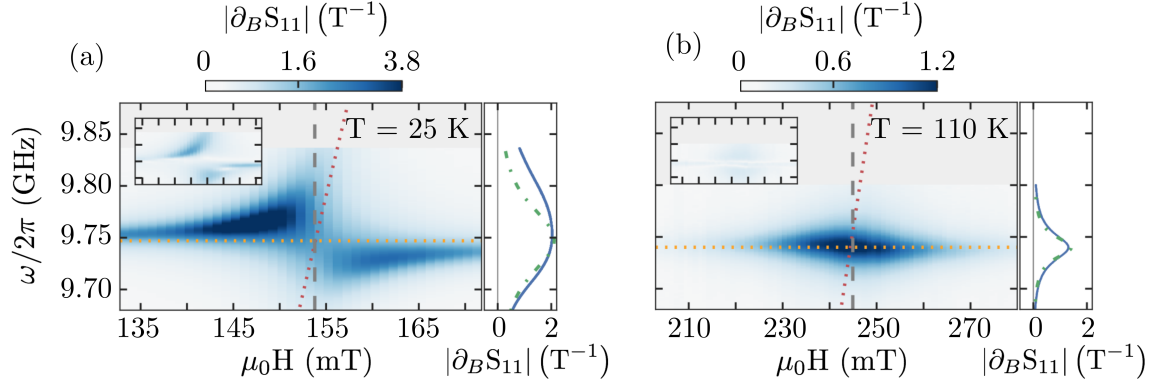
Figure 5.6: The magnetic field derivative of the reflection spectra at (a) 25 K and (b) 110 K. At 110 K the system is still weakly coupled, however at 25 K strong coupling can be observed, indicating the temperature control of the coupling strength. Horizontal and diagonal dashed lines indicate the uncoupled cavity and FMR dispersions respectively. Inset: Residuals of the fit to Eq. (3.91) using the same scale. Line cuts: Data (blue, solid line) and fit (green, dashed line) at the crossing point where $\omega_r = \omega_c$, which is indicated by the dashed, vertical line. A modified version of this figure was originally published in Ref. [40].

previously discussed, reflection measurements are prone to a field independent standing wave background signal. Therefore we have analyzed the field derivative of the reflection spectra, $\partial_B S_{11} = \frac{\partial S_{11}}{\partial(\mu_0 H)}$, which removes the standing wave background [40]. Typical $\partial_B S_{11}$ data at 25 K and 110 K are shown in Fig. 5.6 (a) and (b) respectively. Since we are examining the field derivative of the spectra the field independent cavity mode is not observed. Instead we will only observe a signal when the microwave cavity modes have hybridized with the field dependent FMR mode and therefore adopt a field dependence. At 25 K we observe an anticrossing, indicating strong coupling which can be observed over a field range of more than 40 mT. On the other hand, at 110 K the system is weakly coupled and we only observe a field derivative signal near the crossing point where the greatest hybridization effect is present. In both Fig. 5.6 (a) and (b) the horizontal and diagonal dashed lines indicate the uncoupled cavity and FMR mode dispersions respectively while the vertical dashed line shows the crossing point $\omega_r = \omega_c$.

The spectra shown in Fig. 5.6 indicate qualitatively that we have tuned from the weak to strong coupling regime. In order to quantitatively verify that we have realized a temperature controlled coupling strength, and in particular that we have not again simply changed the damping properties of either the cavity or spin system, we must extract the temperature dependence of the coupling strength. In the strongly

coupled case, observed at 25 K in Fig. 5.6 (a), this can be done by analyzing the peak splitting at the crossing point $\omega_r = \omega_c$, while for a weakly coupled system where there is no peak splitting, which we observe at 110 K in Fig. 5.6 (b), it is possible to extract the coupling strength from the line width enhancement of the microwave cavity [225]. However, since we wish to analyze the transition from a strongly to weakly coupled system, neither of these two simplified approaches is appropriate. Instead the full expression of Eq. (3.90) must be used to extract the coupling strength [40]. Therefore, taking the field derivative of Eq. (3.90) we performed full 2D fits, where all fits of constant H have shared parameters. The residuals of these fits for the 25 K and 110 K data are shown in the insets of Fig. 5.6 and a fit to the cut at $\omega_r = \omega_c$ (experimental data shown as a blue solid curve) is indicated by a green dashed line. As indicated by both the residual plot and the line cut, at high temperatures the fits are nearly indistinguishable from the experimental data. At low temperatures however there is an increased discrepancy due to the presence of a second resonance mode that appears in the GdIG sample. The exact origin of this additional resonance mode is unclear, however it may result form spatial inhomogeneities of the sample [40]. Regardless, even at low temperatures the fits are still sufficient to determine the coupling strength and damping parameters, which are plotted in Fig. 5.7.
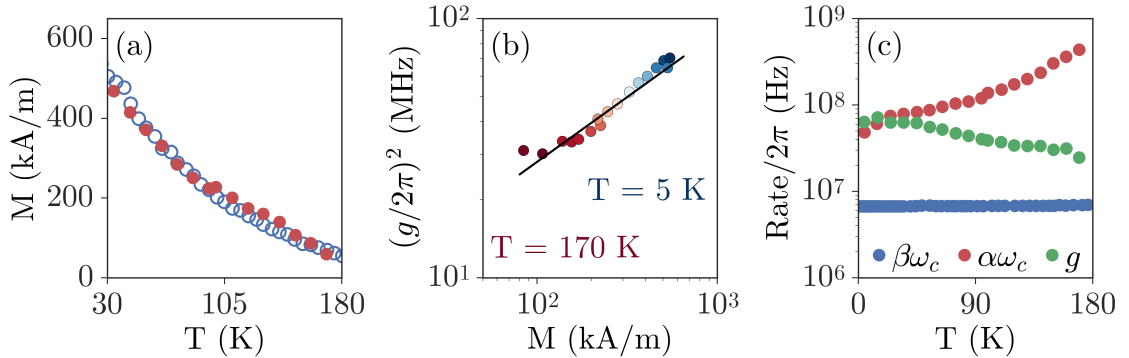
Figure 5.7: (a) Comparison of effective magnetization extracted from FMR dispersion (red solid circles) and net magnetization measured by SQUID magnetometry (blue hollow circles). (b) Coupling rate as a function of the net magnetization. Symbols indicate data extracted from fits to Eq. (3.91) and the black solid line is a fit to $g = \sqrt{M}g_0$. (c) The spin decay rate (Gilbert damping), α (red), cavity decay rate, β (blue), and coupling strength, g (green), as a function of temperature. At low temperatures the increasing coupling rate and decreasing spin decay rate allow our system to enter the strongly coupled regime. The data used in this figure was originally published in Ref. [40].

In our fitting we use the Kittel dispersion, $\omega_r = \gamma\sqrt{H(H + M_0)}$, to describe the FMR, treating M_0 (which will be temperature dependent) as a fitting parameter with $\gamma = 28 \times 2\pi\,\mu_0$ GHz/T fixed. Therefore we can compare the effective magnetization, M_0, to the net magnetization measured by our SQUID measurements. These results are plotted in Fig. 5.7 (a) where blue hollow circles are the SQUID measurements (the same as in Fig. 5.5) and red solid circles are the fitting results. The excellent agreement indicates that the dominant anisotropy contribution in our GdIG thin film is due to shape anisotropy, and we are therefore justified in taking $M_0 = M$. Any slight deviations which we observe between M and M_0 may be attributed to the fact that γ may increase slightly with decreasing temperature [40, 226]. The temperature dependent coupling strength, g^2, determined from our fits, is plotted in Fig. 5.7 (b) as a function of M. From 5 K $< T <$ 170 K we observe a change in magnetization of approximately one order of magnitude. The straight black line confirms the expected scaling $g = g_0\sqrt{M}$, with $g = 0$ at $M = 0$. Thus we have succeeded in verifying the $\sqrt{N_s}$ scaling of the coupling strength predicted by our quantum model [34, 40]. Moreover we have demonstrated the ability to tune the coupling strength in-situ using the temperature dependence in a compensating ferrimagnet. From the slope of the linear fit we can determine the single spin-photon coupling rate as $g_0 = 0.072$ Hz, which agrees reasonably well with the value of 0.043 Hz observed in paramagnetic systems [46].

Although we have clear evidence supporting the temperature dependence of the coupling strength, in order to verify that our system indeed transitions from strong to weak coupling we must also examine the spin and photon loss rates. This information is presented in Fig. 5.7 (c). The cavity and spin damping are plotted as blue and red circles respectively, with the coupling strength shown in green. As anticipated the cavity damping is essentially frequency independent, although slight temperature variations may be observed due to contraction of the cavity at low temperatures, which requires mechanical adjustment to restore the original resonance frequency. On the other hand the damping of the spin system increases drastically with temperature, in agreement with previous reports [226]. This increase in the spin damping is one of the key reasons why strong coupling in GdIG cannot be observed at high temperatures.[7] Using these fit results we find that $C > 1$ for $T < 90$ K. We have thus confirmed that temperature induced strong to weak transitions are possible, further

---

[7]It is also for this reason that strong coupling in other commonly used ferromagnetic materials, such as permalloy, is difficult to achieve.

confirming the physical picture developed by our phase correlation model. While any method which achieves in-situ coupling strength control is physically interesting, the fact that ultra low temperatures must be used to reach strong coupling in GdIG does not easily translate into either device applications or simple adaptation for the study of basic CMP properties. On the other hand, further consideration of our electrodynamic phase correlation model reveals another possible means to tune the coupling strength.

5.4 ANGULAR CONTROL OF COUPLING STRENGTH

To develop our phase correlation model in Sec. 3.3 we explicitly incorporated the magnetization dynamics driven by a microwave magnetic field using the LLG equation. The result of the LLG equation is that the magnetization dynamics are determined by the linear response function χ^+, so that for the elliptically polarized modes which are relevant to our system, $m^+ = \chi^+ h^+$. The detailed nature of the coupling strength, such as its temperature dependence, relationship to the filling factor and spin density and its geometric details, are therefore determined by χ^+. In this sense the coupling strength generally depends on some set of parameters, $\mathbf{p}$, which allows us to write $g = g(\mathbf{p})$, and we typically treat the problem phenomenologically by measuring g for our given experimental conditions. However, as we have seen in the case of the spin density relation, $g \propto \sqrt{N_s}$, it is possible to make certain dependencies explicit. It is fruitful to combine this reasoning with our understanding of magnetization dynamics. When undergoing magnetization precession at low microwave powers, the magnetization will precess about the external magnetic field direction, which acts as a bias. Since this precession is due to a magnetic torque of the form $\mathbf{M} \times \mathbf{h}$, only the component of the microwave magnetic field which is perpendicular to the total magnetization M, and hence perpendicular to the static field H, will drive the precession. Using the angle θ between the rf microwave field h^+ and the static bias field H, defined in the inset of Fig. 5.8 (a), the relevant component of the microwave field is therefore $h^+|\sin(\theta)|$ and we may write $m^+ = \chi^+ h^+|\sin(\theta)|$. Thus we can include this geometric dependence explicitly in the coupling strength so that

$$g = g_0|\sin(\theta)|, \tag{5.2}$$

where g_0 is the coupling strength at $\theta = 90°$. We can therefore make the replacement $g \to g_0 |\sin(\theta)|$ in the hybridized dispersion or transmission formulas to explicitly reveal the geometric dependence of the hybridized modes. Physically Eq. (5.2) tells us that when the microwave and static magnetic fields are aligned we cannot effectively drive the magnetization dynamics and therefore the coupling in our system is minimized. On the other hand, when the microwave and static magnetic fields are perpendicular, we drive magnetization dynamics most efficiently and therefore the coupling in our system is at a maximum. The angle θ therefore describes how effectively we are able to drive the magnetization dynamics, or how efficiently we are able to couple the spin and photon systems. Experimentally it is possible to control θ and therefore we can realize a new method of in-situ coupling strength control.

To verify this behaviour experimentally we used the UMS1 experimental setup. The cavity we used in this experiment had a diameter of 36 mm, a height of 10 mm and was designed to have a TM_{011} mode at $\omega_c/2\pi = 6.34$ GHz. The unloaded damping of this mode was $\beta = 3 \times 10^{-4}$ (Q = 1670). The simple, circular mode profile of the TM_{011} mode, as shown in the inset of Fig. 5.8 (a), is an important feature which allows us to systematically control θ. A YIG(2.6 μm)/Pt(10 nm) bilayer on a GGG substrate was placed on the lid of the cavity, near the outer edge. This sample had lateral dimensions of 10 mm $\times$ 7 mm, and a measured saturation magnetization of $\mu_0 M_0 = 160$ mT, a Gilbert damping of $\alpha = 3.6 \times 10^{-4}$ and a gyromagnetic ratio of $\gamma = 27.6 \times 2\pi \, \mu_0 \text{GHz/T}$. The Pt was deposited in strips of lateral dimension 10 mm $\times$ 1 mm on top of the YIG. As we have done in previous experiments, the static magnetic field was applied in the sample plane so that the FMR follows the Kittel equation $\omega_r = \gamma \sqrt{H (H + M_0)}$. With the sample loaded the cavity mode was redshifted by 3 % to 6.155 GHz and the damping increased to $\beta = 1.8 \times 10^{-3}$ (Q = 280).

The angle θ defines the orientation between the static magnetic field and the local microwave field at the sample location. Due to the special profile of the TM_{011} mode we can easily control θ in our experimental setup by rotating the upper lid of the cavity, hence rotating the YIG/Pt bilayer inside of the static magnetic field. This rotation causes a change in the cavity mode frequency and damping of less than 1 %, much less than the 3 % shift due to damping, and therefore this shift is not considered in the transmission measurements. Fig. 5.8 shows the change in cooperativity as θ is tuned between 0 and 360°. The experimental data, determined by extracting the coupling strength from a fit of the transmission data to Eq. (3.89), is shown in blue circles with a fit according to Eq. (5.2) shown as a black solid line. As we anticipate,
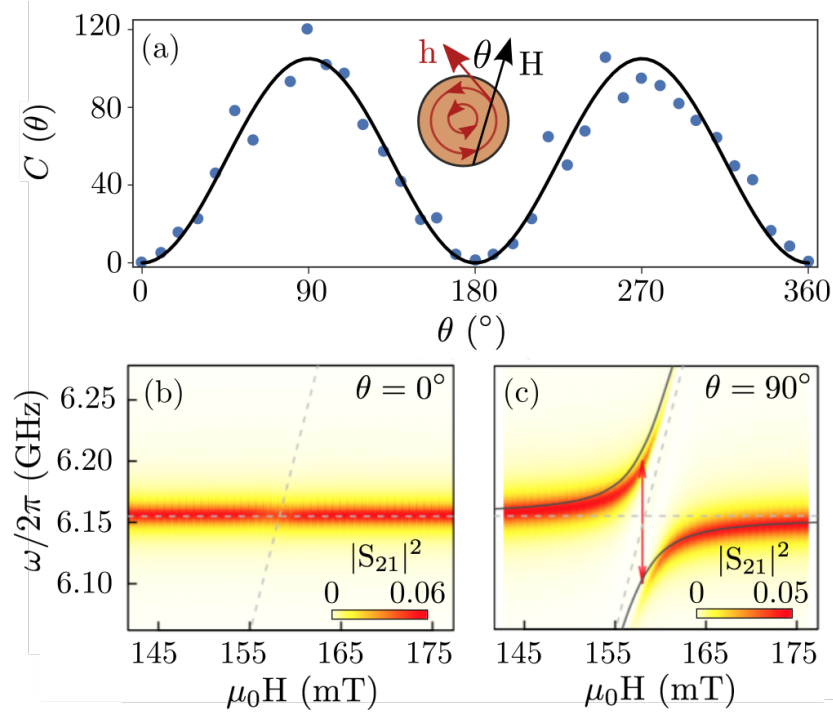
Figure 5.8: Control of the coupling strength by tuning the bias field angle. (a) The inset shows a top view of the cylindrical cavity. The circular profile of the TM_{011} magnetic field h is shown in red with the static field H indicated by a black arrow. θ indicates the local angle between h and H at the sample location. The experimental angular dependent cooperativity is shown as symbols while the black curve is fitted according to Eq. (5.2). (b) Transmission spectra at $\theta = 0°$ and (c) $\theta = 90°$. At $\theta = 0°$ the coupling strength is minimized, we do not efficiently drive magnetization precession, and no coupling is observed. At $\theta = 90°$ the coupling strength is maximized and a clear anticrossing can be seen. Horizontal and vertical dashed lines indicate the uncoupled cavity and FMR dispersions respectively while the solid curves in (d) are a fit according to Eq. (3.89). A modified version of this figure was originally published in Ref. [50].

at $\theta = 0°$ the cooperativity drops nearly to 0, resulting in a weakly coupled system, while the cooperativity is maximized at $\theta = 90°$, resulting in strong spin-photon coupling. This behaviour is confirmed by the transmission measurements shown in Fig. 5.8 (b) and (c). In panel (b), at $\theta = 0°$, the microwaves do not couple strongly to the spin system and therefore a microwave transmission measurement only detects the cavity mode. On the other hand in panel (c), at $\theta = 90°$, a large anticrossing indicates the presence of strong spin-photon hybridization. This experimental behaviour agrees well with the black curve which is calculated according to Eq. (3.89) and demonstrates our ability to realize both strongly and weakly coupled spin-photon hybridization in
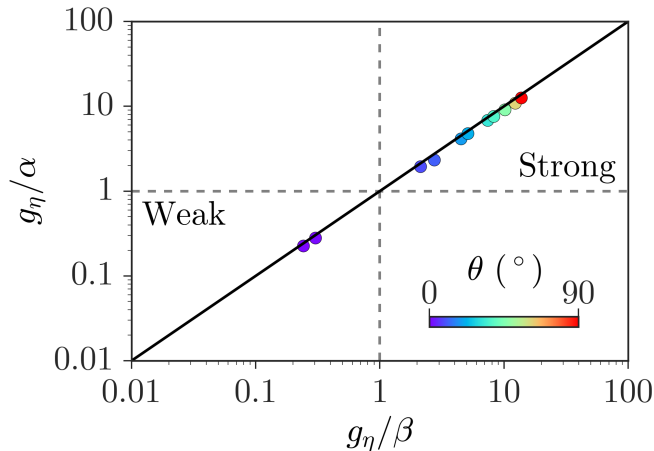
Figure 5.9: The distribution of coupling strengths observed when θ is tuned. Using this method we can systematically tune from weak to strong coupling. For fixed α and β the dissipation normalized coupling strengths which can be achieved in this method will always lie along a line of constant slope, as indicated by the black line. Examples of the coupling strengths we have achieved are shown by circles. A modified version of this figure was originally published in Ref. [179].

an easily adjustable experimental setup [50, 179].

The data which confirms our ability to systematically tune the coupling strength (and hence the cooperativity) over several orders of magnitude is shown in Fig. 5.9. Here we have plotted the two normalized coupling strengths which define the cooperativity, g_η/α and g_η/β. As we tune the angle from 0° to 90° we move along a diagonal line in the $g_\eta/\alpha - g_\eta/\beta$ parameter space, indicated by the solid line. The circles indicate experimental measurements with the colour indicating the angle at which they were measured. This figure explicitly demonstrates our observation of a continuous weak to strong transition. Thus by tuning the torque which drives the magnetization precession we are able to systematically tune the coupling strength. This method provides a useful experimental tool for the development of cavity spintronics. In the next section we demonstrate how such coupling strength control can be combined with our electrical detection technique to realize non-local spin current control over macroscopic distances.

5.5 NON-LOCAL MANIPULATION OF SPIN CURRENT

Spin current generation and manipulation is the kernel of spintronics. As we have discussed in detail, spin pumping is a powerful mechanism for the generation of spin current, and through our electrical detection experiments we have already demonstrated that spin-photon hybridization will influence the spin current generated in this fashion [48, 49]. Throughout spintronics there are also a variety of existing techniques which allow spin current manipulation. For example, Datta and Das [227] proposed the spin field-effect transistor, in which spin current is manipulated by a gate voltage via a local spin-orbit interaction in a semiconductor channel [228]. Alternatively, the exchange interaction is also commonly used to manipulate spin current, for example, spin current may drive magnetization dynamics through spin transfer torque [129, 229, 230]. However since spin-orbit and exchange interactions have characteristic length scales of $\sim$ nm, the control offered by these interactions is inherently short ranged. Actually, since spin current injection is a diffusive process,[8] devices which utilize spin-orbit or exchange interaction for spin current control are limited by the $\sim$ μm spin diffusion length,[9] which is determined by the rate at which the angular momentum carried by the spin current can be dissipated, for example by transferring to the lattice. While this length scale is an improvement over the fundamental interaction length, realization of a long distance ($\gg \mu$m) spin current manipulation would be beneficial for spintronic applications. In the final section of this chapter we turn our attention to systematic long-range spin current control, which we realize by combining our local electrical detection technique with the angular control of spin-photon coupling [50].

As discussed in Sec. 3.3, the spin current is proportional to $|m|^2$. Therefore the hybridized spin current can be determined by solving for m in Eq. (3.88). In doing so it is convenient to define the detuning parameters,

$$\Delta_c = \frac{\omega - \omega_c}{\beta \omega_c}, \tag{5.3}$$

$$\Delta_r = \frac{\omega - \omega_r}{\alpha \omega_c}, \tag{5.4}$$

and the spin-photon cooperativity $C_1 = g_1^2/\alpha\beta\omega_c^2$. Here the subscript 1 is a sample label, in anticipation of the fact that we will soon consider a system with multiple

---

[8]Which is allowed because spin current, unlike charge current, need not be conserved.

[9]This is another advantage of YIG. Since it has a very small damping, the corresponding spin diffusion length is large.

spin devices. In terms of the detunings, the real part of the transmission denominator in Eq. (3.90), which determines the hybridized dispersion, can be written as [50]

$$\Delta_c \Delta_r = 1 + C_1. \tag{5.5}$$

The *maximum* spin current amplitude, I_{s1}, will occur on-shell, that is when the hybridized quasiparticles satisfy Eq. (5.5), and therefore, evaluating $|m|^2$ from Eq. (3.88) and imposing the constraint of Eq. (5.5), the maximum spin current amplitude can be written as,

$$I_{s1} \propto \frac{C_1}{(\Delta_c + \Delta_r)^2}. \tag{5.6}$$

Eq. (5.6) describes how the spin current amplitude can be locally controlled by tuning the cooperativity. This of course makes sense — we already know that the spin current is influenced by hybridization and therefore if we control the coupling strength we would anticipate that the spin current is locally controlled. With our ability to systematically control the coupling strength we can therefore systematically control the spin current of the single spin system.

However, we find a more intriguing effect when we consider two identical spin systems (which therefore have the same spin resonance properties) coupled to a single cavity mode.[10] This three mode system is described by the generalized 3×3 matrix of Eq. (4.13), under the assumption that the two magnetic samples couple to the cavity mode with coupling strengths g_1 and g_2 respectively, but do not directly couple to each other. Therefore, in analogy with the case of a single spin system, we find that the real part of the dispersion produces the constraint

$$\Delta_c \Delta_r = 1 + C_1(\theta) + C_2, \tag{5.7}$$

where C_1 and C_2 are the cooperativities of the two spin ensembles respectively. We can also analogously calculate the maximum spin current of each sample, I_{s1} and I_{s2}, finding

$$I_{s1} \propto \frac{C_1(\theta)}{(\Delta_c + \Delta_r)^2}, \tag{5.8}$$

---

[10]The constraint that the spin systems be identical makes the theoretical formalism more transparent, highlighting the key physics involved. However the effect we describe in this section could be realized even with distinct spin devices.

$$I_{s2} \propto \frac{C_2}{(\Delta_c + \Delta_r)^2}.$$ (5.9)

For completeness we note that the pattern we observe for one and two spin systems extends more generally, so that if we have n identical samples the real part of the dispersion can be written as,

$$\Delta_c \Delta_r = 1 + \sum_{i=1}^{n} C_i$$ (5.10)

and the maximum spin current produced in the ith spin ensemble is [50]

$$I_{si} \propto \frac{C_i}{(\Delta_c + \Delta_r)^2}.$$ (5.11)

An intriguing effect is now observed by carefully examining Eqs. (5.7), (5.8) and (5.9). Eq. (5.7) describes a constraint on the detunings which depends on the cooperativities of both samples. Therefore, even though the spin current of each device only depends directly on the local cooperativity (the numerator of Eqs. (5.8) and (5.9)) it will be influenced by the global properties of the system (the denominator of Eqs. (5.8) and (5.9)). These global properties depend on the constraint of Eq. (5.7) and therefore if we locally tune one sample we can expect that a second sample, which is not directly tuned in any way, will also be manipulated! In this way we can attempt to experimentally realized non-local spin current manipulation.

The experimental setup to test such an idea is shown in Fig. 5.10. Panel (a) indicates the schematic idea, which is to use the cavity photon as a bridge to carry information from the first sample, denoted as YIG$_1$, to the second sample, denoted as YIG$_2$. Therefore by locally tuning YIG$_1$ we will observe an effect at a well separated YIG$_2$. In the experimental setup shown in Fig. 5.10 (b), a YIG/Pt bilayer (YIG$_1$) is placed on the lid of a microwave cavity and wired out for electrical detection. Meanwhile an identical YIG/Pt bilayer (YIG$_2$) is placed at the bottom of the cavity and is also wired out for electrical detection. As indicated in the figure, rotation of the cavity lid enables tuning of the angle θ between the local microwave and static field at the YIG$_1$ location. The position of YIG$_2$ is fixed so that the microwave and static magnetic fields are perpendicular and maximum hybridization will be observed between the cavity and YIG$_2$.

The experimental setup used in this experiment was similar to that described for
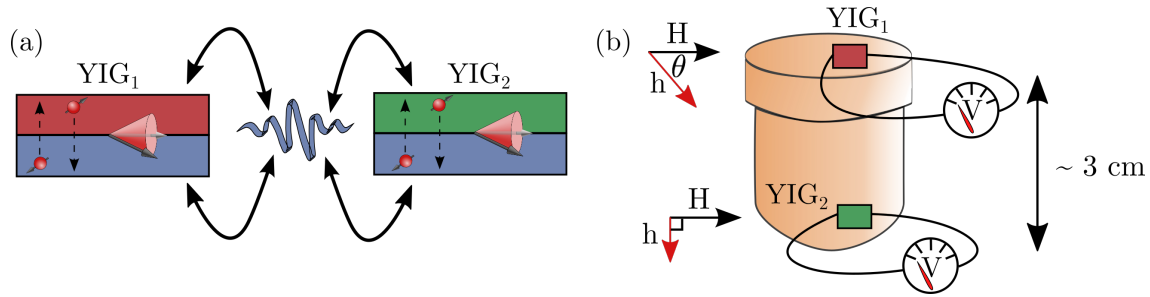
Figure 5.10: Experimental setup used to demonstrate non-local spin current manipulation. (a) The general idea is to use the cavity photon, which is coupled to both spin systems, as a bridge to carry information from YIG_1 to YIG_2. Therefore if we locally tune YIG_1, we can observe the influence at YIG_2. (b) YIG_1 is placed on the lid of the microwave cavity and can be rotated within the static magnetic field, H. YIG_2, at the bottom of the cavity, has a fixed orientation with respect to H.

the angular cooperativity measurements of Sec. 5.4. We used a cylindrical microwave cavity with a diameter of 36 mm and a height of 10 mm. This cavity had an unloaded TM_{011} mode at $\omega_c/2\pi = 6.34$ GHz with $\beta = 3 \times 10^{-4}$ ($Q = 1670$). YIG_1 was a YIG(2.6 μm)/Pt(10 nm) bilayer on a GGG substrate with lateral dimensions of 10 mm $\times$ 7 mm. The saturation magnetization was $\mu_0 M_0 = 160$ mT, the Gilbert damping was $\alpha = 3.6 \times 10^{-4}$ and the gyromagnetic ratio was $\gamma = 27.6 \times 2\pi \, \mu_0$GHz/T. The Pt was deposited in strips of lateral dimension 10 mm $\times$ 1 mm on top of the YIG. Again, the static magnetic field was applied in the sample plane. With just YIG_1 loaded on the cavity lid the cavity mode was redshifted by 3 % to 6.155 GHz and the damping increased to $\beta = 1.8 \times 10^{-3}$ ($Q = 280$). An identical YIG/Pt bilayer, YIG_2, was placed on the bottom of the cavity. With both samples loaded the cavity mode was redshifted by another 3 % to $\omega_c/2\pi = 5.960$ GHz with a damping of $\beta = 5.2 \times 10^{-2}$ ($Q = 200$). Again, tuning of the angle θ only changed the cavity mode frequency by a negligible amount, less than 1 %.

Fig. 5.11 shows the global properties of the single and two spin systems, which are determined by the constraint of Eq. (5.7). Panels (a) - (c) are the same as Fig. 5.8 and are included here again for easy comparison to panels (d) and (e), which show the transmission properties of the two spin system at (d) $\theta = 0°$ and (e) $\theta = 90°$. While a noticeable increase in the dispersion gap is observed between $\theta = 0°$ and $\theta = 90°$ in panels (d) and (e), this difference is not as striking as the case of a single YIG sample. This is because when both spin systems are in the cavity, YIG_2 is not tuned and always maximally coupled to the cavity mode. ω_{gap} observed in Fig. 5.12
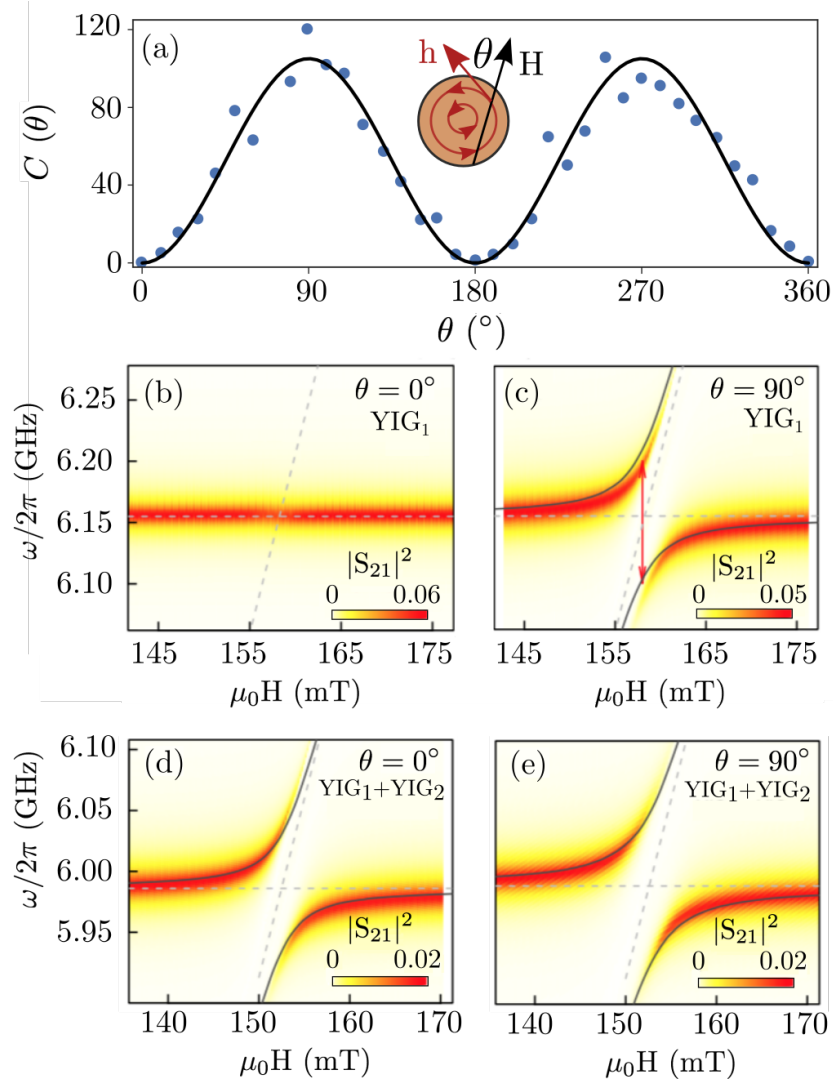
Figure 5.11: Global properties of the single and two spin system. Panels (a) - (c) are the same as Fig. 5.8 and are shown again here for easy comparison. (a) Angular dependence of the cooperativity measured with a single YIG/Pt bilayer. (b) Microwave transmission with a single YIG/Pt sample placed on the lid of the cavity measured at (b) $\theta = 0°$, where the minimum coupling is observed, and (c) $\theta = 90°$, where the maximum coupling is observed. (d) Microwave transmission with both YIG/Pt bilayers inside the cavity at $\theta = 0°$ and (e) $\theta = 90°$. In this measurement only the angle of the YIG sample at the top of the cavity is tuned, while the YIG placed at the bottom of the cavity is strongly coupled at all angles. A modified version of this figure was originally published in Ref. [50].

(d) and (e) is therefore a superposition of both YIG samples coupled to the cavity and never goes to zero, even when the coupling of YIG_1 is zero. Nevertheless, the change to the global properties of the three mode system is evident.

To demonstrate both local and non-local control of the spin current we measured the voltage generated due to spin pumping in each YIG/Pt bilayer by sweeping the magnetic field H at a fixed microwave frequency of 6 GHz and microwave output power of 100 mW. As shown in Fig. 5.12 (a), when θ is tuned from 0° to 90°, the voltage measured from YIG_1, and hence the spin current generated, is increased as the field torque on the magnetization increases. In this sense we can directly (or locally) control the spin current in YIG_1. We also note that the expected $V(H) = -V(-H)$ symmetry is observed. The simultaneous voltage output from YIG_2 is shown in Fig. 5.12. Here we observe the inverse effect. As θ is increased the amplitude of the spin current in YIG_2, which is spatially separated from YIG_1 and not directly tuned in any way, decreases. Using a spin Hall angle of 2.3×10^{-3} [191] and Eq. (2.9), we can calculate the maximum spin current amplitude at each θ using the measured voltage data. These results are shown in Fig. 5.12 (c) and (d) using open circles for YIG_1 and YIG_2 respectively. Since the external magnetic field was not rotated during the measurement the spin currents from both samples maintain the same sign [50]. Both local and non-local control of the spin current is observed. The solid curve for YIG_1 (YIG_2) is calculated according to Eq. (5.8) (Eq. (5.9)) using the constraint of Eq. (5.7), which agrees well with the trends observed experimentally [50].

The non-local spin current control which we observe originates from the influence of the global hybridization on local electrical detection measurements. To highlight how this originates based on our theoretical formalism using cavity and FMR detunings, we plot the $\Delta_c - \Delta_r$ dispersion following from Eq. (5.7) in Fig. 5.13 (a) and (b) for different values of the cooperativity $C_1(\theta)$. The arrows in each figure indicate the direction of increasing $C_1(\theta)$. Panel (a) is plotted with a colour scale that indicates the amplitude of I_{s1}, calculated from Eq. (5.8), with the colour scale of panel (b) indicating the amplitude of I_{s2} according to Eq. (5.9). The two hybridized modes are only excited when the cavity and FMR detunings are either both positive or both negative, reflecting the fact that both cooperativities are positive. Based on Fig. 5.13 (a) and (b) we can summarize the spin current features of this three mode coupled system as follows: (i) The hybridized modes of the coupled system rely on the sum of cooperativities of all magnetic samples with the coupling strength increasing when more magnetic samples are added; (ii) The spin current pumped by each magnetic sample depends on both the global properties of the normal mode detunings and the local cooperativity with the cavity mode; and (iii) The amplitude of I_{s1} (spin current in the directly tuned sample) increases as C_1 is increased, while I_{s2} (spin current of
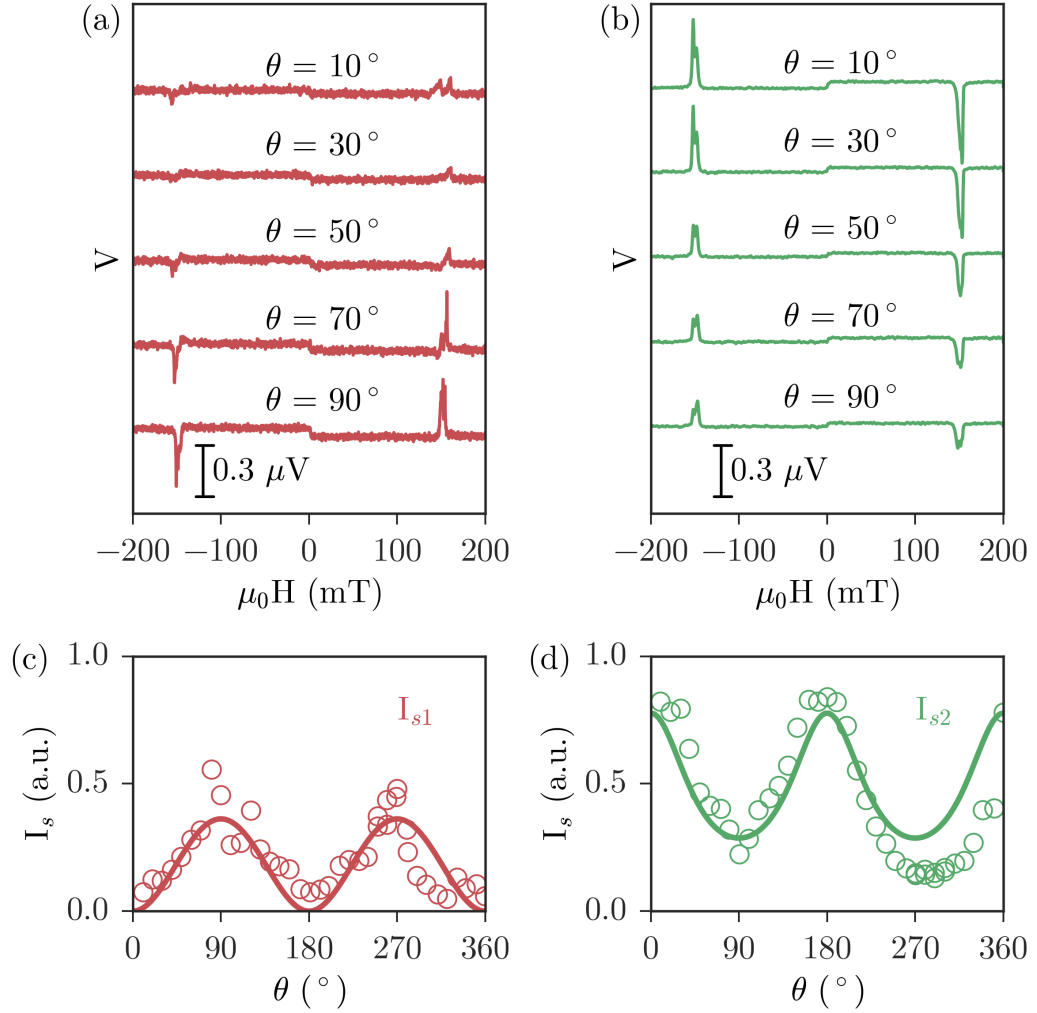
Figure 5.12: (a) The voltage generated in YIG_1 is locally tuned by controlling the cooperativity, while (b) the YIG_2 voltage signal is simultaneously controlled nonlocally, with no direct manipulation. Converting the voltage signal into the spin current amplitude the angular dependence of (c) I_{s1} and (d) I_{s2} is observed. A modified version of this figure was originally published in Ref. [50].

the distant sample) has the opposite behaviour, decreasing as C_1 is increased. In general, since the spin current in the directly controlled sample is proportional to its cooperativity, while the spin current in the non local sample is inversely proportional, the two spin currents will always change in opposite directions. However if, for example, three devices were used, it may be possible to locally tune two samples in such a way that the spin current in a third remains unchanged.

In our experiment we measured the spin current by sweeping the magnetic field
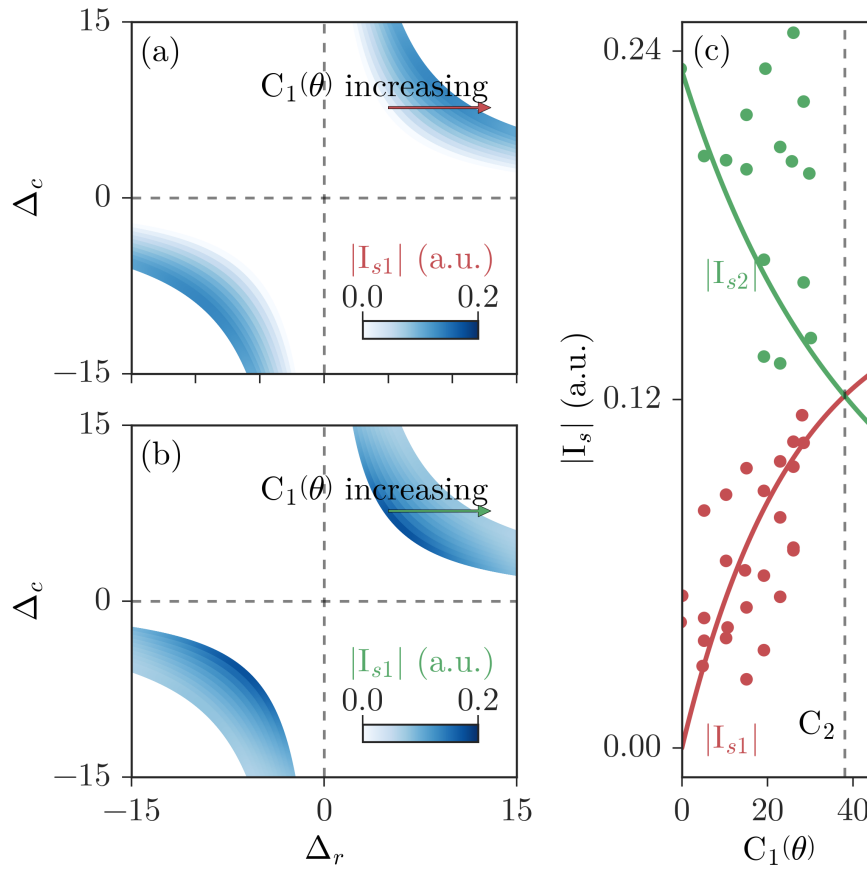
Figure 5.13: The cavity-FMR detuning dispersion calculated using Eq. (5.7) for (a) YIG_1 and (b) YIG_2. The colour scale indicates the spin current amplitudes, I_{s1} and I_{s2}, which are calculated using Eq. (5.8) and Eq. (5.9) respectively for different cooperativities $C_1(\theta)$. The change in $C_1(\theta)$ is indicated by the red and green arrows for I_{s1} and I_{s2} respectively. (c) Along the arrows, at a fixed cavity frequency detuning of $\Delta_c = 7.7$, the amplitudes of both spin currents are plotted as a function of $C_1(\theta)$. Symbols indicate experimental data and the solid curves are calculations using Eqs. (5.8) and (5.9). The vertical dashed line indicates the fixed cooperativity of YIG_2 in our experiment. A modified version of this figure was originally published in Ref. [50].

at a fixed microwave frequency, corresponding to a fixed cavity mode frequency detuning of $\Delta_c = 7.7$. This position is indicated by the arrows in Fig. 5.13 (a) and (b). Along these arrows the amplitudes of both spin currents are plotted as a function of C_1 in Fig. 5.13 (c). The solid curves are I_{s1} and I_{s2}, calculated using Eqs. (5.8) and (5.9) respectively. The data plotted in this manner is effectively "third order" compared to the raw data of Fig. 5.12 (a) and (b). By this we mean that we

have first calculated the spin currents from the raw voltage measurement, and then calculated the cooperativity for each field orientation. As a result several sources of additional uncertainty have been introduced. For example, the spin Hall angle is notorious for its large uncertainties [231], and in our case has an uncertainty of $\sim 50\%$ [191]. Additionally, the determination of the coupling strength, which is needed for the cooperativity calculation, is difficult for angles where the coupling strength, and hence amplitude, is small. For this reason there are large uncertainties present in Fig. 5.13 (c), which make a quantitative comparison between theory and experiment using this method difficult. Nevertheless, the qualitative agreement between our model and the experimental data indicates that the non-local manipulation of spin current in YIG_2, which we detect locally through spin pumping, is due to the local cooperativity control of YIG_1. This point may perhaps be better emphasized by the angular control demonstrated in Fig. 5.13 (d). This experiment therefore demonstrates one way in which cavity spintronics, and strong spin-photon coupling, allows us to reach beyond the limits of conventional spintronics by utilizing the emergent properties of the cavity-magnon-polariton.

5.6 CONCLUSION

In this chapter we have presented a variety of control methods which may be used to manipulate strongly coupled spin-photon systems. By controlling cavity damping we realized continuous tuning between the strong and weak coupling regimes, illustrating that at high Q hybridization will significantly modify the FMR dispersion. This highlights the importance of understanding the strong spin-photon coupling behaviour even in conventional spintronic and magnetic characterization techniques, such as traditional cavity based FMR measurements. We also used our tuneable cavity quality to examine the effect of non-resonant FMR line width enhancement, finding significant effects due to hybridization which again push us beyond conventional spintronics. In order to directly tune the coupling strength we used both the temperature dependent magnetization of a compensating ferrimagnet and field torque control. Both methods allowed us to again observe the strong to weak transition, while the former technique verified the expected $g \propto \sqrt{N_s}$ scaling of the coupling strength and the latter technique enabled a local control mechanism which we exploited to demonstrate non local spin current control. In the next chapter we turn to a more detailed discussion of the hybridized eigenspectrum, which plays an important role in the exact definition

of "strong" coupling and can be exploited to observe switching phenomena in the hybridized modes.

5.7 ACKNOWLEDGEMENTS

EXCEPTIONAL POINTS IN THE
SPIN-PHOTON SYSTEM

6.1 INTRODUCTION

We already know that damping plays an important role in spin-photon hybridization, as evidenced by the damping evolution which provides a striking signature of strong coupling. Additionally we found that, at least in principle, damping will influence the size of the Rabi gap (see Eq. (3.11)), although in the strongly coupled regime these effects are negligible and the gap becomes damping independent. At the same time we often take the presence of a gap in the dispersion and the fact that the cooperativity exceeds one to go hand in hand, taking both as simultaneous indications of strong coupling. However if the gap depends on the damping this should not generally be true and therefore the condition for the onset of $\omega_{\mathrm{gap}} \neq 0$ must actually be more complex. This line of thinking leads to two questions: (i) What is the correct definition of strong coupling? and (ii) How can we observe the damping influence on the Rabi gap? It turns out that the answer to these two questions is related and leads us to a much deeper understanding of the spin-photon hybridization.

The key physical idea underlying these questions is that of the exceptional point (EP), discussed in detail in Sec. 6.2. In general the presence of damping means that we have an open system which, thus far, we have successfully described using the complex matrix of Eq. (3.88). In this chapter we will examine the impact of interpreting this complex matrix as a non-Hermitian Hamiltonian which governs the dynamics of the CMP. We will see that such a viewpoint naturally leads to a variety of intriguing phenomena which we will search for in our spin-photon system. For example, in such systems an EP, where the eigenvalues and eigenvectors coalesce, may

be present in the eigenspectrum. The location of the EP in the coupling strength and dissipation parameter space defines the transition between a gapped and ungapped dispersion meaning that the location of the EP, and not the condition $C > 1$, should define the strong to weak transition. This understanding directly answers the first question we have asked above, and indirectly answers the second — we can observe the influence of damping by leaving the strong coupling regime and approaching the EP. However by gaining this understanding we actually gain additional insight into the spin-photon hybridization.

Using the concept of the EP we demonstrate in Sec. 6.3 a geometric mode switching effect whereby we can encircle the EP, returning to the same location in the $g - H$ parameter space, and find that the eigenmodes have switched. This observation highlights the role of the EP in spin-photon hybridization and indicates that our system provides an interesting playground for the exploration of non-Hermitian physics, which includes such intriguing phenomena as parity-time symmetry breaking [232–235] and has relevance to, for example, controllable coherence in lasing systems [236] and the breakdown of adiabatic evolution in waveguides [237, 238]. In this manner by answering a few simple questions using the idea of the EP we actually open the door to a wide range of interesting physics which we hope can be explored further to gain additional physical insight and develop novel cavity spintronic technologies.

6.2 THE PHYSICS OF EXCEPTIONAL POINTS

Formally an exceptional point (EP) is a branch point of the eigenspectrum — a point about which the eigenspectrum is discontinuous — first investigated in a mathematical context by Kato [239]. Such a branch point defines the topological features of the eigenspectrum [234] and this very general mathematical definition leads to the ubiquitous presence of EPs across a variety of physical systems [240–248]. In our case, by examining the square root that appears in the hybridized dispersion, it is actually easy to understand mathematically how such a point arises. If we allow the spin and photon parameters to vary it is possible that the square root argument, which until now we have assumed is positive, actually becomes negative. Therefore for some set of parameters this argument must become zero. This special location in the coupling and dissipation parameter space marks the exceptional point. The physical consequence of this point is therefore also evident. If the root in the hybridized dispersion is real, there is a gap in the eigenspectrum as we observe in strong coupling, while if

the root is imaginary there is no gap in the dispersion (which is determined from the real part of the hybridized mode) and instead the coupling influence will be observed in the damping evolution. If the root is exactly zero, there will be no gap in either the dispersion or the line width evolution at the crossing point and the eigenvalues will coalesce at this point. Therefore physically the EP marks the transition between strong coupling, where a gap in the dispersion can be observed, and weak coupling, where no gap can be seen. Interestingly the EP itself need not be reached to observe a drastic influence on the hybridization [234]. This fact is important for the spin-photon system, since, as we will see below, the exact location of the EP occurs at one special location in the coupling strength and dissipation rate parameter space which requires a detailed balance between g, α and β. Experimentally reaching this point exactly would be extremely difficult, however it is possible to move around the EP location and observe the influence on the spin-photon hybridization.

The fact that the EP relies on the presence of dissipation is intimately connected to the non-Hermitian nature of our system. Actually most systems with EPs fall into this category — that is EPs are most commonly observed in open systems with a real coupling strength where the presence of dissipation is accounted for by an effective non-Hermitian Hamiltonian [234]. However EPs also have other physical origins and have been used in a variety of interesting ways. For example, in optomechanical systems with an effective negative mass and real coupling strength EPs signal the onset of synchronization [248]. On the other hand EPs resulting from purely dissipative interactions (purely imaginary coupling) have been used to realize non-reciprocal energy transfer between hybridized modes [247], and EPs due to complex coupling strengths have been exploited to realize enhanced sensitivity of microcavities [249].

To examine the EP in our hybridized spin-photon system, we note that by defining the matrix H,

$$H = \begin{pmatrix} \tilde{\omega}_c & g \\ g & \tilde{\omega}_r \end{pmatrix},$$ (6.1)

the general coupled equations of motion in Eq. (3.88) can be written as,

$$H \left| X \right\rangle = -i \frac{d \left| X \right\rangle}{dt}$$ (6.2)

where $\left\langle X \right| = (h, m)$ and, as we have done previously, we assume a harmonic time dependence for h and m. Therefore we can immediately see that the effective Hamiltonian H which we have defined is non-Hermitian due to the cavity and spin dissi-

pation rates, which appear in $\tilde{\omega}_c$ and $\tilde{\omega}_r$ respectively, and an EP should exist. The eigenvalues of H are given by,

$$\tilde{\omega}_\pm = \frac{1}{2}\left[\tilde{\omega}_c + \tilde{\omega}_r \pm \sqrt{(\tilde{\omega}_c - \tilde{\omega}_r)^2 + 4g^2}\right] \tag{6.3}$$

and therefore by writing the hybridized modes in the form $\tilde{\omega}_\pm = \omega_\pm + i\Delta\omega_\pm$ we have,

$$(\tilde{\omega}_+ - \tilde{\omega}_-)^2 = (\tilde{\omega}_c - \tilde{\omega}_r)^2 + 4g^2. \tag{6.4}$$

At the crossing point, where $\omega_r = \omega_c$, the real and imaginary parts of Eq. (6.3) yield two conditions which must be satisfied by the hybridized eigenmodes,

$$(\omega_+ - \omega_-)(\Delta\omega_+ - \Delta\omega_-) = 0, \tag{6.5}$$
$$(\omega_+ - \omega_-)^2 = (\Delta\omega_+ - \Delta\omega_-)^2 - \omega_c^2(\beta - \alpha)^2 + 4g^2. \tag{6.6}$$

Eq. (6.6) will be satisfied if:

(i) $\Delta\omega_+ = \Delta\omega_-$,

(ii) $\omega_+ = \omega_-$,

or

(iii) $\omega_+ = \omega_-$ and $\Delta\omega_+ = \Delta\omega_-$.

These conditions correspond to the following physical behaviour:

(i) resonance anticrossing, line width crossing,

(ii) resonance crossing, line width anticrossing,

(iii) resonance crossing, line width crossing.

Which of these conditions is satisfied depends on the coupling strength according to Eq. (6.6). If $g > \omega_c|\beta - \alpha|/2$ then $\omega_+ > \omega_-$ at the crossing point and condition (i) must be satisfied, which is simply the traditional observation of strong spin-photon coupling. On the other hand, if $g < \omega_c|\beta - \alpha|/2$, since $(\omega_+ - \omega_-)^2 \geq 0$ and $(\Delta\omega_+ - \Delta\omega_-)^2 \geq 0$, we must have $\omega_+ = \omega_-$ and $\Delta\omega_+ \neq \Delta\omega_-$ at the crossing point. The transition between condition (i) and (ii) occurs when $g = g_{EP} = \omega_c|\beta - \alpha|/2$.

At this point both the resonance frequency and line width will merge, and therefore the hybridized dispersion will completely coalesce. This special value of the coupling strength defines the exceptional point, marking the transition between an anticrossing and a crossing with $g \neq 0$. The physical behaviour of the coupled system in different coupling regimes is summarized in Table 6.1.

The coalescence of eigenvalues at the EP also occurs in a similar manner near diabolic points which are associated with Berry's phase [250, 251]. However the EP is unique in that it not only signals the coalescence of eigenvalues, but also the merging of the eigenvectors. Using the eigenvectors derived in Eq. (A.10), we see that when $g = \omega_c |\beta - \alpha|/2$ and $\omega_c = \omega_r$ the normalized eigenvectors are identical and given by

$$ X_{\pm} = \frac{1}{\sqrt{2}} \begin{pmatrix} 1 \\ i \, \text{sign}\,(\alpha - \beta) \end{pmatrix}. \tag{6.7} $$

This merging of eigenvectors is the defining property of the EP and is an interesting consequence of the non-Hermiticity of our Hamiltonian. While Hermitian systems may have an eigenvalue degeneracy, their eigenvectors are generally orthogonal,[1] however there is no such constraint for a non-Hermitian system.

Since the location of the EP depends on a balance between dissipation and coupling rates, we could hope to observe the influence of an exceptional point by controlling these parameters. This provides an interesting venue to apply the cavity damping and coupling strength control mechanisms that we have developed and pre-

Table 6.1: Behaviour of the hybridized dispersion at the crossing point, $\omega_r = \omega_c$, for different coupling regimes.

Dispersion Constraint	Condition	Physical Description
$\Delta\omega_+ = \Delta\omega_-$	$g > \frac{\omega_c|\beta - \alpha|}{2}$	resonance anticrossing, line width crossing
$\omega_+ = \omega_-$	$g < \frac{\omega_c|\beta - \alpha|}{2}$	resonance crossing, line width anticrossing
$\omega_+ = \omega_-$ and $\Delta\omega_+ = \Delta\omega_-$	$g = g_{\text{EP}} = \frac{\omega_c|\beta - \alpha|}{2}$	resonance crossing, line width crossing

---

[1]If a Hermitian system is non-compact the eigenvectors need not be orthogonal. This can be realized for infinite dimensional Hilbert spaces, leading to EPs in certain Hermitian systems as well [248].
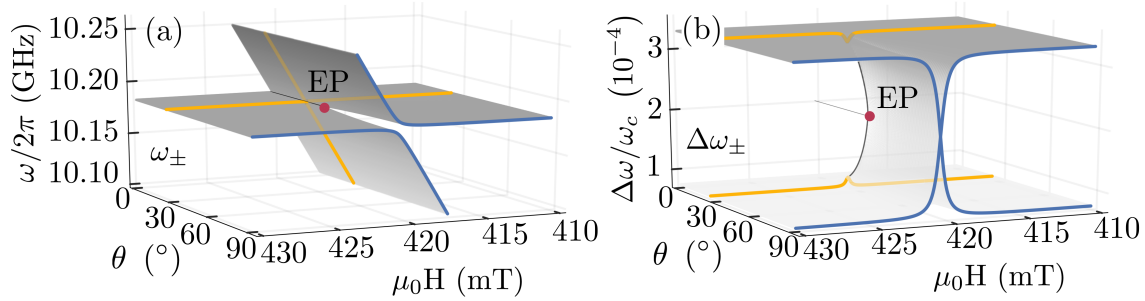
Figure 6.1: The eigenvalue structure of the hybridized spin-photon system. These schematic plots are calculated according to Eq. (3.89) with the coupling strength tuned by the angle θ. In both panels the exceptional point (EP) is denoted by a solid red circle. (a) The eigenvalue dispersion. For large coupling strengths an anticrossing is observed (blue curve). However for smaller, but non-zero, coupling a dispersion crossing may be seen (yellow curve). (b) The line width evolution. In the strong coupling regime a line width crossing is seen (blue curve), whereas when the coupling is reduced a line width gap is found (yellow curve). A modified version of this figure was originally published in Ref. [61].

sented in Ch. 5. In particular we can tune the cavity damping by adjusting the external feedline coupling, and also conveniently control the coupling strength by tuning the angle between the microwave and bias fields. In the latter case g can be systematically tuned as $g = g_0 |\sin(\theta)|$ which allows us to carefully adjust our location near the EP. Fig. 6.1 shows a schematic diagram of the changes observed in the eigenspectrum when the coupling strength is tuned in such a way, calculated according to Eq. (6.3). In panel (a) $\omega_\pm$ is shown. The global structure is that of two intersecting Riemann sheets, which meet at the EP, indicated by a red circle. At a large fixed coupling strength (large θ) an anticrossing is observed, as indicated by the blue curve, while at a small fixed coupling strength (small θ) a crossing is observed, shown by the yellow curve. The corresponding line width, $\Delta\omega_\pm$, is shown in Fig. 6.1 (b). Here the eigenspectrum takes the form of two sheets which fold into each other. In this case the EP marks the position where the sheets separate. As expected we now observe the opposite behaviour. At large coupling strengths the blue curve indicates a line width crossing, while at small coupling strengths an anticrossing is observed, as shown by the yellow curve. By exploiting our coupling strength control mechanism we can explore this spin-photon hybridization experimentally [61].

6.3 OBSERVING THE SPIN-PHOTON EXCEPTIONAL POINT

6.3.1 *Influence of Exceptional Point on Dispersion*

In order to observe the transition from dispersion crossing to anticrossing, we performed microwave transmission measurements of the coupled spin-photon system on the UMS1 experimental setup while controlling the angle θ [61]. In this experiment the cylindrical cavity, with diameter of 25 mm, was set to a height of 33 mm. At this position we observed a TM$_{011}$ mode at $\omega_c/2\pi = 10.183$ GHz. The pin length was adjusted in order to achieve a loaded cavity damping of $\beta_L = 7.6 \times 10^{-4}$ ($Q = 660$). To create a cavity-magnon-polariton we placed a 0.3 mm diameter YIG sphere on the lid of the cavity, 2 mm from the outer edge. The uncoupled FMR frequency was found to follow the relation $\omega_r = \gamma (H + H_A)$ with a gyromagnetic ratio of $\gamma = 28 \times 2\pi \ \mu_0$GHz/T, a shape anisotropy of $\mu_0 H_A = $ -57 mT and a Gilbert damping of $\alpha = 1.5 \times 10^{-4}$. Therefore we expect $g_{\mathrm{EP}} = 3.1$ MHz. By measuring ω_{gap} at $\theta = 90°$ we find that $g_0 = 6.0$ MHz and therefore we predict the location of the EP at $\theta_{\mathrm{EP}} = \arcsin (g_{\mathrm{EP}}/g_0) = 33°$. For $\theta > \theta_{\mathrm{EP}}$ we expect to see a dispersion anticrossing and line width crossing, while for $\theta < \theta_{\mathrm{EP}}$ we will instead expect a dispersion crossing and line width gap, even though our system is coupled. We note that the YIG diameter and pin configuration have been chosen so that the EP is located roughly in the middle of our accessible coupling strength parameter range. If the damping would be less, or the YIG sphere would be larger (resulting in a greater coupling strength) the location of the EP would occur at very small angles, making experimental distinction difficult.

The results of this experiment are presented in Fig. 6.2. We performed measurements at two angles, $\theta = 90° > \theta_{\mathrm{EP}}$, corresponding to the largest achievable coupling strength, and $\theta = 26° < \theta_{\mathrm{EP}}$, at a position nearby but past the EP. The resulting transmission mappings are shown in Fig. 6.2 (a) and (b) respectively. At $\theta = 90°$ a clear anticrossing is observed, while at $\theta = 26°$ only the cavity mode, with a small absorption window following the antiresonance, is observable. This behaviour becomes clearer by fitting the transmission spectra. The result of Lorentz fits to the frequency swept data are shown in Fig. 6.2 (c) - (f). In all panels symbols are the fitting results and solid curves are calculated according to Eq. (6.3). At $\theta = 90°$ we observe a dispersion anticrossing in panel (c) and a line width crossing in panel (e). Conversely, at $\theta = 26°$ an anticrossing is no longer distinguishable. Instead, in panel
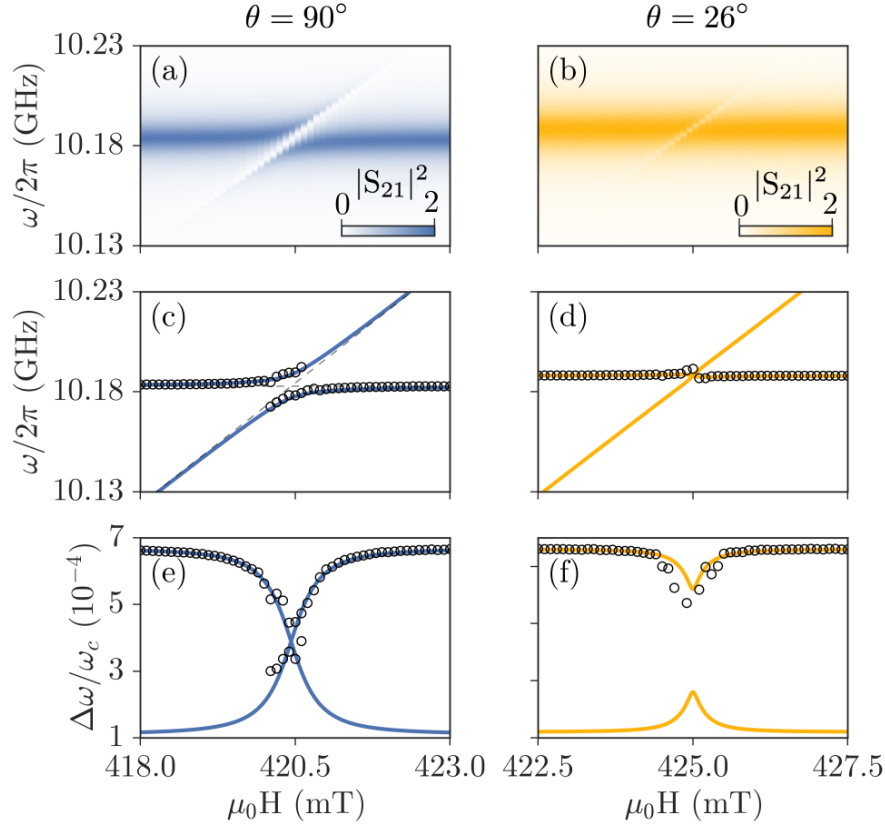
Figure 6.2: The influence of the exceptional point on the hybridized spin-photon dispersion. The microwave transmission mapping, collected in the UMS1 setup, for (a) $\theta = 90°$ ($g = 6$ MHz) and (b) $\theta = 26°$ ($g = 2.6$ MHz). At $\theta = 90°$ a clear anticrossing is observed. However after crossing the EP, at $\theta = 26°$, an anticrossing is no longer distinguishable. Dispersion fitting results for (c) $\theta = 90°$ and (d) $\theta = 26°$ respectively. The line width fits are shown in (e) for $\theta = 90°$ and (f) for $\theta = 26°$. The former shows the expected crossing while the latter shows a gap. The solid curves are calculated according to Eq. (3.89). The data shown in this figure was originally published in Ref. [219].

(d), it appears that the FMR dispersion crosses the cavity dispersion and in panel (f) we observe a line width anticrossing. Due to these features care must be taken when fitting the data for $\theta < \theta_{\mathrm{EP}}$. For most fields only one peak is observable and we can perform a straightforward fit to a Lorentz function. However near the crossing point a small peak splitting occurs due to the FMR absorption and presence of an antiresonance. Therefore in this regime we fit the dominant peak to a combination of Lorentz and dispersive line shapes. In this way we can accurately follow the dominant mode systematically from low to high fields. However the low amplitude FMR-like

mode, which is only excited near the crossing point due to the weak coupling, cannot be reliably fit, which is why this data is not seen in Fig. 6.2 (d) and (f). We note that the observed behaviour is described well by our model, including the small deviation of the hybridized mode near the crossing point at $\theta = 26°$, which can be seen in Fig. 6.2 (d).

From our experimental data we can also more closely examine the relationship between the Rabi gap and the cooperativity. In general when we have an anticrossing, so that $\Delta\omega_+ = \Delta\omega_-$, the Rabi gap is written as $\omega_{\mathrm{gap}} = \sqrt{4g^2 - \omega_c^2 (\beta - \alpha)^2}$, which follows from Eq. (6.3). When we are far into the strong coupling regime, where $g \gg \alpha, \beta$, the effect of damping is negligible and we simply write $\omega_{\mathrm{gap}} \sim 2g$. This equation provides a useful way to determine the coupling strength without any fitting requirement. However as we approach the EP, this approximation is no longer valid and the full expression for ω_{gap}, which includes the effects of damping, must be used. At the EP, where $g = \omega_c|\beta - \alpha|/2$ we can compute the cooperativity, $C_{\mathrm{EP}} = g^2/\alpha\beta\omega_c^2 \sim 1/4\,(\alpha/\beta + \beta/\alpha - 2)$ [61]. As C_{EP} is determined solely by the damping, we see that if $\alpha/\beta \gtrsim 6$ (or $\beta/\alpha \gtrsim 6$), $C_{\mathrm{EP}} > 1$, which means that a dispersion crossing could be observed even though the cooperativity may exceed one. Indeed, applying this estimation to our experiment we find that the resonance crossing observed in Fig. 6.2 (d) occurs at $C = 1.3$. This leads to an important point regarding the definition of strong coupling. Typically the following two statements are taken to be synonymous when describing strong coupling: (i) The cooperativity exceeds one; and (ii) There is an anticrossing in the dispersion. However we have found that it is possible to observe a dispersion crossing even when the cooperativity exceeds one. This suggests that, if we want to maintain the physical picture that strong coupling corresponds to an anticrossing, it would be better to use the location of the EP, rather than the cooperativity, to define the strong to weak transition. However we note that this distinction is only relevant in a narrow regime near the EP and in general having a cooperativity greater than one is still a good rule of thumb for the observation of an anticrossing.

6.3.2 *Mode Switching*

Understanding the role of the EP not only clarifies the strong to weak transition but it can also be used to observe a geometric mode switching effect. To understand this behaviour we examined the global eigenspectrum as illustrated in Fig. 6.3, observing
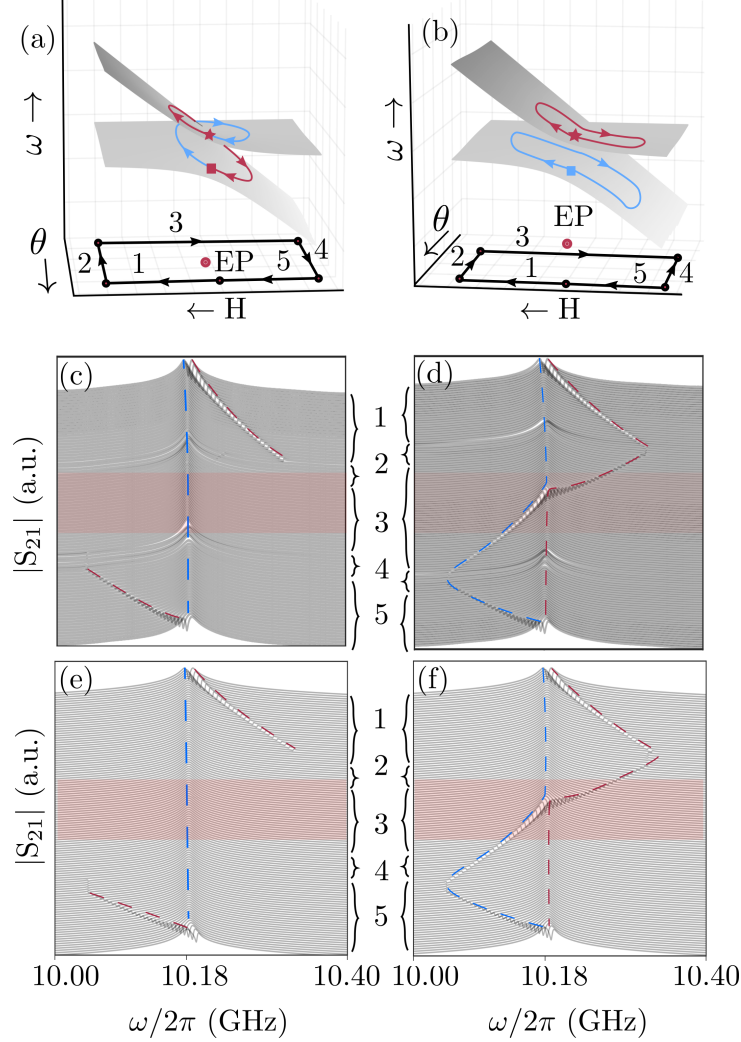
Figure 6.3: (a) Path taken to encircle the EP. A square (star) denotes the starting (ending) positions, while the red and blue curves indicates the path taken by mode 1 (ω_+) and mode 2 (ω_-) respectively. When the EP is circled the two paths are connected. (b) Without encircling the EP each mode behaves independently as shown by the red (mode 1, ω_+) and blue (mode 2, ω_-) curves. (c) Transmission spectra observed while encircling the EP. From top to bottom the system is tuned along paths $1 \to 5$. One mode stays constant at the cavity frequency while the other mode shifts to high frequencies, disappears, and reappears at low frequencies. Therefore the modes have switched positions. (d) When the EP is not encircled an anticrossing occurs during path 3 and therefore the modes maintain their relative orientations. This key difference along path 3 is highlighted with red shading. (e) The theoretical spectra calculated according to Eq. (3.89) when the EP is encircled and (d) when it is not. The blue and red dashed curves in (c) - (f) are a guide for the eyes. A modified version of this figure was originally published in Ref. [61].

what happens to the eigenmodes as we move in the $\theta - H$ plane (effectively in the $g - H$ plane). In panel (a) we consider a closed $\theta - H$ path which starts and ends at the same location and encloses the EP. The red and blue curves placed on the Riemann sheet show the dynamic behaviour of each eigenmode as we move along this path. Starting from the red square, the initially lower eigenmode follows the blue spiral upwards, transitioning to the upper sheet while the upper eigenmode follows the red path, transitioning to the lower sheet. Therefore when we return to the same starting $\theta - H$ coordinates, the initially lower eigenmode is now located at the upper sheet and vice versa, so, even though we start and end at the same location, we find that the eigenvalues have switched![2] This means that in order to continuously tune each eigenmode to its initial configuration we must take a second path around the EP. This is in contrast to the behaviour shown in Fig. 6.3 (b), where the path in the $\theta - H$ plane does not enclose the EP. In this case after one continuous loop in the $\theta - H$ plane the lower mode, shown in blue, starts and ends at the blue square while the upper mode, shown in red, starts and ends at the red star. Therefore in this case the eigenmodes each move independently on their own Riemann sheet and when we return to our original $\theta - H$ location the eigenmodes have returned to their original locations.

Such a switching effect was realized experimentally using the paths shown in Fig. 6.3 (a) and (b). To circle the EP we began at the crossing point $(\mu_0 H, \theta) = (420.5$ mT, $90°)$ and increased the magnetic field along path 1 to reach $(430$ mT, $90°)$. The coupling strength was then decreased along path 2 until we reached $(430$ mT, $15°)$, well past the EP for which we have calculated $\theta_{\text{EP}} = 33°$.[3] We then proceeded to decrease the magnetic field along path 3 until we reached $(415$ mT, $15°)$ and increased the coupling strength along path 4 until reaching $(415$ mT, $90°)$. Finally we increased the magnetic field along path 5 back to the crossing point at $(420.5$ mT, $90°)$.

The transmission spectra which we measured as we followed such a path are shown in Fig. 6.3 (c). To follow the mode evolution along these paths we artificially label the high frequency mode at the initial position (top spectra of Fig. 6.3 (c)) mode 1 and the low frequency mode at the initial position mode 2. Of course such a labelling is

---

[2]Actually, as the hybridized modes evolve they will not only interchange but also acquire a geometric phase [251]. However, as we do not directly detect the eigenvector, but rather observe the switching by following the eigenmode evolution, our experiment is not sensitive to this phenomena, which has been observed in coupled microwave cavities [234, 252]

[3]As the coupling strength decreases the amplitude of this mode also decreases drastically, and therefore in order to track the mode for the entire path we cannot decrease beyond $\theta = 15°$ in our experiment, although this would not be necessary anyway, as we only require $\theta < \theta_{\text{EP}}$.

not meaningful when looking only at a single spectra, since we will always observe two modes and the frequency of these modes is path independent and determined from Eq. (6.3). However by carefully tuning the position in the $\theta - H$ parameter space we can follow the evolution of the modes relative to their starting position and it is for this purpose, to follow the mode evolution, that we assign such labels. In the spectra of Fig. 6.3 (c) we see that as the system is tuned along path 1, mode 1 shifts out to high frequencies and the amplitude decreases sharply. Meanwhile mode 2 remains fixed near the cavity resonance frequency. As we follow paths 2, 3 and 4, mode 2 remains near the cavity frequency while the mode 1 amplitude continues to decrease and is therefore difficult to see.[4] However, as we increase the field along path 5, back towards the starting point, we find that mode 1 reappears at low frequencies while mode 2 remains in the initial position and is therefore now at a higher frequency than mode 1. Therefore once we have returned to the same location in the $\theta - H$ plane the eigenmodes have switched; the eigenmode at low (high) frequencies has continuously evolved to appear at high (low) frequencies after a complete path around the EP. In Fig. 6.3 (e) we plot the corresponding calculated transmission spectra using our general model of Eq. (3.90), treating the impedance matching parameter (amplitude) η (determined by the cavity-feedline coupling) as a fitting parameter with $\eta = 1 \times 10^{-6}$ for all spectra. Our model reproduces the expected switching behaviour very well. The slight shifts which occur in the experimental data, notably in the transition between paths 1 and 2 and paths 3 and 4, are due to the mechanical rotation of the cavity lid, which induces slight variations of the cavity mode and damping. These variations are less than 3 % and therefore do not influence the key switching behaviour which we observe.

To verify that this switching behaviour is due to encircling the EP, we performed a similar experiment where the EP was not enclosed by our path, as shown in Fig. 6.3 (b). The path taken here is nearly the same as the one taken previously, however path 3 is now at $\theta = 70°$ so that $\theta > \theta_{\text{EP}}$. The transmission spectra observed along this modified path are shown in Fig. 6.3 (d), where the spectra from top to bottom correspond to the path from $1 \rightarrow 5$. In this case mode 1 again shifts to high frequencies along path 1 with mode 2 fixed at ω_c. Along path 2 and the first part of path 3, mode 2 again remains at the cavity mode frequency while mode 1 shifts to low frequencies as the field is decreased. However, when the crossing point is encountered along path

---

[4]During the dynamic experiment the low intensity mode can be followed by carefully examining the spectra on a dB scale and comparing each spectra to its predecessor.

3, mode 2 begins to shift towards low frequencies while mode 1 remains fixed at ω_c. Along paths 4 and 5 mode 1 remains at ω_c at a higher frequency than mode 2. Therefore in this case, when the EP is not enclosed by our $\theta - H$ path, mode 2 remains at a lower frequency than mode 1 for the entire path and no switching is observed. In this case it is also possible to perform a theoretical calculation according to Eq. (3.90), with the results shown in Fig. 6.3 (f). Indeed in this case the calculation shows no mode switching and agrees well with our experimental observation. Therefore even though we do not directly tune our system to the EP position, we indeed observe a drastic influence of the EP on the behaviour of the hybridized modes. Thus the EP has more influence than simply determining whether a Rabi gap can or cannot be observed [61].

As mentioned previously EPs exist in a wide variety of physical systems and therefore several interesting applications of similar switching effects have been developed. For example, state transfer schemes have been realized in waveguide systems [238], whereby the waveguide transmission will depend on the injection direction, and switching has been used to facilitate energy transfer in optomechanical devices [247]. An interesting feature unique to the spin-photon system is the ability to easily add additional modes, thereby enabling an engineered system with multiple EPs. We have already discussed the case of additional magnon modes in the context of higher order spin waves and multiple magnetic samples. However it is also possible to couple the single FMR mode to multiple, closely spaced cavity modes. Such a system would be described in a manner analogous to the two-spin system by generalizing Eq. (3.88) [61],

$$
\begin{pmatrix} \omega - \tilde{\omega}_{c1} & 0 & g_1 \\ 0 & \omega - \tilde{\omega}_{c2} & g_2 \\ g_1 & g_2 & \omega - \tilde{\omega}_r \end{pmatrix} \begin{pmatrix} h_1 \\ h_2 \\ m \end{pmatrix} = \begin{pmatrix} \omega_{c1} h_{01} \\ \omega_{c2} h_{02} \\ 0 \end{pmatrix}.
\tag{6.8}
$$

Here g_1 and g_2 are the coupling rates of the cavity modes h_1 and h_2 to the spin system m respectively, h_{01} and h_{02} are the amplitudes of each cavity mode, which depend on the coupling between the microwave feedlines and the cavity, and there is no direct intercavity coupling between h_1 and h_2. The global eigenmode structure calculated according to Eq. (6.8) is plotted in Fig. 6.4 (a). This structure is a natural generalization of the two-mode system we have investigated in depth, with three intersecting Riemann sheets and two EPs now defining the eigenmode behaviour. The red spiralling curve indicates a possible path which would encircle both EPs. By tuning the EP locations one could imagine other trajectories which would encircle

either EP, or both, and would therefore allow various combinations of mode switching, where different combinations of the eigenmodes are interchanged. For the purpose of simply demonstrating that such a system can be realized we performed an experiment with the 25 mm diameter cylindrical microwave cavity at a height of 36.5 mm. In this configuration we observe a TM_{012} mode at $\omega_{c1}/2\pi = 12.383$ GHz ($\beta_{L1} = 4.8 \times 10^{-4}, Q_1 = 1000$) and a TE_{211} mode at $\omega_{c2} = 12.337$ GHz ($\beta_{L2} = 2.7 \times 10^{-4}, Q_2 = 1900$), as indicated in Fig. 6.4 (b). These two modes were coupled to a 1-mm diameter YIG sphere which had $\alpha = 1 \times 10^{-4}$, $\gamma = 28 \times 2\pi \, \mu_0$GHz/T and $H_A = -80$ mT. The dispersion we observe at $\theta = 61°$ is shown by open circles in Fig. 6.4 (b). We now observe three hybridized modes. From low to high fields the high frequency mode evolves from ω_{c1} to the FMR dispersion, the mid frequency mode evolves from ω_{c2} to ω_{c1} and the low frequency mode evolves from the FMR dispersion to ω_{c2}. A fit according to the dispersion of Eq. (6.8) is plotted as a solid black curve. From this fit we find a maximum YIG-ω_{c1} and YIG-ω_{c2} coupling strength of $g_{01} = 30$ MHz and $g_{02} = 16$ MHz respectively. The fact that $g_{01} \sim 2g_{02}$ reflects the different mode
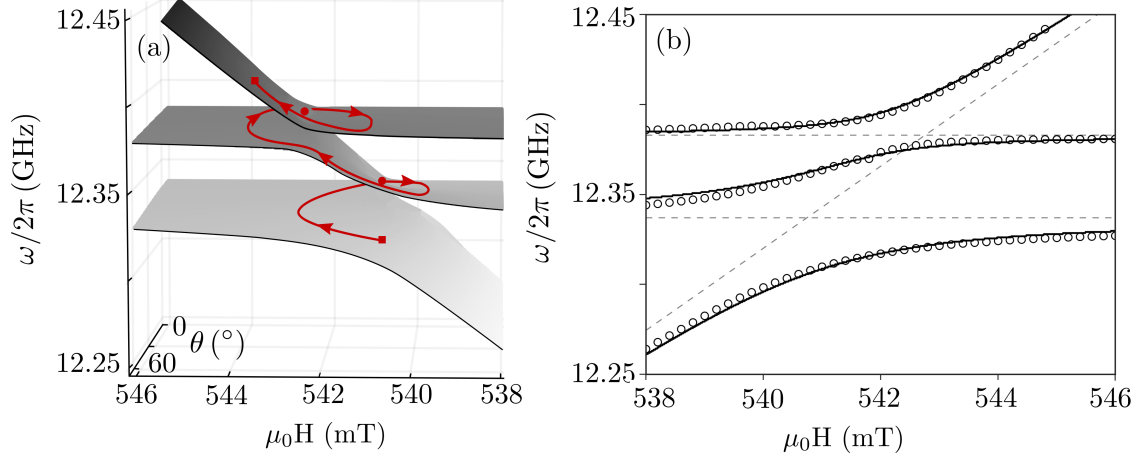
Figure 6.4: (a) The dispersion of a three-mode spin-photon system consisting of two cavity modes and one FMR mode. The grey sheets are calculated as the roots of the matrix determinant in Eq. (6.8) using our experimental parameters. The red lines, resembling an Archimedean spiral, indicate a theoretical path which would encircle both EPs. (b) Experimental dispersion of the three-mode system in the strong coupling regime where two anticrossings are observed. This dispersion was measured at $\theta = 61°$. The circles are experimental data while the black curve is calculated using Eq. (6.8). The two horizontal dashed lines indicate the uncoupled cavity modes while the diagonal dashed line is the uncoupled FMR dispersion. A modified version of this figure was originally published in Ref. [61].

profiles and means that $\theta_{\mathrm{EP}}^{\mathrm{TM}} < \theta_{\mathrm{EP}}^{\mathrm{TE}}$ for an appropriately tuned cavity damping. This suggests that by using different cavity modes it is indeed possible to tune the EP location. We hope that by providing this proof-of-principle demonstration further exploration of the EP physics in spin-photon systems and its applications may be undertaken.

6.4 CONCLUSION

In the final chapter of this dissertation we have explored the concept of the exceptional point as it relates to the coupled spin-photon system. While the motivation for this exploration was to clarify the role of dissipation on the size of the Rabi gap and carefully define strong coupling, we have found that the EP, which helps clarify these issues, also has a more dramatic influence on the spin-photon hybridization. In response to our initial motivation we found that to reconcile the idea of strong coupling with the opening of a dispersion gap we must define strong coupling as the region $g > g_{\mathrm{EP}}$. In particular we found that even when $C > 1$ we may find that $\omega_{\mathrm{gap}} = 0$. This condition is intimately tied to the dissipation in the system — in the case that there is no dissipation a dispersion gap will always exist for $g \neq 0$. Realizing that the hybridization is influenced by an EP, we were able to observe a mode switching phenomena and demonstrate the proof-of-principle concept of engineered multi EP spectra in the hybridized spin-photon system. We hope that this realization could be explored further, both to gain physical insight and to develop new cavity spintronic technologies. In this context we note that very recently the spin-photon EP has indeed been utilized to realize coherent perfect absorption, whereby the coupled spin-photon system absorbs all incident energy [62].

6.5 ACKNOWLEDGEMENTS

The results presented in this chapter were performed in a collaborative environment and published as such in Ref. [61]. While the author's detailed contributions have already been summarized in Ch. 1, it is also necessary to acknowledge the collaborators who contributed to the work presented in this chapter. In particular: Lihui Bai contributed to the discussion and interpretation of the exceptional point and mode switching experiment; Can-Ming Hu supervised and provided insight on all aspects of the presented work. Outside of these contributions, all work and development

presented in this chapter was performed by the author of this dissertation.

7

SUMMARY OF CONTRIBUTIONS

High spin density ferrimagnets will hybridize with microwave cavity photons to form a newly discovered quasiparticle, the cavity-magnon-polariton (CMP). This hybridization can be understood within the general framework of polaritons observed throughout condensed matter systems, where material resonances couple to light, mixing their properties in physically interesting and technologically useful ways. Based on this realization it is evident that the case of the spin-photon system should be described by the combined effort of the Landau-Lifshitz-Gilbert and Maxwell equations. Avoiding extraneous details, an elegant way to approach this problem, and capture the key physics relevant to hybridization, is to model the microwave cavity and hence Maxwell's equations, as an RLC circuit. This approach captures all experimental resonance and dissipation properties and reveals that spin-photon hybridization results from coherent electrodynamic phase correlation [34, 48].

From another perspective the result of hybridization can be viewed as a new quasiparticle, in which case we should think in terms of a quantum picture. Indeed a model of the Heisenberg ferromagnet coupled to second quantized electromagnetic fields also reproduces all observed spectral features and is in exact agreement with the classical approach in the harmonic limit [34]. This leads to the observation that, on a very general level, the key properties of the CMP can be described as a set of coupled harmonic oscillator [34]. Each of these theoretical perspectives adds to our physical insight and reproduces the key signatures of spin-photon hybridization: an anticrossing in the dispersion spectrum and line width evolution of the coupled modes.

One way to experimentally probe the spin-photon system is through measuring the microwave transmission of a high spin density material, typically yttrium-iron-garnet

(YIG), inside of a microwave cavity [34, 40, 48–50, 61, 179, 219]. However in addition to this technique, electrical detection of the spin current generated in YIG/Pt bilayers also reveals the signatures of hybridization [48, 49]. The fact that strong coupling can be detected through spin pumping is a boon for spintronics, indicating that the spin current is influenced by hybridization and enabling novel methods of spin current control.

Through these techniques great strides have been taken in understanding spin-photon coupling. For example, we have learned that spin-wave modes will also hybridize with microwave photons and have a coupling strength which is inversely proportional to the mode index for standing spin waves [48, 49]. Additionally a location of microwave transmission suppression, an antiresonance, has been observed in the CMP spectra [219]. Actually, the antiresonance is a universal feature of the hybridization, occurring at the uncoupled FMR frequency, which allows accurate characterization of the uncoupled FMR dispersion even in the presence of strong coupling which distorts the eigenmodes. The antiresonance also helps to interpret the phase behaviour of the coupled system, where phase jumps of π are observed in the transmission spectra at each eigenmode and also at the antiresonance [219].

For both the technological development of cavity spintronics, and to gain physical insight, a variety of hybridization control mechanisms have been implemented. Since the hybridization is controlled by the cooperativity, which is the ratio of coupling rate to dissipation rates, the coupled spin-photon properties can be manipulated by either directly tuning the coupling rate or by manipulating the dissipation of either subsystem. As an example, the cavity dissipation rate may be controlled by tuning the external loss rates at the microwave ports, thereby manipulating the loaded damping of the system [48, 49]. In this way it is possible to systematically tune from strong to weak coupling. Such measurements have revealed the importance of coupling strength characterization even before the performance of conventional cavity based FMR measurements, which may actually be influenced by the lingering effects of hybridization [48, 49]. In a similar vein, damping control has revealed that the FMR line width may be drastically influenced by coupling even away from resonance. This important result indicates that conventional Gilbert damping and inhomogeneous broadening are insufficient to describe the FMR damping characteristics when strong coupling may exist [48].

Direct control of the coupling strength has also been successfully implemented. In one approach a compensated ferrimagnet with a strongly temperature dependent

magnetization allowed the systematic control of the coupling strength by cooling to liquid helium temperatures [40]. Using this technique the strong to weak transition was again realized and additionally the dependence of the coupling strength on the root of the number of spins was observed. A more device friendly way to tune the coupling strength can be realized by exploiting the coupling mechanism inherent to the spin-photon system. Since the Zeeman interaction is the source of coupling, the strength of the hybridization should depend on the orientation between the magnetization and the magnetic field. Experimentally this means that by tuning the orientation of the magnetic bias field relative to the dynamic microwave field the coupling strength can be controlled [50, 179]. An exciting application of this technique was realized by utilizing electrical detection with two spin devices [50]. Controlling the bias field orientation of one spin system will of course locally tune the spin current in that device. However it was revealed that, through hybridization effects, the spin current in a second well separated sample will also be controlled. Therefore the cavity spintronic system can be used to perform non-local spin current manipulation.

Based on these results it is clear that cavity spintronics holds great potential for physical discovery as well as the development of spintronic and quantum information technologies. Indeed cavity spintronics is on an upswing. As of 2014 (at the beginning of this dissertation research) there had been 3 papers published in the field (and the name cavity spintronics did not exist). However in the last four years that number has grown to approximately 100 publications, many in influential journals such as Physical Review Letters, Nature and Science. Put into that context this dissertation adds an important brick in the foundation of cavity spintronics and we anticipate that the models we have developed and the clear experimental observations we have made will pave the way for future development. In many ways this is already happening. For example, electrical detection techniques have been explored by other groups and the exceptional point physics we have outlined has formed the basis for interesting new applications [62]. With the rapid expansion of the cavity spintronics community, promising new developments, such as multiplet states and extremely high quality planar devices [75] and the intermingling of ideas between cavity quantum electrodynamics [28], cavity optomechanics [253, 254] and quantum optics [198] it is indeed an exciting time for the new frontier of cavity spintronics.

A

ADDITIONAL DETAILS FOR HARMONIC OSCILLATOR MODEL

In this appendix we present a few additional details regarding the harmonic oscillator simplification presented in Sec. 3.2.1 and the normal mode calculation of Sec. 3.2.2.

A.1 SIMPLIFICATION OF HARMONIC OSCILLATOR DISPERSION

For the frequency dispersion we can easily find analytic expressions for the real and imaginary components of the eigenvalues using de Moivre's theorem. For a complex number $z = re^{i\theta}$, $\sqrt{z} = \sqrt{r}\left[\cos\left(\theta/2\right) + i\sin\left(\theta/2\right)\right]$ and therefore from Eq. (3.9) we find,

$$\omega_\pm = \frac{1}{2}\left[\omega_c + \omega_r \pm \frac{1}{\sqrt{2}}\left[|z| + \left(\omega_c - \omega_r\right)^2 - \omega_c^2\left(\beta - \alpha\right)^2 + \frac{1}{4}\kappa^4\omega_c^2\right]^{1/2}\right], \qquad (A.1)$$

$$\Delta\omega_\pm = \frac{1}{2}\left[\omega_c\left(\alpha + \beta\right) \pm \frac{1}{\sqrt{2}}\frac{2\omega_c\left(\beta - \alpha\right)\left(\omega_c - \omega_r\right)}{\left[|z| + \left(\omega_c - \omega_r\right)^2 - \omega_c^2\left(\beta - \alpha\right)^2 + \frac{1}{4}\kappa^4\omega_c^2\right]^{1/2}}\right], \quad (A.2)$$

where

$$|z| = \sqrt{\left[\left(\omega_c - \omega_r\right)^2 - \omega_c^2\left(\beta - \alpha\right)^2 + \frac{1}{4}\kappa^4\omega_c^2\right]^2 + 4\omega_c^2\left(\beta - \alpha\right)^2\left(\omega_c - \omega_r\right)^2}. \qquad (A.3)$$

Here we have defined $\operatorname{Re}\left(\tilde{\omega}_\pm\right) = \omega_\pm$ and $\operatorname{Im}\left(\tilde{\omega}_\pm\right) = \Delta\omega_\pm$.

A.2 SIMPLIFICATION OF HARMONIC OSCILLATOR TRANSMISSION SPECTRA

S_{21} can be written in terms of $\omega_\pm$ as,

$$S_{21} \propto \frac{\omega - \tilde{\omega}_r}{(\omega - \tilde{\omega}_+)(\omega - \tilde{\omega}_-)}. \tag{A.4}$$

Near the eigenmodes we can make an expansion of the form $\omega = \omega_\pm + \epsilon = \omega_\mp \pm \delta\omega + \epsilon$, where $\delta\omega = \omega_+ - \omega_-$ and ϵ is small compared to ω. Assuming the two eigenmodes are well separated, meaning we are sufficiently far from the crossing point or strongly coupled, $\delta\omega \gg \epsilon$, and $\delta\omega \gg \Delta\omega_\pm$. If we also assume that we are not too close to the FMR mode, so that $\omega_\pm - \omega_r \gg \epsilon$ we find

$$|S_{21}|^2_\pm \propto \frac{(\omega_\pm - \omega_r)^2 + 2(\omega - \omega_\pm)(\omega_\pm - \omega_r)}{\delta\omega^2 \left[(\omega - \omega_\pm)^2 + \Delta\omega_\pm\right]^2}, \tag{A.5}$$

where $|S_{21}|^2_\pm = |S_{21}(\omega \sim \omega_\pm)|^2$. Therefore we may write the transmission spectra near either eigenmode as

$$|S_{21}|^2_\pm \propto L + (\omega_\pm - \omega_r)^{-1} D \tag{A.6}$$

as in Eq. 3.13.

For the field swept case we can also simplify our expression for the transmission spectra by expanding near $\tilde{\omega}_e$. In this case we can write

$$S_{21} \propto \frac{\omega - \tilde{\omega}_r}{\omega_r - \tilde{\omega}_e} \tag{A.7}$$

and provided we are several line widths away from the FMR frequency, $\omega - \omega_r \gg \alpha\omega_c$, S_{21} can be written as

$$|S_{21}|^2 \propto \frac{(q\Delta\omega_e + \omega_r - \omega_e)^2}{(\omega_r - \omega_e)^2 + \Delta\omega_e^2} \tag{A.8}$$

as we found in Eq. (3.15).

A.3 NORMAL MODES OF HARMONIC OSCILLATOR

Using the classical rotating wave approximation and in the absence of a driving force, the equations of motion given by Eq. 3.4 become

$$
\begin{pmatrix} \omega - \tilde{\omega}_c & -\frac{\kappa^2 \omega_c}{2} \\ -\frac{\kappa^2 \omega_c}{2} & \omega - \tilde{\omega}_r \end{pmatrix} \begin{pmatrix} x_1 \\ x_2 \end{pmatrix} = 0. \tag{A.9}
$$

The normalized eigenvectors of the CMP are therefore determined to be,

$$
X_\pm = \frac{1}{\sqrt{2\Omega}} \begin{pmatrix} \pm\sqrt{\Omega \mp \Delta} \\ \sqrt{\Omega \pm \Delta} \end{pmatrix} \tag{A.10}
$$

where $\Omega = \sqrt{(\tilde{\omega}_r - \tilde{\omega}_c)^2 + \kappa^4 \omega_c^2}$ and $\Delta = \tilde{\omega}_r - \tilde{\omega}_c$, which allows us to immediately write the transformation between hybridized and spin/photon states in Eq. (3.16).

B

ADDITIONAL DETAILS FOR QUANTUM CALCULATION

In this appendix we present additional background information and derivations associated with the Heisenberg ferromagnet-cavity photon Hamiltonian and Green's function calculation of Sec. 3.4.2 and Sec. 3.4.4.

B.1 HEISENBERG FERROMAGNET FOR LOWEST MAGNON BAND

To simplify the full Heisenberg spin-s Hamiltonian of Eq. 3.45 we begin by taking the lowest magnon band in the long wavelength limit where we can neglect the dipole-dipole interactions so that,

$$H_s = -\frac{1}{2} \sum_{i,j} \left[J_{ij} \mathbf{S}_i \cdot \mathbf{S}_j - g\mu_B B_z \sum_j S_j^z \right], \tag{B.1}$$

where we use the notation $J_{ij} = J\left(\mathbf{r}_i - \mathbf{r}_j\right)$ and $\mathbf{S}_i = \mathbf{S}\left(\mathbf{r}_i\right)$. Changing to the spin ladder operators and making the Holstein-Primakoff transformation as described in Sec. 3.4.2,

$$H_s = -\frac{s}{2} \sum_{ij} J_{ij} \left[b_i^\dagger b_j + b_i b_j^\dagger - b_j^\dagger b_j - b_i^\dagger b_i + 2 \right] + g\mu_B B_z \sum_j \left(b_j^\dagger b_j - s \right). \tag{B.2}$$

The sum in Eq. (B.2) is over nearest neighbours, thus if we assume $\mathfrak{z}$ nearest neighbours at positions ζ and Fourier transform the bosonic operators, $b_j = N_s^{-1/2} \sum_k e^{i\mathbf{k}\cdot\mathbf{r}_j} b_k$,

we find,

$$H_s = -\frac{1}{2}s^2 J\mathfrak{z}N_s - sg\mu_B B_z N_s - \frac{sJ}{s}\left[\sum_{k,\zeta} e^{i\mathbf{k}\cdot\boldsymbol{\zeta}}b_k^\dagger b_k + e^{-i\mathbf{k}\cdot\boldsymbol{\zeta}}b_k b_k^\dagger - 2b_k^\dagger b_k\right] + g\mu_B B_z \sum_k b_k^\dagger b_k. \tag{B.3}$$

Here we have also used the identity $\delta(\mathbf{k}-\mathbf{q}) = N_s^{-1}\sum_j e^{-i(\mathbf{k}-\mathbf{q})\cdot\mathbf{r}_j}$. Using the commutation relation $[b_k, b_q^\dagger] = \delta_{kq}$ and the fact that our lattice has a centre of symmetry so that $\sum_\zeta e^{i\mathbf{k}\cdot\boldsymbol{\zeta}} = \sum_\zeta e^{-i\mathbf{k}\cdot\boldsymbol{\zeta}}$,

$$H_s = \sum_k \left[Js\left(\mathfrak{z} - \sum_\zeta e^{i\mathbf{k}\cdot\boldsymbol{\zeta}}\right) + g\mu_B B_z\right] b_k^\dagger b_k - \frac{1}{2}s^2 J\mathfrak{z}N_s - sg\mu_B B_z N_s. \tag{B.4}$$

Therefore by defining,

$$\omega_k^s = \left[Js\left(\mathfrak{z} - \sum_\zeta e^{i\mathbf{k}\cdot\boldsymbol{\zeta}}\right) + g\mu_B B_z\right], \tag{B.5}$$

and

$$E_0 = -\frac{1}{2}s^2 J\mathfrak{z}N_s - sg\mu_B B_z N_s, \tag{B.6}$$

we arrive at Eq. (3.48). Note that for our cubic lattice in the $k \to 0$ limit,

$$\hbar\omega_{k\to 0}^s = g\mu_B B_z, \tag{B.7}$$

which is just the FMR dispersion. Including higher order terms in k would yield the exchange spin wave dispersion.

B.2 DETAILS OF INPUT-OUTPUT FORMALISM

In this section we derive the relationships between input and output fields and the bath photons. The Heisenberg equations of motion for the two baths are

$$\dot{c}_q = -\frac{i}{\hbar}[c_q, H] = -i\omega_q c_q + \lambda_c a, \tag{B.8}$$

$$\dot{d}_q = -\frac{i}{\hbar}[d_q, H] = -i\omega_q d_q + \lambda_d a, \tag{B.9}$$

which can be solved in terms of the bath states at either $t_i < t$ or $t_f > t$, corresponding to initial and final states before and after interaction with the cavity,

$$c_q(t) = e^{-i\omega_q(t-t_i)} c_q(t_i) + \lambda_c \int_{t_i}^{t} d\tau e^{-i\omega_q(t-\tau)} a(\tau),$$

$$c_q(t) = e^{-i\omega_q(t-t_f)} c_q(t_i) - \lambda_c \int_{t}^{t_f} d\tau e^{-i\omega_q(t-\tau)} a(\tau) \qquad \text{(B.10)}$$

with analogous expressions for d_q. Using these solutions a sum over cavity modes becomes,

$$\lambda_c \sum_q c_q = \lambda_c \sum_q e^{-i\omega_q(t-t_i)} c_q(t_i) + \lambda_c^2 \sum_q \int_{t_i}^{t} d\tau e^{-i(\omega_q-\omega_c)(t-\tau)} \left[e^{-i\omega_c(\tau-t)} a(\tau) \right],$$

$$\lambda_c \sum_q c_q = \lambda_c \sum_q e^{-i\omega_q(t-t_f)} c_q(t_f) - \lambda_c^2 \sum_q \int_{t}^{t_f} d\tau e^{-i(\omega_q-\omega_c)(t-\tau)} \left[e^{-i\omega_c(\tau-t)} a(\tau) \right]$$

$$\text{(B.11)}$$

with similar expressions for d_q. Fermi's golden rule can be used to define the external coupling rate for the cavity mode to the bath as,

$$2\kappa_c(\omega_c) = 2\pi\lambda_c^2\rho = 2\pi\lambda_c^2 \sum_q \rho(\omega_q), \qquad \text{(B.12)}$$

where $\rho(\omega_q)$ is the density of states of the photon bath for mode q and $\rho = \sum_q(\omega_q)$ is the full density of states. For a single mode of the cavity $\rho(\omega_q) = \delta(\omega_c - \omega_q)$ and therefore we can write

$$2\int_{-\infty}^{\infty} d\nu\kappa_c(\omega_c+\nu) e^{-i\nu(t-\tau)} = 2\pi\lambda_c^2 \sum_q \int_{-\infty}^{\infty} d\nu e^{-i\nu(t-\tau)}\delta(\omega_c+\nu-\omega_q). \qquad \text{(B.13)}$$

Under a Markov approximation κ_c is approximately constant near ω_c and therefore

$$2\kappa_c\delta(t-\tau) = \lambda_c^2 \sum_q e^{-i(\omega_q-\omega_c)(t-\tau)} \qquad \text{(B.14)}$$

where we have used the definition of the delta function $\delta(\omega) = (2\pi)^{-2} \int e^{-i\omega t} dt$. Therefore

$$\lambda_c \sum_q c_q(t) = \lambda_c \sum_q e^{-i\omega_q(t-t_i)} c_q(t_i) + 2 \int_{t_i}^t d\tau k_c \delta(t-\tau) e^{-i\omega_c(\tau-t)} a(\tau),$$

$$\lambda_c \sum_q c_q(t) = \lambda_c e^{-i\omega_q(t-t_f)} c_q(t_f) - 2 \int_t^{t_f} d\tau k_c \delta(t-\tau) e^{-i\omega_c(\tau-t)} a(\tau). \qquad \text{(B.15)}$$

Assuming that $a(\tau) e^{-i\omega_c(\tau-t)}$ goes smoothly to 0 as $t \to \pm\infty$,

$$\int_{t_i}^t d\tau \delta(t-\tau) e^{i\omega_c(\tau-t)} a(\tau) = \frac{1}{2} a(t), \qquad \text{(B.16)}$$

and thus if we define the input and output modes as the wave packets

$$c_{\text{in}}(t) = -\frac{1}{\sqrt{2\pi\rho}} \sum_q e^{-i\omega_q(t-t_i)} c_q(t_i),$$

$$c_{\text{out}}(t) = \frac{1}{\sqrt{2\pi\rho}} \sum_q e^{-i\omega_q(t-t_f)} c_q(t_f), \qquad \text{(B.17)}$$

we find

$$\lambda_c \sum_q c_q(t) = -\sqrt{2\kappa_c} c_{\text{in}}(t) + \kappa_c a(t), \qquad \text{(B.18)}$$

$$\lambda_c \sum_q c_q(t) = \sqrt{2\kappa_c} c_{\text{out}}(t) - \kappa_c a(t). \qquad \text{(B.19)}$$

Therefore

$$c_{\text{in}}(t) + c_{\text{out}}(t) = \sqrt{2\kappa_c} a(t),$$
$$d_{\text{in}}(t) + d_{\text{out}}(t) = \sqrt{2\kappa_d} a(t). \qquad \text{(B.20)}$$

B.3 PHOTON GREEN'S FUNCTION

The bare photon Hamiltonian is simply a harmonic oscillator

$$H = \hbar\omega_c \left(a^\dagger a + \frac{1}{2} \right) = \frac{p^2}{2} + \frac{1}{2}\omega_c^2 x^2, \qquad \text{(B.21)}$$

where

$$x = \sqrt{\frac{\hbar}{2\omega_c}}\left(a + a^\dagger\right), \qquad p = -i\sqrt{\frac{\hbar\omega_c}{2}}\left(a - a^\dagger\right), \tag{B.22}$$

and we have set the mass to unity. We wish to find the retarded Green's function

$$G_R^0 = -i\theta\left(t\right)\left\langle\left[x\left(t\right), x\left(0\right)\right]\right\rangle. \tag{B.23}$$

In the Heisenberg picture, $a\left(t\right) = a^{-i\omega_c t}$, and therefore the propagator is given by

$$P_0 = \left\langle x\left(t\right) x\left(0\right)\right\rangle = \frac{\hbar}{2\omega_c}\left\langle aa^\dagger e^{-i\omega_c t} + a^\dagger a e^{-i\omega_c t}\right\rangle,$$
$$P_0 = \frac{\hbar}{2\omega_c}e^{-i\omega_c t}, \tag{B.24}$$

where we have made use of the fact that we are using the vacuum state. The time domain Green's function is therefore,

$$G_R^0 = -\theta\left(t\right)\frac{\hbar}{\omega_c}\sin\left(\omega t\right). \tag{B.25}$$

To Fourier transform to the frequency domain we introduce an infinitesimal parameter ϵ which determines the pole structure within our integration contour,

$$G_R^0 = \frac{i\hbar}{2\omega_c}\int_0^\infty \theta\left(t\right)\left(e^{i\omega_c t} - e^{-i\omega_c t}\right)e^{i\omega t - \epsilon t}dt,$$
$$G_R^0 = -\frac{\hbar}{2\omega_c}\left[\frac{1}{\omega - \omega_c + i\epsilon} - \frac{1}{\omega + \omega_c + i\epsilon}\right]. \tag{B.26}$$

Then setting $\epsilon \to 0$ and introducing damping by replacing $\omega_c \to \omega_c - i\Gamma_c$ we obtain the result of Eq. (3.84),

$$G_R^0\left(\omega\right) = \frac{\hbar}{2\omega_c}\left[\frac{1}{\omega - \omega_c + i\Gamma_c} - \frac{1}{\omega + \omega_c - i\Gamma_c}\right]. \tag{B.27}$$

B.4 DERIVATION OF T-MATRIX FOR THE EXTERNAL PHOTON BATH

In this section we use a standard quantum field theory approach to determine the T-matrix of the external photon bath, following Ref. [255], and therefore prove Eq. (3.81) [34]. For further details on the formalism see, e.g. Ref. [177]. To relate the retarded propagators to the T-matrix we construct a generating functional, which

includes both the bath and cavity photons, as,

$$Z[\eta, \bar{\eta}] = \int \mathcal{D}c \mathcal{D}\bar{c} \mathcal{D}a \mathcal{D}\bar{a} e^{iS[c,\bar{c},a,\bar{a}]+i\bar{\eta}\cdot c + i\eta\cdot\bar{c}}, \tag{B.28}$$

where $c, \bar{c}, a, \bar{a}$ are time dependent complex variables which replace the bosonic fields of the bath and cavity photons, $c, c^\dagger$, and $a, a^\dagger$ respectively. $\bar{\eta}, \eta$ are auxiliary fields used to compute the correlation functions. Here

$$\bar{\eta} \cdot c = \sum_{\beta,q} \int dt \bar{\eta}_{\beta q}(t) c_{\beta q}(t), \tag{B.29}$$

where β sums over both the left (L) and right (R) photon baths, and q sums over all modes in each bath. S is the full action, $S = S_{\text{bath}} + S_{\text{ph}} + S_{\text{int}}$ which includes a left and right photon bath, the cavity photons, and an interaction term between the bath and cavity photons. In the standard way we may write the non-interacting actions in terms of the Green's functions

$$S_{\text{bath}} = -\sum_{\beta,q} \int dt \bar{c}_{\beta q} \left(G_{\beta q}^0\right)^{-1} c_{\beta q}, \tag{B.30}$$

$$S_{\text{cav}} = -\int dt \bar{a} G^{-1} a, \tag{B.31}$$

where $G_{\beta q}^0$ is the bare bath photon Green's function and G^{-1} is the Green's function of the cavity photons. The action for the cavity-bath interaction is

$$S_{\text{int}} = \sum_{\beta,q} \lambda \int dt \left[\bar{a} c_{\beta q} + a \bar{c}_{\beta q}\right]. \tag{B.32}$$

In Eq. B.32 we have again implemented a Markov approximation, i.e. we have assumed that the interaction strength (cavity-bath coupling) is mode independent. The full Green's function for the bath photon can then be calculated as

$$G_{\beta q_f, \beta' q_i}(t - t') = \frac{\delta^2}{\delta\bar{\eta}_{\beta q_f}(t) \delta\eta_{\beta' q_i}(t_i)} Z \Big|_{\bar{\eta}, \eta \to 0}. \tag{B.33}$$

To compute the Green's function we complete the square in Eq. (B.28) by shifting the bath variables,

$$c_{\beta q} = c'_{\beta q} + \int dt' G_{\beta q}^0(t - t') \eta_{\beta q}(t'). \tag{B.34}$$

Since this is just a shift of variables the measures stay the same but the action becomes,

$$S = \sum_{\beta,q} \int dt \left[-\bar{c}'_{\beta q} \left(G^0_{\beta q} \right)^{-1} c'_{\beta q} + i \int dt' \bar{\eta}_{\beta q} \left(t \right) G^0_{\beta q} \left(t - t' \right) \eta_{\beta q} \left(t' \right) \right.$$
$$\left. + \int dt' \left[\lambda \bar{a} G^0_{\beta q} \left(t - t' \right) \eta_{\beta q} \left(t' \right) + \lambda a G^0_{\beta q} \left(t - t' \right) \bar{\eta}_{\beta q} \left(t' \right) \right] \right]. \tag{B.35}$$

Therefore, applying the variation of Eq. (B.33) to the generating functional with the action in Eq. (B.35), we find

$$G_{\beta q_f, \beta' q_i} \left(t - t' \right) = \delta_{\beta \beta'} \delta_{q_i q_f} G^0_{\beta q_i} \left(t - t' \right) - \int dt'' dt''' G^0_{\beta_f q_f} \left(t - t'' \right) G \left(t'' - t''' \right) G^0_{\beta' q_i} \left(t''' - t \right). \tag{B.36}$$

Comparing Eq. (B.36) to Eq. (3.80) we can identify

$$\mathcal{T} \left(\omega \right) \propto \lambda^2 G_R, \tag{B.37}$$

proving Eq. (3.81).

B.5 DIAGRAMMATIC CALCULATION OF PHOTON RETARDED GREEN'S FUNCTION

Here we show how to calculate the full retarded function by computing the photon self energy using a diagrammatic approach [34]. The second order process due to H_{int} in Eq. (3.56) is the annihilation of a photon and creation of a magnon, followed by the annihilation of the magnon and creation of another photon. This process is shown in Fig. B.1 (a), where dashed lines represent photon propagation, solid lines represent magnon propagation and vertices represent interactions governed by H_{int}. Accordingly P_0 and R_0 are the propagators for the photon and magnon respectively which were evaluated in Sec. B.3. The Feynman rules for our theory are straight forward and we can simply read off

$$P_2 = N_s \alpha_c^2 P_0^2 + R_0. \tag{B.38}$$

The diagram of Fig. B.1 (a) is the only one allowed by our theory. At higher orders we simply have multiples of the same diagram, as shown in Fig. B.1 (b). Thus the
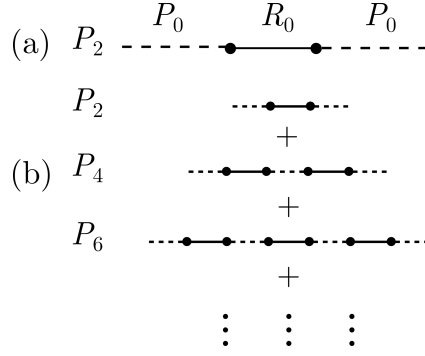
Figure B.1: (a) The second order process due to H_{int}. A photon (dashed line) is annihilated and a magnon is created followed by the annihilation of the magnon and creation of another photon. (b) The higher order processes follow a geometric series, allowing summation to obtain the full photon Green's function. Figure modified from Ref. [34].

diagram with $2n$ vertices is

$$P_{2n} = P_0 \left(N_s \alpha_c^2\right)^n (P_0 R_0)^n. \tag{B.39}$$

Summing all diagrams using a geometric series we find the full photon propagator in the interacting theory,

$$P(\omega) = \int dt \, \langle x(t)x(0)\rangle \, e^{i\omega t} = \sum_{n=0}^{\infty} P_0 \left(N_s \alpha_c^2\right)^n (P_0 R_0)^n = \left[(P_0)^{-1} - N_s \alpha_c^2 R_0\right]^{-1}. \tag{B.40}$$

From Eq. (B.23) we see that

$$G_R^0 (\omega) = P_0 (\omega) + P_0 (-\omega) \tag{B.41}$$

and therefore using Eq. B.26 we find

$$P_0 (\omega) = \frac{1}{\omega - \omega_c + i\Gamma_c}, \qquad R_0 = \frac{1}{\omega - \omega_r + i\Gamma_r}. \tag{B.42}$$

Thus, combining Eq. (B.42) with Eq. B.41 we have

$$P(\omega) = \left(\omega - \omega_c + i\Gamma_c - \frac{N_s \alpha_c^2}{\omega - \omega_r - i\Gamma_r}\right)^{-1}, \tag{B.43}$$

and therefore we finally find the photon retarded function in the interacting theory

$$G_R\left(\omega\right) = P\left(\omega\right) + P\left(-\omega\right)$$

$$G_R\left(\omega\right) = \left(\omega - \omega_c + i\Gamma_c - \frac{N_s\alpha_c^2}{\omega - \omega_r + i\Gamma_r}\right)^{-1} - \left(\omega + \omega_c - i\Gamma_c - \frac{N_s\alpha_c^2}{\omega + \omega_r - i\Gamma_r}\right)^{-1}.$$

$$(B.44)$$

CALIBRATION OF TRANSMISSION/REFLECTION DATA

The majority of microwave transmission experiments performed in this dissertation allowed direct calibration of the entire microwave transmission line. In this case a routine calibration procedure was performed directly using the VNA. However in certain instances the experimental setup may not facilitate this simple calibration procedure. For example, if the microwave properties are measured using a microwave generator and spectrum analyzer rather than a VNA, or if large standing wave modes exist during reflection measurements, post experiment calibration of the data may be necessary. In our case such a procedure was necessary for data collected using the Bruker cavity, where the entire feedline leading from the waveguide to the cavity was not accessible. In this appendix we describe such an approach based on Ref. [215], which was applied to the reflection data from the Bruker cavity presented in Sec. 5.2.

A general complex S parameter can be described by the equation [185],

$$\mathrm{S} = \frac{-i\beta\omega_c\overline{\mathrm{S}}}{(\omega - \omega_c) + i\beta\omega_c},$$ (C.1)

so that $|\mathrm{S}|^2$ has a Lorentz line shape.[1] Taking the rotating wave approximation and the limit $K \to 0$ in Eq. 3.34, which we derived for the phase correlation model, we find exact agreement with Eq. C.1. Based on Eq. (C.1) plotting $\mathrm{Re}\,(\mathrm{S})$ versus $\mathrm{Im}\,(\mathrm{S})$ should produce a circle, centred on the real axis, which intersects the real axis at the origin and the resonance frequency $\omega = \omega_c$. However experimental measurements

---

[1]Of course S_{11} and S_{21} will differ by an offset (as we found using the input-output formalism, $\mathrm{S}_{11} = -1 + \mathrm{S}_{21}$), but this constant offset still leaves a Lorentz line shape and the calibration we describe here applies in both cases.

will not obey this ideal behaviour due to shifts induced by, for example, the detailed nature of the feedline-cavity coupling, or potential cross talk. These effects could shift both the origin and phase of the S parameter,

$$S \rightarrow (S + X) \, e^{i\varphi}, \tag{C.2}$$

where X represents a shift to S in the complex plane and φ is a phase shift which rotates the circle. The influence of X and φ is highlighted in Fig. C.1 (a), where a set of ideal spectra is shown by red squares and a set of realistic raw data is shown by green circles.

To remove the effects of the shift and rotation we must calibrate the data. To demonstrate how this is done we work with a set of typical microwave reflection data, S_{11}. In addition to experiencing the phase shift φ, realistic experimental data may also have a travelling phase shift, due to the length of the feedlines. This results in a constant linear shift in the microwave phase, as shown clearly by the green curve in Fig. C.1 (d). In the complex plane such a travelling phase results in a multivalued function for the microwave transmission/reflection parameter, as shown by the green symbols in Fig. C.1 (b). To correct for this frequency dependent phase shift we simply subtract the frequency slope of S_{11} away from the cavity resonance. We can then correct for the shift X by performing a least squares fit to a circle, which determines the centre position X, and subtracting this centre point from the data. The last step is to rotate the spectra to correct for the shift φ. Do do this we define a reference point in the complex S_{11} plane, $\mathbf{p}_{\text{ref}}$, which lies half way between the first and last points on the $\mathbf{S}_{11}$ circle. Denoting the location of the first and last points as $\mathbf{p}_i$ and $\mathbf{p}_f$ respectively, the reference point is therefore

$$\mathbf{p}_{\text{ref}} = \frac{\mathbf{p}_i - \mathbf{p}_f}{2} + \mathbf{p}_f. \tag{C.3}$$

As shown in Fig. C.1 (a) $\mathbf{p}_{\text{ref}}$ lies at an angle φ from the $\text{Re}\,(S_{11})$ axis, and therefore once we know $\mathbf{p}_{\text{ref}}$ we can determine φ and rotate our data by multiplying by $e^{-i\varphi}$. Fig. C.1 (b) shows the effect of this calibration procedure on the experimental data. The green circles indicate the raw data, blue triangles show the data after correcting for the linear phase shift resulting from the feedlines and the red squares show the data after applying the rotation and shift correction. The effect of the calibration is shown on $|S_{11}|$ and the phase of S_{11}, ϕ_{11}, in Fig. C.1 (c) and (d) respectively. In
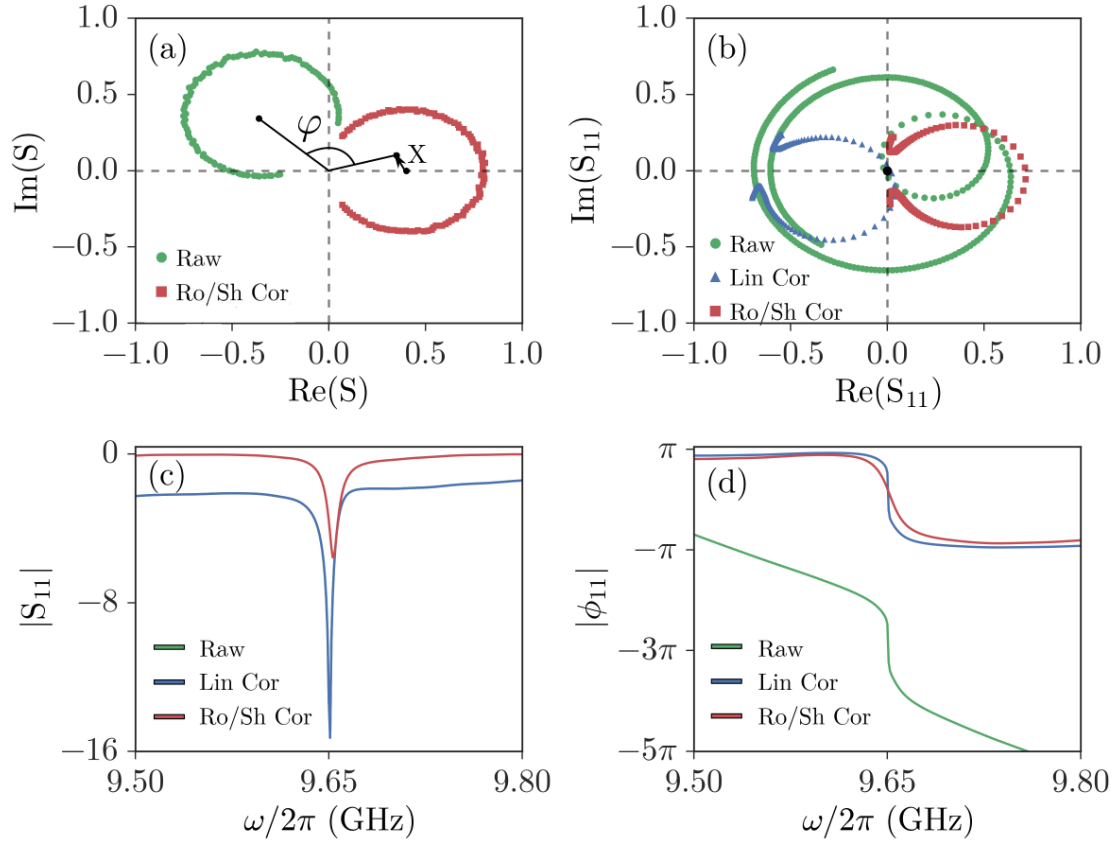
Figure C.1: (a) The effect of a translation X and phase shift φ is illustrated. The red squares indicate a set of ideal spectra that is unshifted, while the green circles show the realistic raw data which would be observed. (b) The effect of microwave calibration in the complex S_{11} plane. Green circles are typical raw reflection spectra, blue triangles show the data after correcting for the travelling phase and the red squares show the data after rotation and shift correction. (c) The effect of microwave calibration on the reflection spectra. The green and blue curves show the raw data and data after correcting for the travelling phase, respectively. Note that these two curves are identical as we plot the absolute value of the spectra here. The red curve is the rotation and shift corrected spectra. (d) The effect of microwave calibration on the reflection phase. The green curve is the raw data, which shows a large linear phase shift. The blue curve shows the data after correcting for this travelling phase, while the red curve shows the phase after rotation and shift correction.

panel (c), the raw data and the data after the linear correction are identical, as we are plotting the absolute value and so the phase information is not relevant. However the effect of the travelling phase can easily be seen by the slope of the green curve in panel (d).

D

LIST OF ABBREVIATIONS

In the table below we summarize abbreviations commonly used in this dissertation.

Abbreviation	Full Name
CMP	Cavity-magnon-polariton
EP	Exceptional point
Fe	Iron
FMI	Ferromagnetic insulator
FMR	Ferromagnetic resonance
GdIG	Gadolinium-iron-garnet
LLG	Landau-Lifshitz-Gilbert
LNA	Low noise amplifier
NM	Normal metal
Pt	Platinum
SSW	Standing spin wave
VNA	Vector network analyzer

YIG	Yttrium-iron-garnet

LIST OF VARIABLES

In the table below we collect the definitions of some variables which are commonly used in this dissertation. This list is in no way exhaustive, focussing instead on notations which may become muddled due to other similarly defined variables.

Table E.1: List of commonly used, or easily confused, variables.

Variable	Description
ω	Angular frequency of microwave field.
ω_m	Angular frequency corresponding to saturation magnetization, M_0, $\omega_m = \gamma M_0$.
$\tilde{\omega}_r$	Complex angular ferromagnetic resonance frequency, $\tilde{\omega}_r = \omega_r - i\alpha\omega$ ($\tilde{\omega}_r = \omega_r - i\alpha\omega_c$ for ω near ω_c). Controlled by static magnetic field, $\tilde{\omega}_r = \tilde{\omega}_r(H)$.
ω_r	Real part of the complex angular ferromagnetic resonance frequency, $\omega_r = \mathrm{Re}\,(\tilde{\omega}_r)$.
$\Delta\omega_r$	Imaginary part of the complex angular ferromagnetic resonance frequency, $\Delta\omega_r = \mathrm{Im}\,(\tilde{\omega}_r)$. This gives the frequency line width of ferromagnetic resonance.
$\tilde{\omega}_c$	Complex angular cavity frequency, $\tilde{\omega}_c = \omega_c - i\beta\omega_c$. $\tilde{\omega}_c$ is a function of the cavity height but is independent of the static magnetic field.

LIST OF VARIABLES

ω_c — Angular cavity resonance frequency, $\omega_c = \mathrm{Re}\left(\tilde{\omega}_c\right)$.

$\Delta\omega_c$ — Line width of angular cavity resonance frequency, $\Delta\omega_c = \mathrm{Im}\left(\tilde{\omega}_c\right)$

$\tilde{\omega}_\pm$ — Complex angular frequency of hybridized spin-photon modes. $\tilde{\omega}_+$ ($\tilde{\omega}_-$) is the high (low) frequency branch. Controlled by static magnetic field, $\tilde{\omega}_\pm = \tilde{\omega}_\pm\left(H\right)$.

$\omega_\pm$ — Field dispersion of the hybridized modes, given by the real part of the hybridized complex angular frequency, $\omega_\pm\left(H\right) = \mathrm{Re}\left(\tilde{\omega}_\pm\right)$.

$\Delta\omega_\pm$ — Frequency line width of the hybridized spin-photon modes, $\Delta\omega_\pm\left(H\right) = \mathrm{Im}\left(\tilde{\omega}_\pm\right)$

$\tilde{\omega}_e$ — Complex hybridized angular "Kittel" frequency. In the limit of zero spin-photon coupling, $\tilde{\omega}_e \rightarrow \tilde{\omega}_r$. $\tilde{\omega}_e$ is controlled by the angular microwave frequency ω.

ω_e — Frequency dispersion of the hybridized mode, $\omega_e\left(\omega\right) = \mathrm{Re}\left(\tilde{\omega}_e\right)$.

$\Delta\omega_e$ — Field line width of the hybridized mode, $\Delta\omega_e\left(\omega\right) = \mathrm{Im}\left(\tilde{\omega}_e\right)$.

ω_{gap} — Rabi gap between the hybridized modes, $\omega_{\mathrm{gap}} = \left(\omega_+ - \omega_-\right)|_{\omega_r=\omega_c}$.

α — Gilbert damping of magnetostatic modes. $\alpha = \mathrm{Im}\left(\tilde{\omega}_r\right)/\omega$.

β_{int} — Intrinsic damping of the microwave cavity. Determined by, for example, material conductivity, surface roughness and shape.

β_{ext} — Extrinsic damping of the microwave cavity. Determined by coupling between microwave feedlines (or pins) and cavity.

β_L — Loaded cavity damping. $\beta_L = \beta_{\mathrm{int}} + \beta_{\mathrm{ext}}$ determines the experimental line width of the cavity mode.

Q — Quality factor of cavity, $Q = 1/2\beta_L$.

β — Cavity damping parameter. Notation used for simplicity when the input and output ports are not explicitly needed. Experimentally β is equivalent to the loaded cavity quality, β_L.

M_0	Effective magnetization (saturation magnetization) which appears in the Kittel equation.
γ	Gyromagnetic ratio.
M	Net magnetization measured through SQUID magnetometry. In our experiments $M = M_0$.
θ_{SH}	Spin Hall angle which characterizes the efficiency of spin pumping.
θ_c	Cone angle of FMR precession. All of our experiments were performed at low microwave power, resulting in small θ_c.
θ	Angle between microwave and static magnetic fields. Used to control the coupling strength.
H_r	Ferromagnetic resonance field.
ΔH	Ferromagnetic resonance line width.
H	External static magnetic field.
h	Microwave magnetic field.
S_{21}	Microwave transmission parameter.
S_{11}	Microwave reflection parameter.
$\mathbb{S}_c$	Spectral function of microwave cavity.
$\mathbb{S}_m$	Spectral function for microwave absorption by magnetization.
κ	Dimensionless coupling strength. Defined for harmonic oscillator model.
K_m	Coupling strength which defines the phase correlation between microwave field and current through Ampère's law. Used in phase correlation model. Dimensions of inverse metres.

K_c	Coupling strength which defines the phase correlation between magnetization precession and current (voltage) through Faraday's law. Used in phase correlation model. Dimensions of metres.
K	Dimensionless coupling strength which defines ω_{gap} in phase correlation model, $K = \sqrt{K_m K_c}$.
g	Coupling rate with units of frequency.
g_η	Dimensionless coupling rate, g/ω_c.
C	Cooperativity, which helps characterize strong versus weak coupling, $C = g_\eta/\alpha\beta$.
a, $a^\dagger$	Cavity photon creation and annihilation operators.
b, $b^\dagger$	Magnon creation and annihilation operators.
c_q, $c_q^\dagger$	Bath photon creation and annihilation operators for port 1 (or port c).
d_q, $d_q^\dagger$	Bath photon creation and annihilation operators for port 2 (or port d).
c_1, $c_2^\dagger$	Creation and annihilation operators for the hybridized modes. Obtained from a and b by a Bogoliubov transformation.
κ_c	Dissipation rate of c bath photons. Used in input-output formalism.
κ_d	Dissipation rate of d bath photons. Used in input-output formalism.
λ_c	Coupling rate of bath photons at port c to cavity photons. Used in input-output formalism.
λ_d	Coupling rate of bath photons at port d to cavity photons. Used in input-output formalism.

BIBLIOGRAPHY

[1] P. Kovtun, J. Phys. A Math. Theor. **45**, 1 (2012), arXiv:1205.5040.

[2] D. Forster, *Hydrodynamic Fluctuations, Broken Symmetry, and Correlation Functions* (W. A. Benjamin, 1975).

[3] N. Seiberg, in *Quantum Struct. Sp. Time* (World Scientific, 2007) pp. 163–213, arXiv:hep-th/0601234.

[4] S. El-Showk and K. Papadodimas, JHEP **10**, 106 (2012), arXiv:1101.4163.

[5] T. Padmanabhan, Mod. Phys. Lett. A **30**, 1540007 (2015), arXiv:1410.6285.

[6] C. P. Poole, H. A. Farach, R. J. Creswick, and R. Prozorov, *Superconductivity* (Academic Press, 2007).

[7] Y. Tokura, M. Kawasaki, and N. Nagaosa, Nat. Phys. **13**, 1056 (2017).

[8] L. H. Hartwell, J. J. Hopfield, S. Leibler, and A. W. Murray, Nature **402**, C47 (1999).

[9] A.-L. Barabási and Z. N. Oltvai, Nat. Rev. Genet. **5**, 101 (2004).

[10] D. A. Harper and P. Lewis, J. Econ. Behav. Organ. **82**, 329 (2012).

[11] A. Barabási and R. Albert, Science **286**, 509 (1999).

[12] B. MacWhinney, Annu. Rev. Psychol. **49**, 199 (1998).

[13] P. W. Anderson, Science **177**, 393 (1972).

[14] R. B. Laughlin, *A Different Universe: Reinventing Physics From The Bottom Down* (Basic Books, 2005).

[15] C.-M. Hu, Phys. in Can. **72**, 76 (2016), arXiv:1508.01966.

[16] J. M. D. Coey, *Magnetism and Magnetic Materials* (Cambridge University Press, 2010).

[17] V. K. Arkad'yev, J. Russ. Phys.-Chem. Soc. **44**, 165 (1912).

[18] J. H. E. Griffiths, Nature **158**, 670 (1946).

[19] Y. Suzuki, APL Mater. **3**, 1 (2015).

[20] E. L. Albuquerque and M. G. Cottam, *Polaritons in Periodic and Quasiperiodic Structures* (Elsevier, 2004).

[21] B. Lax and K. J. Button, *Microwave Ferrites and Ferrimagnetics* (McGraw-Hill, 1962).

[22] B. Hillebrands and K. Ounadjela, eds., *Spin Dynamics in Confined Magnetic Structures I*, Topics in Applied Physics (Springer, 2002).

[23] M. Harder, Y. Gui, and C.-M. Hu, Phys. Rep. **661**, 1 (2016), arXiv:1605.00710.

[24] N. Bloembergen and R. Pound, Phys. Rev. **203**, 1949 (1954).

[25] M. A. W. Schoen, J. M. Shaw, H. T. Nembach, M. Weiler, and T. J. Silva, Phys. Rev. B **92**, 184417 (2015), arXiv:1508.05265.

[26] S. Klingler, H. Maier-Flaig, C. Dubs, O. Surzhenko, R. Gross, H. Huebl, S. T. B. Goennenwein, and M. Weiler, Appl. Phys. Lett. **110**, 092409 (2017), arXiv:1612.02360.

[27] J. W. Rao, S. Kaur, X. L. Fan, D. S. Xue, B. M. Yao, Y. S. Gui, and C.-M. Hu, Appl. Phys. Lett. **110**, 262404 (2017).

[28] S. Haroche and J.-M. Raimond, *Exploring the Quantum: Atoms, Cavities, and Photons.* (Oxford University Press, 2006).

[29] Ö. O. Soykal and M. E. Flatté, Phys. Rev. Lett. **104**, 077202 (2010), arXiv:0907.3926.

[30] Ö. O. Soykal and M. E. Flatté, Phys. Rev. B **82**, 104413 (2010), arXiv:1005.3068.

[31] H. Huebl, C. W. Zollitsch, J. Lotze, F. Hocke, M. Greifenstein, A. Marx, R. Gross, and S. T. B. Goennenwein, Phys. Rev. Lett. **111**, 127003 (2013), arXiv:1207.6039.

[32] X. Zhang, C.-L. Zou, L. Jiang, and H. X. Tang, Phys. Rev. Lett. **113**, 156401 (2014), arXiv:1405.7062.

[33] Y. Tabuchi, S. Ishino, A. Noguchi, T. Ishikawa, R. Yamazaki, K. Usami, and Y. Nakamura, Science **349**, 405 (2015), arXiv:1410.3781.

[34] M. Harder, L. Bai, C. Match, J. Sirker, and C. Hu, Sci. China Physics, Mech. Astron. **59**, 117511 (2016), arXiv:1601.06049v1.

[35] G. B. G. Stenning, G. J. Bowden, L. C. Maple, S. A. Gregory, A. Sposito, R. W. Eason, N. I. Zheludev, and P. A. J. de Groot, Opt. Express **21**, 1456 (2013).

[36] B. Bhoi, T. Cliff, I. S. Maksymov, M. Kostylev, R. Aiyar, N. Venkataramani, S. Prasad, and R. L. Stamps, J. Appl. Phys. **116**, 243906 (2014), arXiv:1409.5499.

[37] S. A. Gregory, G. B. G. Stenning, G. J. Bowden, N. I. Zheludev, and P. A. J. de Groot, New J. Phys. **16**, 063002 (2014).

[38] S. Kaur, B. Yao, Y.-S. Gui, and C.-M. Hu, J. Phys. D. Appl. Phys. **49**, 475103 (2016), arXiv:1507.06940.

[39] D. Zhang, W. Song, and G. Chai, J. Phys. D. Appl. Phys. **50**, 205003 (2017).

[40] H. Maier-Flaig, M. Harder, S. Klingler, Z. Qiu, E. Saitoh, M. Weiler, S. Geprägs, R. Gross, S. T. B. Goennenwein, and H. Huebl, Appl. Phys. Lett. **110**, 132401 (2017), arXiv:1701.08969.

[41] M. Goryachev, S. Watt, J. Bourhill, M. Kostylev, and M. E. Tobar, Phys. Rev. B **97**, 155129 (2017), arXiv:1711.09980.

[42] L. V. Abdurakhimov, S. Khan, N. A. Panjwani, J. D. Breeze, S. Seki, Y. Tokura, J. J. L. Morton, and H. Kurebayashi, (2018), arXiv:1802.07113.

[43] D. I. Schuster, A. P. Sears, E. Ginossar, L. DiCarlo, L. Frunzio, J. J. L. Morton, H. Wu, G. A. D. Briggs, B. B. Buckley, D. D. Awschalom, and R. J. Schoelkopf, Phys. Rev. Lett. **105**, 140501 (2010).

[44] Y. Kubo, F. R. Ong, P. Bertet, D. Vion, V. Jacques, D. Zheng, A. Dréau, J. F. Roch, A. Auffeves, F. Jelezko, J. Wrachtrup, M. F. Barthe, P. Bergonzo, and D. Esteve, Phys. Rev. Lett. **105**, 140502 (2010), arXiv:1006.0251.

[45] I. Chiorescu, N. Groll, S. Bertaina, T. Mori, and S. Miyashita, Phys. Rev. B **82**, 024413 (2010), arXiv:1004.3605.

[46] E. Abe, H. Wu, A. Ardavan, and J. J. L. Morton, Appl. Phys. Lett. **98**, 251108 (2011).

[47] B. M. Garraway, Philos. Trans. A. Math. Phys. Eng. Sci. **369**, 1137 (2011).

[48] L. Bai, M. Harder, Y. P. Chen, X. Fan, J. Q. Xiao, and C.-M. Hu, Phys. Rev. Lett. **114**, 227201 (2015), arXiv:1504.01335.

[49] H. Maier-Flaig, M. Harder, R. Gross, H. Huebl, and S. T. B. Goennenwein, Phys. Rev. B **94**, 054433 (2016), arXiv:1601.05681.

[50] L. Bai, M. Harder, P. Hyde, Z. Zhang, C.-M. Hu, Y. P. Chen, and J. Q. Xiao, Phys. Rev. Lett. **118**, 217201 (2017), arXiv:1706.00347.

[51] M. Goryachev, W. G. Farr, D. L. Creedon, Y. Fan, M. Kostylev, and M. E. Tobar, Phys. Rev. Appl. **2**, 054002 (2014), arXiv:1408.2905.

[52] X. Zhang, C.-L. Zou, L. Jiang, and H. X. Tang, Phys. Rev. Lett. **113**, 156401 (2014), arXiv:1405.7062.

[53] J. Bourhill, N. Kostylev, M. Goryachev, D. L. Creedon, and M. E. Tobar, Phys. Rev. B **93**, 144420 (2016), arXiv:1512.07773v2.

[54] N. J. Lambert, J. A. Haigh, and A. J. Ferguson, J. Appl. Phys. **117**, 053910 (2015), arXiv:1506.02902.

[55] X. Zhang, C. Zou, L. Jiang, and H. X. Tang, J. Appl. Phys. **119**, 023905 (2016).

[56] M. Goryachev, M. Kostylev, and M. E. Tobar, (2017), arXiv:1710.06601.

[57] P. Hyde, L. Bai, M. Harder, C. Match, and C.-M. Hu, Appl. Phys. Lett. **109**, 152405 (2016), arXiv:1606.03469.

[58] N. J. Lambert, J. A. Haigh, S. Langenfeld, A. C. Doherty, and A. J. Ferguson, Phys. Rev. A **93**, 021803 (2016), arXiv:1506.06049v2.

[59] X. Zhang, C.-L. Zou, N. Zhu, F. Marquardt, L. Jiang, and H. X. Tang, Nat. Commun. **6**, 8914 (2015), arXiv:1507.02791v1.

[60] A. Morin, C. Lacroix, and D. Menard, in *2016 17th Int. Symp. Antenna Technol. Appl. Electromagn.*, Vol. 114 (IEEE, 2016) pp. 1–2.

[61] M. Harder, L. Bai, P. Hyde, and C.-M. Hu, Phys. Rev. B **95**, 214411 (2017), arXiv:1702.04797.

[62] D. Zhang, X.-Q. Luo, Y.-P. Wang, T.-F. Li, and J. Q. You, Nat. Commun. **8**, 1368 (2017).

[63] Y.-P. Wang, G.-Q. Zhang, D. Zhang, X.-Q. Luo, W. Xiong, S.-P. Wang, T.-F. Li, C.-M. Hu, and J. Q. You, Phys. Rev. B **94**, 224410 (2016), arXiv:1609.07891.

[64] Y.-P. Wang, G.-Q. Zhang, D. Zhang, T.-F. Li, C.-M. Hu, and J. Q. You, Phys. Rev. Lett. **120**, 057202 (2018), arXiv:1707.06509.

[65] A. Osada, R. Hisatomi, A. Noguchi, Y. Tabuchi, R. Yamazaki, K. Usami, M. Sadgrove, R. Yalla, M. Nomura, and Y. Nakamura, Phys. Rev. Lett. **116**, 223601 (2016), arXiv:1510.01837.

[66] X. Zhang, N. Zhu, C.-L. Zou, and H. X. Tang, Phys. Rev. Lett. **117**, 123605 (2016), arXiv:1510.03545.

[67] J. A. Haigh, S. Langenfeld, N. J. Lambert, J. J. Baumberg, A. J. Ramsay, A. Nunnenkamp, and A. J. Ferguson, Phys. Rev. A **92**, 063845 (2015), arXiv:1510.06661.

[68] Y. Liu, J. You, and Q. Hou, Sci. Rep. **6**, 21775 (2016).

[69] S. Viola Kusminskiy, H. X. Tang, and F. Marquardt, Phys. Rev. A **94**, 033821 (2016), arXiv:1604.07053.

[70] C. Braggio, G. Carugno, M. Guarise, A. Ortolan, and G. Ruoso, Phys. Rev. Lett. **118**, 107205 (2017), arXiv:1609.08147.

[71] S. Kaur, B. M. Yao, J. W. Rao, Y. S. Gui, and C.-M. Hu, Appl. Phys. Lett. **109**, 032404 (2016).

[72] Z. Tay, W. Soh, and C. Ong, J. Magn. Magn. Mater. **451**, 235 (2018).

[73] R. Hisatomi, A. Osada, Y. Tabuchi, T. Ishikawa, A. Noguchi, R. Yamazaki, K. Usami, and Y. Nakamura, Phys. Rev. B **93**, 174427 (2016), arXiv:1601.03908.

[74] Y. Tabuchi, S. Ishino, A. Noguchi, T. Ishikawa, R. Yamazaki, K. Usami, and Y. Nakamura, Comptes Rendus Phys. **17**, 729 (2016), arXiv:1508.05290.

[75] B. M. Yao, Y. S. Gui, J. W. Rao, S. Kaur, X. S. Chen, W. Lu, Y. Xiao, H. Guo, K. P. Marzlin, and C. M. Hu, Nat. Commun. **8**, 1437 (2017).

[76] R. G. E. Morris, A. F. van Loo, S. Kosen, and A. D. Karenowska, Sci. Rep. **7**, 11511 (2017), arXiv:1610.09963.

[77] M. Born and E. Wolf, *Principles of Optics*, 7th ed. (Cambridge University Press, 1999).

[78] A. V. Kavokin, J. J. Baumberg, G. Malpuech, and F. P. Laussy, *Microcavities* (Oxford University Press, 2007).

[79] D. L. Mills and E. Burstein, Reports Prog. Phys. **37**, 817 (1974).

[80] A. Dreismann, H. Ohadi, Y. Del Valle-Inclan Redondo, R. Balili, Y. G. Rubo, S. I. Tsintzos, G. Deligeorgis, Z. Hatzopoulos, P. G. Savvidis, and J. J. Baumberg, Nat. Mater. **15**, 1074 (2016).

[81] M. Specht, J. D. Pedarnig, W. M. Heckl, and T. W. Hänsch, Phys. Rev. Lett. **68**, 476 (1992).

[82] A. Hoffmann and S. D. Bader, Phys. Rev. Appl. **4**, 047001 (2015).

[83] T. Kuschel and G. Reiss, Nat. Nanotechnol. **10**, 22 (2015).

[84] A. Manchon, Nat. Phys. **10**, 340 (2014).

[85] G. E. Bauer, E. Saitoh, and B. J. Van Wees, Nat. Mater. **11**, 391 (2012), arXiv:1107.4395v1.

[86] A. A. Serga, A. V. Chumak, and B. Hillebrands, J. Phys. D. Appl. Phys. **43**, 264002 (2010).

[87] J. Åkerman, Science **308**, 508 (2005).

[88] Y. S. Gui, L. Bai, and C.-M. Hu, Sci. China Physics, Mech. Astron. **56**, 124 (2012).

[89] W. Zhao and G. Prenat, *Spintronics-based Computing* (Springer, 2015).

[90] S. Bhatti, R. Sbiaa, A. Hirohata, H. Ohno, S. Fukami, and S. N. Piramanayagam, Mater. Today **20**, 530 (2017).

[91] S. Maekawa, S. O. Valenzuela, E. Saitoh, and T. Kimura, eds., *Spin Current* (Oxford University Press, 2012).

[92] G. E. Uhlenbeck and S. Goudsmit, Nature **117**, 264 (1926).

[93] S. Goudsmit and G. E. Uhlenbeck, Physica **6**, 273 (1926).

[94] G. E. Uhlenbeck and S. Goudsmit, Naturwissenschaften **13**, 953 (1925).

[95] W. Gerlach and O. Stern, Zeitschrift für Phys. **9**, 353 (1922).

[96] W. Gerlach and O. Stern, Zeitschrift für Phys. **9**, 349 (1922).

[97] W. Gerlach and O. Stern, Zeitschrift für Phys. **8**, 110 (1922).

[98] L. Landau and E. Lifshitz, Phys. Z. Sowjetunion **169**, 14 (1935).

[99] T. Gilbert, IEEE Trans. Magn. **40**, 3443 (2004).

[100] M. C. Hickey and J. S. Moodera, Phys. Rev. Lett. **102**, 137601 (2009), arXiv:0812.3184.

[101] R. M. White, *Quantum Theory of Magnetism* (Springer, 2007).

[102] S. A. Wolf, D. D. Awschalom, R. A. Buhrman, J. M. Daughton, V. Molnár, M. L. Roukes, A. Y. Chtchelkanova, and D. M. Treger, Science **294**, 1488 (2001).

[103] S. A. Wolf, A. Y. Chtchelkanova, and D. M. Treger, IBM J. Res. Dev. **50**, 101 (2006).

[104] C. Chappert, A. Fert, and F. N. Van Dau, Nat. Mater. **6**, 813 (2007).

[105] J. F. Gregg, Nat. Mater. **6**, 798 (2007).

[106] S. Bandhopadhyaya and M. Cahay, *Introduction to Spintronics* (CRC Press, 2008).

[107] M. W. Wu and A. Hoffmann, eds., *Solid State Phys.*, Vol. 64 (Elsevier, 2013).

[108] M. N. Baibich, J. M. Broto, A. Fert, F. N. Van Dau, and F. Petroff, Phys. Rev. Lett. **61**, 2472 (1988).

[109] G. Binasch, P. Grünberg, F. Saurenbach, and W. Zinn, Phys. Rev. B **39**, 4828 (1989).

[110] G. Xiao, in *Handb. Spin Transp. Magn.*, edited by H.-J. M. Drouhin, J.-E. Wegrowe, and M. Razeghi (Chapman and Hall/CRC, 2011) pp. 665–684.

[111] J. Åkerman, in *Handb. Spin Transp. Magn.*, edited by H.-J. M. Drouhin, J.-E. Wegrowe, and M. Razeghi (Chapman and Hall/CRC, 2011) pp. 685–697.

[112] N. F. Mott, Proc. R. Soc. A Math. Phys. Eng. Sci. **156**, 368 (1936).

[113] E. Tsymbal and D. G. Pettifor, in *Solid State Phys.*, Vol. 56, edited by H. Ehrenreich and F. Spaepen (Academic Press, 2001) pp. 113–237.

[114] W. Thomson, Proc. R. Soc. London **8**, 546 (1856).

[115] Y. Kajiwara, K. Harii, S. Takahashi, J. Ohe, K. Uchida, M. Mizuguchi, H. Umezawa, H. Kawai, K. Ando, K. Takanashi, S. Maekawa, and E. Saitoh, Nature **464**, 262 (2010).

[116] G. F. Dionne, *Magnetic Oxides* (Springer, 2009).

[117] V. Cherepanov, I. Kolokolov, and V. L'vov, Phys. Rep. **229**, 81 (1993).

[118] M. A. Gilleo, in *Ferromagn. Mater.*, Vol. 2, edited by E. P. Wohlfarth (North-Holland, 1980) pp. 1–53.

[119] F. Bertaut and F. Forrat, C. R. Acad. Sci. Paris **242**, 382 (1956).

[120] S. Geller and M. A. Gilleo, Acta Crystallogr. **10**, 239 (1957).

[121] R. Metselaar and P. K. Larsen, Solid State Commun. **15**, 291 (1974).

[122] S. Wittekoek, T. J. Popma, J. M. Robertson, and P. F. Bongers, Phys. Rev. B **12**, 2777 (1975).

[123] F. J. Bruni, in *Cryst. Magn. Appl.*, edited by C. J. M. Rooijmans (Springer, 1978) pp. 53–70.

[124] A. Ramirez and R. Kleiman, J. Appl. Phys. **69**, 5252 (1991).

[125] E. E. Anderson, Phys. Rev. **134**, A1581 (1964).

[126] S. Geschwind and L. R. Walker, J. Appl. Phys. **30**, S163 (1959).

[127] S. Geller, J. Remeika, R. Sherwood, H. Williams, and G. Espinosa, Phys. Rev **137**, 1034 (1965).

[128] A. Janossy and P. Monod, Phys. Rev. Lett. **37**, 612 (1976).

[129] R. H. Silsbee, A. Janossy, and P. Monod, Phys. Rev. B **19**, 4382 (1979).

[130] Y. Tserkovnyak, A. Brataas, and G. Bauer, Phys. Rev. Lett. **88**, 117601 (2002), arXiv:cond-mat/011024.

[131] A. Brataas, Y. Tserkovnyak, G. E. W. Bauer, and B. I. Halperin, Phys. Rev. B. **66**, 060404(R) (2002), arXiv:cond-mat/0205028.

[132] M. V. Costache, M. Sladkov, S. M. Watts, C. H. Van Der Wal, and B. J. Van Wees, Phys. Rev. Lett. **97**, 216603 (2006), arXiv:cond-mat/0609089.

[133] X. Wang, G. E. W. Bauer, B. J. Van Wees, A. Brataas, and Y. Tserkovnyak, Phys. Rev. Lett. **97**, 216602 (2006).

[134] E. Saitoh, M. Ueda, H. Miyajima, and G. Tatara, Appl. Phys. Lett. **88**, 182509 (2006).

[135] Y. Tserkovnyak, A. Brataas, G. Bauer, and B. Halperin, Rev. Mod. Phys. **77**, 1375 (2005), arXiv:cond-mat/0409242.

[136] A. Brataas, Y. Tserkovnyak, G. E. W. Bauer, and P. J. Kelly, in *Spin Curr.*, edited by S. Maekawa, S. O. Valenzuela, E. Saitoh, and T. Kimura (Oxford University Press, 2012) pp. 87–135.

[137] Y. Shiomi and E. Saitoh, Phys. Rev. Lett. **113**, 266602 (2014).

[138] Y. Tserkovnyak, A. Brataas, and G. Bauer, Phys. Rev. B **66**, 224403 (2002), arXiv:cond-mat/0208091.

[139] S. Mizukami, Y. Ando, and T. Miyazaki, J. Magn. Magn. Mater. **226**, 1640 (2001).

[140] S. Mizukami, Y. Ando, and T. Miyazaki, Phys. Rev. B **66**, 104413 (2002).

[141] R. Urban, G. Woltersdorf, and B. Heinrich, Phys. Rev. Lett. **87**, 217204 (2001).

[142] B. Heinrich, Y. Tserkovnyak, G. Woltersdorf, A. Brataas, R. Urban, and G. E. W. Bauer, Phys. Rev. Lett. **90**, 187601 (2003), arXiv:cond-mat/0210588.

[143] K. Lenz, T. Toliński, J. Lindner, E. Kosubek, and K. Baberschke, Phys. Rev. B **69**, 144422 (2004).

[144] M. Tokaç, S. A. Bunyaev, G. N. Kakazei, D. S. Schmool, D. Atkinson, and A. T. Hindmarch, Phys. Rev. Lett. **115**, 056601 (2015).

[145] J. Li, L. R. Shelford, P. Shafer, A. Tan, J. X. Deng, P. S. Keatley, C. Hwang, E. Arenholz, G. van der Laan, R. J. Hicken, and Z. Q. Qiu, Phys. Rev. Lett. **117**, 076602 (2016).

[146] J. Sinova, S. O. Valenzuela, J. Wunderlich, C. H. Back, and T. Jungwirth, Rev. Mod. Phys. **87**, 1213 (2015), arXiv:1411.3249v1.

[147] M. I. D'yakonov and V. I. Perel, JETP Lett. **13**, 467 (1971).

[148] J. E. Hirsch, Phys. Rev. Lett **83**, 1834 (1999), arXiv:cond-mat/9906160.

[149] E. M. Chudnovsky, Phys. Rev. Lett. **99**, 206601 (2007), arXiv:0805.3724.

[150] E. M. Chudnovsky, Phys. Rev. B **80**, 153105 (2009), arXiv:0911.0396.

[151] Y. K. Kato, R. C. Myers, A. C. Gossard, and D. D. Awschalom, Science **306**, 1910 (2004).

[152] J. Wunderlich, B. Kaestner, J. Sinova, and T. Jungwirth, Phys. Rev. Lett. **94**, 047204 (2005), arXiv:cond-mat/0410295.

[153] C. P. Wen and C. P. Wen, IEEE Trans. Microw. Theory Tech. **17**, 1087 (1969).

[154] J. D. Jackson, *Classical Electrodynamics*, 3rd ed. (John Wiley & Sons, Inc., 1999).

[155] L. C. Andreani, in *Strong Light Matter Coupling*, edited by A. Auffèves, D. Gerace, M. Richard, S. Portolan, M. d. F. Santos, L. C. Kwek, and C. Miniatura (Word Scientific, 2014) Chap. 2.

[156] W. L. Barnes, A. Dereux, and T. W. Ebbesen, Nature **424**, 824 (2003).

[157] W. L. Barnes, J. Opt. A Pure Appl. Opt. **8**, S87 (2006).

[158] H. Deng, H. Haug, and Y. Yamamoto, Rev. Mod. Phys. **82**, 1489 (2010).

[159] G. Khitrova and H. M. Gibbs, Rev. Mod. Phys. **71**, 1591 (1999), arXiv:cond-mat/0402594v3.

[160] V. Timofeev and D. Sanvitto, *Exciton Plaritons in Microcavities* (Springer, 2013).

[161] K. B. Tolpygo, Ukranian J. Phys. **53**, 93 (2008).

[162] K. Huang, Nature **167**, 779 (1951).

[163] K. Huang, Proc. R. Soc. A Math. Phys. Eng. Sci. **208**, 352 (1951).

[164] C. H. Henry and J. J. Hopfield, Phys. Rev. Lett. **15**, 964 (1965).

[165] A. Hartstein, E. Burstein, A. A. Maradudin, R. Brewer, and R. F. Wallis, J. Phys. C Solid State Phys. **6**, 1266 (1973).

[166] M. G. Cottam and D. R. Tilley, *Introduction to Surface and Superlattice Excitations* (Cambridge University Press, 1989).

[167] M. I. Kaganov, N. B. Pustyl'nik, and T. I. Shalaeva, Physics-Uspekhi **40**, 181 (1997).

[168] R. W. Sanders, R. M. Belanger, M. Motokawa, V. Jaccarino, and S. M. Rezende, Phys. Rev. B **23**, 1190 (1981).

[169] R. Belanger, V. Jaccarino, and S. Geschwind, J. Magn. Magn. Mater. **31**, 681 (1983).

[170] R. E. Camley and D. L. Mills, Phys. Rev. B **26**, 1280 (1982).

[171] M. Jensen, S. Feiven, T. Parker, and R. Camley, Phys. Rev. B **55**, 2745 (1997).

[172] H. Georgi, Annu. Rev. Nucl. Part. Sci. **43**, 209 (1993).

[173] N. Arkani-Hamed, H. Georgi, and M. D. Schwartz, Ann. Phys. **305**, 96 (2003), arXiv:hep-th/0210184.

[174] C. P. Burgess, Living Rev. Relativ. **7**, 5 (2004), arXiv:gr-qc/0311082.

[175] B. D. Josephson, Phys. Lett. **1**, 251 (1962).

[176] L. Onsager, Phys. Rev. **65**, 117 (1944).

[177] M. E. Peskin and D. V. Schroeder, *An Introduction to Quantum Field Theory* (CRC Press, 1995).

[178] L. D. Landau and E. M. Lifshitz, *Mechanics*, 3rd ed. (Elsevier, 1976).

[179] L. Bai, K. Blanchette, M. Harder, Y. P. Chen, X. Fan, J. Q. Xiao, and C. M. Hu, IEEE Trans. Magn. **52**, 1000107 (2016).

[180] C. Kittel, Phys. Rev. **71**, 270 (1947).

[181] C. Kittel, Phys. Rev. **73**, 155 (1948).

[182] U. Fano, Phys. Rev. **124**, 1866 (1961).

[183] J.-P. Connerade, *Highly Excited Atoms* (Cambridge University Press, 1998).

[184] S. Kaur, *Study of on-chip cavity magnon polariton devices*, Master's, University of Manitoba (2017).

[185] D. M. Pozar, *Microwave Engineering*, 3rd ed. (John Wiley & Sons, Inc., 2005).

[186] I. S. Maksymov, J. Hutomo, D. Nam, and M. Kostylev, J. Appl. Phys. **117**, 193909 (2015), arXiv:1503.07282.

[187] Y. Cao, P. Yan, H. Huebl, S. T. B. Goennenwein, and G. E. W. Bauer, Phys. Rev. B **91**, 094423 (2015), arXiv:1412.5809.

[188] B. M. Yao, Y. S. Gui, Y. Xiao, H. Guo, X. S. Chen, W. Lu, C. L. Chien, and C.-M. Hu, Phys. Rev. B. **92**, 184407 (2015), arXiv:1509.05804.

[189] J. Krupka, P. Aleshkevych, B. Salski, P. Kopyt, and A. Pacewicz, Sci. Rep. **7**, 5750 (2017).

[190] A. Pacewicz, J. Krupka, B. Salski, P. Kopyt, and P. Aleshkevych, Phys. status solidi - Rapid Res. Lett. **12**, 1800144 (2018).

[191] L. Bai, P. Hyde, Y. S. Gui, C.-M. Hu, V. Vlaminck, J. E. Pearson, S. D. Bader, and A. Hoffmann, Phys. Rev. Lett. **111**, 217602 (2013), arXiv:1308.4041.

[192] E. Jaynes and F. Cummings, Proc. IEEE **51**, 89 (1963).

[193] M. Tavis and F. W. Cummings, Phys. Rev. **170**, 379 (1968).

[194] T. Holstein and H. Primakoff, Phys. Rev. **58**, 1098 (1940).

[195] N. Majlis, *The Quantum Theory of Magnetism* (World Scientific, 2000).

[196] M. P. Silverman, *More Than One Mystery: Explorations in Quantum Interference* (Springer, 1994).

[197] A. Kreisel, F. Sauli, L. Bartosch, and P. Kopietz, Eur. Phys. J. B **71**, 59 (2009), arXiv:0903.2847.

[198] D. F. Walls and G. J. Milburn, *Quantum Optics*, 2nd ed. (Springer, 2008).

[199] A. A. Clerk, M. H. Devoret, S. M. Girvin, F. Marquardt, and R. J. Schoelkopf, Rev. Mod. Phys. **82**, 1155 (2010).

[200] H.-P. Breuer and F. Petruccione, *The Theory of Open Quantum Systems* (Oxford University Press, 2002).

[201] B. Zare Rameshti, Y. Cao, and G. E. W. Bauer, Phys. Rev. B **91**, 214430 (2015), arXiv:1503.02419v1.

[202] V. V. Dodonov and A. V. Dodonov, Phys. Rev. B **96**, 054419 (2017).

[203] S. Kaur, B. M. Yao, J. W. Rao, Y. S. Gui, and C.-M. Hu, Appl. Phys. Lett. **109**, 032404 (2016).

[204] H. J. Juretschke, J. Appl. Phys. **31**, 1401 (1960).

[205] H. J. Juretschke, J. Appl. Phys. **34**, 1223 (1963).

[206] M. Johnson and R. H. Silsbee, Phys. Rev. Lett. **55**, 1790 (1985).

[207] M. V. Rybin, D. S. Filonov, P. A. Belov, Y. S. Kivshar, and M. F. Limonov, Sci. Rep. **5**, 8774 (2015), arXiv:1409.7511.

[208] C. Sames, H. Chibani, C. Hamsen, P. A. Altin, T. Wilk, and G. Rempe, Phys. Rev. Lett. **112**, 043601 (2014), arXiv:1309.2228.

[209] Y.-P. Wang, G.-Q. Zhang, D. Zhang, T.-F. Li, C.-M. Hu, and J. Q. You, Phys. Rev. Lett. **120**, 057202 (2018), arXiv:1707.06509.

[210] S. Ramo, J. R. Whinnery, and T. Van Duzer, *Fields and waves in communication electronics* (John Wiley & Sons, Inc., 1994).

[211] P. Hyde, L. Bai, M. Harder, C. Dyck, and C.-M. Hu, Phys. Rev. B **95**, 094416 (2017), arXiv:1703.00074.

[212] W. G. Egan and H. J. Juretschke, J. Appl. Phys. **34**, 1477 (1963).

[213] M. A. Gilleo and S. Geller, Phys. Rev. **110**, 73 (1958).

[214] M. Sparks, *Ferromagnetic Relaxation Theory* (McGraw Hill, 1964).

[215] P. J. Petersan and S. M. Anlage, J. Appl. Phys. **84**, 3392 (1998), arXiv:cond-mat/9805365.

[216] D. D. Stancil and A. Prabhakar, *Spin Waves: Theory and Applications* (Springer, 2009).

[217] J. F. Dillon, Phys. Rev. **105**, 759 (1957).

[218] S. Klingler, A. Chumak, T. Mewes, B. Khodadadi, C. Mewes, C. Dubs, O. Surzhenko, B. Hillebrands, and A. Conca, J. Phys. D. Appl. Phys. **48** (2015), arXiv:1408.5772.

[219] M. Harder, P. Hyde, L. Bai, C. Match, and C.-M. Hu, Phys. Rev. B **94**, 054403 (2016), arXiv:1606.03056.

[220] A. Azevedo, L. H. Vilela-Leão, R. L. Rodríguez-Suárez, A. F. Lacerda Santos, and S. M. Rezende, Phys. Rev. B **83**, 144402 (2011).

[221] M. Harder, Z. X. Cao, Y. S. Gui, X. L. Fan, and C.-M. Hu, Phys. Rev. B **84**, 054423 (2011), arXiv:1105.3236.

[222] A. Lagendijk and B. A. van Tiggelen, Phys. Rep. **270**, 143 (1996).

[223] R. L. Fagaly, Rev. Sci. Instrum. **77**, 1 (2006).

[224] R. Pauthenet, J. Appl. Phys. **29**, 253 (1958).

[225] P. F. Herskind, A. Dantan, J. P. Marler, M. Albert, and M. Drewsen, Nat. Phys. **5**, 494 (2009).

[226] B. A. Calhoun, J. Overmeyer, and W. V. Smith, Phys. Rev. **107**, 993 (1957).

[227] S. Datta and B. Das, Appl. Phys. Lett. **56**, 665 (1990).

[228] J. Nitta, T. Akazaki, H. Takayanagi, and T. Enoki, Phys. Rev. Lett. **78**, 1335 (1997).

[229] J. Slonczewski, J. Magn. Magn. Mater. **159**, L1 (1996).

[230] L. Berger, Phys. Rev. B **54**, 9353 (1996).

[231] L. Liu, R. A. Buhrman, and D. C. Ralph, (2011), arXiv:1111.3702.

[232] C. M. Bender and S. Boettcher, Phys. Rev. Lett. **80**, 5243 (1998), arXiv:physics/9712001.

[233] C. M. Bender, S. Boettcher, N. Maxico, and P. N. Meisinger, J. Math. Phys. **40**, 2201 (1999).

[234] I. Rotter, (2010), arXiv:1011.0645.

[235] W. D. Heiss, J. Phys. A Math. Theor. **45**, 444016 (2012), arXiv:1210.7536.

[236] M. Liertzer, L. Ge, A. Cerjan, A. D. Stone, H. E. Türeci, and S. Rotter, Phys. Rev. Lett. **108**, 173901 (2012), arXiv:1109.0454.

[237] E.-M. Graefe, A. A. Mailybaev, and N. Moiseyev, Phys. Rev. A **88**, 033842 (2013), arXiv:1207.5235.

[238] J. Doppler, A. A. Mailybaev, J. Böhm, U. Kuhl, A. Girschik, F. Libisch, T. J. Milburn, P. Rabl, N. Moiseyev, and S. Rotter, Nature **537**, 76 (2016), arXiv:1603.02325.

[239] T. Kato, *Perturbation Theory for Linear Operators* (Springer, 1966).

[240] M. Philipp, P. von Brentano, G. Pascovici, and A. Richter, Phys. Rev. E **62**, 1922 (2000).

[241] C. Dembowski, B. Dietz, H.-D. Gräf, H. L. Harney, A. Heine, W. D. Heiss, and A. Richter, Phys. Rev. Lett. **90**, 034101 (2003), arXiv:nlin/0212023.

[242] B. Dietz, T. Friedrich, J. Metz, M. Miski-Oglu, A. Richter, F. Schäfer, and C. A. Stafford, Phys. Rev. E **75**, 027201 (2007), arXiv:cond-mat/0612547.

[243] B. Peng, S. K. Özdemir, S. Rotter, H. Yilmaz, M. Liertzer, F. Monifi, C. M. Bender, F. Nori, and L. Yang, Science **346**, 328 (2014), arXiv:1410.7474.

[244] B. Zhen, C. W. Hsu, Y. Igarashi, L. Lu, I. Kaminer, A. Pick, S.-L. Chua, J. D. Joannopoulos, and M. Soljačić, Nature **525**, 354 (2015), arXiv:1504.00734.

[245] M. Khanbekyan, H. A. M. Leymann, C. Hopfmann, A. Foerster, C. Schneider, S. Höfling, M. Kamp, J. Wiersig, and S. Reitzenstein, Phys. Rev. A **91**, 043840 (2015).

[246] C. Hahn, Y. Choi, J. W. Yoon, S. H. Song, C. H. Oh, and P. Berini, Nat. Commun. **7**, 12201 (2016).

[247] H. Xu, D. Mason, L. Jiang, and J. G. E. Harris, Nature **537**, 80 (2016), arXiv:1602.06881.

[248] N. R. Bernier, L. D. Tóth, A. K. Feofanov, and T. J. Kippenberg, (2017), arXiv:1709.02220.

[249] W. Chen, S. K. Özdemir, G. Zhao, J. Wiersig, and L. Yang, Nature **548**, 192 (2017).

[250] W. D. Heiss, Phys. Rev. E **61**, 929 (2000), arXiv:quant-ph/9909047.

[251] W. Heiss, Eur. Phys. J. D **7**, 1 (1999), arXiv:quant-ph/9901023.

[252] C. Dembowski, H. D. Gräf, H. L. Harney, A. Heine, W. D. Heiss, H. Rehfeld, and A. Richter, Phys. Rev. Lett. **86**, 787 (2001).

[253] M. Aspelmeyer, T. J. Kippenberg, and F. Marquard, *Cavity Optomechanics*, edited by M. Aspelmeyer, T. J. Kippenberg, and F. Marquardt (Springer, 2014).

[254] M. Aspelmeyer, T. J. Kippenberg, and F. Marquardt, Rev. Mod. Phys. **86**, 1391 (2014), arXiv:0712.1618.

[255] R. Chirla, A. Manolescu, and C. P. Moca, Phys. Rev. B **93**, 155110 (2016), arXiv:1512.08093.